Version 10.0
December 2007

Near Infrared Camera and Multi-Object Spectrometer Instrument Handbook for Cycle 17

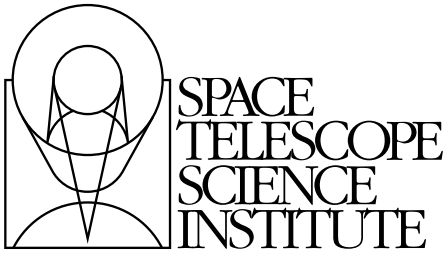

Space Telescope Science Institute
3700 San Martin Drive
Baltimore, Maryland 21218
help@stsci.edu

Operated by the Association of Universities for Research in Astronomy, Inc., for the National Aeronautics and Space Administration

User Support

For prompt answers to questions, please contact the STScI Help Desk.

- **E-mail:** help@stsci.edu
- **Phone:** (410) 338-1082
  (800) 544-8125 (U.S., toll free)

World Wide Web

Information and other resources are available on the NICMOS World Wide Web site:

- **URL:** http://www.stsci.edu/hst/nicmos

Revision History

Version	Date	Editors
10.0	December 2007	E. Barker, T. Dahlen, A. Koekemoer, L. Bergeron, R. de Jong, H. McLaughlin, N. Pirzkal, B. Shaw, T. Wiklind
9.0	October 2006	E. Barker, N. Pirzkal, K. Noll, S. Arribas, L. Bergeron, R. de Jong, A. Koekemoer, H. McLaughlin, T. Wiklind, C. Xu
8.0	October 2005	A. Schultz, K. Noll, E. Barker, S. Arribas, L. Bergeron, R. de Jong, S. Malhotra, B. Mobasher, T. Wiklind, C. Xu
7.0	October 2004	K. Noll, A. Schultz, E. Roye, S. Arribas, L. Bergeron, R. de Jong, S. Malhotra, B. Mobasher, T. Wiklind, C. Xu
6.0	October 2003	E. Roye, K. Noll, S. Malhotra, D. Calzetti, S. Arribas, L. Bergeron, T. Böker, M. Dickinson, B. Mobasher, L. Petro, A. Schultz, M. Sosey, C. Xu
5.0	October 2002	S. Malhotra, L. Mazzuca, D. Calzetti, S. Arribas, L. Bergeron, T. Böker, M. Dickinson, B. Mobasher, K. Noll, L. Petro, E. Roye, A. Schultz, M. Sosey, C. Xu
4.1	May 2001	A. Schultz, S. Arribas, L. Bergeron, T. Böker, D. Calzetti, M. Dickinson, S. Holfeltz, B. Monroe, K. Noll, L. Petro, M. Sosey
4.0	May 2000	T. Böker, L. Bergeron, D. Calzetti, M. Dickinson, S. Holfeltz, B. Monroe, B. Rauscher, M. Regan, A. Sivaramakrishnan, A. Schultz, M. Sosey, A. Storrs
3.0	June 1999	D. Calzetti, L. Bergeron, T. Böker, M. Dickinson, S. Holfeltz, L. Mazzuca, B. Monroe, A. Nota, A. Sivaramakrishnan, A. Schultz, M. Sosey, A. Storrs, A. Suchkov.
2.0	July 1997	J.W. MacKenty, C. Skinner, D. Calzetti, and D.J. Axon
1.0	June 1996	D.J. Axon, D. Calzetti, J.W. MacKenty, C. Skinner

Citation

In publications, refer to this document as:
Barker, E., Dahlen, T., et al. 2007, "NICMOS Instrument Handbook", Version 10.0, (Baltimore: STScI).

Send comments or corrections to:
Space Telescope Science Institute
3700 San Martin Drive
Baltimore, Maryland 21218
E-mail: help@stsci.edu

Table of Contents

Acknowledgments

The technical and operational information contained in this Handbook is the summary of the experience gained both by members of the STScI NICMOS group and by the NICMOS IDT (P.I.: Rodger Thompson, U. of Arizona) encompassing Cycle 7, Cycle 7N and Cycles 11-15. Special thanks are due to Marcia Rieke, Glenn Schneider and Dean Hines (U. of Arizona), whose help has been instrumental in many sections of this Handbook. We are also indebted to Wolfram Freudling (ST-ECF) for major contributions to the section on the NICMOS grisms.

We also appreciate the contributions of Ilana Dashevsky, Tom Wheeler, and Susan Rose.

CHAPTER 1:

Introduction and General Considerations

In this chapter . . .

The Near Infrared Camera and Multi-Object Spectrometer, NICMOS, provides HST with infrared imaging and spectroscopic capabilities between 0.8 and 2.5 microns. Above the earth's atmosphere, NICMOS provides access to this complete spectral range without hindrance from atmospheric emission or absorption at a sensitivity and angular resolution not possible from the ground. The sky background for NICMOS is much more stable and 100 to 300 times lower in the *J* and *H* bands than for ground-based telescopes (refer to Figure 4.17). It is a factor of 1.5 to 2 times lower in the *K* band.

NICMOS, which operated from February 1997 until November 1998 using an onboard exhaustible cryogen, was revived with the installation of the NICMOS Cooling System (NCS) during the Servicing Mission SM3B, in February 2002. The NCS provides active cooling through a series of closed circuit loops containing cryogenic gas.

This Handbook provides the instrument specific information needed to propose HST observations (Phase I), design accepted proposals (Phase II, in conjunction with the Phase II Proposal Instructions), and understand NICMOS in detail. The Handbook has been revised from its original versions to include the performance with the NCS.

This chapter explains the layout of the Handbook and how to get additional help and information through the Help Desk and STScI World Wide Web pages. It also lists the supported capabilities of NICMOS and includes basic recommendations on how to use the instrument.

1.1 Purpose

The *NICMOS Instrument Handbook* is the basic reference manual for the Near Infrared Camera and Multi-Object Spectrometer and describes the instrument's properties, performance, and operations. A description of the image reduction and calibration can be found in the *NICMOS Data Handbook*. The Handbooks are maintained by the NICMOS Instrument Group at STScI.

We designed the document to serve three purposes:

- To provide instrument-specific information for preparing observing proposals with NICMOS.
- To provide instrument-specific information to support the design of Phase II programs for accepted NICMOS proposals (in conjunction with the Phase II Proposal Instructions).
- To provide technical information about the current operation and performance of the instrument, which can help in understanding problems and interpreting data acquired with NICMOS.

This Handbook is not meant to serve as a manual for the reduction and analysis of data taken with NICMOS. For this, please refer to the *HST Data Handbook*.

Document Conventions

This document follows the usual STScI convention in which terms, words, and phrases which are to be entered by the user in a literal way on a proposal are shown in a typewriter font (e.g., `SAMP-SEQ=STEP16`, `MULTIACCUM`). Names of software packages or commands (e.g., **synphot**) are given in bold type.

Wavelength units in this Handbook are in microns (μm) and fluxes are given in Janskys (Jy), unless otherwise noted.

1.2 Layout

NICMOS provides direct imaging in broad, medium, and narrow-band filters at a range of spatial resolutions in the near infrared from 0.8 to 2.5 microns, together with broad-band imaging polarimetry, coronagraphic imaging and slitless grism spectroscopy. Figure 1.1 provides a road map to navigating this document.

The chapters of this Handbook are as follows:

- *Chapter 1:Introduction and General Considerations*, describes the Handbook layout, where to find help and additional documentation, and important advice for preparing NICMOS proposals.
- *Chapter 2:Overview of NICMOS*, provides an introduction to the capabilities of NICMOS under NCS operations, the basic physical and imaging layout, and a summary of the detectors' operations.
- *Chapter 3:Designing NICMOS Observations*, shows in tabular form the required steps for designing a NICMOS observing program, guides users through some of the technical details for choosing the optimal configuration for a given observation, and provides the reader with a "map" for the subsequent chapters.
- *Chapter 4:Imaging*, provides a description of NICMOS's imaging capabilities including camera resolutions and throughputs, image quality and effects of cosmic rays. The infrared background seen by NICMOS is also described here.
- *Chapter 5:Coronagraphy, Polarimetry and Grism Spectroscopy*, provides detailed information on coronagraphic imaging, grism spectroscopy, and polarimetry.
- *Chapter 6:NICMOS Apertures and Orientation*, describes the aperture definitions and the sky-projected orientation of the instrument.

- *Chapter 7:NICMOS Detectors*, describes the basic properties of the detectors used in the three cameras including their physical characteristics, capabilities and limitations. Performance descriptions are based on calibrations under NCS operations.
- *Chapter 8:Detector Readout Modes*, explains the data taking modes which take advantage of the non-destructive readout capabilities of the NICMOS arrays. While nearly all observers will choose to use `MULTIACCUM` mode, we give descriptions of other modes to help proposers/users choose the most appropriate ones for their observations.
- *Chapter 9:Exposure Time Calculations*, provides information for performing signal-to-noise calculations, either by using pencil and paper, or using software tools that are provided on the World Wide Web (WWW).
- *Chapter 10:Overheads and Orbit Time Determination*, provides information to convert from a series of planned science exposures to an estimate of the number of orbits, including spacecraft and NICMOS overheads. This chapter applies principally to the planning of Phase I proposals.
- *Appendix A:Imaging Reference Material*, provides summary information and filter transmission curves for each imaging filter, ordered by camera and increasing wavelength.
- *Appendix B:Flux Units and Line Lists*, provides formulae and tables for the conversion of flux units, and a list of common infrared spectral lines.
- *Appendix C:Bright Object Mode*, describes the BRIGHTOBJ read-out mode.
- *Appendix D:Techniques for Dithering, Background Measurement and Mapping*, describes the implementation of a pre-defined set of patterns which accomplish dithering and chopping from the field of interest, and allow easy generation of large mosaic images.
- *Appendix E:The NICMOS Cooling System*, describes the system that has cooled NICMOS since Cycle 11.

Figure 1.1: Roadmap for Using the NICMOS Instrument Handbook

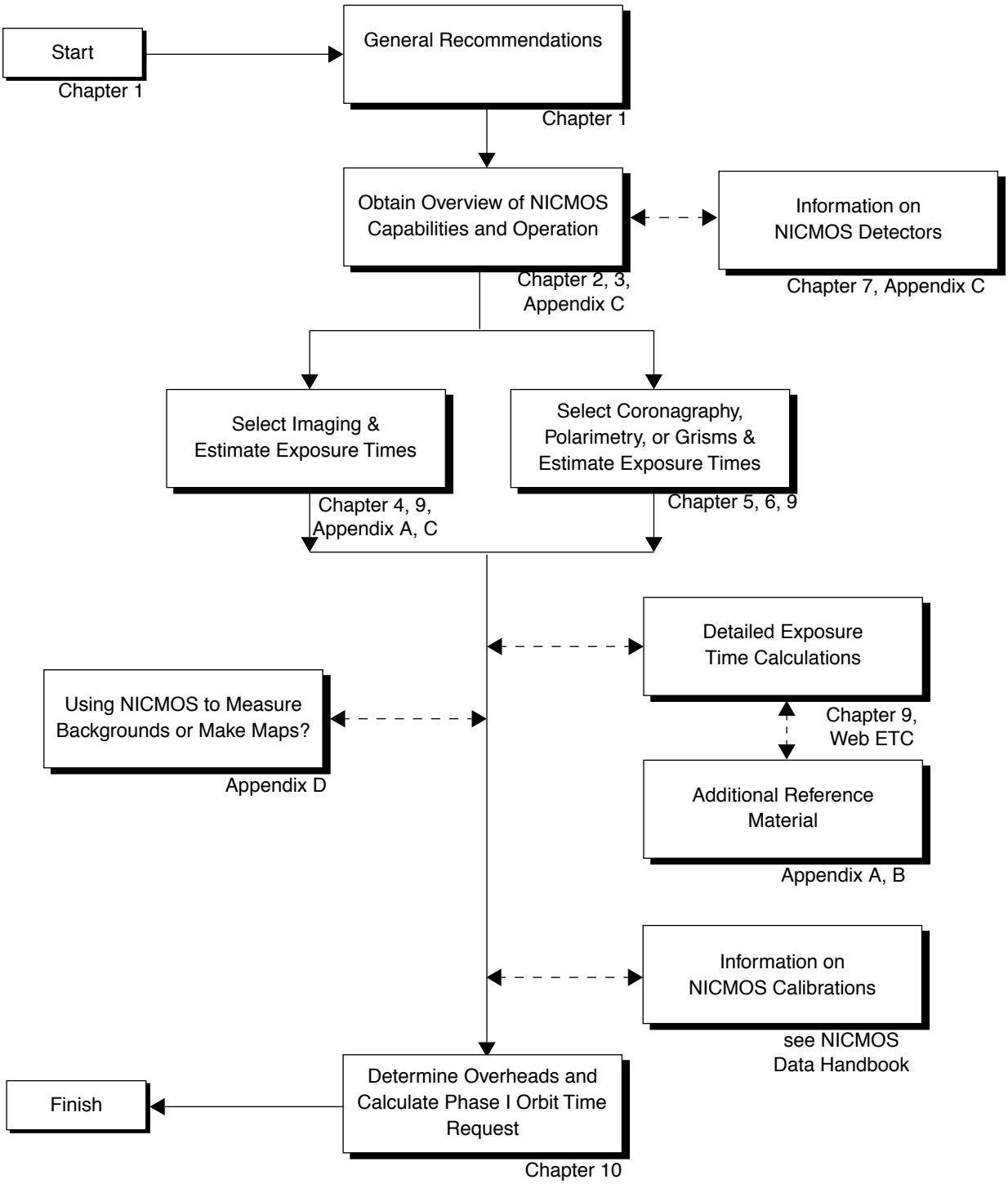

1.3 NICMOS Proposal Preparation

The *NICMOS Instrument Handbook* and the current *Call for Proposals* (CP) should be used when assembling NICMOS Phase I Proposals. The CP provides policy and instructions for proposing. In addition, the *HST Primer* provides a basic introduction to the technical aspects of HST and its instruments and explains how to calculate the appropriate number of orbits for your Phase I observing time requests. The *NICMOS Instrument Handbook* contains detailed technical information about NICMOS, describing its expected performance, and presenting suggestions for use.

If the Phase I proposal is accepted, the proposer will be asked to submit a Phase II program in which the exact configurations, exposure times and sequences of observations that NICMOS and the telescope should perform are specified. To assemble the Phase II program the observer is referred to the *NICMOS Instrument Handbook* and to the *Phase II Proposal Instructions*. These instructions describe the rules and syntax that apply to the planning and scheduling of NICMOS observations and provide relevant observatory information.

1.4 The Help Desk at STScI

STScI maintains a Help Desk. The Help Desk staff at STScI quickly provide answers to any HST-related topic, including questions regarding NICMOS and the proposal process. The Help Desk staff have access to all of the resources available at the Institute, and they maintain a database of answers so that frequently asked questions can be immediately answered. The Help Desk staff also provide STScI documentation, in either hardcopy or electronic form, including instrument science reports, instrument handbooks, and the like. Questions sent to the Help Desk are usually answered within two working days. Commonly, the Help Desk staff will reply with the answer to a question, but occasionally they will need more time to investigate the answer. In these cases, they will reply with an estimate of the time needed to supply a full answer.

We ask proposers to please send all initial inquiries to the Help Desk. If a question requires a NICMOS Instrument Scientist to answer it, the Help Desk staff will put a NICMOS Instrument Scientist in contact with the proposer. By sending requests to the Help Desk, proposers are guaranteed that someone will provide them with a timely response.

To contact the Help Desk at STScI:

- **Send e-mail (preferred method)**: help@stsci.edu
- **Phone**: (410) 338-1082

The Space Telescope European Coordinating Facility (ST-ECF) also maintains a help desk. European users should generally contact the ST-ECF for help: all other users should contact STScI. To contact the ST-ECF Help Desk:

- **Send e-mail**: stdesk@eso.org

1.5 The NICMOS Instrument Team at STScI

STScI provides a team of Instrument Scientists, Scientific Programmers, and Data Analysts who support the development, operation and calibration of NICMOS. The team is also responsible for supporting NICMOS users, as well as maintaining and updating the NICMOS Instrument and Data Handbooks.

1.6 Supporting Information and the NICMOS Web Site

The NICMOS Instrument Team at STScI maintains a World Wide Web page, as part of the STScI home page. The URL for the STScI NICMOS page is:

`http://www.stsci.edu/hst/nicmos`

1.7 NICMOS History in Brief

In order to understand the list of recommendations for proposal preparation given below, a brief history of the Instrument is presented here. A more detailed description of the NICMOS chronology, from installation on HST until its present status, is given in Chapter 2.

During its first operational period, which went from February 1997 (date of installation on HST) to January 1999, NICMOS was passively cooled by sublimating N_2 ice. Science observations were obtained from the beginning of June 1997 until mid-November 1998, during which period the cryogen kept the detectors' temperature around 60 K, with a slow upward trend, from 59.5 K to ~62 K, as the N_2 was sublimating. On January 3, 1999, the

cryogen was completely exhausted, marking the official end of NICMOS operations under this cooling regime. NICMOS was revived in March 2002 when the NICMOS Cooling System (NCS) was installed. NCS was activated and NICMOS was cooled down to the current operating temperature of 77.15 K.

NICMOS offers infrared capabilities in three cameras, NIC1, NIC2, and NIC3, characterized by three magnification factors (see Chapter 2). The three cameras had been built to be parfocal and to operate simultaneously. A few months before launch, however, the NICMOS dewar underwent thermal stresses, which made the three cameras no longer parfocal (although they still retain the capability to operate simultaneously). Even worse, shortly after installation on HST, the NICMOS dewar developed a deformation which had two consequences: 1. It pushed the NIC3 focus outside the range of the Pupil Alignment Mechanism (PAM); 2. It created a "heat sink", which caused the Nitrogen ice to sublimate at a quicker pace, thus shortening the lifetime of the instrument (from the expected 4.5 years down to about 2 years). A couple of months after the start of the short, the instrument stabilized at the operating configuration which remained during the duration of its 'cryogenic lifetime' with NIC1 and NIC2 in focus and practically parfocal, NIC3 out of focus relative to the other two cameras and with its best focus slightly outside the PAM range. During Cycle 7 and Cycle 7N, two observing campaigns were organized to obtain in-focus NIC3 observations by moving the HST secondary mirror.

The current NICMOS operating configuration is nearly the same as Cycle 7 and 7N: NIC1/NIC2 close to being parfocal and in focus, NIC3 is non-parfocal with the other two cameras with the optimal focus slightly out of the PAM range. NIC3 is perfectly usable with the best achievable focus. See Chapter 4 for NIC3 operations in Cycle 11 and subsequent.

1.8 Three-Gyro Guiding

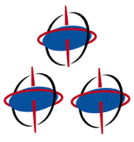

We anticipate that all HST observations in Cycle 17 will be undertaken in the Three-Gyro Science Mode, providing greater scheduling flexibility and greater sky coverage (at any epoch) than in Cycles 14, 15 and 16. Proposers should plan their observations accordingly, using the Target Availability Table in the Primer (Table 6.1) and the visibility tools on the HST Phase I Proposal Roadmap Web site.

1.9 Recommendations for Proposers

We give here a summary of general recommendations for both Phase I and Phase II proposal preparation. Recommendations are based our experience with NICMOS. However, observers are strongly advised to read the technical sections that follow in order to develop an optimal observation strategy based on the demands of their individual scientific goals. Also the *Advisories* page maintained on the NICMOS WWW site should be consulted for updates.

Recommendations for Phase I proposals:

- NIC1 (NIC2) offers diffraction-limited capabilities at *J*- (*H*-) band and longer wavelengths, while NIC3 offers high sensitivity (due to the lower angular resolution) with the largest field-of-view among the three cameras (see Section 2.3.2). In particular, NIC3 reaches fainter magnitudes than the other two cameras (for the same exposure time) for observations which are *not* limited by photon noise from source + background, i.e. where read-out or dark noise are significant. This is true for most observations of faint targets. However, the poor spatial sampling of NIC3 can limit its sensitivity for faint point sources, and also limits photometric accuracy for point sources.
- When choosing NIC3, proposers should be aware that this camera is slightly out-of-focus, with a typical loss of peak flux around 20% and a loss of encircled energy of about 10%–15% at 0.2" radius. Chapter 4 should be consulted for the detailed performance of the out-of-focus NIC3.
- The highest sensitivity gain relative to ground-based observations is at wavelengths shorter than 1.8 μm. The background at *J* and *H* seen by HST is a few hundred times smaller than at ground-based observatories. The background at *K* is only marginally better on HST, due to the telescope's thermal emission. However, observations in the thermal regime (longward of 1.8 μm) may be more advantageous with NICMOS if high angular resolution is a requirement for the science goal. Also, with NICMOS, one gains in stability of the thermal background.
- Observations of extended sources in the thermal regime (longward of 1.8 μm) may need to obtain background observations as well (chopping off the target). Given the stability of the thermal background, however, it will not be necessary to get background measurements more frequently than once per orbit. For point sources or extended sources which do not fill the camera field-of-view, images of the thermal background can be obtained with dithering (see recommendations below).

- For the purpose of removing cosmic rays, photon and cosmic-ray persistence, detector artifacts, and for averaging out flat-field sensitivity variations, observers are strongly advised to *dither* an observation as much as possible. This implies dividing single-orbit observations into at least three exposures and multi-orbit observations into two exposures per orbit. The general advice of dithering is generally not applicable to observations of faint sources around/near bright ones. If the bright source saturates the detector, the saturated pixels will be affected by persistence; in this case, the observers have two options: 1. Not dithering, to avoid placing the faint target on the saturated pixels; 2. Dithering by large amounts (by roughly one full detector quadrant) to move away from the persistence-affected region.
- The dithering requirement poses a practical upper limit of ~1,500 seconds to the longest integration time for a *single* exposure. This is roughly equivalent to having 2 exposures per orbit. Observers wishing to detect faint targets should work out their S/N requirements by determining (e.g., with the ETC) the S/N achieved in a single exposure and then co-adding *n* exposures according to $\sqrt{n}$, until the desired S/N is achieved. The latter is an essential step given the large read-out noise of the NICMOS detectors.
- In the case of crowded fields, observers are advised to dither their observations with sub-pixel sampling. In post-processing, the images should be combined with the MultiDrizzle software (Koekemoer *et al.*, 2002 HST Calibration Workshop, p337), otherwise the limiting sensitivity of NICMOS will not be reached due to PSF overlap and confusion.
- Proposers who want to use the NIC3 grisms should be aware that the spectral resolution quoted in the Handbook (R~200) is *per pixel*; the actual resolution, calculated over 2 pixels, is R~100.
- Observers proposing to use the NICMOS coronagraphic hole may want to consider observing the same object twice in the same orbit, or back-to-back in adjacent orbits, with an in-between roll of the spacecraft for optimal PSF subtraction.
- Observers proposing to use the NICMOS coronagraphic hole may want to consider adding contemporary flat-field observations.

Recommendations for Phase II proposals:

- For fields containing faint targets only, the linear `MULTIACCUM` sequences (`SPARS`...) should be preferred. They are best suited for removing instrumental effects from the astronomical data. However, for fields containing both bright and faint sources, logarithmic

sequences should be preferred (`STEP`...), as they offer the largest dynamic range and allow the calibration software to recover saturated targets.

- When designing dithering patterns, observers should take into account that the sensitivity across each detector changes by as much as a factor ~2.5 at short wavelengths and by a factor ~2 at long wavelengths. The sensitivities used in the ETC and in this Handbook are average values across each detector. The sensitivity variations will mostly affect observers interested in the full field-of-view.
- The NIC3 PSF is undersampled and intrapixel sensitivity variations are large in this camera (see NICMOS ISR 2003-009). Photometry on point sources can vary by >0.2 mag in *J* and up to 0.2 mag in *H* depending on the placement within a pixel. Observers are encouraged to consider sub-pixel dithering in their NIC3 observations; 4–6 dithering positions minimum are recommended.
- The bottom 10–15 rows of the three cameras' fields of view are somewhat vignetted and interesting targets should not be placed in this region.
- For coronagraphic observations: coronagraphic hole movements and HST focus changes (breathing) will result in residual noise during PSF subtraction. PSF stars should be observed close in time to the primary target.
- HST absolute pointing is only good to about 1 arcsecond ($1\sigma = 0.33''$); dithering patterns should be designed to place science targets away from the edges of the cameras by at least this amount.

1.10 Supported and Unsupported NICMOS Capabilities

As was done for all the HST instruments for past Cycles, we have established a set of core scientific capabilities of NICMOS which will be supported. These capabilities cover an enormous range of science applications.

Supported capabilities include:

- NIC1, NIC2, and NIC3 observations in any filter or polarizer/grism. NIC3 comes "as is", namely slightly out-of-focus (see Chapter 4 for a detailed explanation of the NIC3 capabilities).
- `MULTIACCUM` and `ACCUM` detector readout modes (see Chapter 8 for a discussion of the problems that can be faced when using `ACCUM` mode).
  - The defined `MULTIACCUM` `SAMP-SEQ` exposure time sequences.
  - A subset of the `ACCUM` exposure times as defined in Chapter 8 with NREAD=1 only.
- Coronagraphic observations, including on-board target acquisitions.

Two additional capabilities are "available", but not supported for Cycle 17. The use of these capabilities requires approval from STScI and detailed support for calibration will not be provided.

The unsupported ("available") capabilities are:

- `BRIGHTOBJ` readout mode.

The use of this capability can be proposed upon consultation with a NICMOS Instrument Scientist, and is useful only for target acquisition of extremely bright sources for coronagraphic observations. The use of this capability is strongly discouraged if the acquisition of a target for coronagraphic observations can be obtained with any of the supported capabilities. Proposals which include this unsupported NICMOS capability must include a justification of why the target acquisition cannot be done with a supported configuration, and must justify the added risk of using an unsupported mode in terms of the science payback.

- `DEFOCUS` mode for de-focused observations.

Starting in Cycle 17 there will be an available observing mode for de-focused observations. This mode is classified as "available but unsupported", which means that it is available to observers who request it, but it is not supported through a full calibration program, other than basic verification that the mechanism successfully moves to the commanded de-focused position. When in use, the PAM mechanism will move to a pre-determined position, leading to a decrease in the count rate. The

amount of decrease depends on the filter in use. The de-focus mode can help prevent saturation when short exposures are necessitated by bright objects, but will suffer from a degraded image quality. To implement this mode, the observer should contact the Program Coordinator.

CHAPTER 2:

Overview of NICMOS

In this chapter . . .

2.1 Instrument Capabilities

NICMOS, the Near Infrared Camera and Multi-Object Spectrometer, is an HST axial instrument, containing three cameras designed for simultaneous operation. The NICMOS optics offer three adjacent but not spatially contiguous fields-of-view of different image scales. The instrument covers the wavelength range from 0.8 to 2.5 microns, and contains a variety of filters, grisms, and polarizers. Each camera carries a complement of 19 optical elements, selected through independent filter wheel mechanisms, one per camera. In order to allow operation of the NICMOS detectors and to minimize the thermal background of the instrument, NICMOS needs to be cooled to cryogenic temperatures. The basic capabilities of the instrument are presented in Table 2.1.

IR imaging: NICMOS provides its highest sensitivity from 1.1 to ~2 microns, where it is superior to an 8m class telescope. Chapter 4 discusses the overall throughput of NICMOS and the optical elements available in each camera. The low background which HST offers between 0.8 and 2 microns allows deep photometry. Our estimates of limiting sensitivities per pixel for a 5σ detection in a 3,600 second integration, at an operating temperature of 77.15K, are given in Table 2.2. Users should note that an integration time of 3600 sec is not practical and is for illustrative purposes.

Table 2.1: Overview NICMOS Capabilities

Mode	NIC1	NIC2	NIC3	Comments
Imaging				
• FOV (arcsec)	11×11	19.2×19.2	51.2×51.2	
• Scale (arcsec/pixel)	0.043	0.075	0.2	
• Sensitivity limit (J, H, K)[a]	25.2,23.7,—	26.3,24.8,20.1	26.5,25.6,20.7	S/N = 5, t_{exp} = 3600 s
• Diffraction limit (μm)	1.0	1.75	—	
Grism Spectroscopy				
• Type			MOS slitless	
• R			200	per pixel
• Δλ (μm)			0.8–1.2	G096
			1.1–1.9	G141
			1.4–2.5	G206
• Magnitude limit (Vega H-band)[a]			20.5,20.4,16.6	A0V, S/N=5, t_{exp} = 3600 s
Polarimetry				
• Filter angles (deg)	0, 120, 240	0, 120, 240		
• Δλ (μm)	0.8–1.3	1.9–2.1		
Coronagraphy				
• hole radius (arcsec)		0.3		cold mask

a. Limiting magnitudes are from the NICMOS ETC (see Chapter 9). Infrared passbands (J,H,K) are defined by Bessell and Brett (1988, PASP, 100, 1134).

- ***Grism Spectroscopy***: Camera 3 has three grisms which provide a multi-object spectroscopic capability with a resolving power of R~200 per pixel over the full field of view of the camera. Their wavelength ranges are 0.8 to 1.2 microns, 1.1 to 1.9 microns, and 1.4 to 2.5 microns. Because the grisms are slitless, the spectra of spatially resolved objects are confused and multiple objects can overlap.
- ***Imaging Polarimetry***: Three polarizing filters with pass directions of 0, 120, and 240 degrees are provided for the wavebands 0.8–1.2 microns in Camera 1 and 1.9–2.1 microns in Camera 2.
- ***Coronagraphy***: A 0.3 arcsec radius occulting hole and cold mask, in the intermediate resolution Camera 2, provide a coronagraphic imaging capability.

Chapter 5 discusses these three special capabilities in more detail.

Table 2.2: Limiting Sensitivities in Janskys for S/N = 5 detection of a point source in a standard aperture of diameter 0.5", 0.5", and 1" for NIC1, NIC2, and NIC3, respectively, for a 3600 sec exposure.[a,b].

Camera	Filter	Bandwidth (microns)	Limiting Sensitivity	
			Jansky	Approx. Mag.
NIC1	F110W	0.8–1.35	1.75×10^{-7}	J ≈ 25.2
NIC1	F160W	1.4–1.8	6.26×10^{-7}	H ≈ 23.7
NIC2	F110W	0.8–1.35	6.73×10^{-8}	J ≈ 26.3
NIC2	F160W	1.4–1.8	2.21×10^{-7}	H ≈ 24.8
NIC2	F237M	2.3–2.5	1.71×10^{-5}	K ≈ 20.1
NIC3	F110W	0.8–1.35	5.49×10^{-8}	J ≈ 26.5
NIC3	F160W	1.4–1.8	4.75×10^{-8}	H ≈ 25.6
NIC3	F240M	2.3–2.5	9.83×10^{-6}	K ≈ 20.7

a. S/N calculated for brightest pixel in point source image, using the NICMOS ETC for 77.15K temperature.
b. Limiting magnitudes are from the NICMOS ETC (Chapter 9). Infrared passbands (J,H,K) are defined by Bessell and Brett (1988, PASP, 100, 1134). A0V spectrum assumed to convert between NICMOS passband flux (in Jy) and conventional, Vega-normalized JHK magnitudes.

2.2 Heating, Cooling and Focus

After NICMOS was installed in HST, the dewar was planned to warm up to about 57 K, a temperature never reached during ground testing. The ice expansion caused by this temperature increase resulted in an additional dewar deformation, to the extent that one of the (cold) optical baffles made mechanical contact with the vapor-cooled shield (VCS). The resulting heat flow caused the ice to warm up beyond expectations, to about 60 K, which in turn deformed the dewar more. The motion history of NICMOS and the resulting image quality are discussed in Chapter 4 and a more detailed history of the dewar distortion can be found at:

http://www.stsci.edu/hst/nicmos/design/history

This unexpectedly large deformation had several undesirable effects, the most important of which are:

- The three cameras have significantly different foci, hence parallel observations are degraded. The difference between the NIC1 and NIC2 foci, however, is sufficiently small that an intermediate focus yields good quality images in both cameras.
- The NIC3 focus has moved outside of the range of the PAM. In an attempt to bring it to within the focus range, the secondary mirror was moved during two brief NIC3 campaigns in Cycle 7. During this time, HST performed exclusively NIC3 science, since no other HST instrument was in focus. Because of the extreme impact on all other instruments, no such campaigns are planned in the future. At the maximum PAM position, the degradation in terms of encircled energy at a 0.2" radius is only 5%. This is considered sufficiently small, and NIC3 will be offered “as is” in Cycle 11 and beyond.
- Each camera can be operated in a de-focused mode, where the PAM is set to a non-optimal position relative to mechanical zero. The offset positions are -3mm, -5mm and -0.5mm for NIC1, NIC2 and NIC3, respectively. This mode can be used in grism and imaging modes and is useful for increasing the efficiency when observing bright objects. The photons are spread over a larger area (more pixels), leading to longer exposure times before saturation is reached. In order to select the de-focus mode, the observer will need to contact the Program Coordinator.

The thermal short increased the heat flux into the inner shell (and therefore the solid nitrogen) by a factor of ~2.5 and thereby reduced the lifetime of NICMOS from 4.5 to ~2 years. The cryogen depleted in January 1999, and NICMOS was unavailable for science operation between January 1999 and June 2002, when the NICMOS cooling system (NCS) was activated and reached expected operating temperatures. The installation of the NCS, a mechanical cryocooler, re-enabled NICMOS operation and restored infrared capability to HST. The NCS is capable of cooling the NICMOS dewar to temperatures 75–86 K, significantly higher than during Cycle 7. Therefore, many NICMOS parameters are different from Cycle 7. Most notably, with the higher operating temperature, the detector quantum efficiency (DQE) increased by ~30–50%.

The temperature control provided by the NCS is good enough to keep the NICMOS temperature at 77.15±0.10 K, as measured by the mounting cup temperature sensor. However, there are indications of a slow drift between the actual temperature of the detectors and the temperature measured at the mounting cup. The NICMOS team is presently investigating this issue.

2.3 NICMOS Instrument Design

2.3.1 Physical Layout

NICMOS is an axial bay instrument which replaced the Faint Object Spectrograph (FOS) in the HST aft shroud during the Second HST Servicing Mission in February 1997. Its enclosure contains four major elements: a graphite epoxy bench, the dewar, the fore-optics bench, and the electronics boxes. The large bench serves to establish the alignment and dimensional stability between the HST optics (via the latches or fittings), the room temperature fore optics bench, and the cryogenic optics and detectors mounted inside the dewar. The NICMOS dewar was designed to use solid nitrogen as a cryogen for a design lifetime of approximately 4.5 ± 0.5 years. Cold gas vented from the dewar was used to cool the vapor cooled shield (VCS) which provides a cold environment for both the dewar and the transmissive optical elements (i.e., the filters, polarizers, and grisms). The VCS is itself enclosed within two layers of thermal-electrically cooled shells (TECs).

Figure 2.1 is an overview of the NICMOS instrument; Figure 2.2 shows details of the dewar. The external plumbing at the dewar aft end, which was used for the periodical recooling of the solid nitrogen during ground testing, now forms the interface to the NCS. During SM3B, the NCS was connected to the bayonet fittings of the NICMOS interface plate. This allows the NCS to circulate cryogenic Neon gas through the cooling coils in the dewar, thus providing the cooling power to bring the instrument into the temperature range required for operation. The concept and working principles of the NCS are discussed in Appendix E.

Figure 2.1: Instrument Overview

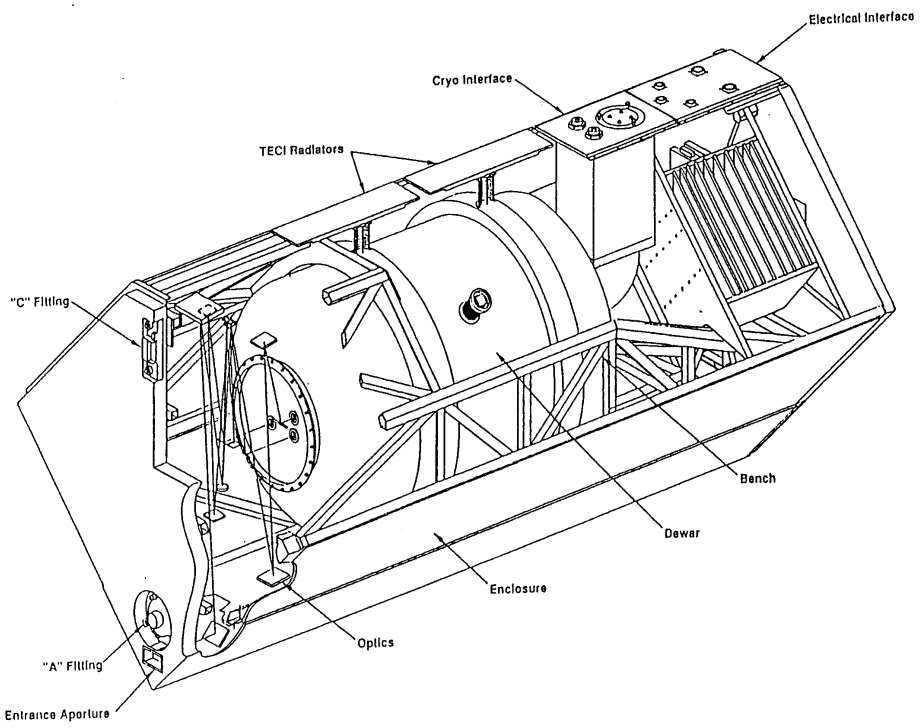

Figure 2.2: NICMOS Dewar

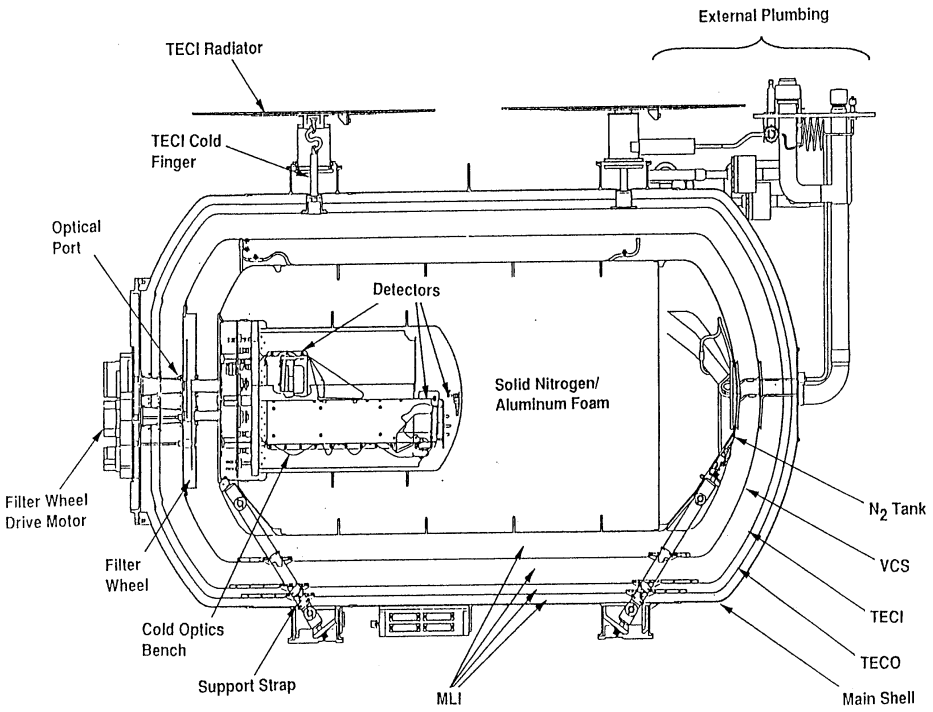

2.3.2 Imaging Layout

The NICMOS fore-optics assembly is designed to correct the spherically aberrated HST input beam. As shown in the left hand panel of Figure 2.3 it comprises a number of distinct elements. The Pupil Alignment Mechanism (PAM) directs light from the telescope onto a re-imaging mirror, which focuses an image of the Optical Telescope Assembly (OTA) pupil onto an internal Field-Offset Mechanism (FOM) with a pupil mirror that provides a small offset capability (26 arcsec). An internal flat field source is also included in the FOM assembly. In addition, the FOM provides correction for conic error in the OTA pupil.

After the FOM, the Field Divider Assembly (FDA) provides three separate but closely-spaced imaging fields, one for each camera (right hand panel of Figure 2.3). The dewar itself contains a series of cold masks to eliminate stray IR emission from peripheral warm surfaces.

A series of relay mirrors generate different focal lengths and magnifications for the three cameras, each of which contains a dedicated 256 × 256 pixel HgCdTe chip that is developed from the NICMOS 3 detector design. NICMOS achieves diffraction limited performance in the high resolution NIC1 longward of 1.0 microns, and in NIC2 longward of 1.75 microns.

Figure 2.3: Ray Diagrams of the NICMOS Optical Train. The left panel shows the fore-optics. The right panel shows the field divider and re-imaging optics for the three cameras.

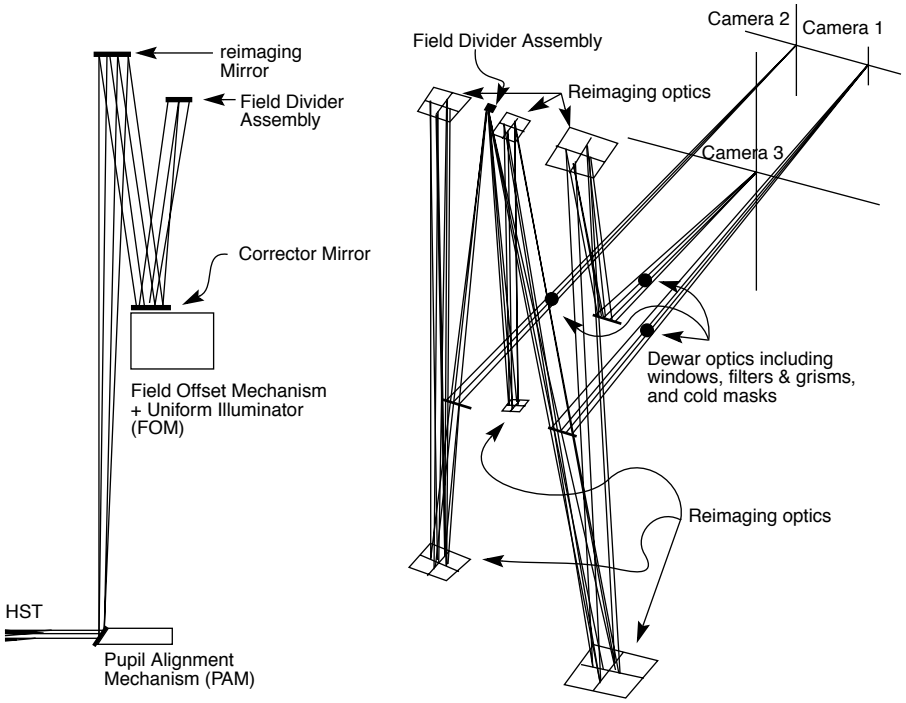

The operation of each camera is separate from the others which means that filters, integration times, readout times and readout modes can be different in each, even when two or three are used simultaneously. The basic imaging properties of each of the cameras are summarized in Table 2.3.

Table 2.3: Basic Imaging Parameters

Parameter	Camera 1	Camera 2	Camera 3
Pixel Size (arcsec)	0.043	0.075	0.2
Field of View (arcsec x arcsec)	11 × 11	19.2 × 19.2	51.2 × 51.2
f ratio	*f*/80	*f*/45.7	*f*/17.2
Diffraction Limited Wavelength (μm)	1.0	1.75	—

2.3.3 Camera NIC1

NIC1 offers the highest available spatial resolution with an 11 × 11 arcsec field of view and 43 milliarcsec sized pixels (equivalent to the WFPC2 PC pixel scale). The filter complement includes broad and medium band filters covering the spectral range from 0.8 to 1.8 microns and narrow band filters for Paschen α, He I, [Fe II] λ 1.64μm, and [S III] λ 0.953 μm, both on and off band. It is equipped with the short wavelength polarizers (0.8 to 1.3 microns).

2.3.4 Camera NIC2

NIC2 provides an intermediate spatial resolution with a 19.2 × 19.2 arcsec field of view and 75 milliarcsec pixels. The filters include broad and medium band filters covering the spectral range from 0.8 to 2.45 microns. The filter set also includes filters for CO, Brackett γ, H_2 S2 (1-0) λ 2.122 μm, Paschen α, HCO_2 + C_2, and the long wavelength polarizers (1.9–2.1 microns). Camera 2 also provides a coronagraphic hole with a 0.3 arcsec radius.

2.3.5 Camera NIC3

NIC3 has the lowest spatial resolution with a large 51.2 × 51.2 arcsec field of view and 200 milliarcsec pixels. It includes broad band filters covering the spectral range 0.8 to 2.3 microns, medium band filters for the CO band (and an adjacent shorter wavelength continuum region), and narrow band filters for H_2 S2 (1-0), [Si VI] λ 1.962 μm, Paschen-α, [Fe II] λ 1.64 μm, and He I λ 1.083 μm. Camera 3 also contains the multi-object

spectroscopic capability of NICMOS with grisms covering the wavelength ranges 0.8–1.2 microns, 1.1–1.9 microns, and 1.4–2.5 microns.

2.3.6 Location and Orientation of Cameras

The placement and orientation of the NICMOS cameras in the HST focal plane is shown in Figure 2.4. Notice that the cameras are in a straight line pointing radially outward from the center of the telescope focal plane. From the observer's point of view the layout of NICMOS is most relevant when trying to plan an observation of an extended source with all three cameras simultaneously. The user must then bear in mind the relative positions and orientations of the three cameras. The gaps between the cameras are large, and therefore getting good positioning for all cameras may be rather difficult.

The position of the NICMOS cameras relative to the HST focal plane (i.e., the FGS frame) depends strongly on the focus position of the PAM. Since independent foci and their associated astrometric solutions are supported for each camera, this is transparent to the observer. However, the relative positions of the NICMOS cameras in the focal plane could affect the planning of coordinated parallels with other instruments.

Figure 2.4: NICMOS Field Arrangement

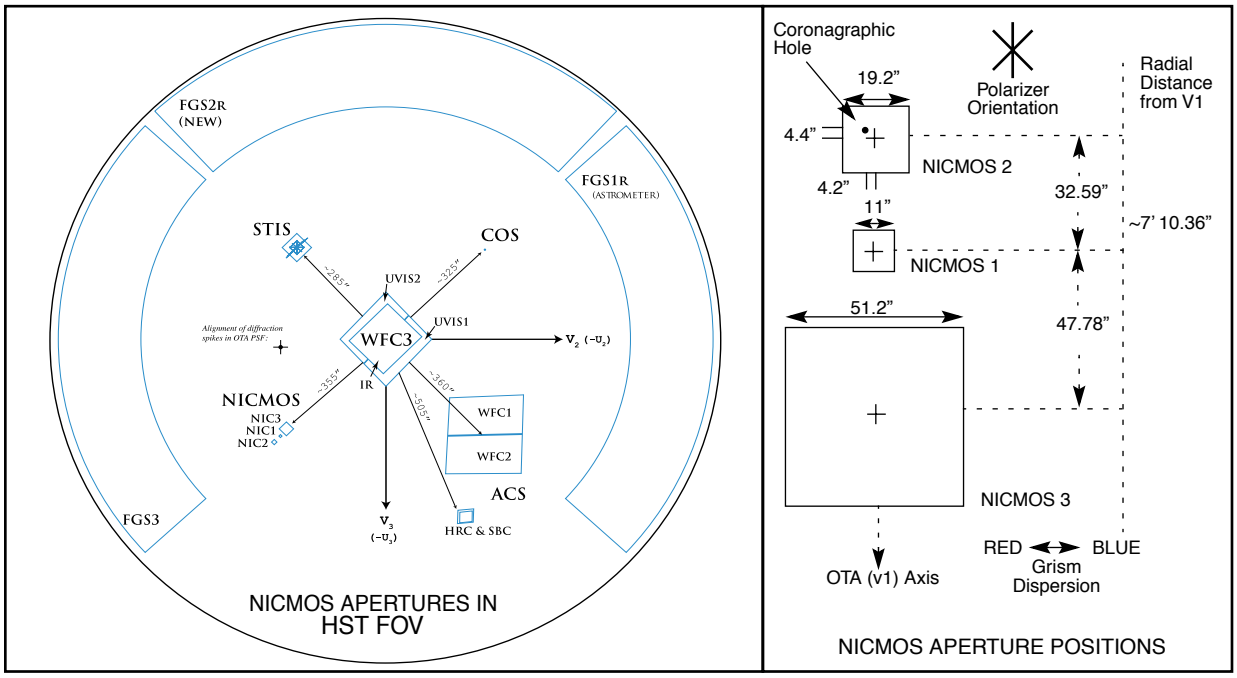

2.4 Basic Operations

In this section, we give a brief description of the basic operations of each NICMOS detector (see Chapter 7 for more details), and compare the infrared arrays to CCDs. We then discuss the target acquisition modes for coronagraphy (see Chapter 5 for a more extensive description of coronagraphy), as well as the simultaneous use of NIC1 and NIC2.

2.4.1 Detectors' Characteristics and Operations

NICMOS employs three low-noise, high QE, 256×256 pixel HgCdTe arrays. Active cooling provided by the NCS keeps the detectors' temperature at ~77.15 K. The detector design is based on the NICMOS3-type design, described in more detail in Chapter 7. Here we summarize the basic properties of the NICMOS detectors most relevant to the planning of observations.

The NICMOS detectors have dark current of about 0.1–0.2 electrons per second and the effective readout noise for a single exposure is approximately 30 electrons.

The NICMOS detectors are capable of very high dynamic range observations and have no count rate limitations in terms of detector safety. The dynamic range, for a single exposure, is limited by the depth of the full well, or more correctly by the onset of strong non-linearity, which limits the total number of electrons which can be accumulated in any individual pixel during an exposure. Unlike CCDs, NICMOS detectors do not have a linear regime for the accumulated signal; the low- and intermediate-count regime can be described by a quadratic curve and deviations from this quadratic behavior is what we define as 'strong non-linearity'. Current estimates under NCS operations give a value of ~120,000 electrons (NIC1 and NIC2) or 155,000 electrons (NIC3) for the 5% deviation from quadratic non-linearity. This non-linearity is corrected in the standard NICMOS pipeline reduction. See Section 4.2.4 for further discussion of the topic.

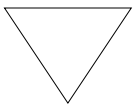

There are no bright object limitations for the NICMOS detectors. However, one must consider the persistence effect. See Section 4.6 Photon and Cosmic Ray Persistence for details.

NICMOS has three detector read-out modes that may be used to take data (see Chapter 8) plus a target acquisition mode (ACCUM, MULTIACCUM, BRIGHTOBJ, and ACQ).

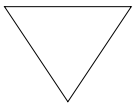

Only ACCUM, MULTIACCUM, and ACQ are supported in Cycle 11 and beyond and ACCUM mode observations are strongly discouraged.

The simplest read-out mode is ACCUM which provides a single integration on a source. A second mode, called MULTIACCUM, provides intermediate read-outs during an integration that subsequently can be analyzed on the ground. A third mode, BRIGHTOBJ, has been designed to observe very bright targets that would otherwise saturate the detector. BRIGHTOBJ mode reads-out a single pixel at a time. Due to the many resets and reads required to map the array there are substantial time penalties involved. BRIGHTOBJ mode may not be used in parallel with the other NICMOS detectors. BRIGHTOBJ mode appears to have significant linearity problems and has not been tested, characterized, or calibrated on-orbit.

Users who require time-resolved images will have to use MULTIACCUM where the shortest spacing between non-destructive exposures is 0.203 seconds.

MULTIACCUM *mode should be used for most observations*. It provides the best dynamic range and correction for cosmic rays, since post-observation processing of the data can make full use of the multiple readouts of the accumulating image on the detector. Exposures longer than about 10 minutes should always opt for the MULTIACCUM read-out mode, because of the potentially large impact of cosmic rays. To enhance the utility of MULTIACCUM mode and to simplify the implementation, execution, and calibration of MULTIACCUM observations, a set of MULTIACCUM sequences has been pre-defined (see Chapter 8). The observer, when filling out the Phase II proposal, needs only to specify the name of the sequence and the number of samples which should be obtained (which defines the total duration of the exposure).

2.4.2 Comparison to CCDs

These arrays, while they share some of the same properties as CCDs**,** are not CCDs and offer their own set of advantages and difficulties. Users unfamiliar with IR arrays should therefore not fall into the trap of treating them like CCDs. For convenience we summarize the main points of comparison:

- As with CCDs, there is read-noise (time-independent) and dark current noise (time-dependent) associated with the process of reading out the detector. The dark current associated with NICMOS arrays is quite substantial compared to that produced by the current generation of CCDs. In addition, there is an effect called *shading* which is a time-variable bias from the last read affecting the readout amplifiers.
- Unlike a CCD, the individual pixels of the NICMOS arrays are strictly independent and can be read non-destructively. Read-out modes have been designed which take advantage of the non-destructive read capabilities of the detectors to yield the optimum signal-to-noise for science observations (see Chapter 7, 8). Because the array elements are independently addressed, the NICMOS arrays do not suffer from some of the artifacts which afflict CCDs, such as charge transfer smearing and *bleeding* due to filling the wells. If, however, they are illuminated to saturation for sustained periods they retain a *memory (persistence)* of the object in the saturated pixels. This is only a concern for the photometric integrity of back to back exposures of very bright targets, as the ghost images take many minutes, up to one hour, to be flushed from the detectors.

2.4.3 Target Acquisition Modes

Most target acquisitions can be accomplished by direct pointing of the telescope. The user should use the Guide Star Catalog-II to ensure accurate target coordinates. Particular care must be exercised with targets in NIC1 due to its small field of view.

However, direct pointing will not be sufficient for coronagraphic observations since the achieved precision ($1\sigma = 0.33''$) is comparable to the size of the coronagraphic spot (0.3"). *Note that this is the HST pointing error only. Possible uncertainties in the target coordinates need to be added to the total uncertainty.*

There are three target acquisition options for coronagraphic observations, which are extensively discussed in Chapter 5:

- On-board acquisition (Mode-2 Acquisition). This commands NICMOS to obtain an image of the target and rapidly position the brightest source in a restricted field of view behind the coronagraphic hole. This is one of the pre-defined acquisition modes in the Phase II proposals (`ACQ` mode).
- The `RE-USE TARGET OFFSET` special requirement can be used to accomplish a positioning relative to an early acquisition image.
- A real time acquisition (`INT-ACQ`) can be obtained, although this is costly in spacecraft time and is a limited resource.

While `ACQ` mode is restricted to coronagraphic observations in Camera 2, the last two target acquisition modes may be useful for positioning targets where higher than normal (1–2 arcsec) accuracy is required (e.g., crowded field grism exposures).

2.4.4 Attached Parallels

While the three NICMOS cameras are no longer at a common focus, under many circumstances it is desirable to obtain data simultaneously in multiple cameras.

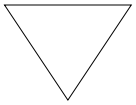

The foci of Cameras 1 and 2 are close enough that they can be used simultaneously, whereas Camera 3 should be used by itself.

Although some programs by their nature do not require more than one camera (e.g., studies of isolated compact objects), observers may nonetheless add exposures from the other camera to their proposals in order to obtain the maximum amount of NICMOS data consistent with efficiently accomplishing their primary science program. Internal NICMOS parallel observations obtained together with primary science observations will be known as *coordinated parallels* and will be delivered to the prime program's observer and will have the usual proprietary period.

CHAPTER 3:

Designing NICMOS Observations

In this chapter. ..

3.1 Overview of Design Process

In the preceding chapters, we provided an overview of the scientific capabilities of NICMOS and the basic layout and operation of the instrument. Subsequent chapters will provide detailed information about the performance and operation of the instrument. In this chapter, we briefly describe the conceptual steps which need to be taken when designing a NICMOS observing proposal. The scope of this description is to refer proposers to the relevant Chapters across the Handbook. The basic sequence of steps in defining a NICMOS observation are shown in a flow diagram in Figure 3.1, and are:

- Identify the science requirements and select the basic NICMOS configuration to support those requirements (e.g., imaging, polarimetry, coronagraphy). Select the appropriate camera, NIC1, NIC2 or NIC3 depending on needs and field of view. Please refer to the detailed accounts given in Chapter 4 and Chapter 5.
- Select the wavelength region of interest and hence determine if the observations will be Background or Read-Noise limited using the Exposure Time Calculator, which is available on the STScI NICMOS Web page (see also Chapter 9 and Appendix A).

- Establish which MULTIACCUM sequence to use. Detailed descriptions of these are provided in Chapter 8. This does not need to be specified in a Phase I proposal. However, if a readout mode other than MULTIACCUM is required, this should be justified in the Phase I proposal.
- Estimate the exposure time to achieve the required signal to noise ratio and check feasibility (i.e., saturation limits). To determine exposure time requirements and assess whether the exposure is close to the brightness and dynamic range limitations of the detectors, the Exposure Time Calculator (ETC) should be used (see Chapter 9).
- If necessary, a chop and dithering pattern should be chosen for better spatial sampling, to measure the background or to enable mapping, and to mitigate bad pixels. See Appendix D.
- If coronagraphic observations are proposed, additional target acquisition exposures will be required to center the target in the aperture to the accuracy required for the scientific goal (e.g., the proposer may wish to center the nucleus of a galaxy in a crowded field behind the coronagraphic spot). The target acquisition overheads must be included in the accounting of orbits.
- Calculate the total number of orbits required, taking into account the overheads. In this, the final step, all the exposures (science and non-science, alike) are combined into orbits, using tabulated overheads, and the total number of orbits required are computed. Chapter 10 should be used for performing this step.

Figure 3.1: Specifying a NICMOS Observation

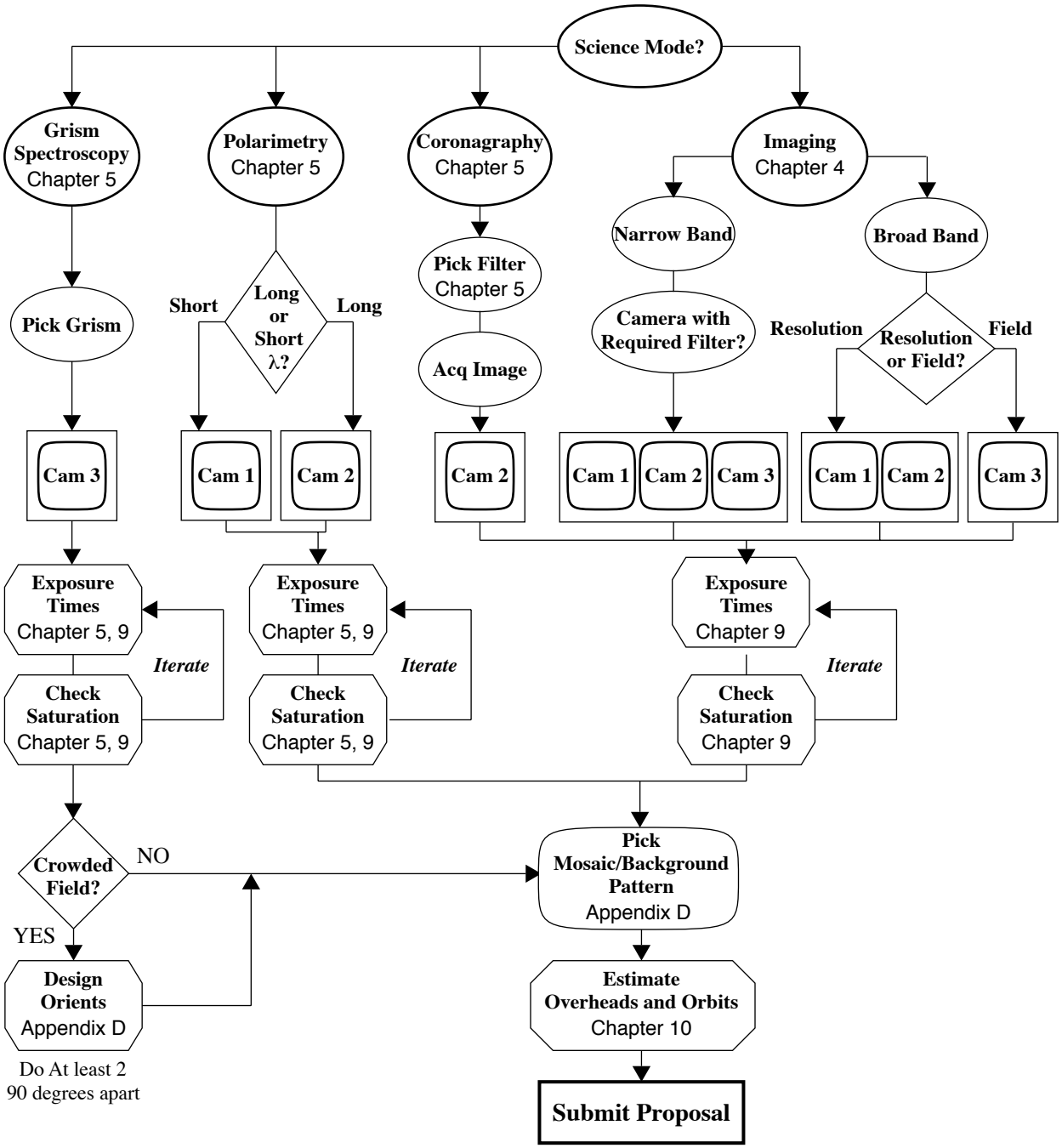

3.2 APT and Aladin

The Astronomer's Proposal Tool (APT) is used to design observations and has a new tool based on the Aladin Sky Atlas Interface to visually inspect fields and objects. This tool gives us many options for future enhancements, and brings a variety of benefits to users including access to a wide variety of images and catalogs, as well as many capabilities for displaying and manipulating images. Detailed information about the Aladin based tool can be found on the APT Web page:

http://apt.stsci.edu.

CHAPTER 4:

Imaging

In this chapter...

4.1 Filters and Optical Elements

In total, there are 32 different filters, three grisms, and two sets of three polarizers available for NICMOS. Each camera has 20 filter positions on a single filter wheel: 19 filters and one blank. As a result, not all filters are available in all cameras. Moreover, the specialized optical elements, such as the polarizers and grisms, cannot be crossed with other filters, and can only be used in fixed bands. In general, the filters have been located in a way which best utilizes the characteristics of NICMOS. Therefore at shorter wavelengths, the most important narrow band filters are located in NIC1 so that the diffraction limited performance can be maintained wherever possible, while those in NIC2 have been selected to work primarily in the longer wavelength range where it will also deliver diffraction limited imaging.

4.1.1 Nomenclature

Following the traditional HST naming convention, the name of each optical element starts with a letter or group of letters identifying what kind

of element it is: filters start with an "F", grisms with a "G", and polarizers with "POL". Following the initial letter(s) is a number which, in the case of filters, identifies its approximate central wavelength in microns, e.g., F095N implies a central wavelength of 0.95 microns. A trailing letter identifies the filter width, with "W" for wide, "M" for medium and "N" for narrow. In the case of grisms, the initial "G" is followed by a number which gives the center of the free-spectral range of the element, e.g., G206. For the polarizers, a somewhat different notation is used, with the initial "POL" being followed by a number which gives the PA of the principal axis of the polarizer in degrees, and a trailing letter identifying the wavelength range it can be used in, which is either "S" for short (0.8-1.3 microns) or "L" for long (1.9-2.1 microns).

Tables 4.1 through 4.3 list the available filters and provide an initial general description of each, starting with NIC1 and working down in spatial resolution to NIC3. Figures 4.1 through 4.3 show the effective throughput curves of all of the NICMOS filters for cameras NIC1, NIC2, and NIC3, respectively, which include the filter transmission convolved with the OTA, NICMOS foreoptics, and detector response. Appendix A provides further details and the individual filter throughput curves.

4.1.2 Out-of-Band Leaks in NICMOS Filters

In order to make use of the high spatial resolution of HST, many observers expect to use NICMOS to observe very red objects (e.g., protostars) at relatively short wavelengths. These objects have very low effective color temperatures. Thus, the flux of such objects at 2.5 microns is expected to be orders of magnitude larger than their flux at desired wavelengths. In such a case, exceptionally good out-of-band blocking is required from the filter since out-of-band filter leaks could potentially have a detrimental impact on photometry. We have, therefore, investigated whether any of the NICMOS filters show evidence for out-of-band levels. The results indicate that actual red leaks were *insignificant or non-existent*.

Table 4.1: NIC 1 Filters.

Name	Central Wavelength (μm)	Wavelength range (μm)	Comment
Blank	N/A	N/A	Blank
F110W	1.025	0.8–1.4	
F140W	1.3	0.8–1.8	Broad Band
F160W	1.55	1.4–1.8	
F090M	0.9	0.8-1.0	
F110M	1.1	1.0–1.2	
F145M	1.45	1.35–1.55	Water
F165M	1.6	1.54–1.74	
F170M	1.7	1.6–1.8	
F095N	0.953	1%	[S III]
F097N	0.97	1%	[S III] continuum
F108N	1.083	1%	He I
F113N	1.13	1%	He I continuum
F164N	1.644	1%	[Fe II]
F166N	1.66	1%	[Fe II] continuum
F187N	1.87	1%	Paschen α
F190N	1.90	1%	Paschen α continuum
POL0S	1.1	0.8–1.3	Short λ Polarizer
POL120S	1.1	0.8–1.3	Short λ Polarizer
POL240S	1.1	0.8–1.3	Short λ Polarizer

Figure 4.1: Filters for NIC 1 (at 78 K).

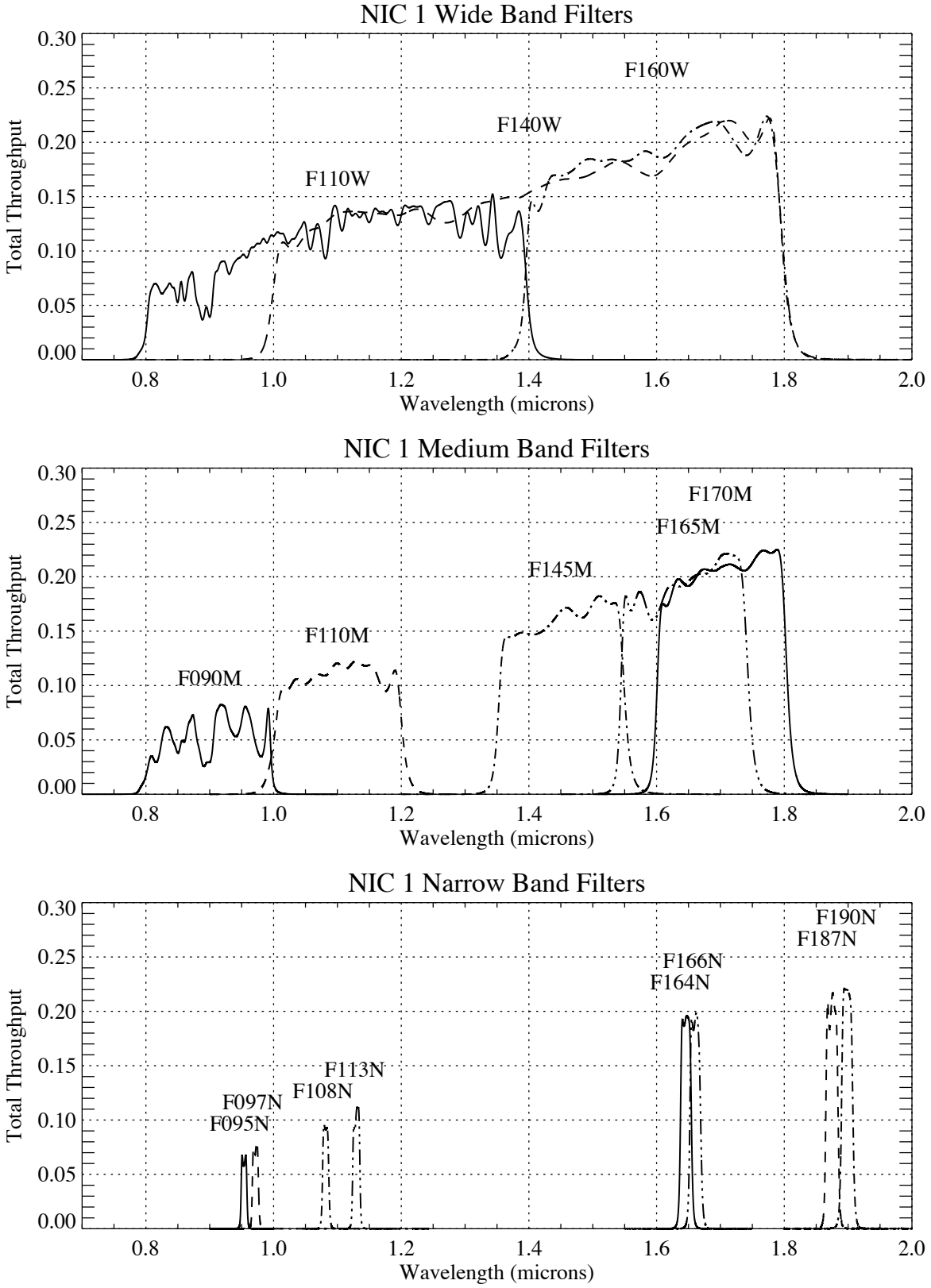

Table 4.2: NIC 2 Filters.

Name	Central Wavelength (μm)	Wavelength range (μm)	Comment
Blank	N/A	N/A	Blank
F110W	1.1	0.8–1.4	
F160W	1.6	1.4–1.8	Minimum background
F187W	1.875	1.75–2.0	Broad
F205W	1.9	1.75–2.35	Broad Band
F165M	1.7	1.54–1.75	Planetary continuum
F171M	1.715	1.68–1.76	HCO_2 and C_2 continuum
F180M	1.80	1.76–1.83	HCO_2 and C_2 bands
F204M	2.04	1.98–2.08	Methane imaging
F207M	2.1	2.01–2.16	
F222M	2.3	2.15–2.29	CO continuum
F237M	2.375	2.29–2.44	CO
F187N	1.87	1%	Paschen α
F190N	1.9	1%	Paschen α continuum
F212N	2.121	1%	H_2
F215N	2.15	1%	H_2 and Br γ continuum
F216N	2.165	1%	Brackett γ
POL0L	2.05	1.89–2.1	Long λ polarizer
POL120L	2.05	1.89–2.1	Long λ polarizer
POL240L	2.05	1.89–2.1	Long λ polarizer

Figure 4.2: Filters for NIC 2 (at 78 K).

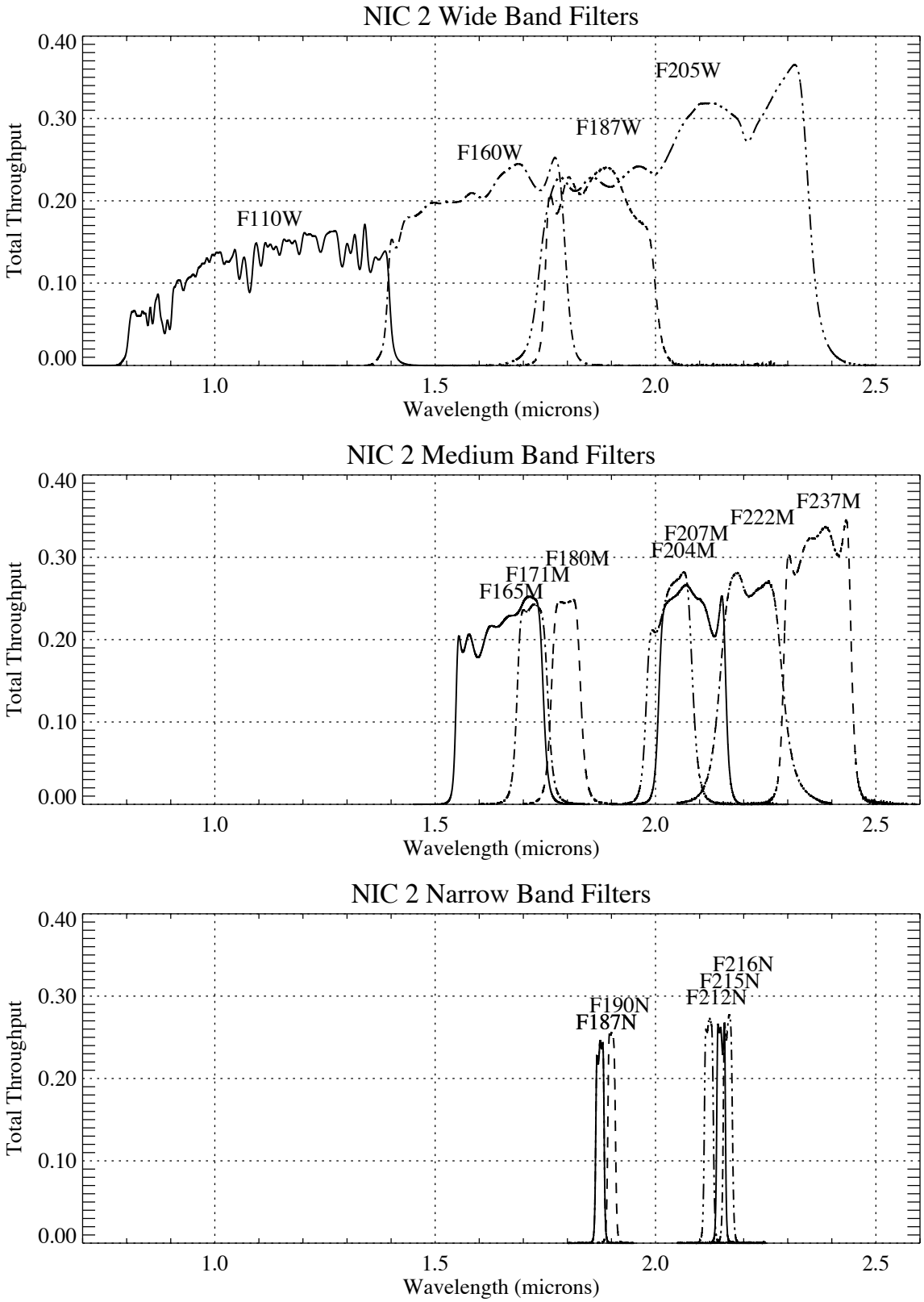

Table 4.3: NIC 3 Filters.

Name	Central Wavelength (μm)	Wavelength range (μm)	Comment
Blank	N/A	N/A	Blank
F110W	1.1	0.8–1.4	
F150W	1.5	1.1–1.9	Grism B continuum
F160W	1.6	1.4–1.8	Minimum background
F175W	1.75	1.2–2.3	
F222M	2.3	2.15–2.28	CO continuum
F240M	2.4	2.3–2.5	CO band
F108N	1.0830	1%	He I
F113N	1.13	1%	He I continuum
F164N	1.644	1%	[Fe II]
F166N	1.66	1%	[Fe II] continuum
F187N	1.875	1%	Paschen α
F190N	1.9	1%	Paschen α continuum
F196N	1.962	1%	[Si VI]
F200N	2.0	1%	[Si VI] continuum
F212N	2.121	1%	H_2
F215N	2.15	1%	H_2 continuum
G096	0.9673	0.8–1.2	GRISM A
G141	1.414	1.1–1.9	GRISM B
G206	2.067	1.4–2.5	GRISM C

Figure 4.3: Filters for NIC 3 (at 78 K).

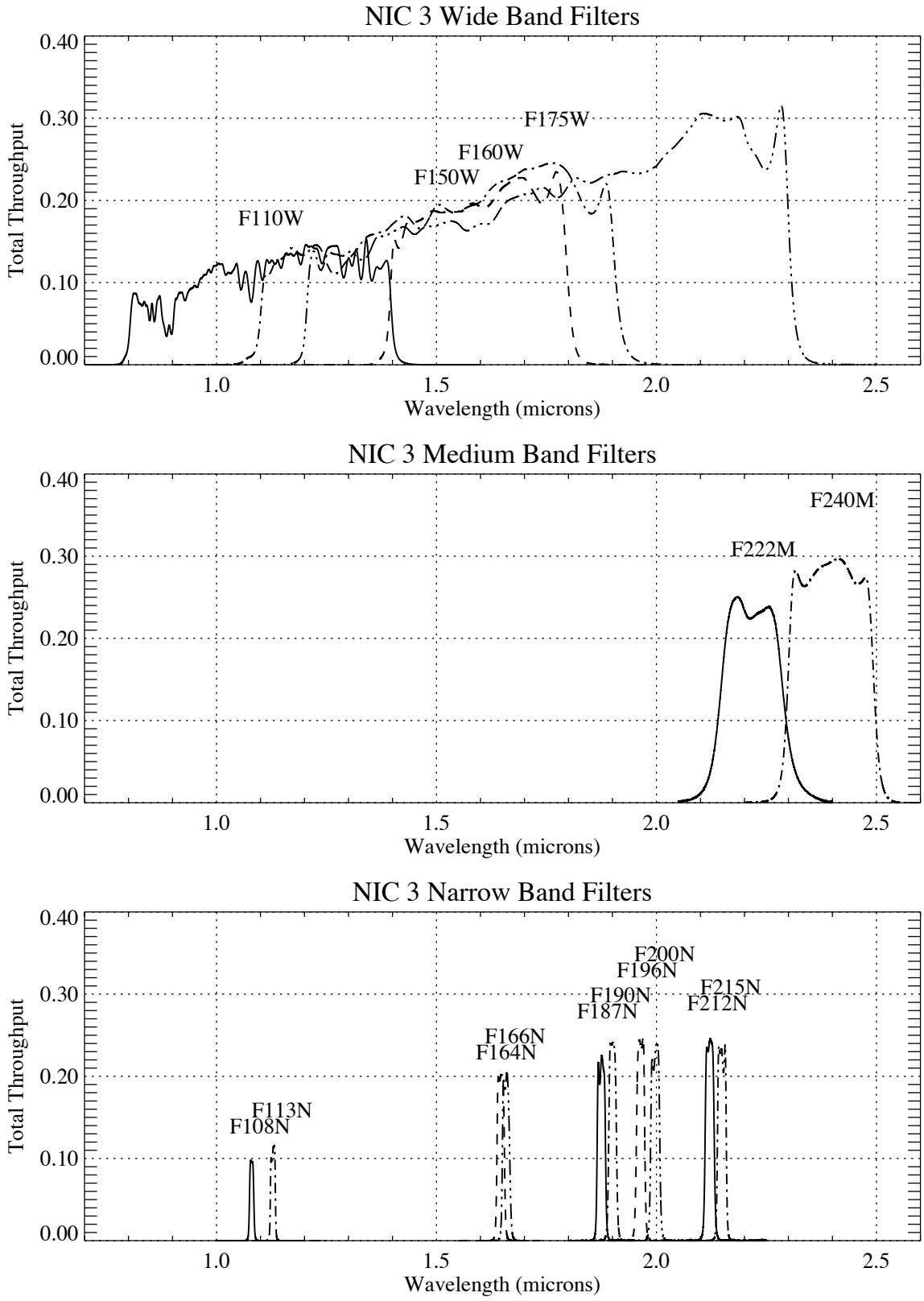

4.2 Photometry

Ground-based near-infrared observations are limited to a set of transparent atmospheric windows, while NICMOS suffers no such restrictions. For this reason, faint flux standards with continuous, empirical spectrophotometry throughout the 0.8 μm < λ < 2.5 μm range were created using the NICMOS grism mode in combination with spectral models. The absolute flux calibration of NICMOS has been calculated using observations of stars for which reliable spectral models, normalized by ground-based photometry in the optical, are available. Two types of flux standards have been observed: pure hydrogen white dwarfs, and solar analog stars. Grism sensitivity is determined directly from flat-field corrected spectra of these stars using their known spectral energy distributions. Filter sensitivities are calculated from imaging measurements according to the synthetic photometry procedure detailed in Koornneef and Coole (1981, ApJ, 247, 860). Since the pipeline calibration cannot utilize color information, the headers of reduced data contain the calibration constant that specifies the equivalent count rate for a spectral energy distribution that is constant with wavelength. For convenience, this calibration constant appears twice, once in Jansky units and once in erg/s/cm^2/Angstrom units.

4.2.1 Solar Analog Absolute Standards

For calibration using solar analogs, a reference spectrum of the Sun is normalized to the flux levels of the NICMOS standards at optical wavelengths. This continuous spectral model is then integrated through the total system throughput function for a given bandpass (including filter, detector, instrument and telescope optics), and the integral flux is compared to the measured count rate from the star in observations through that filter to derive the flux calibration constants. The absolute flux accuracy achieved by this method relies on two assumptions:

1. that the calibrated reference spectrum of the Sun is known with an uncertainty of a few percent (Colina, Bohlin and Castelli, 1996; Bohlin 2007, ASPC, 364, 315), and
2. that the near-infrared spectra of the solar analogs are nearly identical to that of the Sun.

In the past, this method was used to determine the absolute calibration of near-infrared photometry at ground-based observatories. In these cases, the absolute calibration accuracy was estimated to be at least 5%, and for some bands 2% to 3% (Campins, Rieke and Lebofsky, 1985).

Ground-based photometry by Persson *et al*. (1998, AJ, 116, 2475) of several solar analog stars used in the NICMOS calibration program has shown that the stars P330E and P177D (see Bohlin, Dickinson & Calzetti 2001, AJ, 112, 2118; Colina & Bohlin 1997, AJ, 113, 1138; Colina, Bohlin & Castelli 1996, AJ, 112, 307) are most closely matched to the colors of the Sun, and are thus most suitable for NICMOS photometric calibration. P330E is the primary NICMOS solar analog standard for photometric calibration.

4.2.2 White Dwarf Absolute Standards

Pure hydrogen white dwarfs are useful calibration standards because their spectral energy distributions can be accurately modeled from the UV through the near-IR (Bohlin, Dickinson & Calzetti 2001, AJ, 112, 2118; Bohlin 1996, AJ, 111, 1743; Bohlin, Colina & Finley 1995, AJ, 110, 1316). The star G191B2B has therefore served as a primary calibration standard for several HST instruments and was selected for NICMOS observation along with another star, GD153. Using the most up-to-date white dwarf atmosphere models, normalized to the most accurate STIS optical/UV spectra of G191B2B, Bohlin, Dickinson & Calzetti (2001) find satisfactory agreement between the white dwarf and solar analog stars for NICMOS photometric calibration.

4.2.3 Photometric Throughput and Stability

During Cycle 7, NICMOS throughput (i.e. photoelectrons per second detected from a source with given flux) was generally within 20% of pre-launch expectations in all observing modes. At the new, warmer temperature under NCS operations, the detector quantum efficiency is higher at all wavelengths, with the largest improvements at shorter wavelengths. Hence, the photometric zeropoints are significantly different with the NCS in operation compared with Cycle 7. The latest zeropoints are always given at the NICMOS Photometry Web page available at:

`http://www.stsci.edu/hst/nicmos/performance/photometry`.

The photometric stability of NIC1 and NIC2 in Cycle 7 was monitored once a month, and more frequently near the end of the NICMOS Cryogen lifetime. Observations of the solar analog P330E were taken through a subset of filters (5 for NIC1, 6 for NIC2) covering the entire wavelength range of the NICMOS cameras, and dithered through three or four pointings. NIC3 has also been monitored in a similar fashion, although only two filters were used for part of the instrument's lifetime. For most filters and cameras the zeropoints have been stable to within 3% throughout the lifetime of the instrument, although in Cycle 7 there was a small secular drift as the instrument temperature changed.

The monitoring program continued in Cycle 11 and beyond after the NCS was installed. Four filters in each of the cameras were monitored using solar analog P330E. With the switch to Two Gyro Mode in Cycle 14 the white dwarf standard G191B2B was added to the monitoring program to ensure year-round coverage. In the five years since the NCS installation in 2002, there has been a decrease on the order of one percent in sensitivity in NIC2 for all filters. For the other cameras, a similar effect may be present, but this is hard to confirm due to the larger noise in photometry for these cameras. Evidence that this effect involves all three cameras is, however, given by the flat-field monitoring (see Section 7.2.3). No satisfactory explanation has yet been found for this decrease in sensitivity, however, the change in sensitivity is consistent with a drift in detector temperature with time (see NICMOS ISR 2007-002).

4.2.4 Count Rate Dependent Non-linearity

The NICMOS team has determined that NICMOS has a significant count rate dependent non-linearity that also depends on wavelength. This is a different nonlinearity from the well-known total count dependent non-linearity. The non-linearity amounts to 0.05–0.10 mag offset per dex change in incident flux for the shortest wavelength (F090M and F110W), about 0.03 mag/dex at F160W and less than that at longer wavelengths (see Figure 4.4). Objects fainter than the NICMOS standard stars of about 12th magnitude will be measured too faint, objects that are brighter than our standards will seem too bright. The effect depends entirely on the incoming flux rate, so any objects fainter than the night sky (or on top of a bright object) will have a non-linearity offset determined by the background flux. This means that the maximum offsets on dark sky backgrounds at F110W are about 0.25 mag in NIC1 and NIC2, and about 0.16 mag in NIC3. Software has been developed to linearize the counts in imaging observations. More details on the effect and how to correct for it can be found at:

http://www.stsci.edu/hst/nicmos/performance/anomalies/nonlinearity.html.

Figure 4.4: Wavelength dependent non-linearity amounts for all three cameras.

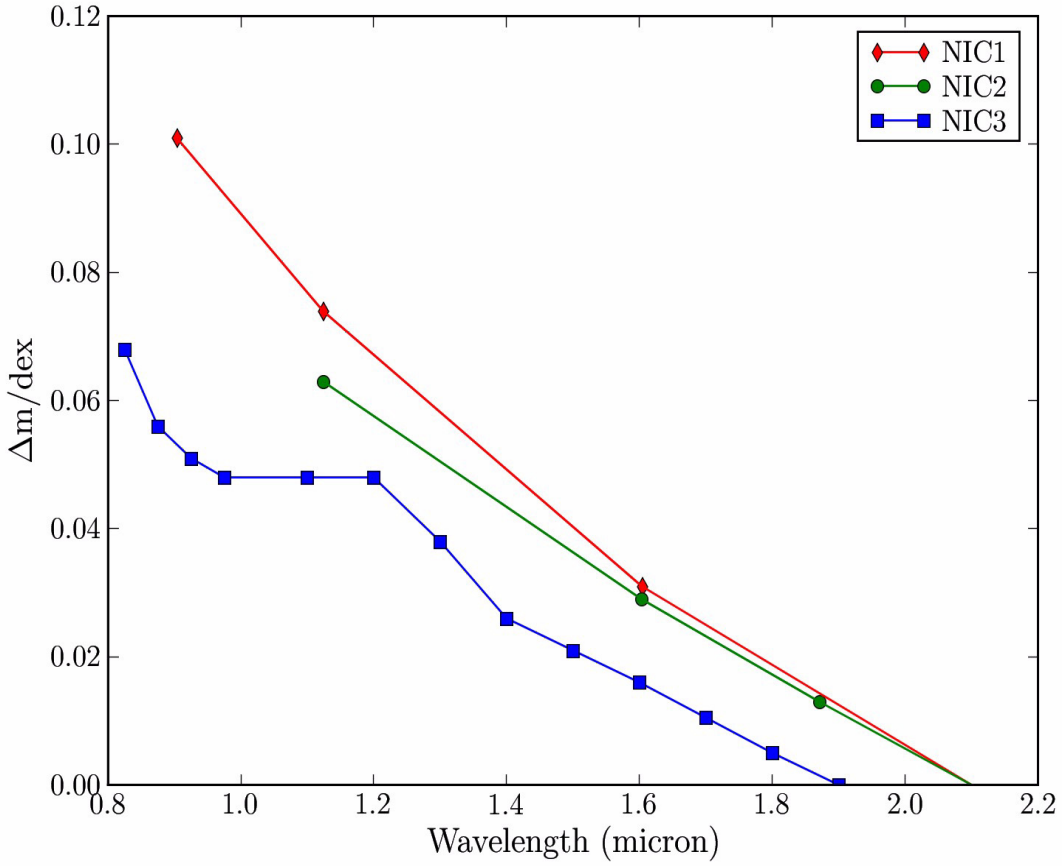

4.2.5 Intrapixel Sensitivity Variations

The response of a pixel in the NICMOS detectors to light from an unresolved source varies with the positioning of the source within the pixel due to low sensitivity at the pixel's edges and dead zones between pixels. The interpixel sensitivity was found to be an important effect and it varies by as much as 30%. This effect has no impact on observations of resolved sources, and little effect on well-sampled point sources (e.g. observations with NIC1 and NIC2 through most filters). However in NIC3, point sources are badly under-sampled, especially at short wavelengths where the telescope diffraction limit is much smaller than the NIC3 pixel size. Therefore, object counts may vary by as much as 30% depending on the wavelength positioning of a star within a pixel. Well-dithered exposures will average out this effect, but NIC3 observations of stars with few dither positions can have significant uncertainties which may limit the achievable quality of point source photometry.

The intrapixel sensitivity in Cycle 7 and possible post-processing solutions are discussed in Storrs *et al*. (1999, NICMOS ISR-99-005) and Lauer (1999, PASP, 111, 1434). This was also investigated for NIC3 in Cycle 11, after the installation of cryo-cooler (C. Xu and B. Mobasher 2003, NICMOS ISR-2003-009).

Compared to Cycle 7, the intrapixel sensitivity after installation of the NCS in Cycle 11 is found to decrease by 27% for both F110W and F160W filters. This is likely due to the increase in the detector temperature (and electron mobility) in Cycle 11 and beyond, leading to a higher rate of electrons absorption by diodes.

4.2.6 Special Situations

Sources with Extreme Colors

We have carried out tests to establish the likely impact on photometric observations of sources of extreme colors induced by the wavelength-dependent flat field. This contributes at most a 3% photometric error for sources with unknown colors. For each filter, we used two sources with different colors assuming the spectral energy distributions to have black-body functions. The first case had a color temperature of 10,000K, and thus is typical of stellar photospheres and the resultant color is representative of the bluer of the sources that will be seen with NICMOS. (It is worth noting that for reflection nebulae illuminated by hot stars, a significantly bluer spectrum is often seen.) The second source had a color temperature of 700K which in ground-based terms corresponds to [J–K] = 5, a typical color encountered for embedded sources, such as Young Stellar Objects (YSOs). (Again, there are sources which are known to be redder. The Becklin-Neugebauer object, for example, has no published photometry at J, but has [H–K] = 4.1, and the massive YSO AFGL2591 has [J–K] = 6.0. YSOs with [J–K] = 7 are known, although not in large numbers.)

An example of a pair of simulated spectra is shown Figure 4.5, for the F110W filter. In this filter an image of a very red source will be dominated by the flat field response in the 1.2 to 1.4 micron interval, while for a blue source the most important contribution will come from the 0.8 to 1.0 micron interval. The results of our study for the most affected filters are shown in Table 4.4. The other filters are better.

- Even for the broadest NICMOS filters the wavelength dependence of the flat field response generates only small photometric errors, typically less than 3% for sources of unknown color. Not surprisingly, the largest errors arise in the 3 broadband filters whose bandpass include some part of the regions where the flat field response changes most rapidly.

- The same results hold true even for filters at the most extreme wavelengths (e.g., F090M, F222M and F240M) because of their small bandwidth.
- It will probably be difficult to obtain photometry to better than the limits shown in Table 4.4 for the F090M, F110W, F140W, F205W and F240M filters, and observers requiring higher accuracy should contact the Help Desk at STScI for guidance.
- These errors can probably be corrected if more accurate photometry is needed, by taking multi-wavelength observations and using an iterative correction technique.
- For observers requiring high precision photometry, these represent non-trivial limits beyond which it will not be possible to venture without obtaining multi-wavelength images. In order to obtain 1% precision using the F110W filter, for instance, observers should observe at least in another wavelength. The color information derived from the pair (or group) of images could then be used to construct a more appropriate flat field image, which could then be applied to improve the color information.

Table 4.4: Photometric Errors for Selected Filters.

Filter	Error (percent)	
	10,000K model	700K model
F090M	<0.1	1.9
F110W	1.1	2.9
F140W	0.7	3.1
F160W	<0.1	0.3
F187W	<0.1	0.3
F205W	0.4	2.1
F222W	<0.1	0.1
F240M	1	0.9

Figure 4.5: Detected Source Spectrum. These are for sources with color temperatures of 700K (solid line) and 10,000K (dashed line). It is easy to see that the detected image will be dominated by the flat field response in the 1.2-1.4 μm region for a 700K source, while for a 10,000K source the detected image will be affected by the flat field response throughout the filter bandpass.

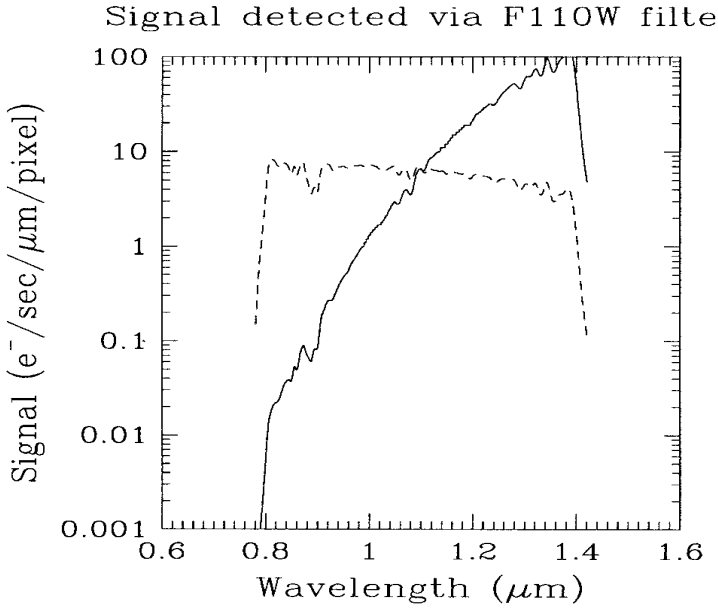

Extended Sources with Extreme Spatial Color Variations

So far, the analysis has been limited to point sources, but some mention should be made of the situation for extended objects. A good example is the YSO AFGL2591. This has an extremely red core of [J–K] = 6, and is entirely undetected optically. However, it also has a large IR nebula which is quite prominent at J and K, and in the red visual region, but much fainter at L, and which is probably a reflection nebula. Spatially, the nebula has highly variable color, some parts of it having fairly neutral or even slightly blue colors in the NICMOS waveband, while other parts are extremely red. Obtaining very accurate measurements of the color of such a source requires the use of images at more than one wavelength and an iterative tool of the kind described earlier. A further example of this kind of complicated object is the prototypical post-AGB object CRL2688, the Cygnus Egg Nebula, which has an extremely blue bipolar reflection nebula surrounding an extremely red core. Techniques which require very accurate measurements of the surface brightness of extended objects, such as the brightness fluctuation technique for distant galaxies, will need to be applied with care given to the photometric uncertainties such as those discussed here.

Creating Color-Dependent Flat Fields

NICMOS ISR-99-002 describes two methods for creating color-dependent flat fields. We have included programs and calibration files for making these flat fields in the software part of the Web site. One way of approaching the problem is to make monochromatic flats by doing a linear least squares fit to several narrowband (and, if necessary for increased wavelength coverage) medium band flats, for each pixel. The slope and intercept images that result from such a fit can be used to determine the detector response to a monochromatic source. This method works best if the desired wavelength is within the range covered by the observed flats; extrapolation with this method gives questionable results.

If the source spectrum is known, a composite flat made from the weighted sum of the narrowband flats in the passband of the observed image can be made. The IRAF script, **interflat.cl**, uses an input spectrum and the calibration database in **STSDAS** to compute composite flats**.** This script is downloadable from:

`http://www.stsci.edu/hst/nicmos/tools/colorflat_intro.html`.

If you have a variety of sources in your image you may want to make several flat fields and apply them to regions defined by some criterion, like color as defined by a couple of narrowband images on either side of the broadband image.

4.3 Focus History

The Pupil Alignment Mechanism (PAM) consists of an adjustable mirror in the NICMOS optical train that can be moved to make small corrections to the NICMOS focus and serves to properly position the pupil image of the telescope primary mirror onto the corrective optic. The motion of the PAM is limited to ±10mm from its zero position. The NICMOS cameras were designed to share a common focus with the PAM close to its zero position. In the current state of the dewar, NIC1 and NIC2 can each be focused within the range of the PAM. NIC3, however, cannot be entirely focused by motions of the PAM alone and remains slightly out of focus although still scientifically usable (see next section).

The focus positions of all three NICMOS cameras have changed since launch due to motion in the dewar. The positions are measured by observations of stars over a range of focus settings on a frequent basis. The focus history since shortly after launch is shown in Figure 4.6. The focus position is given for the detector center. The focus variation across the camera's field of view is ~1.5 mm in PAM space in NIC2, and about half of that in NIC1. The two largest focus excursions, on January 12 and June 4, 1998, are due to the secondary mirror reset used to place NIC3 in focus during NIC3 campaigns. A noticeable improvement in NIC3 focus

occurred after December 17, 1997, when the FOM had been tilted by 16 degrees to reduce vignetting in that camera.

After installation of the NCS the PAM has been positioned to give the best focus for NIC1 and NIC2. This position has proven to be quite stable for NIC1 and NIC2. No additional special focus campaigns for NIC3 are planned. For more information, please see the NICMOS Focus Web page.

Figure 4.6: NICMOS Focus History as of 4 July 2007 (focus at the detector center).

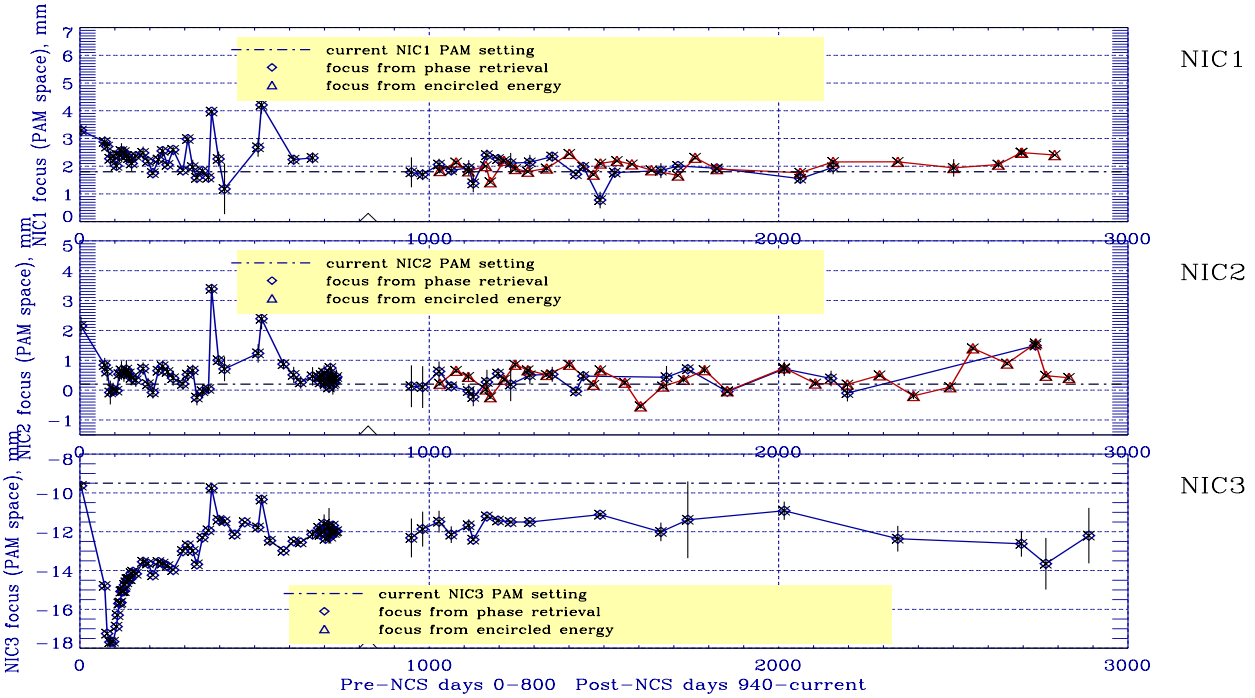

4.4 Image Quality

4.4.1 Strehl Ratios

The high image quality of NICMOS is summarized by the Strehl ratio of the PSF, which is defined as the ratio of the observed-to-perfect PSF peak fluxes. Table 4.5 lists the Strehl ratios for representative filters in all three NICMOS cameras (courtesy of John Krist, STScI). The ratio is very high, between 0.8 and 0.9 for NICMOS images, at all wavelengths and in all Cameras at their optimal focus.

Table 4.5: NICMOS Strehl Ratios

Filter	NIC1	NIC2	NIC3
F110W	0.91	0.89	0.81
F160W	---	0.90	0.86
F222M	---	0.90	0.92

For NIC3, the quoted Strehl ratio is for optimal focus measurements obtained during the Cycle 7 & 7N campaigns.

4.4.2 NIC1 and NIC2

The changes in dewar geometry leading to the degraded focus in NIC3 have also affected NIC1 and NIC2. By measuring the PSFs of stars at a series of PAM positions it was determined that the optimal focus for NIC1 occurred for a PAM position of ~ +1.8 mm and the optimal focus for NIC2 at ~ 0.2 mm after the installation of NCS in 2002. This difference is significant enough that NIC1 and NIC2 are not considered to be parfocal. However, the NIC1 and NIC2 foci are still sufficiently close that the intermediate focus position between the two cameras, NIC1-2, has been defined for simultaneous observations. The compromise focus position has been chosen to share the waveforms error equally between NIC1 and NIC2. The image degradation induced by this compromise focus is smaller than a few percent in each camera, and negligible for most purposes. Most users will find this focus sufficient to reach their scientific goals when using both cameras. Additionally, a separate PAM position at the optimal focus is defined and maintained for each camera.

The encircled energy profiles for NIC1 and NIC2 at representative wavelengths are shown in Figures 4.7 through 4.11.

Figure 4.7: Encircled Energy for NIC1, F110W.

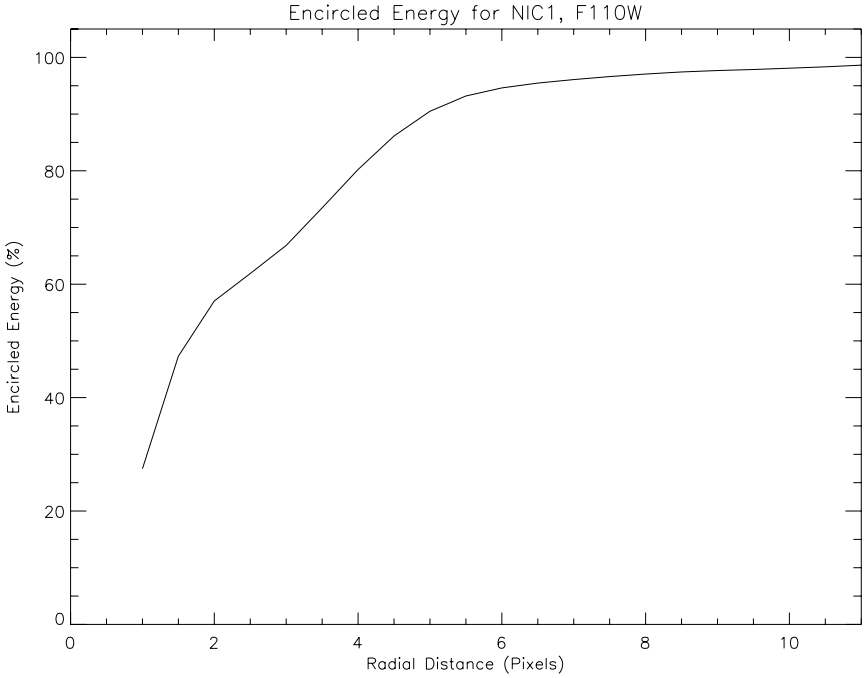

Figure 4.8: Encircled Energy for NIC1, F160W.

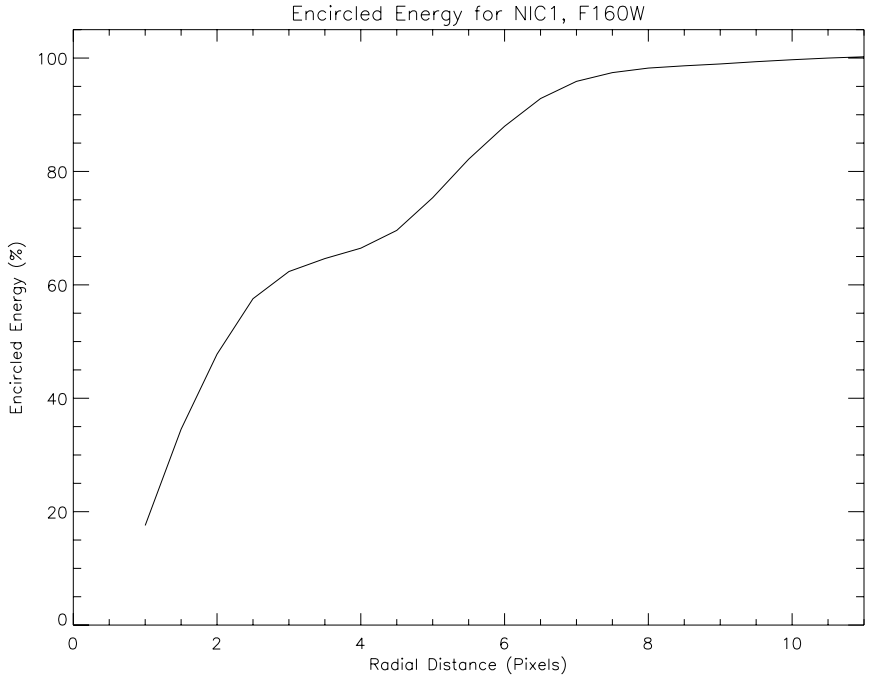

Figure 4.9: Encircled Energy for NIC2, F110W.

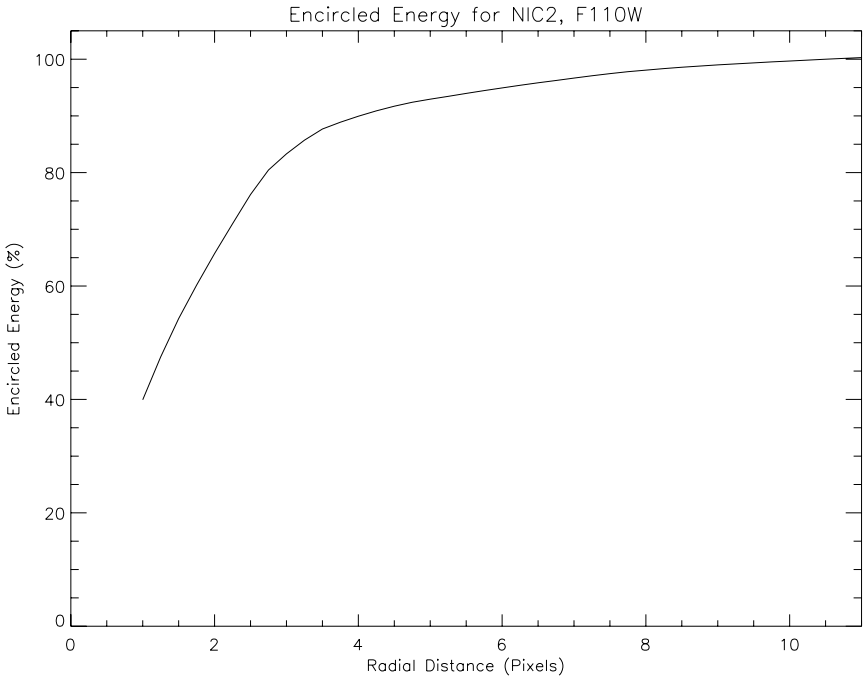

Figure 4.10: Encircled Energy for NIC2, F160W.

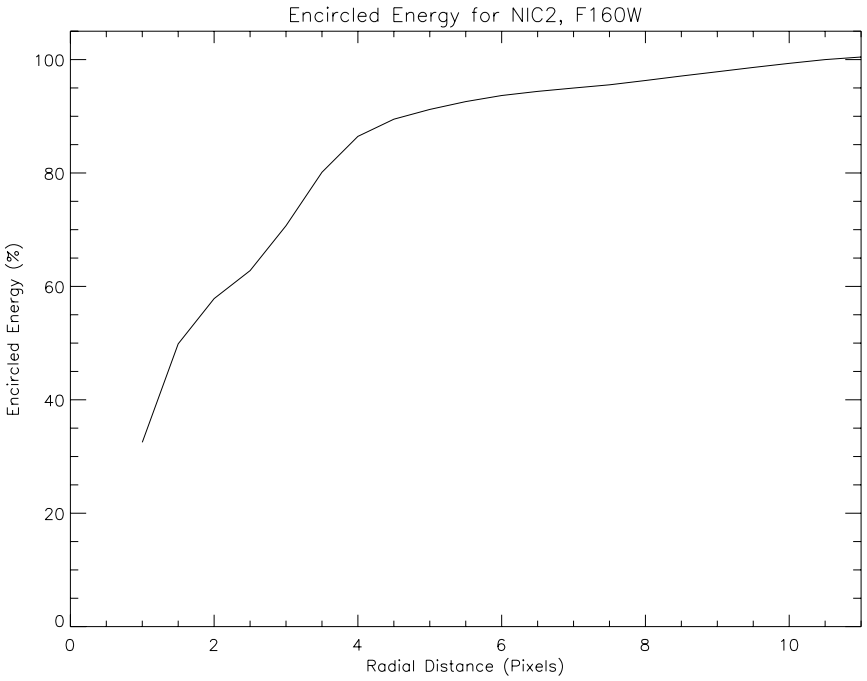

Figure 4.11: Encircled Energy for NIC2, F222M.

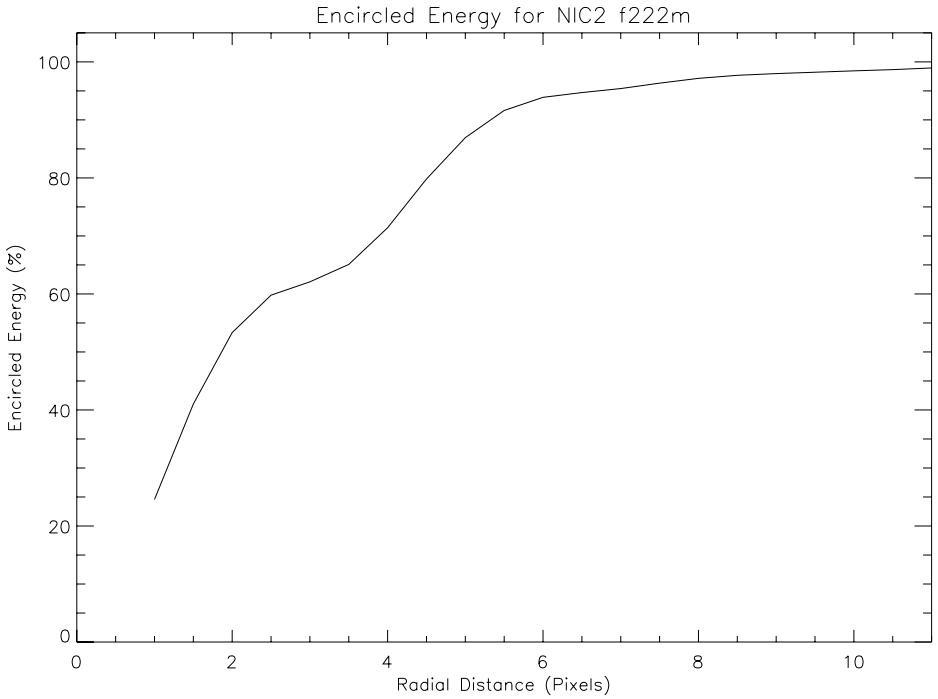

Vignetting in NIC1 and NIC2

The lateral shifts of the NICMOS dewar have resulted in vignetting in all three cameras. The primary source of the vignetting is a slight misalignment of the FDA mask. Relatively small losses in throughput are observed at the bottom ~ 15 rows of both NIC1 and NIC2 as shown in Figure 4.12, but a more substantial vignetting is seen in NIC3.

Figure 4.12 shows the column plot of the ratio of an in-flight flat field to a pre-launch flat field for NIC1 and NIC2 for the F110W filter. The approximately 10% decrease seen near the bottom of the detector (left in the figure) demonstrates that vignetting has reduced the throughput. The decrease in throughput in NIC3 is due to movement of the vignetting edge for the bottom 10-15 rows and is more dramatic.

Figure 4.12: Vignetting in all three NICMOS Cameras as a function of row number.

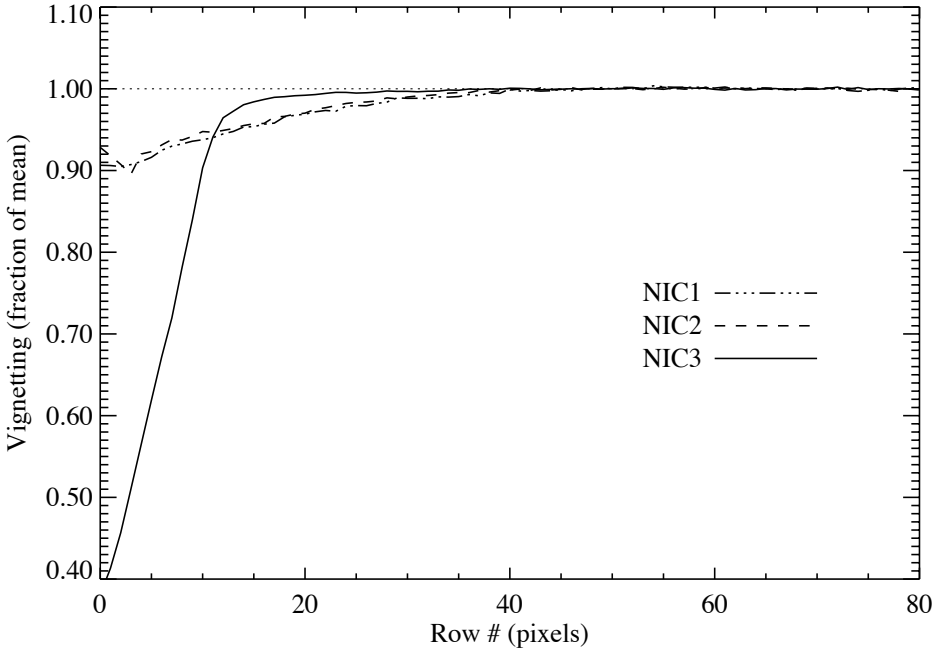

4.4.3 NIC3

NIC3 has suffered the largest shift in focus due to dewar deformation of about –12 mm in PAM space during the final stages of cryogen exhaustion. Early measurements after the installation of NCS in April 2002 confirm this number. This focus shift is outside the range that can be compensated with the PAM (maximum shift is –9.5 mm).

During Cycle 7 and 7N, NIC3 was operated in optimal focus during two special observing campaigns of 2–3 weeks each, in January and June 1998, when the HST secondary mirror was moved to recover optimal focus. Outside those two periods, NIC3 was operated at best internal focus, namely with the PAM at –9.5 mm.

The typical FWHM of NIC3 images (both at optimal and best internal focus) is ~1.3 pixels, with small variations between different wavelengths (NICMOS ISR-98-006); the fractional flux within the first Airy ring ranges from 43% in J to 49% in H to 58% in K with NIC3 in optimal focus. The size of the Airy ring for NIC3 PSF has been calculated for oversampled **TinyTim** PSFs.

Figure 4.13: NIC3 encircled energy at 1.6 microns at optimum focus (PAM=–12 mm, solid line) and at the best achievable focus (PAM=–9.5 mm, dashed line) with the HST secondary mirror at nominal position.

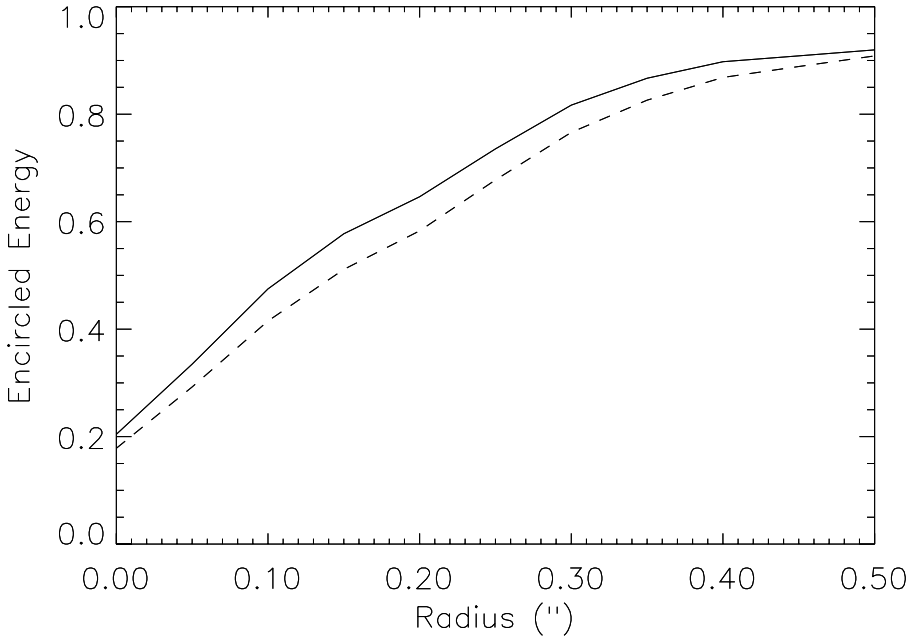

Because NIC3 undersamples the PSF, the degradation of image quality with the PAM mirror at –9.5 mm was found to be relatively small compared to the optimal-focus image quality. Figure 4.13 shows the encircled energy for NIC3 at 1.6 microns for both the optimal focus (PAM=–12 mm at the time of the measurement) and the best focus (PAM=–9.5 mm). Both curves report simulations obtained with **TinyTim** PSFs convolved with the NIC3 pixel response, but the results are very similar to the actual observations. The loss in the peak flux is around 20% and the loss in encircled energy beyond one pixel radius (0.2") is no more than 10–15%. Given the minimal loss of performance with the slight out-of-focus operations, NIC3 will be operated without moving the HST secondary mirror and will be offered "as is" in future Cycles.

Some observers may consider obtaining NIC3 parallel observations, while NIC1 and NIC2 are used for the primary science observations. At the NIC1-2 best focus, the image quality of NIC3 is obviously degraded, with a PSF FWHM over 3 times larger than the NIC3 best focus PSF FWHM. Images are "donut" shaped and, therefore, are not useful for scientific purposes.

Vignetting in NIC3

In addition to focus degradation, NIC3 is also affected by vignetting from two sources. The first is a cold vignetting, due to the lateral shift of the FDA mask, similar to the vignetting affecting NIC1 and NIC2. The second is due to a warm bulkhead edge, which produces elevated thermal

background and degraded image quality over the bottom 25% of the detector (bottom ~60 rows).

The warm vignetting was successfully removed during early 1998 by moving the FOM to a position Y=+16 arcsec, producing a corresponding translation in the NIC3 field-of-view. This translation removed the warm vignetting and slightly improved focus. The price was the introduction of a mild astigmatism, which is, however, below the λ/14 criterion for image quality (except at J, where the wavefront error is λ/10).

The only vignetting left in NIC3 with the FOM at Y=+16 arcsec is the one produced by the FDA and affects the bottom 10–15 rows of the detector, in the same manner as NIC1 and NIC2. NIC3 is now operated with the FOM at the +16 arcsec position as default. The loss in throughput is shown in Figure 4.14.

Figure 4.14: NIC3 Vignetting as a function of FOM offset.

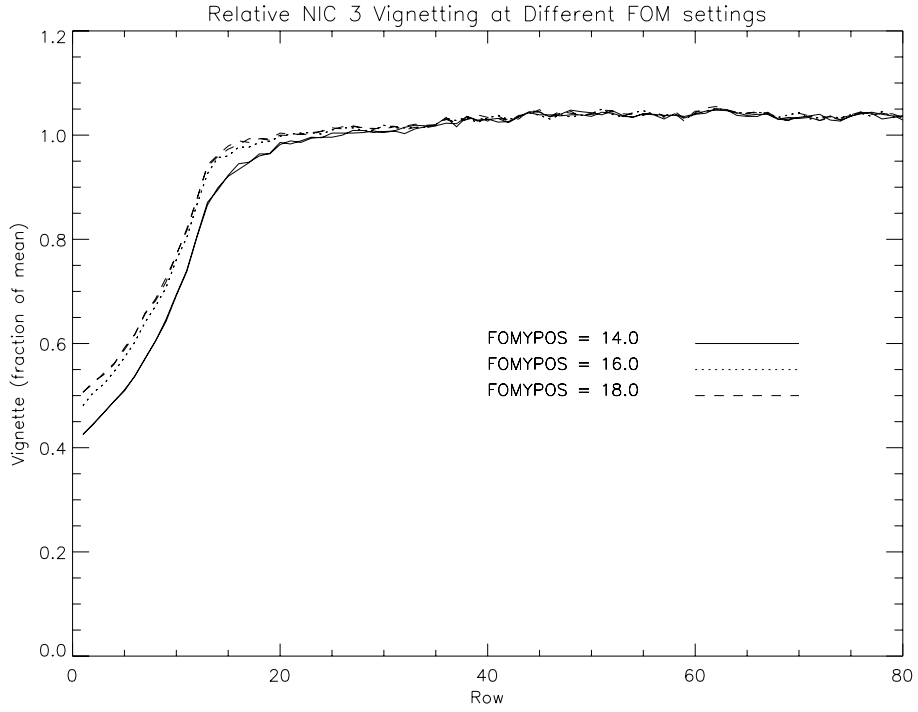

4.4.4 PSF Structure

NICMOS provides full Nyquist sampling beyond 1 μm and ~1.7 μm in NIC1 and NIC2, respectively. In addition to all the properties of diffraction-limited imaging, the NICMOS point spread function (PSF) has a few ‘off-nominal’ characteristics. These are mostly induced by the thermal stress suffered by the dewar early in the instrument’s life.

Each NICMOS camera has a cold mask located at the entrance to the dewar that is designed to block thermal emission from the OTA pupil

obstructions. The NIC2 cold mask also serves as the Lyot stop for the coronagraph. Due to the thermal stress suffered by the NICMOS dewar, the cold masks are slightly misaligned relative to the OTA.

Because of the cold mask misalignment, the diffraction pattern is not symmetric. NICMOS images of point sources show slightly elliptical diffraction rings and the diffraction spikes show alternating light and dark bands and asymmetries. They are caused by unequal offsets between the corresponding pairs of spider diagonals.

Since Cycle 7, the foci for NIC1 and NIC2 have moved slightly in the negative direction, and are therefore somewhat closer together. This improves the quality of the images taken at the NIC1-2 intermediate focus. The focus for NIC3 remains beyond the range of the pupil alignment mechanism (PAM), but has moved in the positive direction, thus improving the image quality over Cycle 7. Figure 4.15 shows the primary PSF for NIC1 at the optimal PAM setting.

Figure 4.15: NIC1 PSF at the optimal PAM setting. The left image is a cross section of the primary PSF pictured to the right.

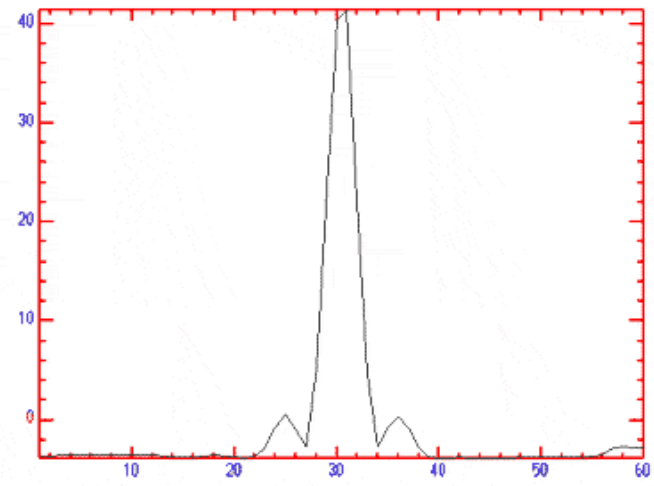

Typical NIC1 PSF with a bright central core, surrounded by the first airy ring

4.4.5 Optical Aberrations: Coma and Astigmatism

Coma and astigmatism in the NICMOS cameras are generally small, with the wavefront error typically less than 0.05 μm, that is, less than 5% of the wavelength at 1 μm. The mean values of coma and astigmatism measured in Cycle 11 along the detector's *x*- and *y*-coordinates, are given in Table 4.6, expressed as wavefront errors. In NIC3, the astigmatism along the detector's *x*-axis increased to ~5% and became more unstable after the nominal FOM *y*-tilt was done in December of 1997. It had been changed from 0 to 16 arcsec in order to reduce the significant vignetting in this camera. With regard to the temporal behavior of NICMOS aberrations, the *y*-coma in all three cameras had been gradually increasing by ~2–5%

during NICMOS operations throughout the 1997–1998 lifetime period (see NICMOS ISR 99-003).

Table 4.6: Mean and standard deviation of NICMOS aberrations.

	NIC1	NIC2	NIC3	
	FOM=0"	FOM=0"	FOM=0"	FOM=16"
x-coma, μm	0.0032 ± 0.002	0.015 ± 0.012	0.026 ± 0.006	0.016 ± 0.012
y-coma, μm	0.022 ± 0.005	–0.044 ± 0.0081	–0.040 ± 0.011	–0.10 ± 0.02
x-astigmatism, μm	0.006 ± 0.003	0.003 ± 0.02	0.003 ± 0.016	0.062 ± 0.020
y-astigmatism, μm	0.024 ± 0.004	0.024 ± 0.004	0.027 ± 0.013	0.040 ± 0.019

4.4.6 Field Dependence of the PSF

The PSF is at least to some extent a function of position in the NICMOS field of view. Preliminary data indicate that this effect is small (less than ~6% on the PSF FWHM) and that only a small degradation will be observed. Movement of the FOM, on the other hand, has been shown to have a greater effect on the PSF quality.

4.4.7 Temporal Dependence of the PSF: HST Breathing and Cold Mask Shifts

The NICMOS PSF suffers from small temporal variations induced by the HST breathing and by variable shifts of the instrument's cold masks (for a review of this topic see Krist *et al*. 1998, PASP 110, 1046).

The HST focus position is known to oscillate with a period of one HST orbit. The focus changes are attributed to the contraction/expansion of the OTA due to thermal variations during an orbital period. These short term focus variations are usually referred to as "OTA breathing", "HST breathing", "focus breathing", or simply "breathing". Breathing affects all data obtained with all instruments onboard HST.

Thermally induced HST focus variations also depend on the thermal history of the telescope. For example, after a telescope slew, the telescope temperature variation exhibits the regular orbital component plus a component associated with the change in telescope attitude. The focus changes due to telescope attitude are complicated functions of Sun angle and telescope roll. More information and models can be found on the "HST Thermal Focus Modeling" Web site at URL:

`http://www.stsci.edu/hst/observatory/focus/thermal.html`.

The telescope attitude also appears to affect the temperature of the NICMOS fore-optics, which are outside the dewar. A noticeable oscillatory

pattern about the NICMOS focus trend lines was found to correlate with temperature variations of the fore-optics. It has not been fully investigated whether or not the correlation of the fore-optics temperature with NICMOS focus changes is an additional focus change, or only reflects the OTA focus change.

Another source of temporal variation for the PSF is the "wiggling" of the cold masks on orbital timescales. This causes asymmetries in the PSFs and residuals in PSF subtracted images.

HST breathing and cold mask "wiggling" produce variations of 5% to 10% on the FWHM of the NIC2 PSFs on typical timescales of one orbit.

4.5 Cosmic Rays

As with CCDs, cosmic ray hits will produce unwanted signal in the output images. However, no lasting damage to the detector pixels is expected from such hits. The NICMOS arrays have been subjected to radiation doses much higher than expected in their entire lifetime in accelerator tests without sustaining any long-term damage or measurable degradation in DQE. Hence, cosmic rays should have little impact on the long-term array performance in orbit.

On-orbit measurement of the distribution of cosmic rays shows 1.2 to 1.6 events/second/Camera for 5σ events. With a typical hit generating a 5σ event in ~2 pixels, this corresponds to 2 to 3 pixels/second/Camera. For a 2000 second integration, about 10% of the pixels in the detector will show cosmic ray events.

The use of `MULTIACCUM` mode makes it possible to filter out cosmic rays since it provides a series of intermediate non-destructive reads, as well as the final image (see Chapter 8). These intermediate reads can be used to identify cosmic ray hits. The calibration pipeline, as described in the NICMOS Data Handbook, can identify and remove cosmic ray hits from `MULTIACCUM` observations.

See below for a more detailed discussion of persistence from massive cosmic ray hits during, e.g., passages in the South Atlantic Anomaly.

4.6 Photon and Cosmic Ray Persistence

HgCdTe detector arrays like those in NICMOS are subject to image persistence. When pixels collect a large amount of charge, they will tend to "glow" for some time after the end of the exposure.

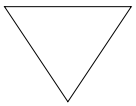

Overexposure of the NICMOS detectors will not cause permanent harm and therefore NICMOS does not have bright object limitations.

The persistent signal appears as an excess dark current and decays exponentially with a time scale of about 160±60 seconds (different pixels show different decay rates), but there is also a long, roughly linear tail to the decay such that persistence from very bright sources remains detectable as much as 30 to 40 minutes after the initial exposure. Subsequent exposures can therefore show residual images. With NICMOS, this can happen under a number of circumstances. Exposures of bright astronomical targets can leave afterimages which appear in subsequent images taken within the same orbit. If you are observing bright objects you should be aware of this potential problem: dithered exposures may contain "ghosts" of bright stars from previous images. It appears that all sources of illumination leave persistent afterimages, but under typical conditions they are most noticeable for sources which have collected 20000 or more ADU during the previous exposure. There is little that can be done to avoid this. If observations are well dithered, then the persistent afterimages can usually be recognized and masked during data processing when combining the images to form a mosaic. This, however, is not done by the standard calibration pipeline.

More insidiously, during regular passages of HST through the South Atlantic Anomaly, the arrays are bombarded with cosmic rays, which deposit a large signal in nearly every pixel on the array. The persistent signal from these cosmic rays may then be present as a residual pattern during exposures taken after the SAA passage. This appears as a "mottled," "blotchy" or "streaky" pattern of "noise" (really signal) across the images, something like a large number of faint, unremoved cosmic rays. These persistent features cannot be removed by the `MULTIACCUM` cosmic ray processing done by the standard pipeline because they are not transient. Rather, they are a kind of signal, like a slowly decaying, highly structured dark current.

Cosmic ray persistence adds non-Gaussian, spatially correlated noise to images and can significantly degrade the quality of NICMOS data, especially for exposures taken less than 30 minutes after an SAA passage. Count rates from moderately bad cosmic ray persistence can be of order

0.05 ADU/second, with large pixel-to-pixel variations reflecting the spatial structure of the signal. The effective background noise level of an image can be increased by as much as a factor of three in the worst cases, although 10% to 100% are more typical. This "noise" is primarily due to the spatially mottled structure in the persistence, not the added Poisson noise of the persistence signal itself. Because HST passes through the SAA many times a day, a large fraction of NICMOS images are affected by cosmic ray persistence to one degree or another. Observations of bright objects are hardly affected, since the persistent signal is usually quite faint. Similarly, short exposures are not likely to be badly affected because the count rate from persistence is low and may not exceed the detector readout noise. But deep imaging observations of faint targets can be seriously degraded. The NICMOS ISR-98-001 (Najita *et al.* 1998) presents a detailed discussion of this phenomenon and its effects on imaging observations.

Starting in Cycle 11, a pair of ACCUM mode NICMOS dark exposures are scheduled after each SAA passage. This provides a map of the persistent cosmic ray afterglow at a time when it is strongest, and has just begun to decay. Experiments using Cycle 7 NICMOS data have shown that it is possible to scale and subtract such "post-SAA darks" from subsequent science exposures taken later in the same orbit, and thus to remove a significant fraction of the CR persistence signal. Doing so comes at the cost of adding some additional pixel-to-pixel Gaussian noise, as the readout and dark current noise from the darks is added in quadrature to that from the science exposures, albeit with a multiplicative scaling that will be < 1, since the CR persistence signal decays with time. Nevertheless, for some, and perhaps most, science programs, we expect that the post-SAA darks may lead to a significant improvement in the quality of NICMOS data taken after SAA passages. Software for implementing this correction has been created (see NICMOS ISR-2003-010 by Bergeron and Dickinson) and successfully tested and is available as a stand-alone routine called `SAAclean` within the **nicmos** package of PyRAF/STSDAS (see NICMOS ISR-2007-001 by Barker et al.) Feedback on this routine can be sent to `help@stsci.edu`.

In addition, observers can plan observations to further minimize the impact of cosmic ray persistence, should it occur. Taking images with as many independent dither positions as possible is one good strategy (which can help in many ways with NICMOS imaging). Without dithers, the persistent pattern will stay fixed relative to the astronomical targets (although its intensity will decay), and co-adding successive exposures will just reinforce the contamination. Dithered images will move the targets relative to the persistence so that it adds incoherently when the data are summed. With well-dithered data (at least three positions), one can also take advantage of the MultiDrizzle software (Koekemoer *et al.*, 2002 HST Calibration Workshop, p337) and associated software in the STSDAS

dither package to identify and mask the worst effects of persistence (as described in the *HST Dither Handbook* v2.0, Koekemoer *et al*. 2002). The HST Data Handbook reports more details on how to handle images affected by cosmic ray persistence.

4.7 The Infrared Background

From the ground, the infrared background is affected by telluric absorption and emission which limits the depth of astronomical imaging. As is well known, between 1 and 2.5 μm there are a number of deep molecular absorption bands in the atmosphere (top panel of Figure 4.16), and the bandpasses of the conventional near-IR bands of JHK were designed to sit in the gaps between these opaque regions (middle panel of Figure 4.16). Unfortunately, outside the absorption features there is also considerable background emission in both lines and continuum. Most of the background between 1 and 2 μm comes from OH and O_2 emission produced in a layer of the atmosphere at an altitude ~87 km (bottom panel of Figure 4.16).

The location of HST above the atmosphere removes these terrestrial effects from the background. Here, the dominant sources of background radiation will be the zodiacal light at short wavelengths and the thermal background emission from the telescope at long wavelengths. The sum of these two components has a minimum at 1.6 microns (roughly the H band). All three NICMOS cameras carry broad-band filters which are centered on this wavelength.

At wavelengths shorter than 1.6 μm, NICMOS reaches the natural background provided by the scattering of sunlight from zodiacal dust, which is, of course, strongly dependent on the ecliptic latitude and longitude. Table 4.7 gives low, high and average values of the zodiacal background as seen by HST (for details refer to Stiavelli 2001, WFC3 ISR 2002-02).

Table 4.7: Zodiacal backgrounds in flux units and in counts (from Stiavelli 2001, WFC3 ISR 2002-02).

Location	erg cm^{-2} s^{-1} Å^{-1} arcsec^{-2}		photons (HST area)$^{-1}$ s^{-1} Å^{-1} arcsec^{-2}	
	1.2μm	1.6μm	1.2μm	1.6μm
Minimum	4.90 □□□□× 10^{-19}	2.20×10^{-19}	0.013	0.008
Typical	7.35×10^{-19}	3.31×10^{-19}	0.020	0.012
Average	8.32×10^{-19}	3.86×10^{-19}	0.023	0.014
Maximum	2.15×10^{-18}	9.64×10^{-19}	0.059	0.035

Figure 4.16: Atmospheric Absorption and Emission Line Spectrum in NICMOS Operational Range.

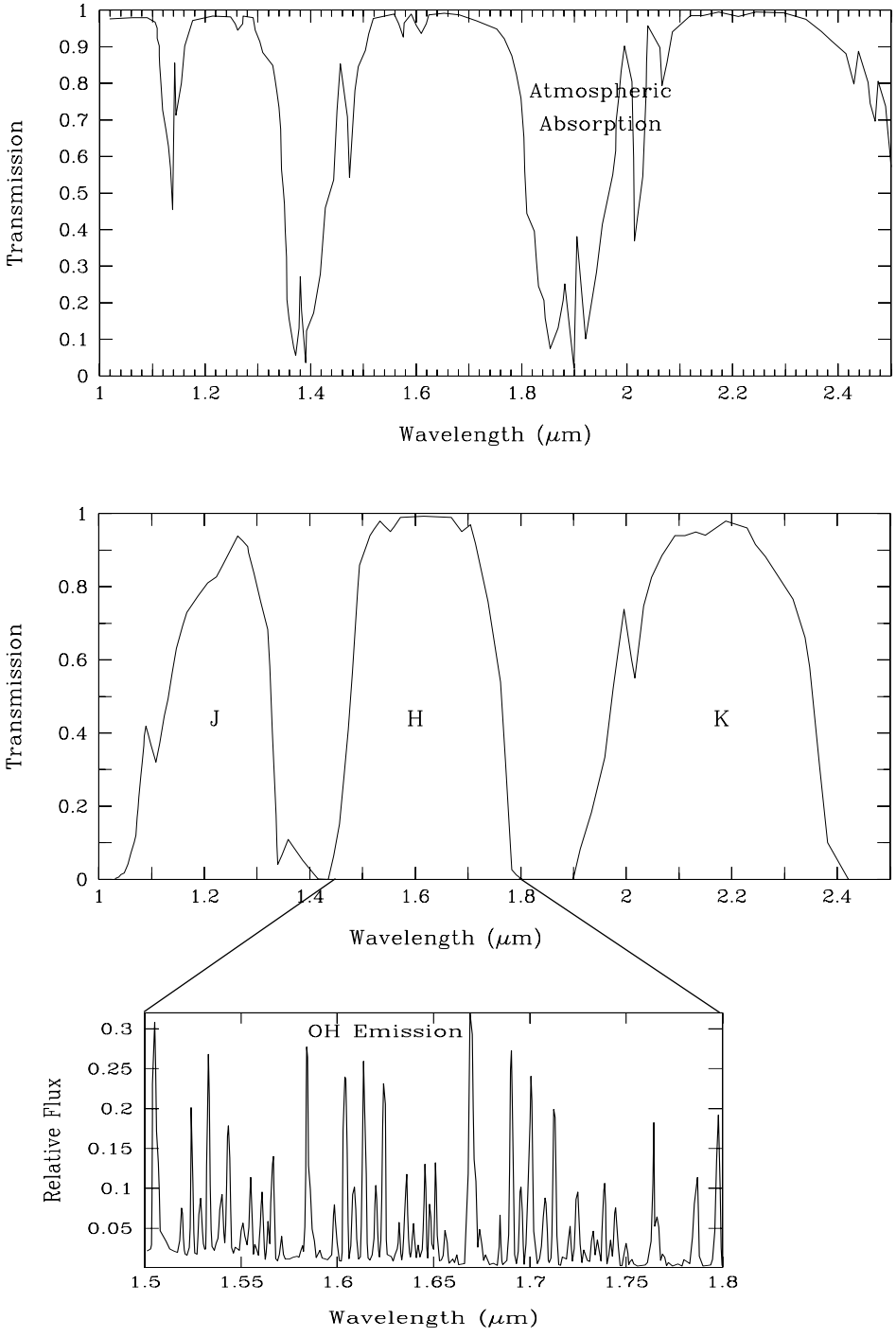

At wavelengths longer than 1.6 microns the HST thermal emission dominates the background seen by NICMOS (Table 4.8). The thermal emission from the HST is composed of the contributions of the telescope's primary and secondary mirrors and of the NICMOS fore-optics. The emission of the HST primary and secondary mirrors can be approximated as a blackbody with effective temperature of ~290 K. The emissivity of each mirror is about 3%. The NICMOS fore-optics are approximated by a blackbody with temperature ~270 K.

Table 4.8: Average background count rates for selected filters in NIC2.

Filter	Sky Background (e^-/s/pix)	Telescope Thermal Background (e^-/s/pix)
F110W	0.188	0.000
F160W	0.118	0.053
F180M	0.020	0.057
F187W	0.056	0.585
F190N	0.004	0.053
F207M	0.033	3.377
F215N	0.005	0.815
F222M	0.033	12.763
F237M	0.035	49.471

Figure 4.17 shows the cumulative HST background as a function of wavelength. This background has been calculated assuming a zodiacal light contribution consistent with the mean observed by COBE for an ecliptic latitude of 45°, and also includes thermal emission by the HST primary and secondary mirrors, the NICMOS optics, and the transmission of all the NICMOS fore-optics. It does not include the transmission of any filter, nor the response of the detectors. For comparison, we report in the same figure the J, H, K_s and K band background as observed from Mauna Kea, Hawaii, averaged over one year (J~16.4, H~15.3, K_s~15.3, K~15.0) and normalized to the HST aperture (2.4m).

Figure 4.17: HST Background as seen by NICMOS. For comparison, the broad-band infrared background seen from Mauna Kea, Hawaii is shown.

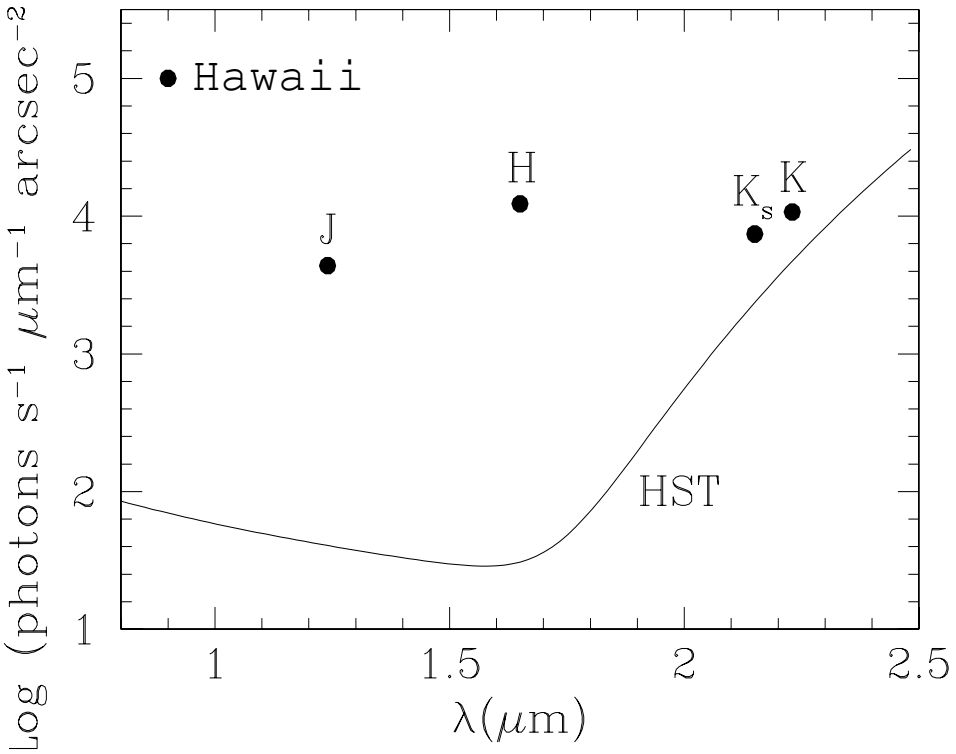

Monitoring of the changes in the thermal background as a function of time, telescope's attitude and slews across the sky has shown that the background is stable to better than 5% on orbital timescales and to about 8% (peak-to-peak) over timescales of several months (see Daou, D. and Calzetti, D. 1998, NICMOS-ISR-98-010). In addition, the thermal background is uniform across each detector, except for NIC3 longward of ~1.8 μm. The lack of significant variations within orbits removes the necessity for rapid dithering or chopping when observing in wavebands affected by thermal background (i.e., longward of ~1.7 μm).

When using NICMOS filters with central wavelengths longer than ~1.7 μm, observers should obtain background measurements as well (through either dithering or chopping). However, given the stability of the HST thermal background, no more than one such measurement per orbit is required.

Table 4.8 lists the measured background for a representative set of NIC2 filters. The Exposure Time Calculator tool on the STScI NICMOS WWW page also produces background count rates for any filter/camera combination.

For pointings very close to the Earth, the zodiacal background may be exceeded by the earthshine. The brightness of the earthshine falls very rapidly with increasing angle from the Earth's limb, and for most observations only a few minutes at the beginning and end of the target visibility period will be significantly affected. The major exception to this behavior is a target in the continuous viewing zone (CVZ). Such targets will always be rather close to the Earth's limb, and so will always see an elevated background, even at shorter wavelengths where zodiacal emission ordinarily dominates. For targets faint enough that the background level is expected to be much brighter than the target, the observer has two options: (1) specify a non-standard Bright Earth Avoidance (BEA) angle, which increases the angle from the Earth's limb from 20 to 25 degrees, or (2) specify the `LOW-SKY` option, which restricts observations to targets more than 40 degrees away from the Earth's limb and restricts scheduling to times when the zodiacal background is no greater than 30% above the minimum achievable level. The second option decreases the available observing (visibility) time during each orbit and implies scheduling constraints. Both of the options above are available but not supported modes, meaning that the observer must request them through a Contact Scientist during the preparation of the phase II proposal.

4.8 The "Pedestal Effect"

The instrumental signature for NICMOS data can be divided into two categories, bias and dark, according to whether or not the signal is noiseless and purely electronic in origin (bias), or noisy and arising from thermal or luminous sources (dark). During detector reset, a net DC bias with a large, negative value (of value -25000 ADU) is introduced. This bias is different in each readout quadrant, but essentially constant within each quadrant.

In addition to the net quadrant bias introduced at array reset, there is some additional offset which is time-variable and, to some degree, stochastic. This variable quadrant bias has been described as the "*pedestal effect*" in many discussions of NICMOS data, although we note here that the term "pedestal" has also been applied to other aspects of NICMOS array behavior. The variable quadrant bias is usually constant over a given array quadrant, but different from one quadrant to another. Its amplitude varies from readout to readout, sometimes drifting gradually, but

occasionally with sharp changes from one readout to another (not always seen in all quadrants simultaneously).

The IRAF scripts **pedsky** and **pedsub** have been developed to remove the pedestal effect. For a more detailed discussion of the pedestal effect and how to remove it, please see the latest version of the NICMOS Data Handbook, Chapter 4: *Anomalies and Error Sources*, at URL:

http://www.stsci.edu/hst/nicmos/documents/handbooks/.

CHAPTER 5:

Coronagraphy, Polarimetry and Grism Spectroscopy

In this chapter . . .

5.1 Coronagraphy

NICMOS Camera 2 (NIC2) has a coronagraphic observing mode which is provided by an occulting hole in the Camera 2 FDA mirror, together with an internal cryogenic mask located at the Lyot plane. The internal cold baffling serves to screen out residual radiation from the edges of the HST primary and secondary mirrors as well as the secondary mirror support structures (pads, spider, and mounts).

Since the FDA mirror is in the image plane, a bright star can be placed such that its core falls onto the occulting hole in the FDA mirror. The star is subsequently re-imaged onto the detector at the focal plane, with its central region occulted. At a radius of 0.3 arcsec, in an idealized PSF, a natural break occurs in the encircled energy profile at 1.6 micron with 93% of the energy in the PSF enclosed. Beyond this radius, the encircled energy profile flattens out toward larger radii.

Figure 5.1: Image of the coronagraphic hole in NIC2. The rough edges created by the final drilling process are evident in this figure.

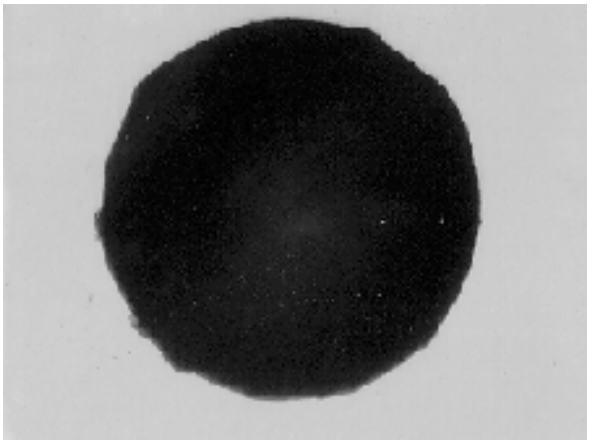

Figure 5.2: Star images. Star imaged outside the hole (left) and within the coronagraphic hole (right). Images were obtained with the F160W filter. Two of the three bright glint regions are marked with arrows. The other is on top of the hole. Images displayed to same stretch.

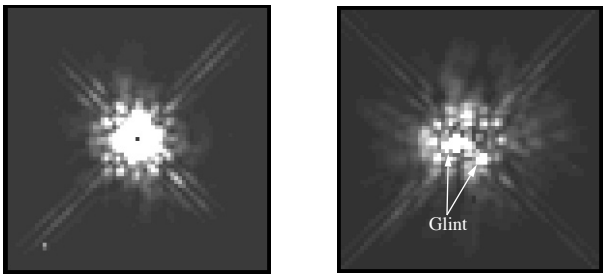

outside hole within hole

The light pattern about the coronagraphic hole is not symmetric due in part to the coronagraphic optics and to the Optical Telescope Assembly (OTA) input PSF. The spectral reflections from the roughness about the hole, and imaged in Camera 2, will vary depending upon the location of the target in the hole. There is one azimuth region where the residual light pattern, historically called *glint*, is brightest. Figure 5.2 presents enlarged images of the same target outside and positioned within the coronagraphic hole displayed to the same stretch. The structure of the scattered light pattern about the hole is different from the NICMOS stellar PSF pattern. The presence of *glint* brings the useful coronagraphic radius at the detector to ~0.4 arcsec.

The FDA mirror and the Camera 2 $f/45$ optics image planes are not exactly parfocal. For nominal Camera 2 imaging, the PAM is positioned to achieve optimal image quality at the detector. For coronagraphic imaging, the PAM is adjusted slightly for optimal coronagraphic performance. The PAM is moved to produce a focused star image at the position of the coronagraphic hole. This results in a very slight degradation of the image quality at the detector. The PAM movement is automatic whenever `OPMODE=ACQ` or `APERTURE=NIC2-CORON` are specified on the Phase II exposure line. If a series of exposures need the `CORON` focus position, only one move is performed.

The tilt of the PAM is changed to compensate for translation from the nominal to coronagraphic setting, and to remove off-axis aberrations.

The NICMOS dewar anomaly caused the coronagraphic hole to migrate to different locations on the detector, during Cycle 7 and 7N. The position of the hole on the detector had been observed to move as much as ~0.25 pixel in three orbits. During the interval April-December 1998, the hole moved about 1 pixel. The movement of the hole is not linear. Rather, the hole "jitters" back and forth along an X-Y diagonal by as much as ±0.5 pixel. The movement of the hole during Cycle 11 is presented in Figure 5.3. The coronagraphic hole has moved, on average, half a pixel per day.

Figure 5.3: Coronagraphic hole location (detector coordinates) during Cycle 11.

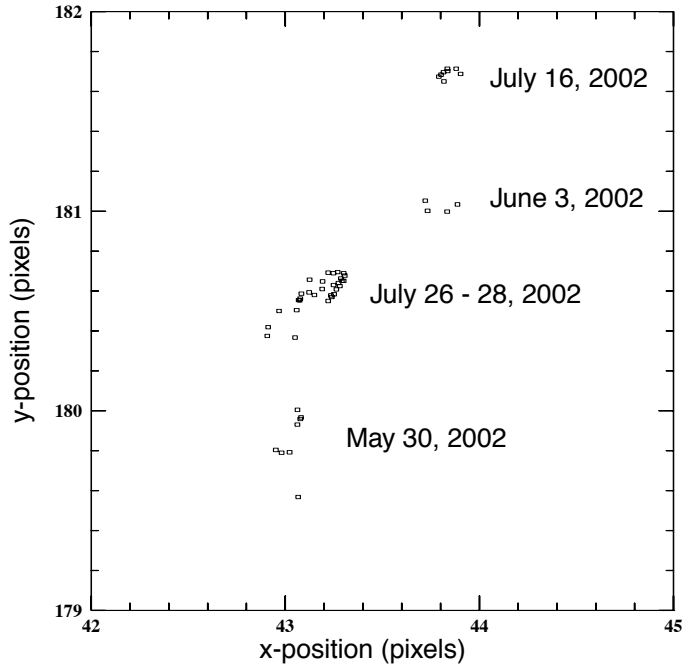

The movement of the hole may cause a problem for coronagraphic observations. Repeat positioning of targets in the coronagraphic hole to a fraction of a pixel is necessary for PSF subtraction. For this reason, the acquisition software is set up to locate the hole position for every acquisition of an astronomical target.

5.1.1 Coronagraphic Acquisitions

Coronagraphic imaging requires an acquisition sequence at the beginning of the observation to position the target in the coronagraphic hole as the size of the coronagraphic hole is smaller than the typical HST blind-pointing errors. The procedure for a coronagraphic acquisition is to first image the target in the `NIC2-ACQ` aperture (128×128 pixel aperture) using blind-pointing and then use either an onboard, reuse target offset, or interactive acquisition to acquire the target. A telescope slew is calculated and commanded to move the image of the target over the position of the hole.

The science exposures are then specified using any of the NICMOS observing modes and any of the NIC2 filters. The science observations following the `ACQ` need to specify the `APERTURE = NIC2-CORON`.

Onboard Acquisition (Mode-2 Acquisition)

The Mode-2 Acquisition for coronagraphy includes two steps: first, the position of the coronagraphic hole is located; second, the target is acquired and placed in the hole.

The location of the coronagraphic hole is determined from pointed flat field observations. Two short F160W filter exposures (7.514 seconds each) with calibration Lamp 1 on (flat field) and two identical exposures with the lamp off (background) are obtained before the acquisition images. The background images are needed because NICMOS does not have a shutter and the flat field images are also imaging the sky. The flight software (FSW) combines the two background and two flat field images by performing a pixel-by-pixel minimum to eliminate cosmic rays (using the lower valued pixel of the two frames). The processed background is subtracted from the processed lamp flat and the image is inverted by subtracting the image from a constant. A small 32×32 pixel subarray containing the hole is extracted and a small checkbox (15×15 pixels) is used to find the centroid and a weighted moment algorithm is applied to determine the flux-weighted centroid within the checkbox. The location of the hole is temporarily stored onboard, but it is not saved in the engineering telemetry sent to the ground.

The target needs to be positioned within the `NIC2-ACQ` aperture, a square 128×128 pixel area on the detector (center at 157, 128) of size 9.6×9.6 arcseconds. Two images of equal exposure are obtained. (The Phase II exposure time is not split.) The two images are pixel-by-pixel

minimized to eliminate cosmic ray hits and a constant value (data negative limit) is added to the processed image. The brightest point source in the acquisition aperture is determined by summing the counts in a checkbox of size 3×3 detector pixels. The algorithm passes the checkbox over the entire acquisition aperture. The brightest checkbox is selected and the location of the target is determined by centroiding the X,Y center of the 3×3 checkbox.

The observer needs only to specify a NICMOS onboard Acquisition (ACQ) to acquire the target. The software schedules the background and flat field observations first, followed by the observations of the target. The exposure times for the pointed background and flat field observations are 7.514 seconds. As an aid to coronagraphic observers, Figure 5.4 presents a plot of counts in the peak pixel for a centered point source obtained with the F160W filter as a function of integration time. The right-hand axis indicates the percentage of full-well for that peak pixel. The true responses of the pixels where the target falls within the FOV will vary. Thus 70% full well should be a reasonably conservative goal for the peak counts needed for a successful acquisition. Over plotted on the figure are diagonal lines which indicate the counts in the peak pixel of a PSF for H-band magnitudes from 8 to 18 (labeled). The shaded region in the lower-right indicates a domain where relatively hot pixels' dark current will result in more counts than faint point-sources, which will cause the acquisition to fail.

Figure 5.4: Coronagraphic point source acquisition exposure times. A goal of 70% full well is recommended for the peak pixel. Over plotted are diagonal lines indicating the estimated counts for different H-band magnitudes. The shaded region on the lower right shows the regime where hot pixels might confuse the acquisition.

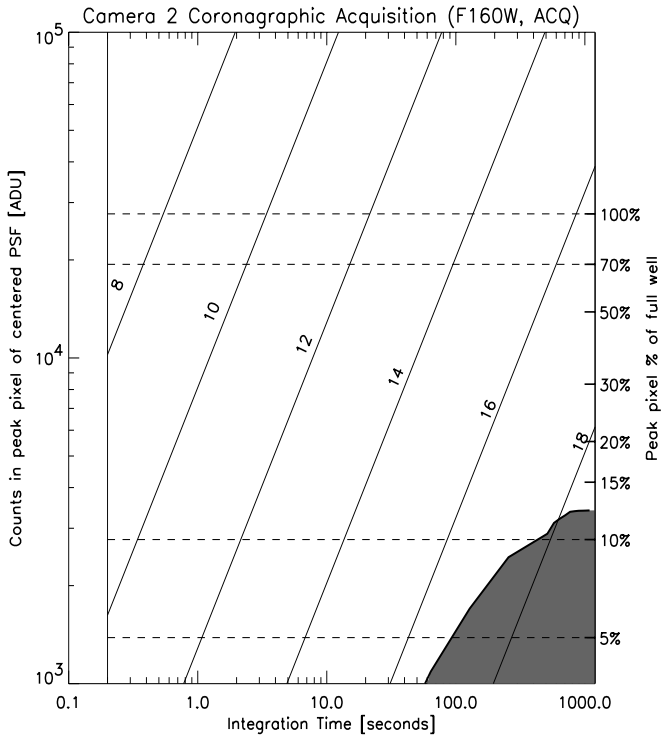

Note that the telescope is not slewed to position the target out of the FOV for the background and flat field observations. If the target saturates the NIC2 detector in 7.514 seconds with the F160W filter, a residual image will be created that will contaminate the onboard target ACQ observation.

Very bright targets will cause saturation, leading to poor results in the centroid solution, and in the subsequent placement behind the occulting hole. To avoid this, a narrow band filter may have to be used to reduce the target flux. Targets brighter than H ~4.0 will saturate the central pixel of the PSF when observed with the F187N filter (narrowest Camera 2 filter) using the shortest ACQ integration time of 0.228 seconds. Since the NICMOS filters are essentially at a pupil plane, there will not be an image shift introduced by using a different filter for the acquisition than for the science observations. Shading will be a problem for centroiding when the target lands near the shading break, as no dark subtraction is performed.

The location of the target and the slew are saved and sent to the ground together with the science observation.

The NICMOS ACQ exposure times, T_ACQ, are quantized with a minimum exposure time of 0.228 seconds. For an ACQ exposure with T_ACQ=0.356 SEC, the overhead to complete the hole finding and location of the target is about 3 minutes which includes the telescope slew to move the hole over the target. A full description of the overheads for Mode-2 Acquisitions is given in Chapter 10.

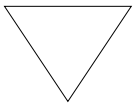

For T_ACQ exposures longer than ~5 minutes the probability of cosmic ray hits occurring in the same pixel in each of the two acquisition images is sufficiently high that observers must instead use an early acquisition to avoid their observations failing due to a false center determination. Early acquisitions are described in the next section. In practice, this should not be a severe restriction as in the F160W filter one will reach a signal-to-noise of 50 at H=17 in only 2–3 minutes.

The flight software processed images are not saved, but the two background, two flat field, and two acquisition ACCUM images are sent to the ground. These images, which are executed in a single target acquisition observation, will be packaged into one data set with the same root name but with different extensions. A full description of the extensions is given in the HST Data Handbook.

Starting from Fall 2003, **calnica** calibrates the ACQ Accum and Accum background images. The Accum F160W flat field is calibrated up through dark subtraction, using a temperature dependent dark constructed on the fly given the exposure time and detector temperature.

Reuse Target Offset (RTO) and Interactive Acquisitions

Bright targets will saturate the NICMOS Camera 2 detector, resulting in possible failure of the onboard software (Mode-2 Acquisition) to successfully acquire and position the target into the coronagraphic hole. Any target that will saturate the detector in the shortest possible Mode-2 `ACQ` exposure time, 0.228 seconds, should be considered a bright target. A variation of the Reuse Target Offset (`RTO`) capability can be used to acquire and position a bright target into the coronagraphic hole. In addition, the onboard acquisition software may not successfully acquire the desired target in a crowded field. For this case, an interactive acquisition (`INT-ACQ`) may be required to successfully acquire the target.

The following discussion describes the necessary steps for a Reuse Target Offset (`RTO`) acquisition to acquire a bright target and position the target into the coronagraphic hole. These steps can also be used for an interactive acquisition of a target in a crowded field. It is recommended for `RTO` acquisition that two orbits be used when observing a bright target except possibly for an `INT-ACQ`. The first orbit is used for the acquisition and the second orbit for the coronagraphic observations.

Images of the target and coronagraphic hole are obtained a few orbits in advance of the coronagraphic observations, and sent to the ground for analysis (`RT ANALYSIS`). The target exposures should be offset from the `NIC2-CORON` aperture fiducial point to avoid having the target fall in the hole.

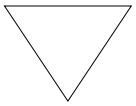

An RTO slew is limited to ~10", taking ~26.5 seconds of time to complete. A target offset of ~9" or less from the hole position is highly recommended to avoid exceeding the 10" limit due to the uncertainty in the target coordinates and proper motion.

The observer needs to specify at least two background, two flat field, and two on-target exposures in the Phase II template. The background and flat field observations should be offset by 18-25 arcseconds from the target position to avoid the diffraction spike from the image of an overexposed target crossing the coronagraphic hole and introducing errors in the measured position of the coronagraphic hole. The recommended pairs of images are needed to remove cosmic ray hits (see NICMOS Instrument Science Report, NICMOS-ISR-031).

OPUS staff will assist the PI in identifying the target, centroiding, and determining offsets. OPUS staff will then provide the offsets to the Flight Operations Team (FOT) at the Space Telescope Science Institute for uplink to the spacecraft in advance of the coronagraphic observations. The ultimate responsibility for determining the offsets will be the PI (or the PI's representative), who must be present at STScI at the time of the target/hole location observations.

5.1.2 PSF Centering

Both the total encircled energy rejection (from the occulted core of the PSF) and the local contrast ratio obtainable in a coronagraphic image depend on the accuracy of the target centering on the coronagraphic hole. The goal is to center the PSF of the occulted source to a precision of a 1/6 pixel at a position *x*=–0.75, *y*=–0.05 pixels from the center of the hole, "the low scatter point". The decrease in the fractional encircled energy due to imprecise centering of the core of an idealized PSF in the coronagraphic hole is 0.3 percent for a 1/4 pixel offset, and 4.4 percent for a 1 pixel (75 milliarcseconds) offset at 1.6 microns.

In addition, a small error in target centering will create an asymmetric displacement of the PSF zonal structures both in and out of the coronagraphic hole, leading to position dependent changes in the local image contrast ratios.

NOTE: During Cycle 7 and 7N, the low scatter point was at pixel location x=–0.75, y=–0.25 from the hole center.

5.1.3 Temporal Variations of the PSF

Temporal variations of the NICMOS PSF due to HST breathing and "wiggling" of the misaligned cold mask in NIC2 are discussed in Chapter 4. Of relevance to coronagraphic observers is that the effects of temporal variations for PSF subtraction can be minimized by obtaining observations of the same PSF in back-to-back orbits or twice in the same orbit, with a roll of the spacecraft between the two observations. The success of this technique is due to the orbital timescale of the PSF temporal variations.

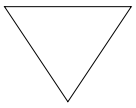

During Cycles 7 and 7N, the NICMOS IDT reported very good results for PSF subtraction when the same target was observed twice in the same orbit with a roll of the spacecraft between observations. Between Cycle 11 and the start of Two Gyro Mode operations during Cycle 14, this observational strategy was available to General Observers (GOs). This strategy was generally not feasible under Two-Gyro Mode. With the return to Three-Gyro Mode in Cycle 17, this strategy will again be available.

Back-to-back coronagraphic observations of the same target with a roll of the spacecraft between observations are scheduled as two separate visits. The two visits are linked close in time by using the Phase II visit-level requirement "AFTER", such as AFTER 01 BY 15 MINUTES TO 30 MINUTES as a requirement on the second visit. The timing link will be used to schedule both visits. Each coronagraphic visit, including guide star

acquisition, ACQ, exposure time, and overhead must not exceed 22 minutes in duration to allow time to roll the telescope between visits.

The roll between two visits must be expressed as a relative orient, such as ORIENT 25D TO 30D FROM 01 as a requirement on the second visit. The permitted amount of spacecraft roll varies throughout the Cycle as the target position changes relative to the Sun. A roll of 6 degrees between visits will take about one minute to complete which does not include the overhead to ramp up and ramp down the motion. A 30 degree roll will take about nine minutes to complete. These roll overheads need to be allowed for in Phase I planning, but they are automatically handled by the scheduling software when the visits are actually scheduled.

5.1.4 FGS Guiding

Two guide star (GS) guiding is strongly recommended when performing coronagraphic observations. For best coronagraphic results, the target should be centered to better than 1/6 pixel.

Coronagraphic observations executed in back-to-back orbits should be scheduled with the same guide star pair, except possibly if a roll of the HST is performed between orbits. This is also critical for Reuse Target Offset (`RTO`) Acquisitions, which require the same guide stars be used for all observations. Switching guide stars between the acquisition and science observations will force the respective target to either be positioned away from the coronagraphic hole or on the edge of the hole.

The use of a single guide star is discouraged for coronagraphic observations. The drift about a single guide star is small, but will yield intense residuals for PSF subtraction. If we represent the linear motion due to gyro drift around a star as $xX = D\sin(at)$, where X equals the linear motion, D the distance from the guide star to the aperture, a the angular gyro drift rate, and t the time since the last FHST (fixed-head star tracker) update, then for D = 20 arcmin (worst case) = 1200 arcsec and a = 0.001 arcsec/sec, for one visibility period t = 50 min = 3000 sec we get X = 0.0175 arcsec or less than 1/4 pixel in Camera 2. For two orbits t = 146 min = 8760 sec, X = 0.051 arcsec or a little over 2/3 pixel in Camera 2.

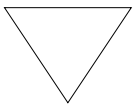

During Cycle 7 and 7N, NICMOS SNAP coronagraphic observations were scheduled with single guide star guiding. Starting with Cycle 11, all NICMOS SNAPSs including coronagraphic observations are scheduled with two-guide star guiding.

For RTO acquisitions, the maximum default slew is 10 arcseconds. This is set by the coordinate uncertainties as specified in the Phase II template. If a slew larger than the default 10 arcseconds is scheduled, it has to be approved by the STScI Commanding Group and the FOT notified that a slew of this size or larger will not force the guide stars out of the FGS field of view (a.k.a. pickle). Increasing the target coordinate uncertainties will increase the slew limit. STScI Commanding will use the coordinate uncertainties to determine the size of the slew request timing. Guide star selection is also affected. If the requested amount of guide star movement will force the guide star out of the pickle, the guide star selection software will not select that star. This may result in single star guiding. One solution to this problem is to decrease the distance between the target star and the hole and correspondingly decrease the target coordinate uncertainties. Note that the NIC2 field-of-view (FOV) is ~19 arcsec on a side.

5.1.5 Cosmic Ray Persistence

Coronagraphic observations scheduled over more than one visibility period will most probably be impacted by an SAA passage and possibly be affected by charged particle induced persistence (see Chapter 4 for a discussion on the cosmic ray persistence). To avoid breaking exposures across visibility periods, coronagraphic observations should be scheduled using the exposure level Special Requirement "SEQ <EXP. LIST> NON-INT", which forces all observations to be within the same visibility window, i.e., without interruptions such as Earth occultations or SAA passages.

5.1.6 Contemporary Flat Fields

One of the coronagraphic calibration problems is "proper" calibration of images near the edge of the hole due to motion of the hole itself. The problem arises from the fact that the OPUS flat field reference files are not contemporary with the coronagraphic images. During Cycle 7 and 7N, the coronagraphic hole moved about 0.1 to 0.2 pixels per month. In addition, there is a second, short term component to the movement along a pixel diagonal (back-and-forth) and, imposed upon this motion, a third component of random jitter composed of a few tenths of a pixel.

The light pattern about the coronagraphic hole is not symmetric due to *glint* (see Section 5.1 and Figure 5.2), and will vary depending upon the location of the target in the hole. Calibrating with a contemporary flat, which has the coronagraphic hole pattern at the correct location, restores the flux level and re-establishes the light pattern about the hole at the time of the observation. For distances greater than ~0.7 arcseconds from the hole (diameter ~17 pixels), the standard, high S/N flat is the best reference file to use for calibration.

"Proper" calibration of coronagraphic images can be achieved with contemporaneous lamp and background observations. These calibration

observations can be scheduled within the time allowed and will increase the scientific return of the science data. Calibration observations are normally obtained as part of the STScI calibration program and GOs are not usually allowed to request calibration data. However, the coronagraphic programs are allowed to obtain lamp and background observations to be used to locate the coronagraphic hole. For RTO Acquisitions, if there are no pressing scientific reasons to fill the remaining acquisition orbit with science observations, then it is recommended that lamp and background observations be obtained to support the coronagraphic science observations.

5.1.7 Coronagraphic Polarimetry

A Cycle 12 commissioning program has shown that the NICMOS Camera 2 polarizing filters can be used successfully in combination with the coronagraph. This significantly enhances the imaging polarimetry mode by enabling polarization measurements of regions near a bright object, such as a star or active galactic nucleus.

Image artifacts within about 2 arcseconds of the coronagraph, caused by scattering off the edge of the hole, are repeatable and induce only a small instrumental polarization (IP ~2%). The calibratable polarization measurements near the hole are limited by this IP component and the current calibration data to about 8–10% (4 sigma in percentage polarization) per 2×2 pixels (approximate resolution element). However, the observed stability of the IP component implies that future refinement to the calibration and further characterization of the scattering about the coronagraphic hole may improve this limit.

Observers considering the use of the coronagraph combined with the polarizing filters should follow the standard recommendations for two-roll coronagraphic imaging, and remember that images through all three polarizers must be obtained at each roll. We also recommend that observers include observations of an unpolarized standard star in addition to their primary target object, and that the standard star be observed at sufficient depth to obtain similar S/N to the primary target in each polarizer. Thus, a minimum of two orbits per target is typically needed; i.e., target star and unpolarized standard star. A single, well-exposed unpolarized standard star should be sufficient for a multi-target science program.

5.1.8 Coronagraphic Decision Chart

The decision chart presented in Figure 5.5 helps guide the proposer through the selection process to construct coronagraphic observations when using an onboard acquisition or an early acquisition image. The process for specifying RTO acquisitions of bright target is presented in NICMOS-ISR-031 (13-Jan-1998). The observer is advised to contact the STScI help desk, help@stsci.edu, for additional information.

Figure 5.5: Coronagraphic Decision Chart

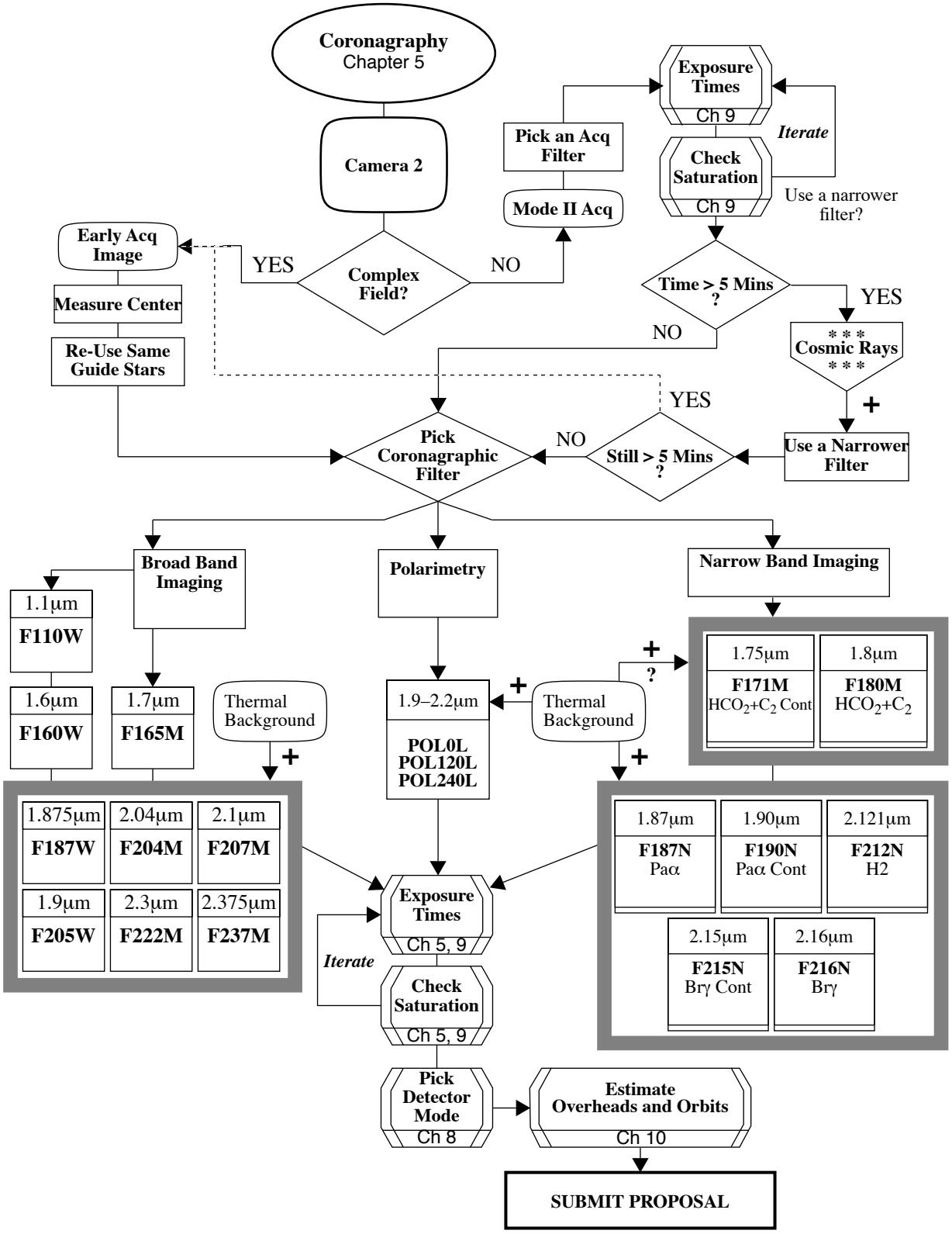

5.2 Polarimetry

NICMOS contains optics which enable polarimetric imaging with high spatial resolution and high sensitivity to linearly polarized light from 0.8 to 2.1 microns. The filter wheels of NIC1 and NIC2 each contain three polarizing filters (sandwiched with band-pass filters) with unique polarizing efficiencies and position angle offsets. The design specified that the position angle of the primary axis of each polarizer (as projected onto the detector) be offset by 120^{o} from its neighbor, and that the polarizers have identical efficiencies. While this clean concept was not strictly achieved in NICMOS, the reduction techniques described in the HST Data Handbook permit accurate polarimetry using both cameras over their full fields of view. A description on NICMOS polarimetry can also be found in Hines, Schmidt, and Schneider (2000)[1].

The spectral coverage is fixed for each camera, and the polarizers cannot be crossed with other optical elements. For NIC1 the polarizers cover the wavelength range 0.8 to 1.3 microns (short wavelength), and for NIC2 the coverage is 1.9 to 2.1 microns (long wavelength). Observations in all three polarizers will provide the mechanism for calculating the degree of polarization and position angle at each pixel. To properly reduce polarimetry data obtained with NICMOS, a new algorithm different from that needed for ideal polarizers has been developed[2,3]. Combined with calibration measurements of polarized and unpolarized stars, this algorithm enables accurate imaging polarimetry to ≤ 1% (in percentage polarization) over the entire field of view in both cameras[4,5].

5.2.1 NIC 1 and NIC2 Polarimetric Characteristics and Sensitivity

The three polarizers in NIC1 are called POL0S, POL120S and POL240S, and in NIC2 are called POL0L, POL120L, and POL240L,

1. Hines, D.C., Schmidt, G.D., & Schneider, G. 2000, “Analysis of Polarized Light with NICMOS”, PASP, 112, 983.

2. Hines, D.C., Schmidt, G.D., & Lytle, D., The Polarimetric Capabilities of NICMOS, in The 1997 HST Calibration Workshop with a New Generation of Instruments, ed. Casertano et al, 1997

3. Sparks, W.B. & Axon, D.J. 1999, “Panoramic Polarimetry Data Analysis”, PASP, 111, 1298.

4. Mazzuca, L., Sparks, B., & Axon, D.J. 1998, “Methodologies to Calibrating NICMOS Polarimetry Characteristics”, ISR, NICMOS-98-017.

5. Mazzuca, L. & Hines, D. 1999, “User’s Guide to Polarimetric Imaging Tools”, ISR, NICMOS-99-004.

where the suffix 0, 120 and 240 indicates the design specifications for the position angle of the polarizer's primary axis (in degrees). A summary of the characteristics of the NIC1 and NIC2 polarizers are given in Table 5.1 below. The final column lists Pixel fraction which is the fraction of total energy of the PSF contained in one pixel, assuming the source to be centered on that pixel.

Table 5.1: Polarizer Characteristics.

Camera	Central (μm)	Mean (μm)	Peak (μm)	FWHM (μm)	Range (μm)	Pixel fraction
NIC 1	1.0450	1.0384	1.0245	0.4750	0.8–1.3	0.048
NIC 2	1.9943	1.9946	1.9100	0.2025	1.9–2.1	0.33

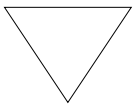

Observations must be obtained at all three primary axis' angles (POL0*, POL120*, and POL240*) to measure the three linear Stokes parameters I, Q and U, from which to derive the polarization intensity, the degree of polarization and the position angle at each pixel.

In each Camera the three polarizers were designed to be identical and to have the position angle of the primary axis of each polarizer offset by 120^{o} from its neighbor. In practice, this was not completely achieved and:

1. Each polarizer in each camera has a unique polarizing efficiency.
2. The offsets between the position angles of the polarizers within each filter wheel differ from their nominal values of 120^{o}.

Table 5.2 below lists for each polarizer the position angle of the primary axis and the filter efficiency (throughput of the filter only).

Table 5.2: Characteristics of the NIC1 and NIC2 polarizers.

Filter	Position Angle	Throughput
POL0S	1.42	0.9717
POL120S	116.30	0.4771
POL240S	258.72	0.7682
POL0L	8.84	0.7313
POL120L	131.42	0.6288
POL240L	248.18	0.8738

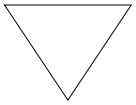

In NIC1 the POL120S filter only has 48% transmission while the POL0S filter has 98%. Observers should consider using POL0S at multiple spacecraft roll angles rather than POL120S.

The instrumental polarization caused by reflections off the mirrors in the NICMOS optical train is small (approximately less than 1%).

As with the imaging filters, sensitivity plots for the two sets of polarizers for both extended and point sources are shown in Appendix A, which also contains throughput curves (convolved with the HST and NICMOS optics and the detector's response) for the polarizers. To work out how many integrations are needed to get the desired S/N, the observer can use the Exposure Time Calculator available on the WWW (see Chapter 1 or Chapter 9). To get the total exposure time required for a polarimetric observation the final answer must be multiplied by three to account for the fact that all three polarizers must be used to get a measurement.

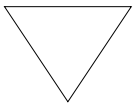

The proposer should be aware that the Exposure Time Calculator computes the intensity based on the highest transmission of all the polarizers for each camera and an unpolarized signal.

For the long wavelength polarizers in NIC2, thermal background must be considered (see Chapter 4 for a description of the thermal background seen by NICMOS and Appendix D for related observing strategies).

For a polarized source, the intensity measured by the detector depends on the orientation of the spacecraft relative to the source in the sky. The range of intensities is given by the Exposure Time Calculator value multiplied by $(1 \pm p\varepsilon_k)$, where p is the fractional polarization of the source and ε_k is the polarizer efficiency.

5.2.2 Ghost images

Multiple ghost images are present in NIC1 and NIC2 polarimetry data, though the NIC2 ghosts are much fainter than in the NIC1. The location of ghosts in each polarizer appears constant on the detector relative to the position of the target (i.e. independent of telescope or object orientation). For example, the NIC1 ghosts are offset between POL0S and POL240s, which produces a very highly polarized signal (100%) in percentage polarization. This allows them to be easily distinguished from real polarized signal. While all emission in the POL0S and POL240S frames will produce ghosts, experience with real data shows that the effect is most important for strong point sources.

Figure 5.6 shows an example of the ghosts in NIC1 POL0S, POL240S, and the percentage of polarization. These ghosts will typically be seen as regions of 100% polarization (seen as white blobs)

Figure 5.6: Ghost Images in NIC1 Polarizers[6]

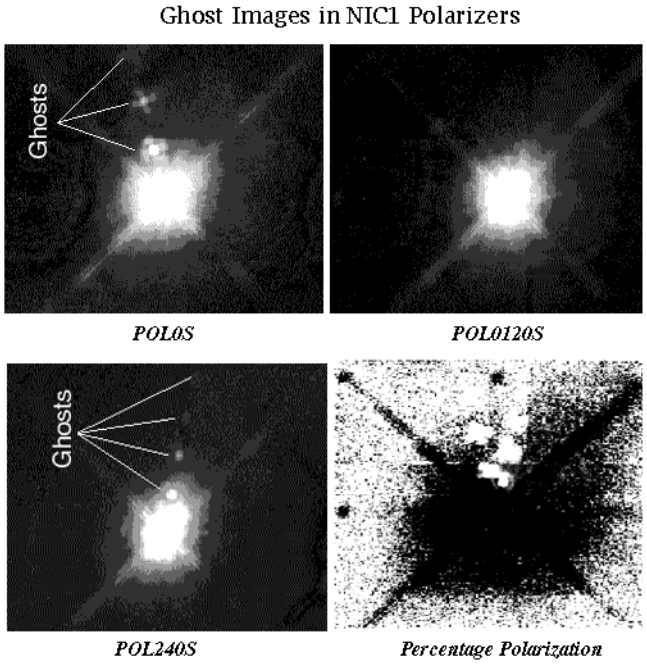

6. Refer to http://ecf.hq.eso.org/nicmos/sardinia/node14.html#2206, “Imaging Polarimetry with NICMOS” for more details.

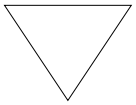

For NIC1, observers may want to consider an additional visit specifying a different ORIENT to recover information lost due to ghosts so that important structures in the object are not near the image ghosts in POL0S and POL240S.

5.2.3 Observing Strategy Considerations

Observers should always use a dither pattern to help alleviate residual image artifacts, cosmic rays, and image persistence, as well as to improve sampling. The best choice for the number and size of the dithers depends on the amount of time available and the goals of the project, but a minimum of four positions will allow optimal sampling and median filtering.

One strong recommendation is to execute a four position pattern separately for each polarizing filter with N+1/2 pixel offsets, where N ≥ 10–50 depending on the structure of the object and the field of view that the observer wants to maintain. N=10 alleviates most persistence problems from point sources, and the additional 1/2 pixel ensures good sampling. The reason for executing a pattern separately for each polarizer is to remove latent images. By the time the pattern completes and starts for the next polarizer, the latent image from the previous polarizer is essentially gone. The same observing process should be applied to each polarizer observation (e.g. POL120L and POL240L). This strategy will result in a minimum of 12 images with which to construct the linear Stokes parameters (I, Q, U).[7]

Exposure times should be set such that the source does not drive the arrays into saturation, and only one exposure should be attempted per dither position because the long decay time for persistence. If more integration time is needed to achieve the desired S/N, the entire dither pattern for each polarizer should be repeated. For the best results, the observing sequence should be POL0*, POL120*, POL240*, then repeat POL0*, POL120*, POL240*, etc.

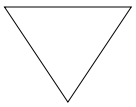

Observers are reminded that for polarimetry observations in NIC2 the thermal background must be considered. In this case, background images need to be obtained in all three polarizers.

7. For more information on dithering, see Appendix D.

The raw polarimetric images obtained through each polarizer are routinely processed by the first stage of the pipeline like any other exposure.

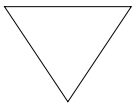

For NICMOS polarimetry, `MULTIACCUM` mode (see Chapter 8) is the only exposure read-out mode recommended.

5.2.4 Limiting Factors

Limiting Polarization

Because the errors for percentage polarization follow a Rice distribution[8], precise polarimetry requires measurements such that $p/\sigma_{p,meas} > 4$, where p is the percentage polarization and σ_p its standard deviation. Therefore, uncertainties 0.5–3% (per pixel) imply that objects should have minimum polarizations of at least 2–12% per pixel.

Binning the Stokes parameters before forming the percentage polarization p and the position angles reduces the uncertainties by $\sim 1/\sqrt{N}$, where N is the number of pixels in the bin. Uncertainties as low as 0.2% in NIC2 should be achievable with bright objects.

Position Angle of Incoming Polarization Relative to NICMOS Orientation

The non-optimum polarizer orientations and efficiencies cause the uncertainty in polarization to be a function of the position angle of the electric vector of the incoming light. For observations with low signal-to-noise ratios (per polarizer image), and targets with lower polarizations, the difference between the signals in the images from the three polarizers becomes dominated by (photon) noise rather than analyzed polarization signal. Therefore, observations that place important incoming electric vectors at approximately 45° and 135° in the NICMOS aperture reference frame should be avoided in NIC1. No such restriction is necessary for NIC2.

Figure 5.7 shows the fractional signal measured in each NICMOS polarizer as a function of incident electric position angle (PA) for 20% polarized light. The lower curves are the differences in fractional signal between images taken with successive polarizers. The vertical dashed lines in the left panel (NIC1) represent the position angles of the incoming

8. Refer to Simmons & Stewart, "Point and Interval Estimation of the True Unbiased Degree of Linear Polarization in the Presence of Low Signal-to-Noise Ratios", A&A 142, pp100–106, 1985.

electric vector where these differences are all small, and thus produce the largest uncertainties in the measured polarization.

Figure 5.7: Fractional signal measured in each NICMOS polarizer as a function of incident electric position angle.[9]

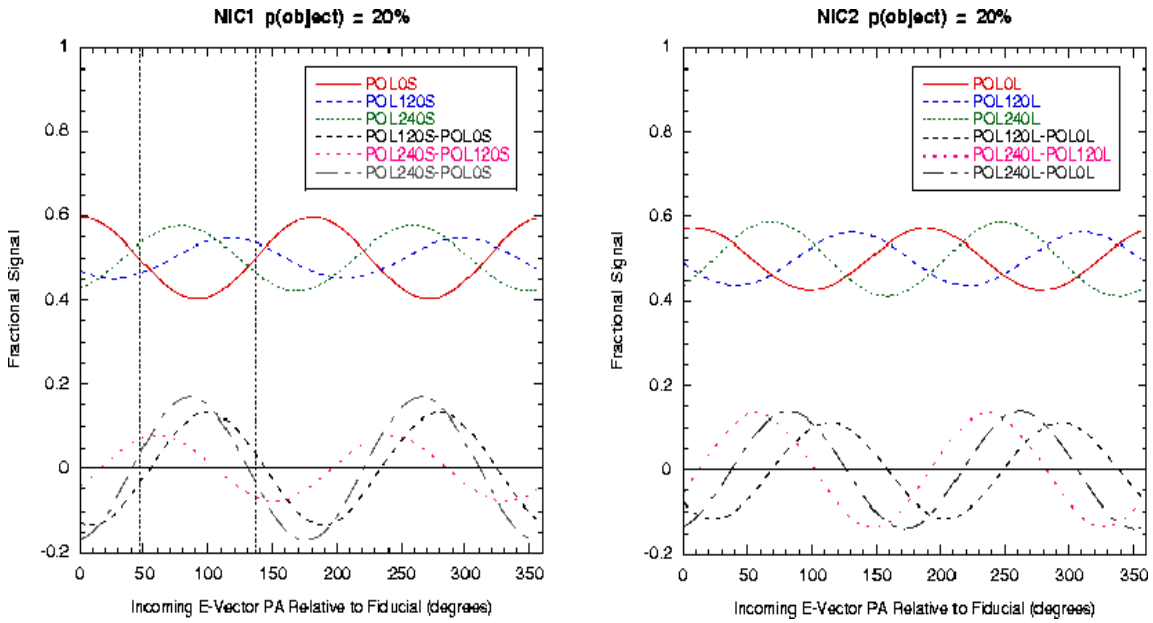

5.2.5 Polarimetry Decision Chart

The decision chart given in Figure 5.8 below helps guide the proposer through the selection process to construct a polarimetry observation.

9. Refer to http://ecf.hq.eso.org/nicmos/sardinia/node14.html#2206, “Imaging Polarimetry with NICMOS” for more details.

Figure 5.8: Polarimetry Decision Chart.

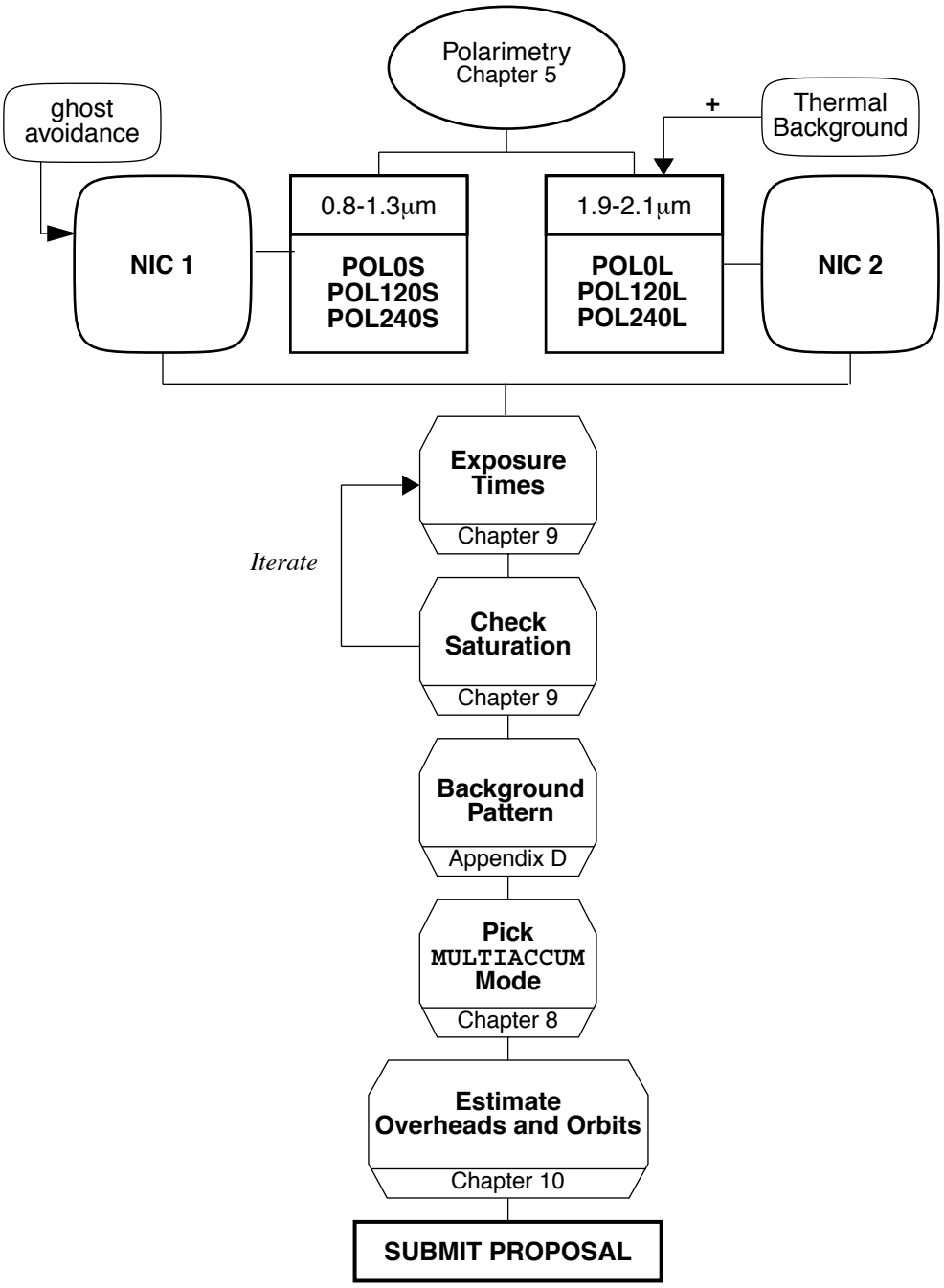

5.3 Grism Spectroscopy

NICMOS provides grism imaging spectroscopy in the spectral range between 0.8 and 2.5 μm with Camera 3.[10] NICMOS is used in this mode of operation without any slit or aperture at the input focus, so all objects in the field of view are dispersed for true multi-object spectroscopy. The grisms reside in the NIC3 filter wheel, therefore the spatial resolution of the spectroscopy is that of this Camera. The filter wheel contains three grisms (G096, G141, G206), of infrared grade fused silica, which cover the entire NICMOS wavelength range with a spectral resolving power of ~200 per pixel.

A grism is a combination of a prism and grating arranged to keep light at a chosen central wavelength undeviated as it passes through the grism. The resolution of a grism is proportional to the tangent of the wedge angle of the prism in much the same way as the resolution of gratings are proportional to the angle between the input and the normal to the grating.

Grisms are normally inserted into a collimated camera beam. The grism then creates a dispersed spectrum centered on the location of the object in the camera field of view. Figure 5.9 shows an example of grism spectra of point sources using G096, G141, and G206. The target is the brightest source in the FOV, although many other sources yield useful spectra as well. The band along the bottom of the images, about ~15–20 rows wide, is due to vignetting by the FDA mask, while the faint dispersed light on the right edge of the G206 grating image is due to the warm edge of the aperture mask.

The two shorter wavelength grisms exploit the low natural background of HST while the longest wavelength grism is subject to the thermal background emission from HST.

Figure 5.9: Grism slitless spectroscopy of point sources, using G096, G141, and G206.

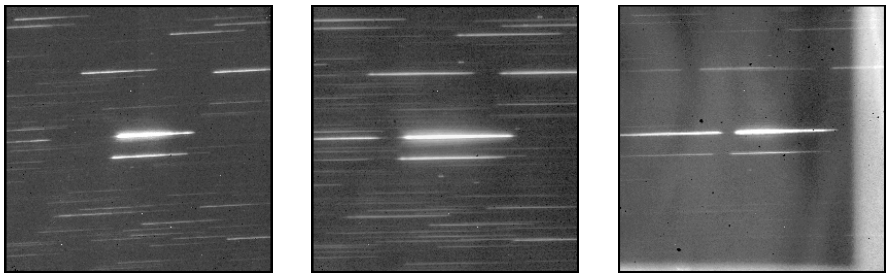

G096 G141 G206

10. NICMOS Instrument Science Report, NICMOS ISR-97-027.

The basic parameters of the NICMOS grisms are given in Table 5.3.

Table 5.3: Grism Characteristics.

Grism	Resolution per Pixel	Central Wavelength (μm)	Wedge Angle (°)	Bandpass (μm)	Lines per mm
G096	200	0.964	5.219	0.8 – 1.2	45.0
G141	200	1.401	5.5889	1.1 – 1.9	30.8
G206	200	2.058	5.6944	1.4 – 2.5	21.1

5.3.1 Observing Strategy

Grism observations are carried out in a similar manner as other NICMOS imaging. For accurate wavelength calibration, it is essential to pair each grism observation with a direct image of the field in NIC3, through an appropriate filter, at the same pointing. This provides the location of each object in the field and aids in the identification of their individual spectra. Because of this natural pairing, most spectroscopy observations will be a two image set, direct and grism images. For estimating the S/N for both the filter and grism observations a NICMOS spectroscopic ETC is available:

http://apt.stsci.edu/webetc/nicmos/nicmos_spec_etc.jsp

There are two separate considerations for the strategy to place the spectra on the NICMOS detector. One is the choice of orientation, the other one is the placement relative to the edges of the detector. The orientation of the spectra relative to the detector is important because the spectra of random objects in the field might overlap the spectra of the target objects. The orientation is also important for slightly extended objects. In such cases, it may be possible to alleviate the superposition of spectra by requesting a specific orientation (roll-angle) of the telescope during the Phase II Proposal submission. For complex fields or extended targets, observations of the same field at three or more different spacecraft orientations are advisable to allow deconvolution of overlapping spectra. A review of the target field to determine if spectral contamination caused by field objects can be avoided, should be the first step in choosing a pointing strategy. If infrared images of the target field are not available, then DSS images should be examined. It is important to find a range of possible roll-angles, since restricting the roll-angle limits the schedulability of the program.

The next step of the pointing strategy is the placement of the target spectra onto the detector. The four different quadrants of the NICMOS detector are read separately. Therefore, differences in the bias level, sensitivity and/or noise between the quadrants are often unavoidable. For that reason, spectra should be placed so that they do not cross the boundary

between the quadrants. The best positions are close to the center of any of the four quadrants of the NICMOS detector, i.e. as close as possible to any of the points (64,64), (192,64), (64,192) or (192,192). The more important part is the x-coordinate of the detector. The pointing of NICMOS is specified for the undispersed image. To place the spectra at the desired position, one has to take into account that the spectra taken through any of the grisms are displaced relative to the position of the undispersed image taken through one of the filters. The offsets in pixels for each grism are listed in Table 5.4. These offsets have to be taken into account when placing the spectra on the detector. In order to place the center of the spectrum at a desired position, the pixel values listed in Table 5.4 have to be added to the specified pixel position on the detector. For example, in order to place a G141 spectrum at the center of the first quadrant, pixel coordinates x=54+6.7, y=64+13 have to be specified. If only a single target is observed, we recommend to split up the integration time into four exposures and place the spectrum at the center of all four quadrants. This improves the flux calibration of extracted spectra.

Table 5.4: Approximate Position of Undispersed Object Relative to the Center of the Spectrum in Pixels.

Grism	Delta X	Delta Y
G096	4.5	10
G141	6.7	13
G206	2.2	–7

We encourage all grism observers to dither their observations. Dithering the target on the detector will minimize image anomalies such as grot affected pixels, cosmic ray hits, pixel sensitivities, and residual persistence images. The sequence of images should always be: direct and grism images at the first dither point, move to next dither position, direct and grism images at the second point, etc. This can be achieved using the pattern syntax (see Appendix D). Because of intrapixel sensitivity variations (See Section 5.3.5), dither spacing should be a non-integer number of pixels, e.g. 2.1 arcsec (10 and a half pixels).

The best dither pattern is to move in both directions (pattern NIC-SPIRAL-DITH). This will improve line fluxes, wavelength measurement of lines, and help to verify broader spectra features. Dithering parallel to the dispersion may result in loss of data off the edge of the detector, or move spectra at a position where they cross the boundary of a quadrant. For a single target, this can easily be avoided by choosing a dither pattern which places the spectrum close to the center of all four quadrants. In a more complex situation with several targets, the design of a dither strategy needs to include the consideration of roll angles.

5.3.2 Grism Calibration

The NICMOS spectroscopic grism mode calibrations were determined from on-orbit observations. Wavelength calibration was carried out by observing planetary nebulae, Vy 2-2 and HB12. The inverse sensitivity curve is derived from observations of the white dwarf G191-B2B and G-dwarf P330E. Grism calibration data reductions were performed at the Space Telescope European Coordinating Facility (ST-ECF). An IDL software package of tasks to extract spectra from pairs of direct and grism images called **NICMOSlook** is available from the ST-ECF NICMOS Web page http://www.stecf.org/instruments/NICMOSgrism .

5.3.3 Relationship Between Wavelength and Pixel

Table 5.5 gives the dispersion relationship in the form:

$$\lambda = m \cdot \Delta x + b \quad ,$$

where Δx is the x coordinate relative to the center of the object on the direct image, and λ is the wavelength in μm. The relationship is plotted in Figure 5.10. The grisms were aligned as accurately as possible along a row or column of the array. However, there is a slight tilt to the spectra; 3.1 degrees for G096, 0.7 degrees for G141, and about 1 degree for G206. Distortion and curvature in the spectrum are negligible.

Table 5.5: Grism wavelength to pixels relationship.

Grism	m	b
G096	-0.00536	0.9487
G141	-0.007992	1.401
G206	-0.01152	2.045

Figure 5.10: Wavelength Versus Pixel Number for each Grism. Note that the actual location of the central wavelength on the detector depends on the position of the source.

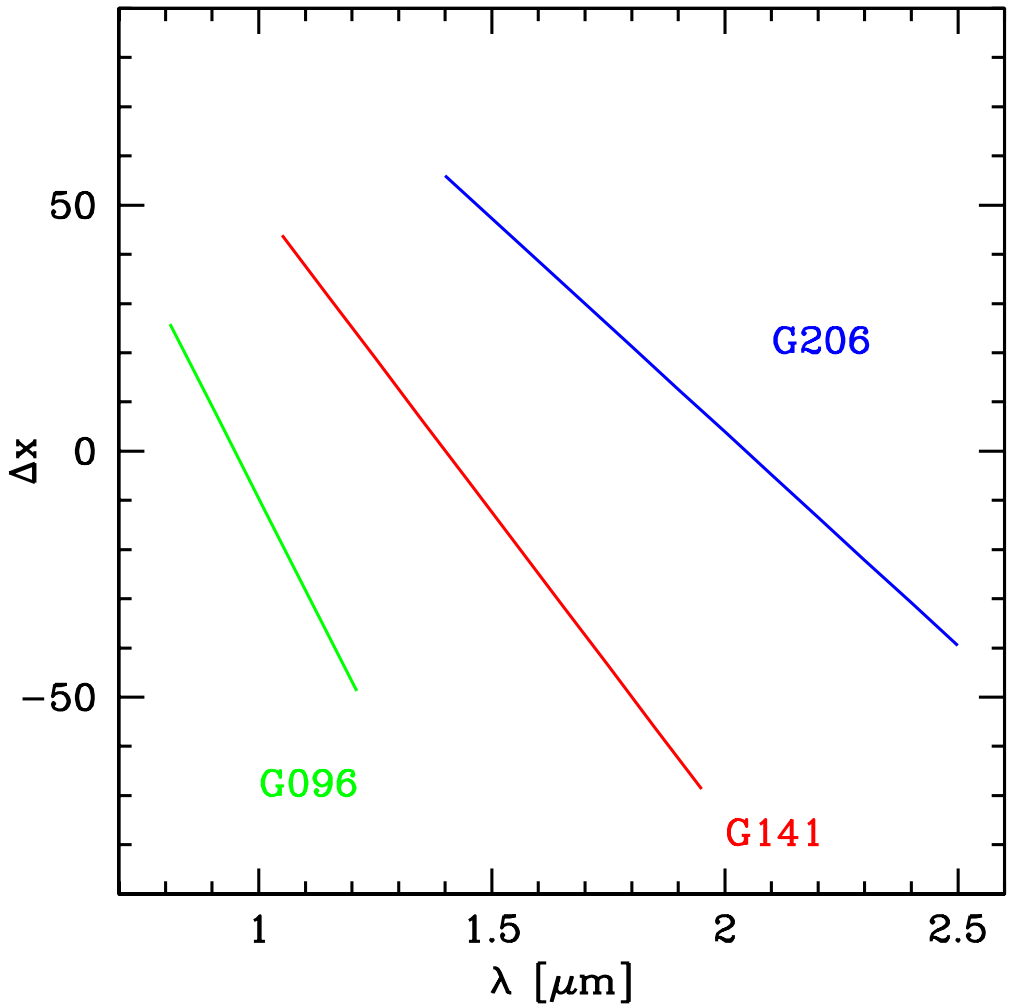

5.3.4 Sensitivity

Background radiation is a greater concern for grisms than for imaging observations. Every pixel on the array receives background radiation over the spectral bandpass of the particular grism, while the source spectrum is dispersed over many pixels. Therefore, the ratio of the source to background flux is much lower for the grisms than for the regular imaging mode filters. The background rate per pixel (sky + telescope) expected with NCS operations is presented in Table 5.6 below for the three grisms. Observing a source with flux at all wavelengths equal to the peak response for each grism will result in a peak count rate equal to the background. The increase in the background flux for the G206 grism is dramatic. Grisms G096 and G141 should therefore be used whenever possible. Despite its

broad wavelength coverage, the G206 grism should be used for the longest wavelengths only. Dithered observations, especially when the field is uncrowded, can often be used to remove the background quite well.

Figure 5.11 gives the sensitivity of each grism as a function of wavelength, as measured for standard stars post-NCS. The signal was measured in an aperture of 10 pixels (2 arcsec) in the spatial direction. Tables 5.7, 5.8, and 5.9 present the basic information for the three NICMOS grisms, as well as the best direct imaging filter to associate with each.

Table 5.6: Grism Background Radiation (sky + telescope).

Grism	Wavelength range microns	Background (e^-/sec/pixel)	Background (Jansky/pix)	Peak Response (DN/sec/mJy)
G096	0.8–1.2	0.364	6.1×10^{-6}	4419
G141	1.1–1.9	2.209	2.1×10^{-5}	7733
G206	1.4–2.5	527.155	4.0×10^{-3}	10260

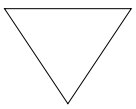

Note that for the G206 grism, the large thermal background limits the exposure times to less than about five minutes, even for faint sources, because the detector will be saturated by the background. See Chapter 4 for more details on the thermal background seen by NICMOS. The dithering/chopping strategies described in Appendix D for background removal should be used with this grism.

Table 5.7: Grism A: G096.

Central (microns)	Mean (microns)	Peak (microns)	FWHM (microns)	Range	Max Trans. (percent)
0.9673	0.9911	1.0010	0.4029	0.8–1.2	69.8
		Direct Imaging Filter F110W			
1.0998	1.1035	1.2035	0.5915	0.8–1.4	94.9

Table 5.8: Grism B: G141. Thermal background is important.

Central (microns)	Mean (microns)	Peak (microns)	FWHM (microns)	Range (microns)	Max Trans. (percent)
1.414	1.5100	1.4020	0.7914	1.1–1.9	74.7

Table 5.8: Grism B: G141. Thermal background is important.

Central (microns)	Mean (microns)	Peak (microns)	FWHM (microns)	Range (microns)	Max Trans. (percent)
Direct Imaging Filter F150W					
1.5035	1.5069	1.6355	0.8020	1.1–1.9	97.7

Figure 5.11: Grism Inverse Sensitivity Curves, G096 (left), G141 (middle), and G206 (right), measured with the post-NCS DQEs (~77.15K).

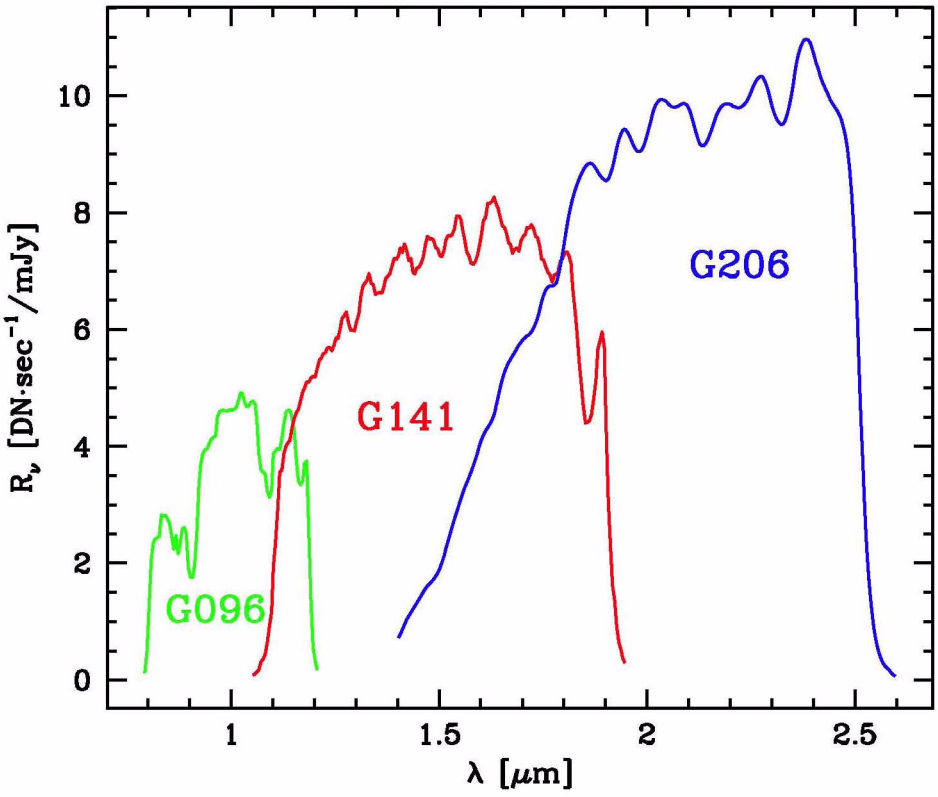

Table 5.9: Grism C: G206. High thermal background. Use only for bright sources, at longest wavelengths.

Central (microns)	Mean (microns)	Peak (microns)	FWHM (microns)	Range (microns)	Max Trans. (percent)
2.067	1.9523	2.0880	1.1575	1.4–2.5	73.4
Direct Imaging Filters F175W, F240M					
1.7530	1.7508	1.9070	1.0940	1.2–2.3	96.6

Table 5.9: Grism C: G206. High thermal background. Use only for bright sources, at longest wavelengths.

Central (microns)	Mean (microns)	Peak (microns)	FWHM (microns)	Range (microns)	Max Trans. (percent)
2.3978	2.3977	2.3155	0.1975	2.3–2.5	92.4

5.3.5 Intrapixel Sensitivity

The same intrapixel sensitivity problem which affects NIC3 images (see Chapter 4) will affect the grism spectra, since the dispersion direction is not exactly aligned with the detector rows: as the heart of the spectrum crosses from one row to the next, the flux will dip by 10-20%. The size of the effect depends on the size of the object. This effect is not obvious in emission line spectra, but can be very clear in continuous spectra. The number and placement of the sensitivity minima within the spectrum will depend on exactly where the spectrum falls on the detector, and the angle between the dispersion direction and the detector X axis. Note that the former changes with the dithering position, and the latter changes between observations. A correction procedure for this effect is available in **NICMOSlook**.

5.3.6 Grism Decision Chart

The decision chart given in Figure 5.12 helps summarize the recommendations of Section 5.3.

Figure 5.12: Grism Decision Chart.

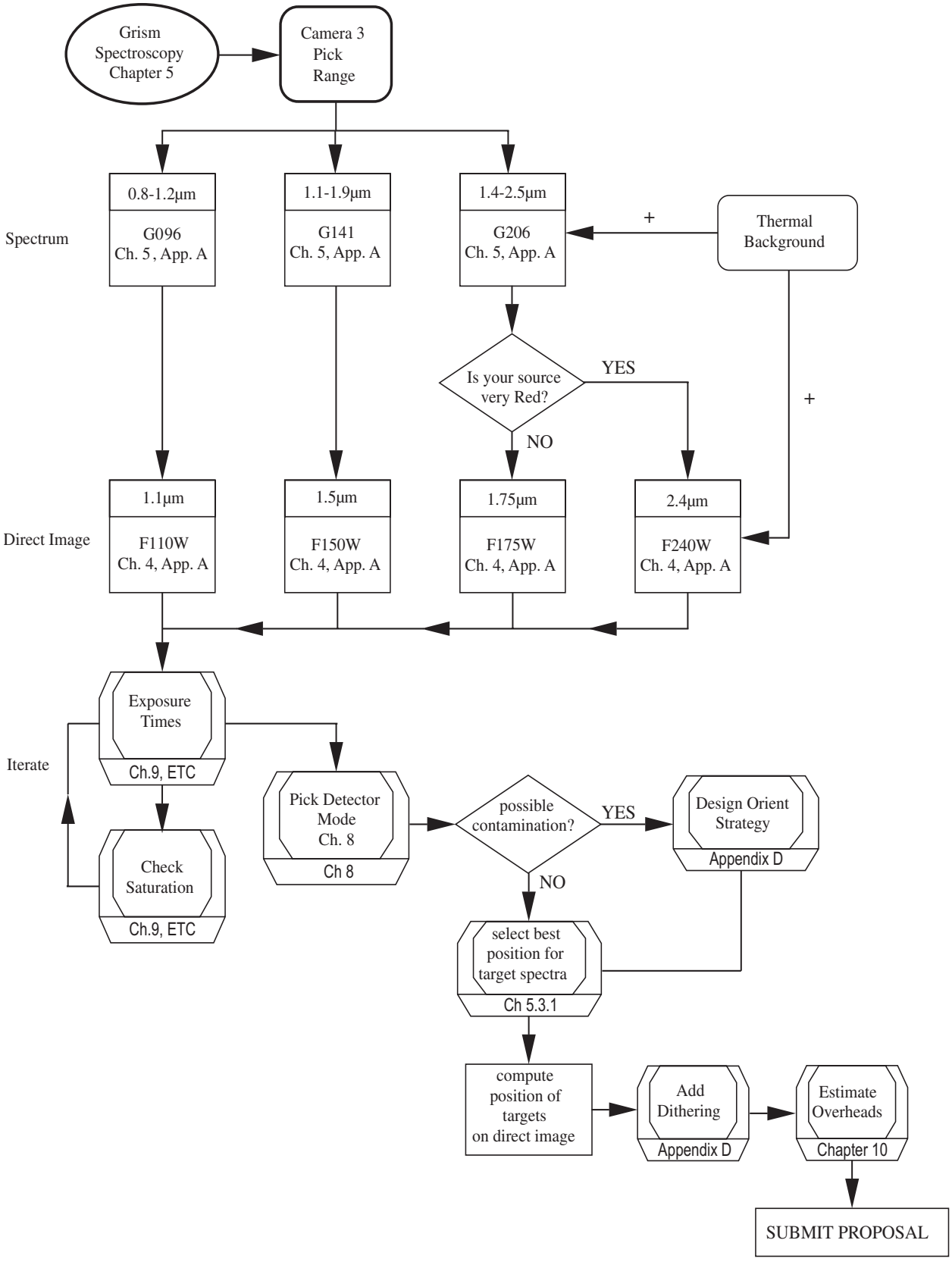

CHAPTER 6:

NICMOS Apertures and Orientation

In this chapter...

6.1 NICMOS Aperture Definitions

Each HST Science Instrument requires its own local coordinate system and apertures to support both target acquisition and small angle maneuvers (SAMs). Apertures are calibrated locations in the HST focal plane relative to the FGS frame. All acquisitions and SAMs are relative to apertures. Any location within the field of view of a NICMOS camera can be specified by the `POSTARG` special requirement (described in the HST Phase II Proposal Instructions).

Each NICMOS camera has two primary apertures. One is positioned at the geometric center of the detector and the other at an *optimal* position close to the center. The first of these apertures is anchored to that fixed location, while the second may be moved in the future. In this way the optimal aperture may be shifted to avoid array defects, even if these are time dependent. Observers with large targets which fill the field of view of a particular camera are generally advised to use the first type of aperture, the "FIX" apertures, while for observers with smaller targets the second type is recommended.

Additional apertures are defined in Camera 2 for use in the automated Mode 2 coronagraphic acquisition.

The names of the defined apertures are listed in Table 6.1 along with a description of their function and their current location.

Observers should note that while apertures are defined by their pixel position in each detector, displacements relative to the default aperture position given with `POSTARG` are expressed in arcseconds (see the Phase II Proposal Instructions for further details).

Table 6.1: NICMOS Aperture Definition

Aperture Name	Description	Position (detector pixels)
NIC1	Optimal center of Camera 1	162,100
NIC1-FIX	Geometric center of Camera 1	128,128
NIC2	Optimal center of Camera 2	149,160
NIC2-FIX	Geometric center of Camera 2	128,128
NIC2-CORON[a]	Center of coronagraphic hole	-
NIC2-ACQ	Center of Mode 2 ACQ region	157,128
NIC3	Optimal center of Camera 3	140,135
NIC3-FIX	Geometric center of Camera 3	128,128

a. NIC2-CORON aperture position not given here as it is time dependent and automatically determined onboard for each coronagraphic acquisition.

6.2 NICMOS Coordinate System Conventions

Figure 6.1 shows how the NICMOS cameras are arranged in the HST field of view. The alignment of each camera is not exact, and the internal coordinate systems attached to each of them differ by small rotations (< 1 degree). The FITS format data files generated for NICMOS observers will have a World Coordinate System specified appropriately for each camera. The adopted coordinate system for all three cameras is summarized in Figure 6.1.

Figure 6.1: Common NICMOS Coordinate System

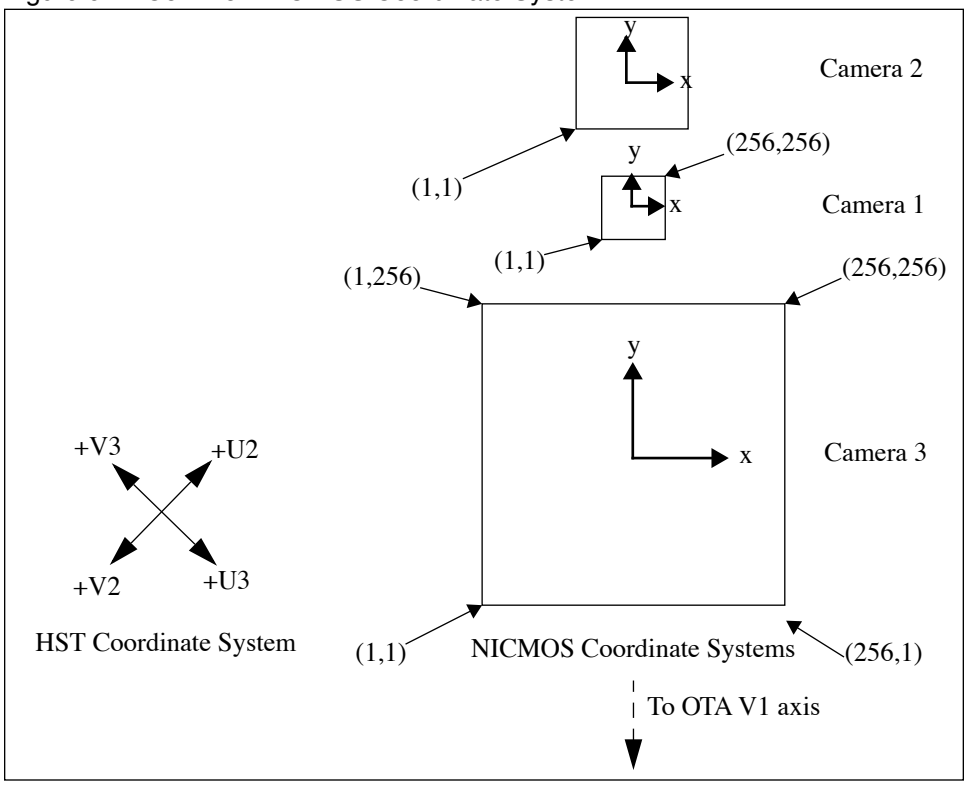

6.3 Orients

NICMOS orientations are specified relative to the +y axis shown in Figure 6.1. Eastward rotations are counterclockwise (in the usual astronomical convention). Spacecraft orientations are specified relative to the U2-U3 telescope axis (Figure 6.2). The NICMOS coordinate system is rotated by approximately 225 degrees from U3 axis. The exact angles for NIC1, NIC2, and NIC3 are 224.6, 224.57, and 224.96 ±0.02 degrees, respectively.

Due to the linear arrangement of the three NICMOS cameras on the sky, it may be advantageous to consider the specification of a unique telescope orientation. However, observers should be aware that such constraints may decrease the duration and number of scheduling opportunities for their observations and, under some circumstances, may make the identification of suitable guide stars impossible.

While the Phase II proposal instructions contain the definitive instructions and examples for specifying the desired orientation for HST, we provide a simple example in Figure 6.2. A binary star with a position angle (PA) 30° measured east from north is to be positioned with the southern star in Camera 3 and the northern star in Camera 2. That is, we want the line connecting the two stars to lie along the NICMOS + y axis. The resulting HST orientation is 225° + 30° = 255°. (`HST ORIENT` = PA + 225° for NICMOS).

Figure 6.2: Definition of Orient for NICMOSWeb

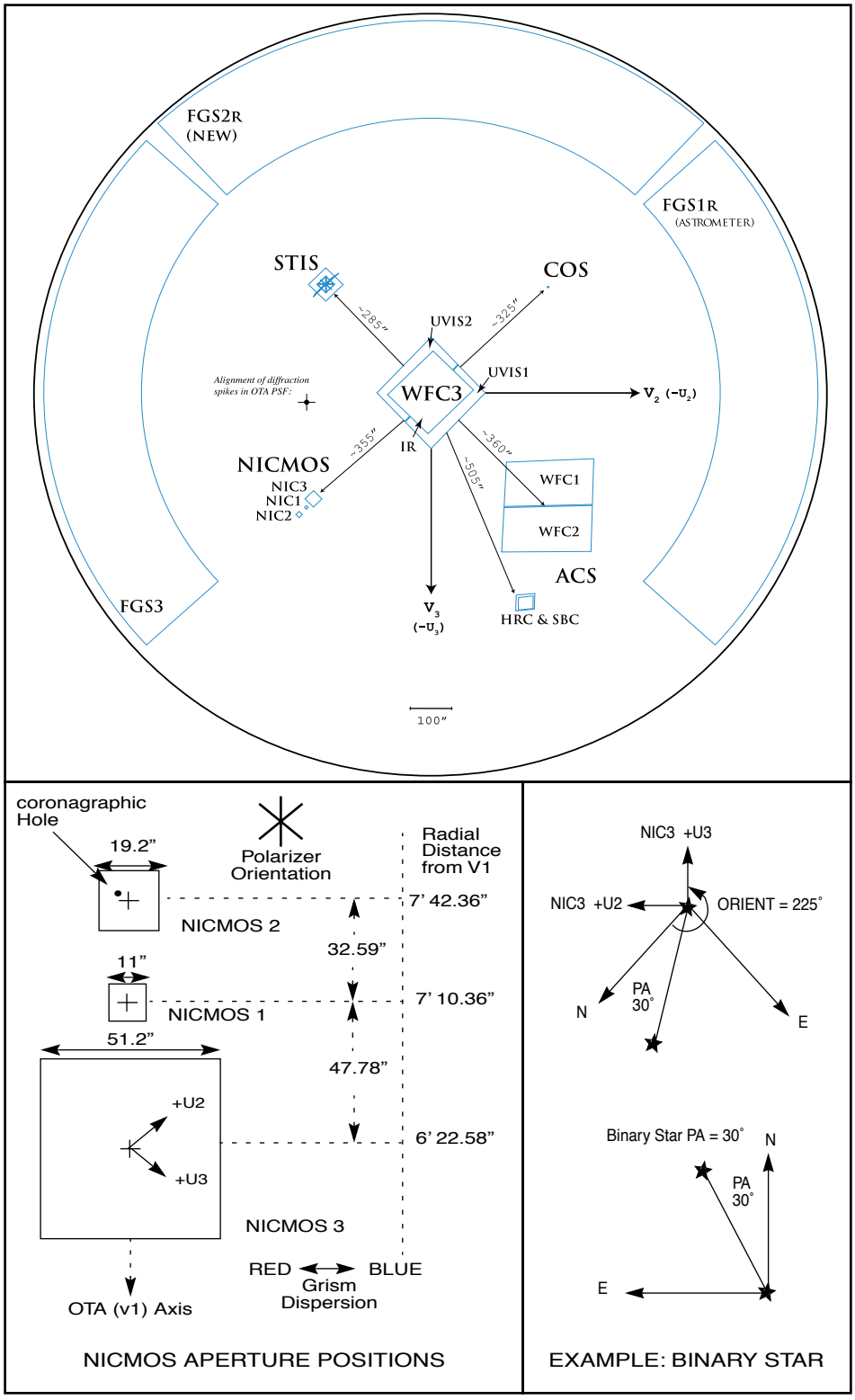

CHAPTER 7:

NICMOS Detectors

In this chapter...

7.1 Detector basics

In this section we briefly describe the operational principles of the NICMOS3 detectors. Figure 7.1 (adapted from McLean 1997) shows the basic physical structure of a photovoltaic HgCdTe detector.

Figure 7.1: Cross-section of a NICMOS3-type detector (not to scale).

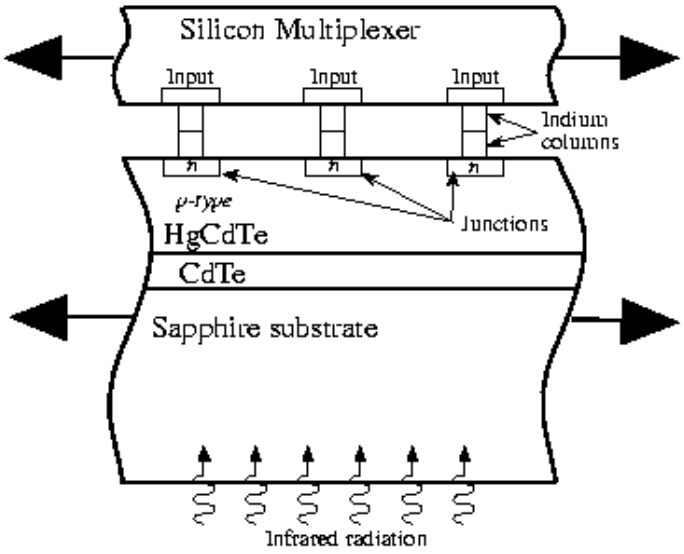

An infrared detector is basically a photodiode, the core of which is a p-n-junction created during the wafer processing. The Fermi-levels of the p- and n-type materials, i.e. the highest occupied energy state of the

electron gas within the semiconductor material, must match, which effectively creates an electric field across the junction. The incident infrared photons free electron-hole pairs into the conductance band at or near the junction which are immediately separated by the electric field. The accumulated charge carriers cause a voltage change across the junction which can be detected and used as a measure of the incident light. One can think of the detector as a capacitor that is discharged by the infrared photons. In practice, the voltage change is monitored by a Si field effect transistor (FET), used as a source follower amplifier. Figure 7.2 shows the equivalent circuit diagram for the NICMOS3 "unit cell".

Figure 7.2: Equivalent circuit diagram of the NICMOS3 unit cell.

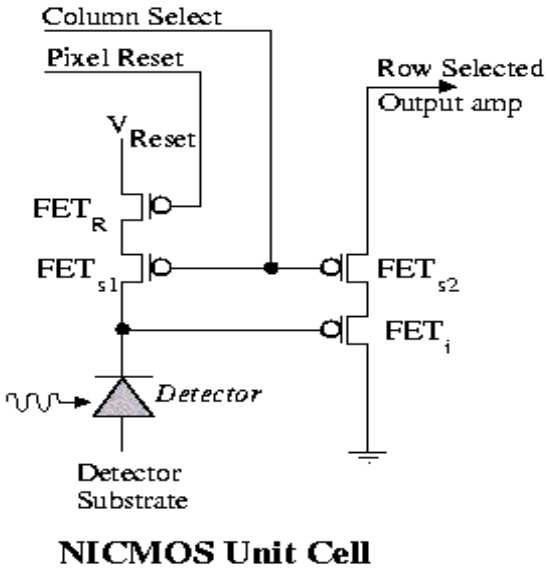

In order to produce an "imaging" detector, a large number of such unit cells, or pixels, are combined into an array. The photon-sensitive layer (HgCdTe in the case of NICMOS3 detectors) and the Si-multiplexer (which contains the array of FETs) are combined in a "hybrid" structure, connected via tiny indium bumps (Figure 7.3). For better mechanical stability, the "hybrid" array structure is put on an infrared-transparent Sapphire substrate. Since each pixel contains its own FET, there is no "bleeding" along columns, as in CCD chips, and bad pixels do not block the rest of the column.

Figure 7.3: Basic “hybrid” structure of infrared array detectors. Top: schematic of the detector array. Bottom: enlarged cross-section of a few unit cells, or pixels.

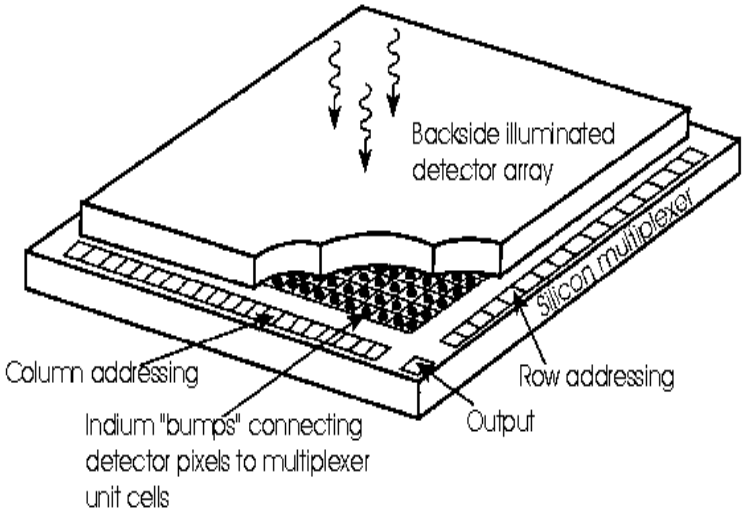

7.2 Detector Characteristics

7.2.1 Overview

Each NICMOS detector comprises 256 × 256 square pixels, divided into 4 quadrants of 128 × 128 pixels, each of which is read out independently. The basic performance of the nominal flight detectors is summarized in Table 7.1. Typically, the read-noise is ~27 e^-/pixel. Only a few tens of bad pixels (i.e., with very low response) were expected, but particulates—most likely specks of black paint, see Section 7.3.6—have increased this number to >100 per detector. The gain, ~5–6 e^-/ADU, has been set to map the full dynamic range of the detectors into the 16-bit precision used for the output science images.

Table 7.1: Flight Array Characteristics. Please see the following sections, which provide more information for each of the quantities listed.

Characteristics	Camera 1	Camera 2	Camera 3
Dark Current (e^- /second)[a]	0.3	0.3	0.3
Read Noise (e^-)[b]	~26	~26	~29
Bad Pixels (including particles)	213 (0.33%)	160(0.24%)	139(0.21%)
Conversion Gain (e^- / ADU)	5.4	5.4	6.5
Well Depth (ADU)	26,900	28,200	32,800
Saturation (ADU)[c] (95% Linearity)	21,500	22,500	26,200
50% DQE Cutoff Wavelength (microns)	2.55	2.53	2.52

a. These numbers are the typical signal level in a "dark" exposure, and can be used for sensitivity calculations. They contain contributions from linear dark current, amplifier glow, and possibly low-level cosmic ray persistence.
b. The quoted readout noise is the RMS uncertainty in the signal of a differenced pair of readouts (measured as the mode of the pixel distribution).
c. Saturation is defined as a 5% deviation from an (idealized) linear response curve.

7.2.2 Dark Current

A NICMOS exposure taken with the blank filter in place should give a measure of the detector dark current. However, the signal in such an exposure consists of a number of different components, such as linear dark current, amplifier glow, shading residuals, and possibly low-level cosmic ray persistence. The linear dark current is the signal produced by the minority carriers inside the detector material. It increases linearly with exposure time, hence the name. It can be measured after subtraction of amplifier glow and correction for shading (both of which we will describe below), avoiding exposures that are heavily impacted by cosmic ray persistence. The NICMOS calibration program has shown that the dark current levels of all three NICMOS cameras are stable and fully consistent with expectations for an operating temperature of ~77 K. This is demonstrated in Figure 7.4, which shows the results of the dark current monitoring program since the installation of the NCS.

Figure 7.4: Results from the NICMOS dark current monitoring program following the installation of the NCS. Shown are the monthly (bi-monthly since January 2003) linear dark current measurements for all three NICMOS cameras. Note that the linear dark current is stable within the measurement errors (a typical error bar for Camera 3 is shown in the upper left corner, the other cameras have errors about half of this).

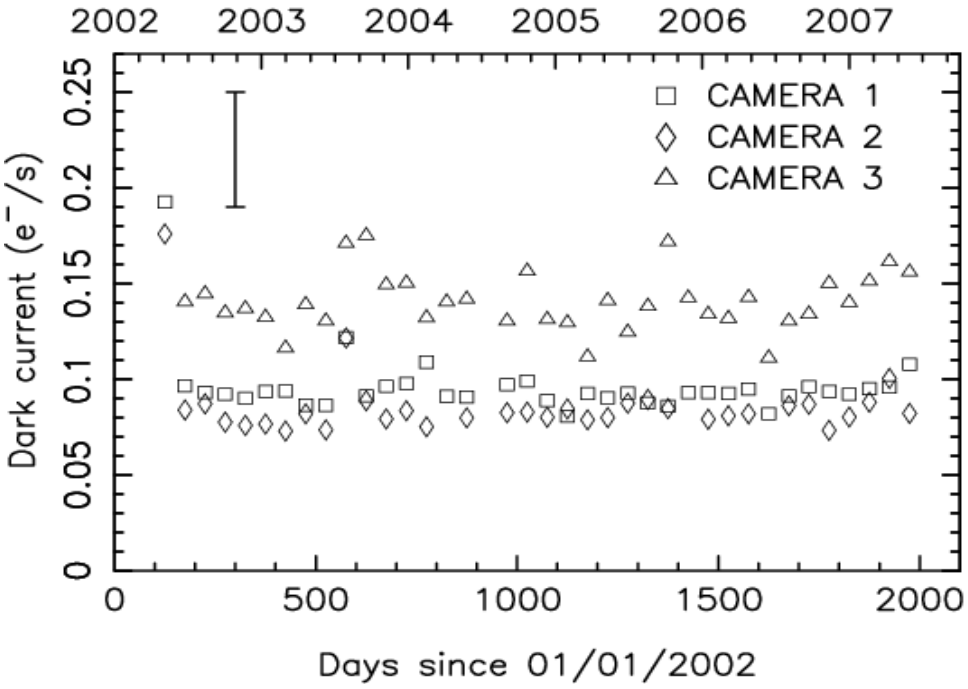

7.2.3 Flat Fields and the DQE

Uniformly illuminated frames—so-called "flat fields"—taken with the NICMOS arrays show response variations on both large and small scales. They also appear to change slightly as a function of time. These fluctuations are due to differences in the (temperature-dependent) Detector Quantum Efficiency (DQE) of the individual pixels. These spatial variations can be corrected in the normal way by flat fielding, which is an essential part of the calibration pipeline. Monitoring of the NICMOS flat-fields since the beginning of the NCS era in 2002, have shown a gradual change in the NICMOS DQE in both average response and spatial structure. These changes amount to between 1% and 3% on average. To correct for the small spatial variations, the NICMOS team has created a set of time dependent flat-fields (NICMOS ISR 2007-002). These flat-fields together with instructions are available at:

http://www.stsci.edu/hst/nicmos/calibration/reffiles/temporal_flat_files/index.html.

Figure 7.5 compares some of the current flat field exposures to those used in Cycle 7/7N. As can be seen both from the morphology of the images and the histograms of pixel values, the amplitude of DQE variations of all three cameras is much reduced at 77.1 K, thus making the response function "flatter". This behavior is explained by the fact that "cold" pixels (i.e. pixels with a lower than average response) show a higher than average DQE increase with temperature.

Figure 7.5: Normalized pre- and post-NCS flat field responses for NIC1 (left) through NIC3 (right) for F110W, F187W, and F113N, respectively. The images are inverted to better display the grot; therefore, the dark regions have higher QE. The color stretch is the same for both temperatures in each camera. The histograms show the "flattening" of the arrays at the higher temperature (narrower distribution). The decrease in the dynamic range between bright and faint targets is a direct result of the decreased well depth at the higher temperature.

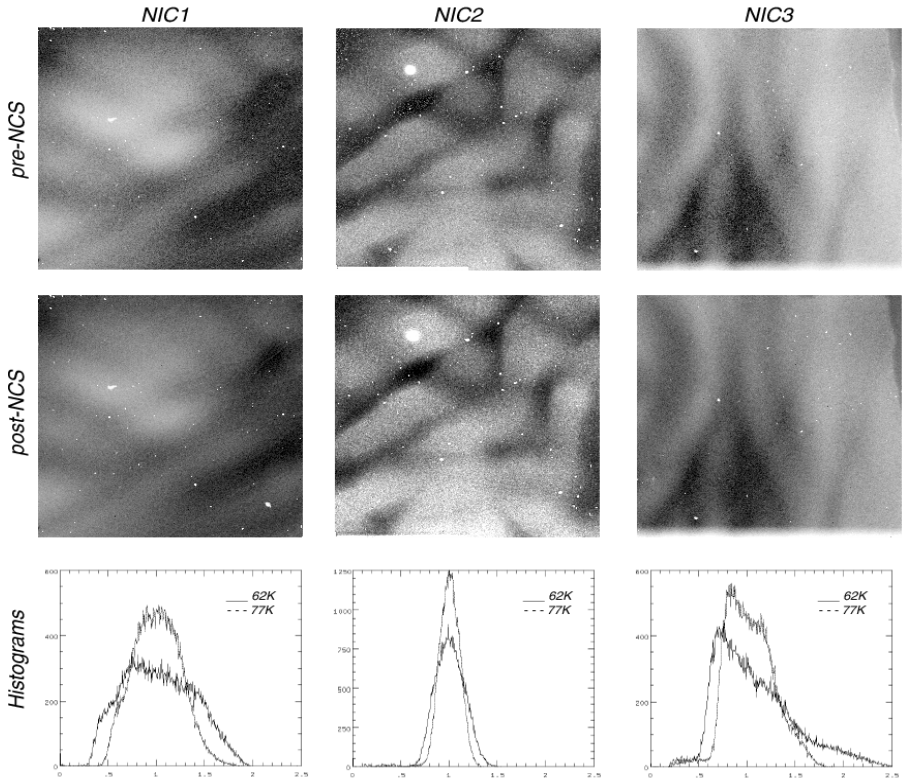

Flat field frames are generated from a pair of “lamp off” and “lamp on” exposures. Both are images of the (random) sky through a particular filter, but one contains the additional signal from a flat field calibration lamp. Differencing these two exposures then leaves the true flat field response. The count rate in such an image is a direct (albeit relative) measure of the DQE. The DQE increase of the three NICMOS cameras between 77.1 K and 62 K as a function of wavelength is presented in Figure 7.6.

Figure 7.6: NICMOS DQE: Comparison between post-SM3B (at operating temperature of 77K) and 1997/1998 (62K) eras.

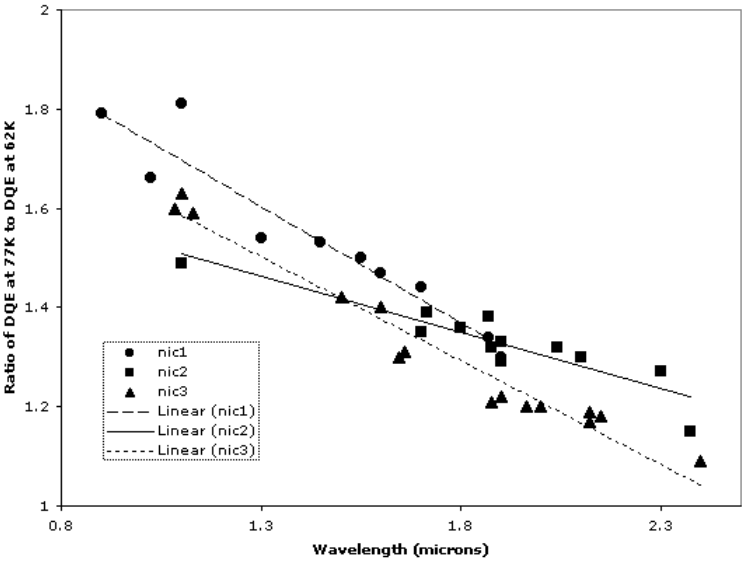

The average response at 77.1 K increased by about 60% at J, 40% at H, and 20% at K. The resulting wavelength dependence of the absolute DQE for NICMOS operations under the NCS is shown in Figure 7.7. Here, we have scaled the pre-launch DQE curve, which was derived from ground testing of the detectors, to reflect the changes measured at the wavelengths of the NICMOS filters. These (somewhat indirect) results have been confirmed by results from the photometric calibration program which uses observations of standard stars to measure the absolute DQE of NICMOS. The fine details in these DQE curves should not be interpreted as detector features, as they may be artifacts introduced by the ground-testing set-up. At the blue end, near 0.9 microns, the DQE at 77.1 K is ~20%; it rises quasi-linearly up to a peak DQE of ~90% at 2.4 microns. At longer wavelengths, it rapidly decreases to zero at 2.6 microns. The NICMOS arrays are blind to longer wavelength emission. When looking at the DQE curve, the reader should bear in mind that this is not the only criterion to be used in determining sensitivity in the near-IR. For example, thermal emission from the telescope starts to be an issue beyond ~1.7 μm. The shot-noise on this bright background may degrade the signal-to-noise obtained at long wavelengths, negating the advantage offered by the increased DQE.

It is important to note, especially for observations of very faint targets for which the expected signal-to-noise is low, that the DQE presented here is only the average for the entire array. Despite the flattening discussed above, the flat field response is rather non-uniform, and thus the DQE curves for individual pixels may differ substantially.

Figure 7.7: Relative increase of the NICMOS DQE as a function of wavelength for operations at 77.1 K, compared to pre-NCS operations at 62 K.

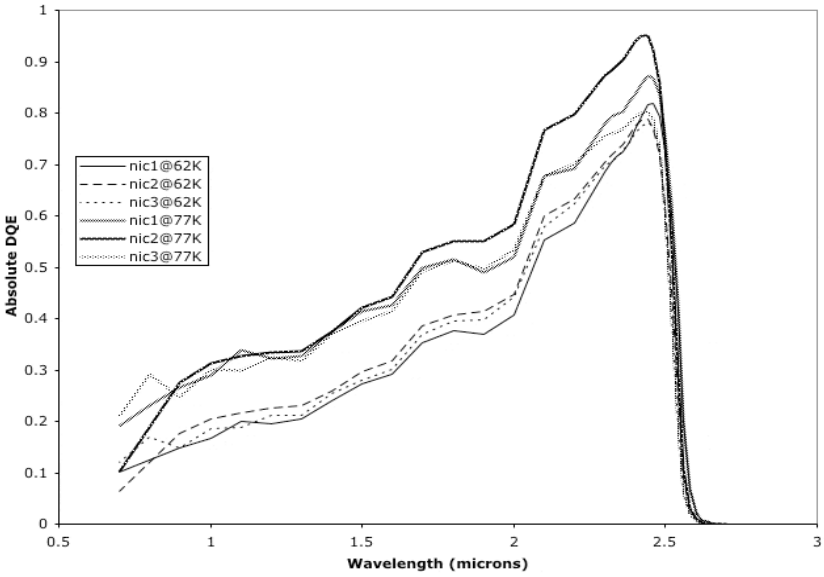

7.2.4 Read Noise

Each detector has four independent readout amplifiers, each of which reads a 128 × 128 quadrant. The four amplifiers of each detector generate very similar amounts of read noise. This is illustrated in Figure 7.8, which compares the pixel read noise distributions for the four quadrants of each NICMOS camera. The distributions for all quadrants are relatively narrow, with a FWHM of about 8 electrons, indicating that there are only few anomalously noisy pixels. The read noise is independent of temperature.

For some scientific programs such as ultra-low background observations (e.g. during the HDF campaigns), read noise can become a non-negligible component of the noise floor. The NICMOS group at STScI therefore has explored a method to lower the read noise in NICMOS data by reducing the digitization noise associated with the conversion from electrons to data numbers (DN). This can, in principle, be achieved by using a different conversion factor (i.e. gain) from e- to DN. Under optimal circumstances, this can produce a read noise reduction of 10–15%, resulting in exposures that reach up to 0.1 mag deeper. For details, we refer to Xu & Boeker (2003; NICMOS ISR-2003-006). However, the use of alternate gain settings requires calibration reference files (e.g. flat field or dark exposures) that have been obtained with the same gain. These files will not be obtained during the NICMOS calibration program. In addition, the CALNICA pipeline is currently not able to process such data correctly. Given the large operational overhead and the rather small scientific benefit, we strongly discourage NICMOS users from requesting non-standard gain settings. In exceptional circumstances, such requests will be considered on a

case-by-case basis with the understanding that proper calibration of such data is the sole responsibility of the GO.

Figure 7.8: Read noise characteristics of the three NICMOS detectors. Each panel shows the pixel distribution of electronics-induced RMS uncertainties, as measured from a series of difference images of short (0.2s) DARK exposures.

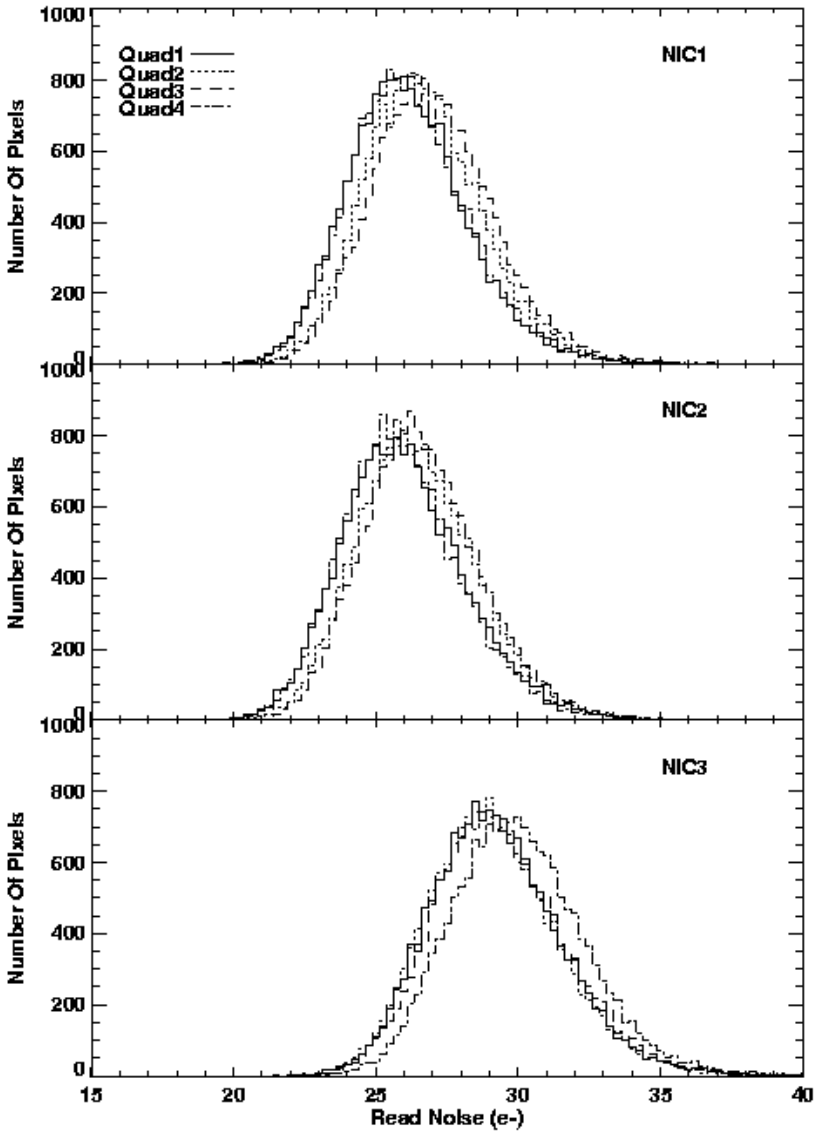

7.2.5 Linearity and Saturation

Throughout Cycle 7, the linearity correction of the calibration pipeline had been based on the assumption that the NICMOS detector response was well approximated by a linear function until pixel counts reached a certain threshold. Therefore, no linearity correction was performed below this

point. However, the ongoing NICMOS calibration program has shown that the detector response is in fact (slightly) non-linear over the full dynamic range. Figure 7.9 illustrates this behavior.

Figure 7.9: Count rate as a function of total accumulated counts for a typical NICMOS detector pixel. Note that the pixel response is non-linear (i.e., the count rate is not constant) over the entire dynamic range.

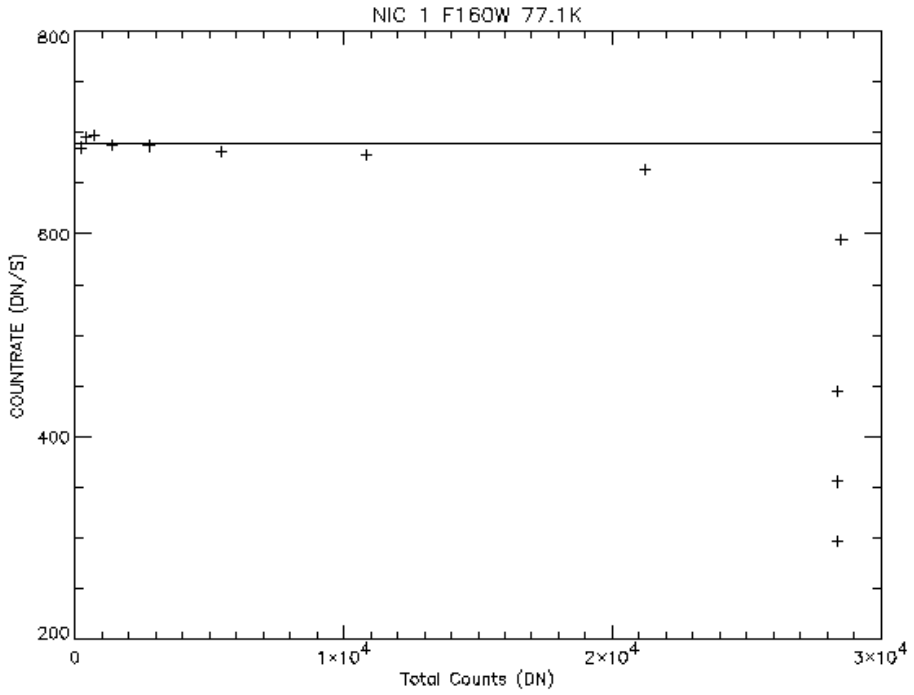

A revised linearity correction was therefore implemented in the NICMOS calibration pipeline (Cycle 11 and beyond), which corrects data over the entire dynamic range between zero and the flux level at which the response function deviates by more than 5% from the linear approximation. Pixels that reach this threshold during an exposure are flagged as saturated, and are not corrected during the pipeline processing. This saturation point typically occurs at about 80% of the well depth.

7.2.6 Count Rate Non-Linearity

NICMOS has a significant count rate dependent non-linearity that also depends on wavelength as described in Section 4.2.4. While we have no physical explanation for the effect at the time of this writing, we currently assume it arises in the detector. Objects fainter than the NICMOS standard stars of about the 12th magnitude will be measured too faint, objects that are brighter than our standards will seem too bright. The maximum offsets on dark sky backgrounds at F110W are about 0.25 mag in NIC1 and NIC2, and about 0.16 mag in NIC3. Software has been developed to linearize the

counts in imaging observations. More details on the effect and how to correct for it can be found at:

http://www.stsci.edu/hst/nicmos/performance/anomalies/nonlinearity.html.

7.3 Detector Artifacts

7.3.1 Shading

The NICMOS arrays exhibit a noiseless signal gradient orthogonal to the direction of primary clocking, which is commonly referred to as *shading*. It is caused by changes of the pixel bias levels as a function of temperature and time since the last readout ("delta-time"). The amplitude of the shading can be as large as several hundred electrons for some pixels under some circumstances. The first pixels to be read show the largest bias changes, with the overall shading pattern decreasing roughly exponentially with row number. The shading is a noiseless contribution to the overall signal, therefore it can be completely removed during pipeline processing once it has been calibrated with delta-time and temperature.

For a given delta-time (and temperature), the bias level introduced by the shading remains constant. For `MULTIACCUM` readout sequences (see Chapter 8) where the time between readouts is increasing logarithmically, the bias level changes with each successive read, and thus the overall shading pattern evolves along the `MULTIACCUM` sequence. We have calibrated the dependence of shading as a function of delta-time for each of the three NICMOS detectors. This information is used by the **calnica** pipeline to construct synthetic dark current reference files for NICMOS observations. The accuracy of this calibration is good (a few percent for most readout times).

The 1999 warm-up monitoring program has shown that the shading signal is temperature dependent. Nevertheless, the good temperature-stability of the NICMOS/NCS system has enabled accurate shading correction of NICMOS data with a single set of dark current reference files. Figure 7.10 presents the shading profiles for each camera at the operating temperature of 77.1 K.

The NICMOS group at STScI will continuously monitor both shading behavior and NICMOS temperature stability, and will provide additional calibration files should this become necessary.

Figure 7.10: Shading profiles for all camera/delta-time combinations measured at 77.1 K (NCS era). The profiles were created by collapsing a dark exposure of the respective integration time along the fast readout direction (after correction for linear dark current and amplifier glow).

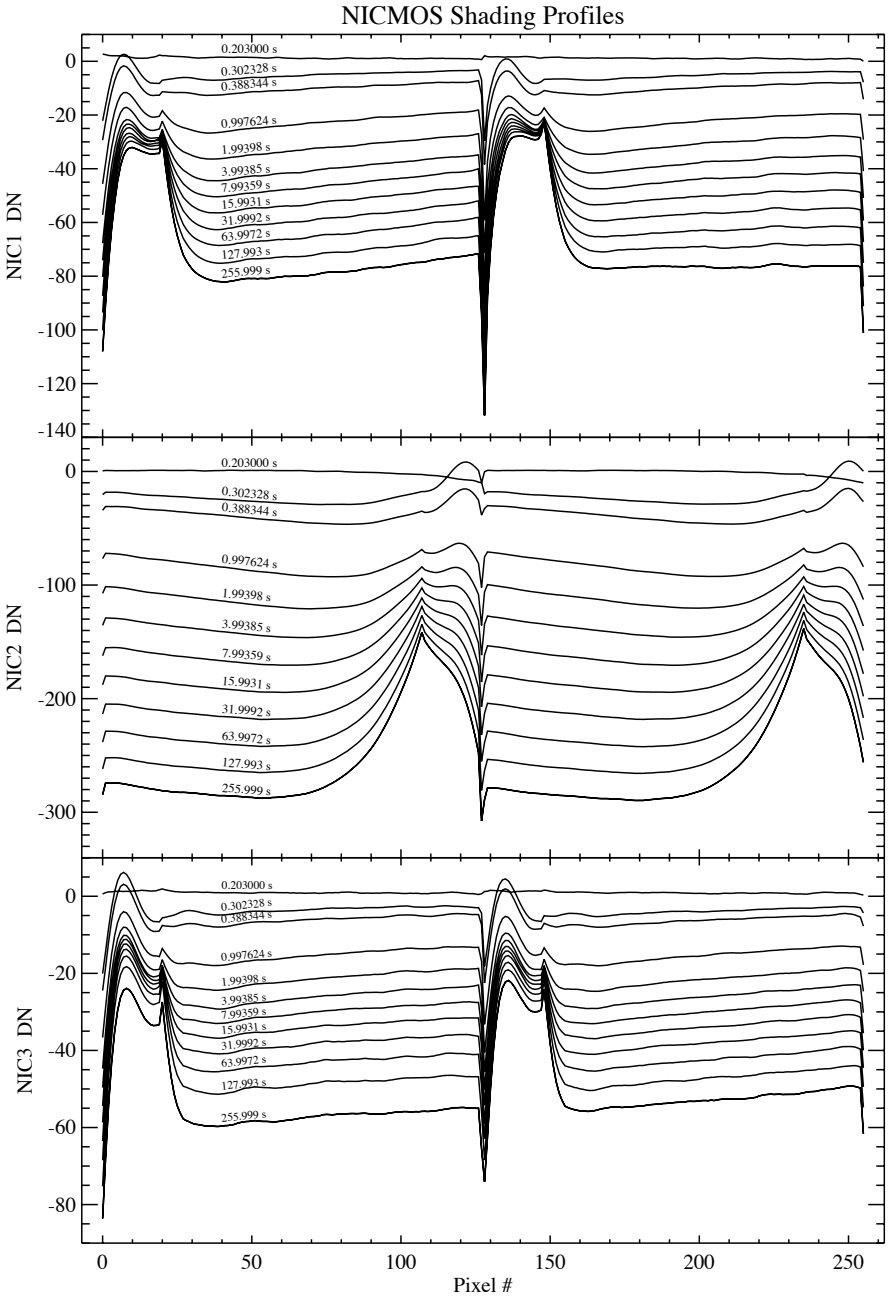

7.3.2 Amplifier Glow

Each quadrant of a NICMOS detector has its own readout amplifier situated close to the corners of the detector. Each time the detector is read out, the amplifier warms up and emits infrared radiation that is detected by the chip. This signal, known as amplifier glow, is largest in the array corners with ~80 e^-/read, and falls rapidly towards the center of the detector where it is about 10 e^-/read. The signal is cumulative with each non-destructive readout of an exposure. It is highly repeatable, and is exactly linearly dependent on number of reads. It also is constant with temperature, as shown in Figure 7.11.

Figure 7.11: Amplifier glow signal as a function of detector temperature.

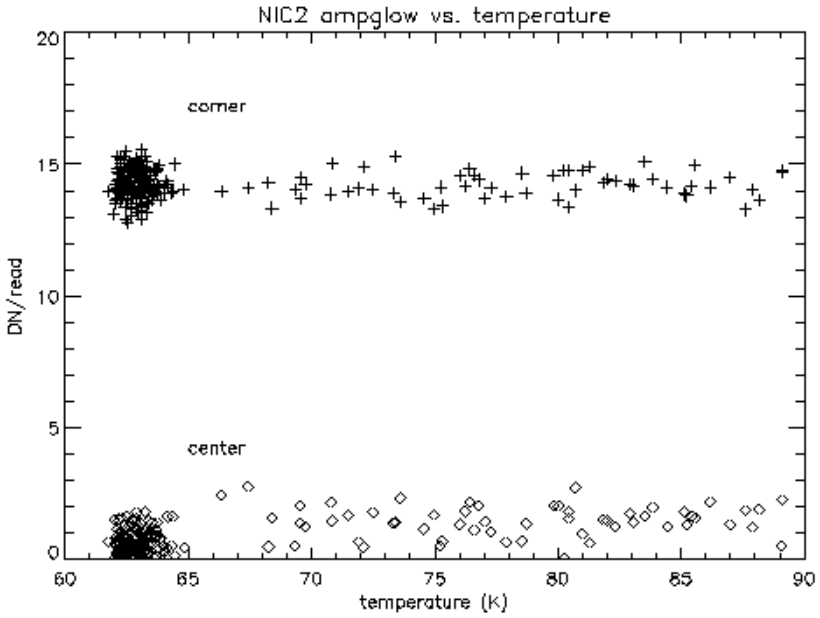

In contrast to the shading, the amplifier glow is a photon signal, and thus is subject to Poisson statistics. It therefore contributes to the total noise in NICMOS exposures. Amp-glow images for all three cameras are shown in Figure 7.12. In case of an `ACCUM` exposure with multiple initial and final reads (see Chapter 8), the photon noise produced by amplifier glow can outweigh the read noise reduction from the multiple reads, especially close to the array corners producing a total noise reduction never larger than ~40 –50%. Similarly, the trade-off between improved cosmic ray rejection, reduced read noise, and increased photon noise in a `MULTIACCUM` sequence is complicated.

Figure 7.12: Amplifier glow for Cameras 1 (left) through 3 (right), on a uniform grayscale, and below a plot of rows (near the bottom) of each camera.

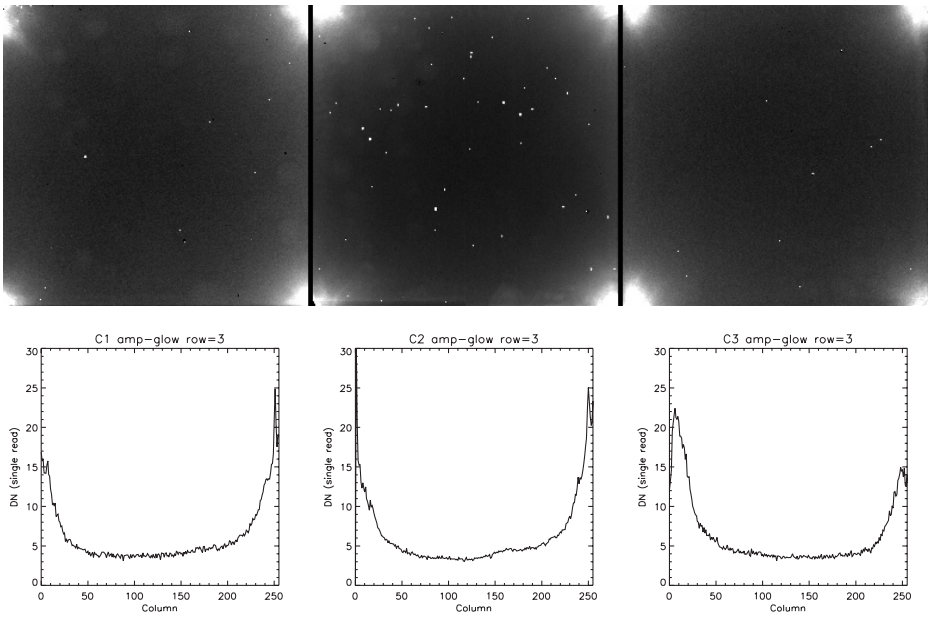

7.3.3 Overexposure of NICMOS Detectors

Effects of photon and cosmic-ray persistence are described in Section 4.6.

7.3.4 Electronic Bars and Bands

Electronic ‘‘bars’’ are an anomaly in NICMOS data taken during Cycles 7 and 7N. They appear as narrow stripes that cross the quadrants of an array, and occur identically in all 4 quadrants at the same rows/columns in each. The bars are caused by pick-up of an amplifier signal on one of the row/column address lines, causing a momentary change in the bias for that pixel.

Similarly, electronic ‘‘bands’’ are caused when one of the NICMOS detectors is reset while another is being read out. The reset pulse causes a sudden jump in the bias of the detector which is being read. The bias jump then appears as an imprint on the image that looks like a band.

The bars typically run the length of a quadrant (128 pixels), and are 3 pixels wide—the first pixel is lower than the mean, the second is at the mean level and the third is higher than the mean, giving the impression of an undersampled sinusoidal spike with an amplitude of up to ~10 DN peak-to-peak. If a bar appears in the 0th readout, it will be subtracted from all the other readouts as part of the normal calibration process, and will appear to be a negative of the above description. The bars run parallel to the

slow readout direction, which is vertical in NIC1, and horizontal in NIC2 and NIC3. They are almost always broken in at least one place, with a shift of 2–10 pixels in the narrow direction. A more detailed description of the electronic bars and bands is given on the NICMOS WWW site:

http://www.stsci.edu/hst/nicmos.

Since Cycle 11, a modified readout sequence has been implemented for the three NICMOS cameras which reduces the probability that a detector will be reset while another is being read. This procedure is completely transparent to users and has significantly reduced the electronic bands problem.

7.3.5 Detector Cosmetics

Each NICMOS detector has a number of pixels that show an anomalous responsivity. Such "bad pixels" come in various flavors. So-called "hot" pixels have a higher than average dark current, and thus show excessive charge compared to the surrounding pixels. On the other hand, "cold pixels" are less sensitive to incident photons than the typical pixel. The anomalously low responsivity of a "cold" pixel could be due to either a lower intrinsic DQE of the pixel, or due to grot (see below). Some pixels do not even respond at all ("dead pixels") to incoming light. Quantitative statistics of the hot/cold pixels in the three NICMOS cameras are given in Table 7.2. It is important to note that the impact of bad pixels on the quality of NICMOS images can be minimized by dithering the observations.

Table 7.2: Bad Pixels in NICMOS

Pixel Characteristics	NIC1	NIC2	NIC3
Cold[a]	467	480	541
Hot[b]	1359	1429	1859

a. Numbers include pixels affected by grot (see Section 7.3.6). A cold pixel is defined as having a response 5 sigma lower than the median value of all pixels.
b. A hot pixel is defined as having more than three times the median dark current of the array.

7.3.6 "Grot"

On-orbit flat field exposures taken after the NICMOS installation in 1997 revealed a population of pixels with very low count rates that had not previously been seen in ground testing. It is believed that these pixels are at least partly obscured by debris on the detector surface, most likely small

paint flakes that were scraped off one of the optical baffles during the mechanical deformation of the NICMOS dewar. Additional grot has collected on the detectors since its revival. NIC1 appears to be the most affected with an additional chunk of grot in the lower right quadrant. This so-called "grot" affects approximately 100–200 pixels in each NICMOS camera. The largest pieces of grot in NIC1 are shown in Figure 7.13. Again, dithering is recommended to minimize the impact of grot.

Figure 7.13: A NIC1 flat field image shows the largest of the groups of pixels affected by debris ("grot"). These bits of "grot" are roughly 5 by 9 pixels (upper left) and 5 by 6 pixels (lower right).

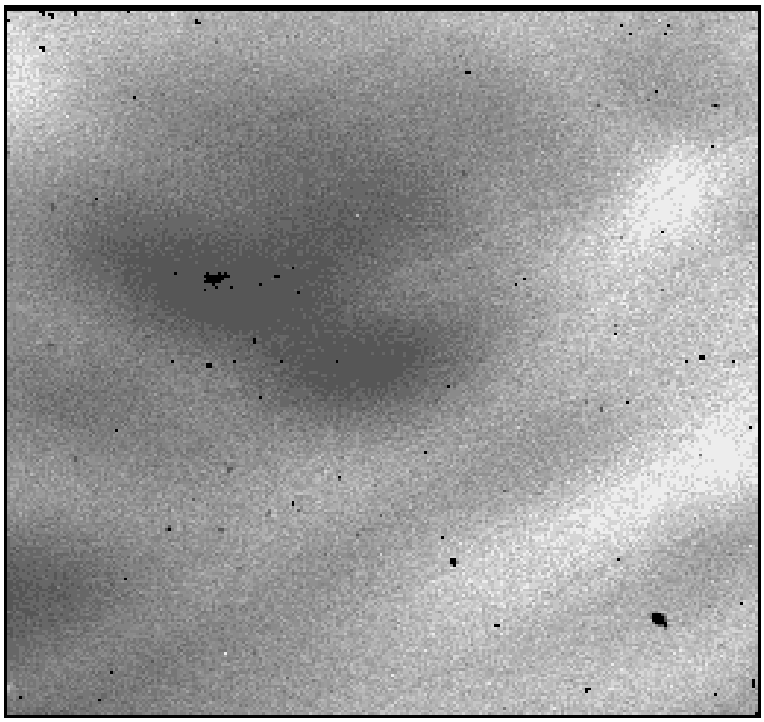

CHAPTER 8:

Detector Readout Modes

In this chapter . . .

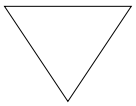

Nearly all observers should use the `MULTIACCUM` ***mode, as it provides the highest quality scientific data.***

8.1 Introduction

NICMOS has four detector readout modes that may be used to take data. After the observing time has been approved, the readout mode will be selected by the observer when completing the Phase II proposal entry. However, potential observers may want to understand the characteristics of the NICMOS readout modes to help design their Phase I proposal.

There are three supported readout modes:

1. Multiple-accumulate Mode.
2. Accumulate Mode.
3. Acquisition Mode.

The ACCUM mode is, however, supported only for NREAD=1. For other configurations the ACCUM mode is available but not supported, i.e. the observer must request the use through a Contact Scientist during preparation of the Phase II proposal. The basic scientific rationale behind each of these modes, and a summary of their capabilities is outlined in Table 8.1, along with a recommendation regarding their use. The Phase II proposal instructions needed to identify the readout modes are given in parentheses under the mode name.

Table 8.1: Readout Modes and their Functions.

Mode	Use	Functionality	Recommendation
Multiple-Accumulate (MULTIACCUM)	Faint targets. Large dynamic range. Optimal image construction. Ground processing of cosmic rays and saturation.	Multiple non-destructive readouts at specific times during an integration. 0.215 < t < 8590 seconds. Number of readouts ≤ 25.	Recommended for most programs. Ensures the highest dynamic range. Most effective for correction of cosmic ray hits and saturation.
Accumulate (ACCUM)	Simplest observing mode. Produces a single image.	t > 0.57 seconds.	MULTIACCUM mode is preferred.
Onboard Acquisition (ACQ)	For coronagraphy only. Locate brightest source in a subarray and reposition telescope to place source in coronagraphic hole.	ACCUM exposures are obtained, combined with cosmic ray rejection, hole located, sources located and centered.	Reasonably bright sources in uncrowded fields. See Chapter 5 for more details.
Bright Object (BRIGHTOBJ)	For coronagraphic acquisition of bright targets which would saturate the arrays in the other modes with the shortest integration time allowed.	reset/read/wait/read each pixel sequentially in a quadrant. 0.001024 < t < 0.2 seconds.	When possible use a narrow filter with MULTIACCUM instead.

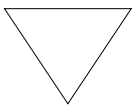

The* BRIGHTOBJ *mode is not supported for Cycle 13 and later cycles; it is, however, an available mode for the special case of acquisition of very bright targets under the coronagraphic hole. See Appendix C for a more detailed description of this mode.

Detector Resetting as a Shutter

NICMOS *does not have a physical shutter mechanism*. Instead, the following sequence of operations are performed to obtain an exposure:

- ***Array reset***: All pixels are set to zero—the bias level.
- ***Array read***: The charge in each pixel is measured and stored in the on-board computer's memory. This happens as soon as practical after the array reset. In effect, a very short exposure image is stored in memory.
- ***Integration***: NICMOS exposes for the period specified for the integration.
- ***Array read***: The charge in each pixel is measured and stored in the on-board computer's memory.

8.2 Multiple-Accumulate Mode

One of the concepts inherent in the operation of the NICMOS arrays is their *non-destructive readout capability.*

During the exposure, all pixels are first *reset* via three separate passes through the detector. The *reset* is immediately followed by a fourth pass through the detector, which *non-destructively reads* and stores the pixel values. This marks the beginning of the integration. The first array read will then be followed by one or more non-destructive readings of the detector. The last non-destructive readout marks the end of the integration. The total integration time is given by the difference in time between the first and the last array read.

The non-destructive nature of the NICMOS readout offers elaborate methods of using the instrument, which aim at optimizing the scientific content of the results. In particular, it is possible to read-out images at intermediate stages of an integration and *return both these and the final image to the ground*. This mode of operation is known as *Multiple-Accumulate* (`MULTIACCUM`). The observer uses this capability by specifying one of the pre-defined `MULTIACCUM` sequences, `SAMP-SEQ` (see next section) and the number of samples `NSAMP` that corresponds to the desired integration time. The list of supported `MULTIACCUM` sequences is given in the next section. These sequences are either linearly spaced or logarithmically spaced. Linearly spaced exposures may be useful for faint targets where cosmic ray filtering is important while logarithmically spaced exposures permit the observation of a wide dynamic range. The process is shown schematically in Figure 8.1 for the case of logarithmically spaced intervals with `NSAMP=4`.

In MULTIACCUM the detector reset is followed by a single read of the initial pixel values (zeroth read). Then a sequence of non-destructive array readouts are obtained at times specified by the selected sequence. Up to 25 readouts can be specified spanning a total integration time from 0.203 seconds to 8590.0 seconds. The last read of the detector array ends the exposure and thus the last NSAMP will be selected to give the total exposure time. All of the readouts, including the initial readout, are stored and downlinked without any onboard processing. For *N* readouts, this mode requires the storage and transmission (downlink) of *N*+1 times as much data volume as for ACCUM mode. (See Section 8.6 for trade-offs between MULTIACCUM and ACCUM readout modes.)

In most cases, MULTIACCUM mode provides the highest quality scientific data. The benefits of obtaining observations in MULTIACCUM mode fall into two areas.

- The dynamic range of the observation is greatly increased. Rather than being limited by the charge capacity of a NICMOS pixel (a few $\times 10^5$ electrons), an observation's dynamic range is in principle limited by the product of the pixel capacity and the ratio of the longest and shortest exposures (8590.0 and 0.203 seconds).
- An image can be reconstructed by processing the stack of readouts to cope with the effects of cosmic rays and saturation.

MULTIACCUM provides the best choice for deep integrations or integrations on fields with objects of quite different brightness.

MOST observers should use MULTIACCUM for their observations. Starting with Cycle 14, the four MIF MULTIACCUM timing sequences (MIF512, MIF1024, MIF2048, and MIF3072) have been replaced with four new SPARS timing sequences (SPARS4, SPARS16, SPARS32, and SPARS128). The new SPARS sequences can be most useful for fields with faint sources; i.e. nebulae, star clusters and galaxies.

Figure 8.1: Example MULTIACCUM with NSAMP = 4.

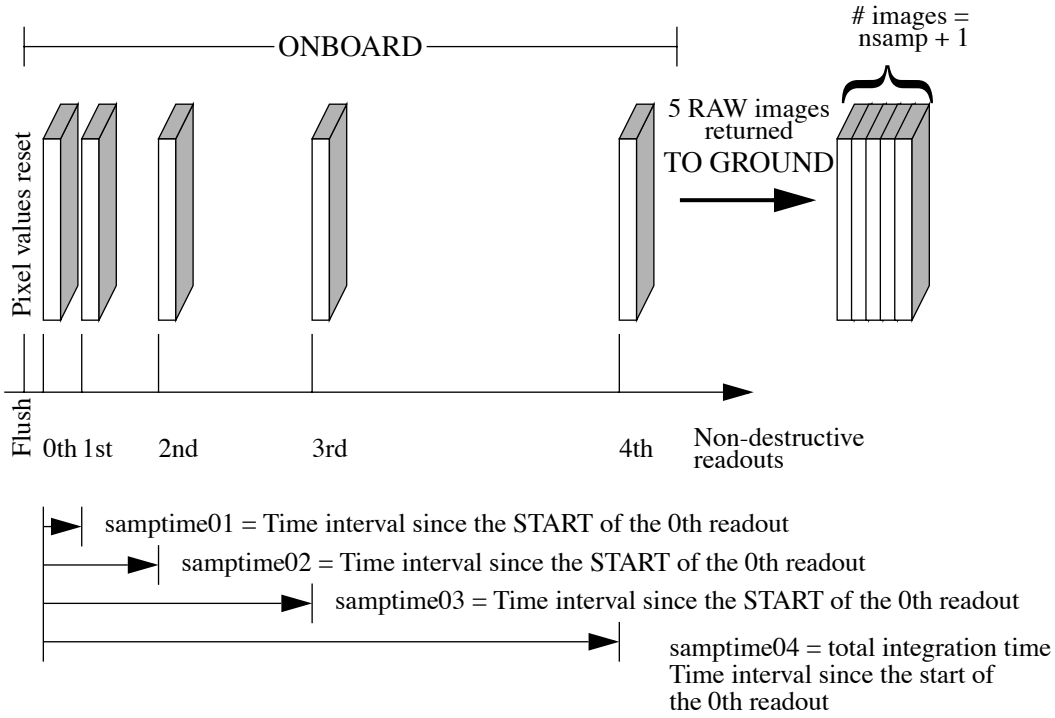

8.3 MULTIACCUM Predefined Sample Sequences (SAMP-SEQ)

For the user's convenience, and to minimize the volume of commanding information to be sent to HST, a set of sequences has been defined which should cover nearly all applications of MULTIACCUM. These are listed in Table 8.2. The observer specifies the name of the sequence and the number of samples to be obtained. The SCAMRR and MCAMRR are to be used when the fastest temporal sampling is desired. The SPARS4, SPARS16, SPARS32, SPARS64, SPARS128 and SPARS256 sequences have relatively few readouts and may be helpful when two or more cameras are operated in parallel (in particular they generally permit a second and third camera to operate in parallel with a minimal impact on the operation of the primary camera). SPARSXX is also recommended for observations of fields where only faint targets are present. The STEPXX sequences all start with three rapid readouts and then are logarithmically spaced to provide a large dynamic range up to their defined time (e.g., STEP64 has log steps up to 64 seconds) and then revert to linear spacing. The STEPXX sequences are recommended for observations involving both bright and faint targets, where high dynamic range is required.

The fastest time to read a single camera is 0.203 seconds, while 0.303 seconds is the fastest time when more than one camera is used. Accordingly, the MULTIACCUM sequences have been set up so that the first read is always the fastest time possible. The second read for all of the sequences, except for the SCAMRR, has a time of 0.606 seconds.

Table 8.2: MULTIACCUM SAMP-SEQs.

Sequence Name	Readout Times					Description
SCAMRR	0.203	0.406	0.609	0.812	1.015	Single camera fastest possible operation.
	1.218	1.421	1.624	1.827	2.030	
	2.233	2.436	2.639	2.842	3.045	
	3.248	3.451	3.654	3.857	4.060	
	4.263	4.466	4.669	4.872	5.075	
MCAMRR	0.303	0.606	0.909	1.212	1.515	Fastest possible operation with 2 or 3 cameras used in parallel.
	1.818	2.121	2.424	2.727	3.030	
	3.333	3.636	3.939	4.242	4.545	
	4.848	5.151	5.454	5.757	6.060	
	6.363	6.666	6.969	7.272	7.575	
STEP1	0.303	0.606	0.995	1.993	2.991	Rapid reads up to 1 second then 1 second steps.
	3.989	4.987	5.985	6.983	7.981	
	8.979	9.977	10.975	11.973	12.971	
	13.969	14.967	15.965	16.963	17.961	
	18.959	19.957	20.955	21.953	22.951	
STEP2	0.303	0.606	0.995	1.993	3.987	Rapid reads up to 2 seconds then 2 second steps.
	5.981	7.975	9.969	11.963	13.957	
	15.951	17.945	19.939	21.933	23.927	
	25.921	27.915	29.909	31.903	33.897	
	35.891	37.885	39.879	41.873	43.867	
STEP8	0.303	0.606	0.995	1.993	3.987	Rapid reads up to 8 seconds then 8 second steps.
	7.981	15.975	23.969	31.963	39.957	
	47.951	55.945	63.939	71.933	79.927	
	87.921	95.915	103.909	111.903	119.897	
	127.891	135.885	143.879	151.873	159.867	
STEP16	0.303	0.606	0.995	1.993	3.987	Rapid reads up to 16 seconds then 16 second steps.
	7.981	15.975	31.969	47.963	63.957	
	79.951	95.945	111.939	127.933	143.927	
	159.921	175.915	191.909	207.903	223.897	
	239.891	255.885	271.879	287.873	303.867	
STEP32	0.303	0.606	0.995	1.993	3.987	Rapid reads up to 32 seconds then 32 second steps.
	7.981	15.975	31.969	63.969	95.969	
	127.969	159.969	191.969	223.969	255.969	
	287.969	319.969	351.969	383.969	415.969	
	447.969	479.969	511.969	543.969	575.969	
STEP64	0.303	0.606	0.995	1.993	3.987	Rapid reads up to 64 seconds then 64 second steps.
	7.981	15.975	31.969	63.969	127.967	
	191.965	255.963	319.961	383.959	447.957	
	511.955	575.953	639.951	703.949	767.947	
	831.945	895.943	959.941	1023.939	1087.937	

Table 8.2: MULTIACCUM SAMP-SEQs.

Sequence Name	Readout Times					Description
STEP128	0.303	0.606	0.995	1.993	3.987	Rapid reads up to 128 seconds then 128 second steps.
	7.981	15.975	31.969	63.969	127.967	
	255.961	383.955	511.949	639.943	767.937	
	895.931	1023.925	1151.919	1279.913	1407.907	
	1535.901	1663.895	1791.889	1919.883	2047.877	
STEP256	0.303	0.606	0.995	1.993	3.987	Rapid reads up to 256 seconds then 256 second steps.
	7.981	15.975	31.969	63.969	127.967	
	255.961	511.961	767.961	1023.961	1279.961	
	1535.961	1791.961	2047.961	2303.961	2559.961	
	2815.961	3071.961	3327.961	3583.961	3839.961	
SPARS4	0.303	0.606	3.998	8.000	12.002	Two rapid readouts then 4 second steps.
	16.004	20.006	24.008	28.010	32.012	
	36.014	40.016	44.018	48.020	52.022	
	56.024	60.026	64.028	68.030	72.032	
	76.034	80.036	84.038	88.040	92.042	
SPARS16	0.303	0.606	15.997	31.998	47.999	Similar to STEP16 but without the rapid initial readouts.
	64.000	80.001	96.002	112.003	128.004	
	144.005	160.006	176.007	192.008	208.009	
	224.010	240.011	256.012	272.013	288.014	
	304.015	320.016	336.017	352.018	368.019	
SPARS32	0.303	0.606	32.004	64.004	96.004	Similar to STEP32 but without the rapid initial readouts.
	128.004	160.004	192.004	224.004	256.004	
	288.004	320.004	352.004	384.004	416.004	
	448.004	480.004	512.004	544.004	576.004	
	608.004	640.004	672.004	704.004	736.004	
SPARS64	0.303	0.606	63.994	127.992	191.990	Similar to STEP64 but without the rapid initial readouts.
	255.988	319.986	383.984	447.982	511.980	
	575.978	639.976	703.974	767.972	831.970	
	895.968	959.966	1023.964	1087.962	1151.960	
	1215.958	1279.956	1343.954	1407.952	1471.950	
SPARS128	0.303	0.606	127.997	255.998	383.990	Similar to STEP128 but without the rapid initial readouts.
	512.000	640.001	768.002	896.003	1024.004	
	1152.005	1280.006	1408.007	1536.008	1664.009	
	1792.010	1920.011	2048.012	2176.013	2304.014	
	2432.015	2560.015	2688.017	2816.018	2944.019	
SPARS256	0.303	0.606	255.996	511.996	767.996	Similar to STEP256 but without the rapid initial readouts.
	1023.996	1279.996	1535.996	1791.996	2047.996	
	2303.996	2559.996	2815.996	3071.996	3327.996	
	3583.996	3839.996	4095.996	4351.996	4607.996	
	4863.996	5119.996	5375.996	5631.996	5887.996	

8.4 Accumulate Mode

The *Accumulate Readout Mode* (ACCUM) generates the simplest basic exposure. In its simplest incarnation, *two array readouts*, illustrated in Figure 8.2, it is analogous to a WFPC2 or ACS readout. Its main difference relative to a MULTIACCUM exposure with NSAMP=2 (or two readouts selected) is that the first array read gets subtracted from the second array read by the on-board computer, and only the difference image is sent to the ground. *In other words, the returned image is the difference between the second and the first pass pixel values, and the integration time is defined as the time between the first and second read of the first pixel*. The minimum exposure time is ~0.6 sec, and the minimum time between successive exposures is ~8–12 seconds. ACCUM does not allow pipeline identification of cosmic ray events or to correct for pixel saturation.

Figure 8.2: Basic NICMOS Readout—Simple Two-Sample Readout.

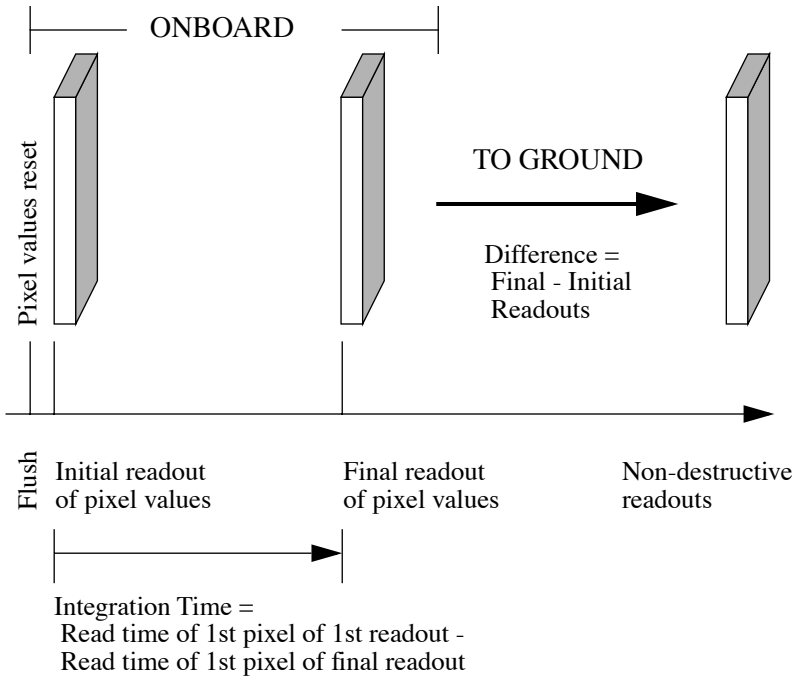

Flush time is 0.615s and is followed immediately by the Initial Readout.

Multiple Initial and Final Sample Readout

In ACCUM mode *multiple initial and final reads* can be obtained in place of the single initial and final readouts. In this case, after the detector array is reset, it will be followed by 1–25 (specified by the NREAD parameter) reads of the initial pixel values which are averaged onboard to define the

initial signal level. After the exposure time has elapsed, the final pixel values are again read NREAD times and averaged onboard. The data downlinked is the difference between the initial and final average signal levels for each pixel. The integration time is defined as the time between the first read of the first pixel in the initial NREAD passes and the first read of the first pixel in the final NREAD passes. The use of multiple reads in ACCUM mode is illustrated in Figure 8.3 for the case of NREAD = 4.

The advantage of this method is a reduction in the read noise associated with the initial and final reads. In theory the read noise should be reduced by $1/(n)^{1/2}$ where *n* is the number of reads. However, the amplifier glow (see Chapter 7) adds extra signal and associated photon noise for each read, especially towards the corners of the array. Amplifier glow is an additive noise source large enough that for NREAD > 9 there is little further gain in noise. In practice, the maximum improvement in effective read noise over a single initial and final read is no larger than a factor 40–50%, due to the added amplifier glow that each read-out adds to the final noise budget. For integrations where source photon noise or dark current noise exceeds the detector read noise, the multiple readouts may not offer much advantage. This option puts a higher burden on the CPU and requires an additional time per readout of 0.6 seconds. This mode does not allow pipeline identification of cosmic ray events or correction for pixel saturation.

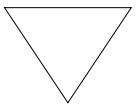

Starting from Cycle 12, ACCUM is available but unsupported for all modes with NREAD > 1. This means that the mode should only be used if dictated by special observing requirements.

Figure 8.3: ACCUM Mode with Four Initial and Final Readouts.

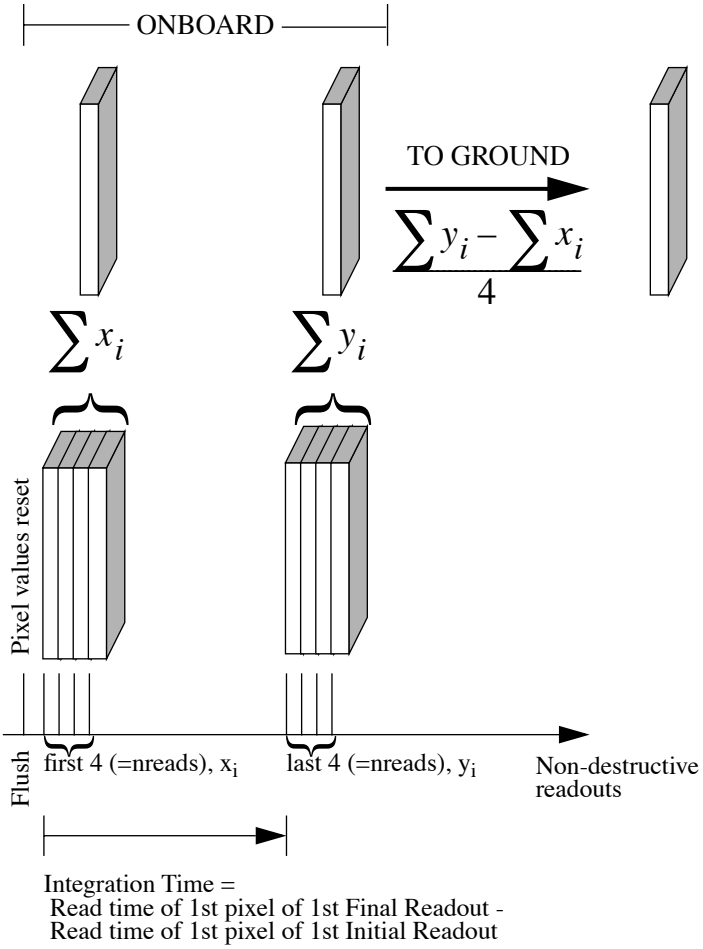

8.5 Read Times and Dark Current Calibration in ACCUM Mode

Because of the effects of shading, and the possibility that the underlying dark current may vary with time since reset, the removal of dark current (for calibration purposes, we implicitly assume shading and amplifier glow is a part of the time variable “dark current”) from NICMOS data is more complicated than for other instruments. The most accurate way to remove the dark current from any observation is a measurement of the dark current with an identical integration time and at the same detector temperature. For ACCUM observations we encourage observers to select exposure times that correspond to existing delta-times of the pre-defined MULTIACCUM

sequences (Table 8.2). These available delta-times are also listed in Table 8.3 below.

Table 8.3: Recommended Exposure Times with Dark Current Calibration.

Time (seconds) (NREAD=1)
0.203
0.303
0.389
0.998
1.994
3.994
7.994
15.994
32.000
63.998
127.994
256.000
383.999
511.998

STScI is not planning to obtain dedicated ACCUM dark observations, but dark reference files for ACCUM observations can be constructed from MULTIACCUM darks with identical delta-times.

8.6 Trade-offs Between MULTIACCUM and ACCUM

There are a variety of advantages to the MULTIACCUM mode. First, the ability present in a MULTIACCUM exposure to filter out CR hits which occur during the exposure is lost in the ACCUM mode. We find for NICMOS that typically between 2 and 4 pixels are hit per second per camera by CRs: most of these are low energy and so can be filtered out of a MULTIACCUM exposure by the calibration pipeline software. In ACCUM mode, the process of CR removal requires separate exposures and has to be done in post-processing. Second, the ability to detect pixel saturation, which again is done automatically for MULTIACCUM observations by the calibration software, can in some circumstances be lost in ACCUM mode.

This is because the time elapsed between the first read for each pixel and the reset immediately prior to the read is approximately 0.2 seconds. During this time, pixels exposed to a bright target will accumulate significant signal, which is then present in the first read. When this is subtracted on-board in ACCUM mode, all the charge accumulated in the time between reset and read will be subtracted. If the pixel has saturated during the exposure, the difference between initial and final reads will be less than the expected saturation value for the pixel, and thus it may be impossible to recognize that the pixel is saturated. Therefore, in the case of bright targets, erroneous signal levels may be recorded in ACCUM mode. Third, in ACCUM mode, even if pixel saturation is detected, it is not possible to repair the data obtained in the saturated pixel. In MULTIACCUM mode, pixels which have saturated can be repaired by using the results of previous, unsaturated reads during the same exposure.

Given that there is so much more information present in a MULTIACCUM dataset than in an ACCUM dataset, it may seem obvious that MULTIACCUM should always be the preferred readout mode. In practice, there can be trade-off in a few specific cases.

Because of the fixed read-out patterns available for use in MULTIACCUM mode (the SAMP-SEQs), in order to make an exposure of total integration time a minute or two, it is necessary in most modes to perform a significant number of readouts. This may lead to a significant volume of data to process. Additionally, the readouts are initially stored in a buffer in the NICMOS flight computer. A maximum of 94 readouts can be stored in this buffer, after which the content of the buffer must be dumped to the Solid State Recorder. A full dump of 94 reads takes about three minutes. The data dumps occur in parallel with the beginning of another set of exposures (and thus do not 'penalize' the available observing time) in the vast majority of, but not all, circumstances. Thus, during the preparation of the Phase II proposals, some observers with very short (1-2 minutes) exposures may consider the trade-offs between ACCUM and MULTIACCUM.

In conclusion, in cases where a multitude of short duration exposures must be made per orbit, and data volume could be a problem, ACCUM may possibly (but not necessarily) be a good choice. In all other cases it is likely that MULTIACCUM will yield the best results, and therefore, we recommend that all observers attempt to use MULTIACCUM.

8.7 Acquisition Mode

Images obtained using the coronagraph in Camera 2 may be taken using any of the detector read-out modes. An ACQ mode observation performs an autonomous on-board acquisition (Mode-2 Acquisition) for subsequent coronagraph images. This mode is described in detail in Chapter 5 (Coronagraphy).

CHAPTER 9:

Exposure Time Calculations

In this chapter . . .

9.1 Overview: Web based NICMOS APT-ETC

In this section we describe some instrument-specific behavior which must be taken into account when estimating required exposure times. The WWW NICMOS Exposure Time Calculator (ETC) provides the most convenient means of estimating count rates and signal-to-noise ratios (SNRs) for imaging observations. The ETC handles either point sources or extended objects and can be accessed from:

http://www.stsci.edu/hst/nicmos/tools/New_APT_ETC

Two NICMOS ETCs are available to observers, an imaging ETC and a Spectroscopic ETC for grism users. Previously, only the imaging ETC was available. The Spectroscopic ETC was delivered on November 8, 2004 along with an updated imaging ETC.

The imaging NICMOS WWW ETC is documented in an Instrument Science Report (Arribas *et al*. 2004, NICMOS ISR 2004-002 and references therein). Recent updates are also explained in its help file (accessible from the user interface). The ETC generates either the exposure time required for a specified SNR or the expected SNR for a user-defined exposure time. It will also indicate the read noise and the source and

background count rate, as well as the saturation-limited exposure time for the object in question.

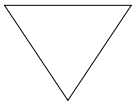

The WWW NICMOS Exposure Time Calculator (ETC) should be regarded as the tool of choice for estimating integration times for NICMOS observations. The ETC provides the most accurate estimates with the most current information on instrument performance; its reference tables are constantly updated with the most recent values of the instrument's characteristics as our knowledge of the NICMOS performance under NCS operations improves. Please check the NICMOS Web site for recent ETC updates.

A few comments about the limitations of making exposure time and SNR estimates are in order here.

NICMOS performance with the NCS has changed (relative to Cycles 7 and 7N) because the instrument now operates at a different temperature. This has improved the Detector Quantum Efficiency (DQE), but has also increased the dark current. The ETC has been updated to use parameters for Cycle 11 and beyond, with a temperature of 77.15K.

The instrumental characteristics used by the ETC are *average* values across the field of view of the camera. The actual sensitivity will vary across the field because of DQE variations (see Chapter 7 for details). A second source of spatial variation not included in the ETC occurs near the corners of the chip because of amplifier glow (see Section 7.3.2).

For photon-limited observations (limited either by the target count rate or the background), SNR increases as the square root of the total observation time, regardless of how the observation is subdivided into individual exposures. However, some NICMOS observations may be significantly affected by read noise, and the net SNR from the sum of several exposures will depend on the relative contributions of read noise and photon noise. Read noise variations that depend on different read sequences are not accounted for in the ETC.

Phenomena such as cosmic ray persistence (Chapter 4) can degrade sensitivity for faint object imaging by increasing the level of background noise. The impact of cosmic ray persistence is not easily quantified because it is non-Gaussian, correlated noise. It is not possible to predict the extent of this effect at the time the observations are planned, so it is not included in the ETC calculations. Additional information on the ETC and its structure can be found in the Instrument Science Reports (ISRs) posted on the STScI NICMOS Instrument Web page.

http://www.stsci.edu/hst/nicmos/

The ETC does *not* take the count rate non-linearity (Section 4.2.4) into account. This is especially relevant for faint and/or low surface brightness observations on a low background at wavelengths shorter than 1.6 microns. The effect depends on the count rate in each individual pixel and is therefore hard to model in the ETC. To correct for this non-linearity, for faint objects ($m_{AB} > \sim 20$) one should use a 0.25 mag fainter object in the ETC for F110W in NIC1 and NIC2, and 0.16 mag fainter for NIC3, when one has an average background. The effect is always less at longer wavelengths and brighter backgrounds.

9.1.1 Instrumental Factors

Detectors

The detector properties which will affect the sensitivity are simply those familiar to ground-based optical and IR observers, namely dark current and read noise, and the detector quantum efficiency (DQE). The dark current and DQEs measured in Cycle 11 are included in this ETC (see Chapter 7 for more details). The variation of the DQE as a function of wavelength and temperature is also taken into account. *The ETC currently does not take the count rate non-linearity described in Section 4.2.4 into account. Faint objects may be affected by as much as 0.25 mag in NIC1 and NIC2, and 0.16 mag in NIC3 at the shorter wavelengths.*

Optics

NICMOS contains a fairly small number of elements which affect the sensitivity. These elements are the filter transmission, the pixel field of view (determined by the NICMOS optics external to the dewar, in combination with the HST mirrors), the reflectivities and emissivities of the various mirrors and the transmission of the dewar window.

Filter transmissions as a function of wavelength were measured in the laboratory and convolved with OTA, NICMOS fore-optics and detector response. The resulting curves are presented in Appendix A.

NICMOS contains a total of seven mirrors external to the dewar, each of which reduces the signal received at the detector. The mirrors are silver coated (except for the field divider assembly which is gold coated) for a reflectivity of 98.5%. The dewar window has a transmission of roughly 93%. Therefore, the combination of optical elements is expected to transmit ~84% of the incoming signal from the OTA.

The sensitivity will obviously be affected by the pixel field of view. The smaller the angular size of a pixel, the smaller the fraction of a given source that will illuminate the pixel, but compensating will be a lower sky background. Finally, the optical efficiency will be degraded further by the reflectivities of the aluminum with MgF_2 overcoated HST primary and secondary mirrors.

Background Radiation

At long wavelengths (> 1.7 microns) the dominant effect limiting the NICMOS sensitivity is the thermal background emission from the telescope. The magnitude of this background mainly depends on the temperatures of the primary and secondary mirrors and their emissivities. At shorter NICMOS wavelengths, sensitivities are affected by the zodiacal background. Both sources of background are described in Chapter 4.

9.2 Calculating NICMOS Imaging Sensitivities

In some situations it may be desirable to go through each step of the calculation. To facilitate calculations when the Web connection is not possible, in this section we provide recipes for determining the signal-to-noise ratio or exposure time by hand. These calculations refer to the brightest pixel (i.e., aperture of 1×1 pixel). These calculations do not take the count rate non-linearity into account described in Section 4.2.4.

9.2.1 Calculation of Signal-to-Noise Ratio

The first step in this process is to calculate the electrons/second/pixel generated by the source. For this we need to know the flux in the central pixel F_j in Jansky/pixel. Please refer to Appendix A to calculate the fraction of flux that will lie in the central pixel for any camera/filter combination, and Appendix B for unit conversions.

Then the electron count in that pixel due to the continuum source is

$$C_c = F_j \gamma_{opt} \gamma_{det} \gamma_{filt} A_{prim} E = F_j \eta_c [e^-/\text{sec/pixel}]$$

where:

γ_{opt} is the transmittance of the entire optical train up to the detector, excluding the filters;

γ_{det} is the detector quantum efficiency;

γ_{filt} is the filter transmittance;

A_{prim} is the unobscured area of the primary;

E is a constant given by:

$$E = 10^{-26}/(h\lambda)$$

where h is Planck's constant and λ the wavelength. The quantities F_j, γ_{opt}, γ_{det} and γ_{filt} are all frequency dependent. The expression for C_c has to be integrated over the bandpass of the filter, since some of the terms vary significantly with wavelength. It should be noted that to determine C_c more accurately, the source flux F_j should be included in the integral over the filter bandpass, since the source flux is bound to be a function of wavelength.

For an emission line with intensity I_{lj} (in W m^{-2} $pixel^{-1)}$ falling in the bandpass of the filter, the counts in e^-/s are given by:

$$C_l = I_{lj}\gamma_{opt}\gamma_{det,\lambda}\gamma_{filt,\lambda}A_{prim}E = \varepsilon_\lambda I_{ij}[e^-/\text{sec/pixel}]$$

where E is defined as before. In this case, the detector quantum efficiency and filter transmission are determined for the wavelength λ of the emission line. The total signal per pixel is the sum of the continuum and line signals calculated above, namely $C_s=C_c+C_l$.

The source signal is superimposed on sky background and thermal background from warm optics. At $\lambda > 1.7$ μm the background is often much brighter than the source. In such cases the observation is background limited, not read noise limited. There is little point in increasing the number of multiple initial and final reads when the observation is background-limited, though multiple exposures and dithering will help cosmic ray removal and correction of other effects such as persistence from previously-observed bright objects.

The other components of unwanted signal are read noise, N_r, and dark current, I_d (in e^-/s/pixel). By read noise, we mean the electronic noise in the pixel signal after subtraction of two reads (double correlated sampling).

It is now possible to calculate the signal-to-noise ratio expected for an exposure of duration t seconds:

$$SNR = \frac{C_s t}{\sqrt{(C_s + B + I_d)t + N_r^2}}$$

where C_s, the count rate in e^-/sec/pixel, is the sum of C_c plus C_{line}, B is the background in e^-/sec/pixel (also listed in Tables 9.1, 9.2, and 9.3), I_d is the dark current in e^-/sec/pixel and N_r is the read-out noise, in e^-/pixel, for one initial and one final read. Although the effective N_r can vary somewhat depending on the readout sequence, ETC considers a fixed value per camera of about 26 e^-.

It is important to note that in these equations, the flux to be entered (either F_j or I_{lj} or both) is *not* the total source flux, but the flux falling on a pixel. In the case of an extended source this can easily be worked out from the surface brightness and the size of the pixel. For a point source, it will be necessary to determine the fraction of the total flux which is contained within the area of one pixel and scale the source flux by this fraction. For Camera 1 in particular, this fraction may be quite small, and so will make a substantial difference to the outcome of the calculation. Appendix A gives the fraction of the PSF falling in the brightest pixel assuming a point source centered on the pixel, for each filter.

The signal-to-noise ratio evaluated by a fit over the full PSF for point sources would, of course, be larger than this central pixel SNR; this discrepancy will be largest for the higher resolution cameras and for the longest wavelengths.

The average values for η_c and ε_λ for each filter are denoted as $\hat{\eta}_c$ and $\hat{\varepsilon}_\lambda$ and are listed in Tables 9.1, 9.2, and 9.3 for a detector temperature of 77.1 K. (Note that the above tables are not necessarily updated and the results in S/N could be off by ~20% (or more) in some cases. The Web based ETC, which is updated and provides more accurate results, should be used for any serious ETC calculation.) For estimating $\hat{\eta}_c$ we have assumed a source with an effective temperature of 5,000K, but the Web based ETC will take the spectral type chosen by the user to integrate over the bandpass. For emission lines in the wings of the filter bandpass, another correction factor may be needed which can be estimated from filter transmission curves in Appendix A.

9.2.2 Saturation and Detector Limitations

Given a particular filter-detector combination and a requested target flux, there is an exposure time above which the detector starts to saturate. The WWW NICMOS ETC will produce this exposure time when it performs the requested estimation.

9.2.3 Exposure Time Calculation

The other situation frequently encountered is when the required signal-to-noise is known, and it is necessary to calculate from this the exposure time needed. In this case one uses the same instrumental and telescope parameters as described above, and the required time is given by:

$$t = \frac{(SNR)^2(C_s + B + I_d) + \sqrt{(SNR)^4(C_s + B + I_d)^2 + 4(SNR)^2 C_s^2 N_r^2}}{2C_s^2}$$

Table 9.1: NIC1 Filter Sensitivity Parameters (per pixel).

Filter	T= 77.15K		
	$\hat{\eta}_c$ [e^-/sec/Jy]	$\hat{\varepsilon}$[e^-/sec/(W/m^2)]	B [e^-/sec]
F090M	0.765E+06	0.161E+19	0.115E-01
F095N	0.433E+05	0.110E+19	0.104E-02
F097N	0.522E+05	0.137E+19	0.104E-02
F108N	0.605E+05	0.199E+19	0.104E-02
F110M	0.135E+07	0.302E+19	0.188E-01
F110W	0.385E+07	0.415E+19	0.532E-01
F113N	0.729E+05	0.231E+19	0.104E-02
F140W	0.608E+07	0.944E+19	0.100E+00
F145M	0.153E+07	0.624E+19	0.170E-01
F160W	0.337E+07	0.948E+19	0.635E-01
F164N	0.149E+06	0.697E+19	0.277E-02
F165M	0.168E+07	0.898E+19	0.284E-01
F166N	0.146E+06	0.691E+19	0.190E-02
F170M	0.176E+07	0.953E+19	0.478E-01
F187N	0.157E+06	0.907E+19	0.213E-01
F190N	0.157E+06	0.951E+19	0.282E-01
POL0S	0.126E+07	0.136E+19	0.177E-01

Table 9.2: NIC2 Filter Sensitivity Parameters (per pixel).

Filter	$\hat{\eta}_c$ [e⁻/sec/Jy]	T=77.15K $\hat{\varepsilon}$[e⁻/sec/(W/m^2)]	B [e⁻/sec]
F110W	0.443E+07	0.458E+19	0.185E+00
F160W	0.371E+07	0.104E+20	0.170E+00
F165M	0.187E+07	0.996E+19	0.818E-01
F171M	0.723E+06	0.930E+19	0.421E-01
F180M	0.693E+06	0.997E+19	0.774E-01
F187N	0.177E+06	0.102E+20	0.446E-01
F187W	0.198E+07	0.105E+20	0.645E+00
F190N	0.172E+06	0.106E+20	0.578E-01
F204M	0.956E+06	0.134E+20	0.153E+01
F205W	0.572E+07	0.199E+20	0.351E+02
F207M	0.127E+07	0.124E+20	0.345E+01
F212N	0.192E+06	0.125E+20	0.697E+00
F215N	0.176E+06	0.123E+21	0.831E+00
F216N	0.190E+06	0.130E+20	0.104E+01
F222M	0.131E+07	0.139E+20	0.130E+02
F237M	0.148E+07	0.195E+20	0.506E+02
POL0L	0.943E+06	0.757E+19	0.120E+01

Table 9.3: NIC3 Filter Sensitivity Parameters (per pixel).

Filter	T= 77.15K		
	$\hat{\eta}_c$ [e^-/sec/Jy]	$\hat{\varepsilon}$[e^-/sec/(W/m^2)]	B [e^-/sec]
F108N	0.657E+05	0.214E+19	0.188E-01
F110W	0.399E+07	0.419E+19	0.119E+01
F113N	0.794E+05	0.242E+19	0.208E-01
F150W	0.673E+07	0.104E+20	0.276E+01
F160W	0.356E+07	0.101E+20	0.104E+01
F164N	0.157E+06	0.747E+19	0.453E-01
F166N	0.151E+06	0.736E+19	0.400E-01
F175W	0.916E+07	0.189E+20	0.108E+03
F187N	0.164E+06	0.940E+19	0.207E+00
F190N	0.172E+06	0.105E+20	0.282E+00
F196N	0.181E+06	0.109E+20	0.613E+00
F200N	0.186E+06	0.111E+20	0.898E+01
F212N	0.184E+06	0.123E+20	0.322E+01
F215N	0.169E+06	0.117E+20	0.384E+01
F222M	0.126E+07	0.136E+20	0.606E+02
F240M	0.182E+07	0.185E+20	0.382E+03

CHAPTER 10:

Overheads and Orbit Time Determination

In this chapter . . .

10.1 Overview

Once the set of science exposures and any additional target acquisition or calibration exposures required for the science program have been determined, they must be converted into a total number of orbits. Generally, this is a straightforward exercise involving tallying up the overheads on the individual exposures and on the selected pattern (see Appendix D), packing the exposure and overhead times into individual orbits, and tallying up the results to determine the total orbit request. This process may need to be iterated, in order to seek the most efficient use of the orbit time.

We refer to the Call for Proposals/Phase I Proposal Instructions for information on the Observatory policies and practices with respect to orbit time requests and for the orbit determination. Below, we provide a summary of the NICMOS specific overheads, and give an example to illustrate how to calculate orbit requirements for Phase I Proposals.

10.2 NICMOS Exposure Overheads

The overheads on exposures are summarized in Table 10.1. All numbers are approximate and, for the observatory level overheads, rounded up to the nearest half minute. These overhead times are to be used (in conjunction with the actual exposure time and the Phase I Proposal Instructions) to estimate the total time in orbits for NICMOS proposal time requests. After an HST proposal is accepted, the observer will be asked to submit a Phase II proposal to allow scheduling of the approved observations. At that time the observer will be presented with actual, up to date overheads by the scheduling software. **Allowing sufficient time for overheads in the Phase I proposal is important; additional time to cover unplanned overhead will not be granted later.**

Overheads can be subdivided into two main categories:

- ***Generic (Observatory Level) Overheads***:
  - The first time an object is acquired, the overhead time for the guide star acquisition must be included.
  - In subsequent contiguous orbits the overhead for the guide star re-acquisition must be included; if the observations are occurring in the continuous viewing zone (CVZ, see the CP/Phase I Proposal Instructions), no guide star re-acquisitions are required.
  - The re-acquisitions can be assumed to be accurate to $\leq$ 10 milli-arcsecs; thus additional target acquisitions or pick-ups are not needed following a re-acquisition.
  - Time must be allowed for each deliberate movement of the telescope; e.g., if a target acquisition exposure is being performed on a nearby star and then offsetting to the target or if a series of exposures in which the target is moved relative to the camera (dithers or chops) are being performed, time for the moves must be allowed.
- ***NICMOS Specific Overheads***:
  - The 19 second set-up time at the beginning of each orbit or at each different telescope pointing is inclusive of the filter selection.
  - For each pattern position, a 15 second overhead is scheduled for filter wheel motion, even if no filter change is executed.
  - Overheads are operating-mode dependent. The overhead for the `BRIGHTOBJ` mode is particularly burdensome, since this mode resets and reads each pixel, one pixel at a time.
  - The target acquisition overhead of (157 + 2 × *exptime*) seconds for coronagraphy needs to be accounted for the first time an object is acquired under the coronagraphic spot. Here, *exptime* is the exposure time needed to observe the target outside the coronagraphic

spot for centroiding. No target re-acquisition is required after a filter change or from one orbit to the next, if the same two guide stars are re-acquired after occultation.

- Overhead times for changing cameras are given in Table 10.2. The values in Table 10.2 include the time to perform the Small Angle Maneuver (to change from one camera to the other) and the time for Instrument reconfiguration (to change PAM position in order to refocus the Cameras). In addition, the observer must include 19 seconds for set-up which includes filter selection.
- The amount of time required to chop depends on the chop throw, and whether an on-target guide star re-acquisition is desired. The telescope can maintain lock on the guide stars if the chop throw is smaller than 1–2 arcminutes.
- In most cases, the data management overhead of 3 minutes will be hidden inside the orbit occultation time or placed in parallel with exposures. The latter, however, does not always happen as the software may not find a good location to place the data management (buffer dump) in parallel. Proposers whose observations require them to obtain multiple sets of 94 read-outs are advised to include the data management overhead for at least half of the times in their orbit computation.

Table 10.1: NICMOS Overheads.

Action	Overhead
Generic (Observatory Level)	
Guide star acquisition	Initial acquisition 6 minutes re-acquisitions on subsequent orbits = 5 minutes per orbit
Spacecraft `POS-TARG` moves	for offsets less than 1 arcminute and more than 10 arcsecs = 1 minute, for offsets between 10 arcsecs and 1 arcsec = 0.5 minute; for offsets less than 1 arcsec in size = 10 seconds
Slew of x arcsecs to new target within an orbit (slew < 1–2 arcmin, same guide stars)	(x + 10) seconds
Spacecraft Roll	0–1 degree ~2 minutes 1–10 degrees ~6 minutes 10–22 degrees ~8 minutes 22–30 degrees ~9 minutes
NICMOS Specific Overheads	
Set-up at beginning of each orbit or at each different telescope pointing—always required. (other than dither/chop maneuvering)	19 seconds
Filter change	15 seconds (shortest 10 seconds, longest 15 seconds)

Exposure overheads:
`ACCUM` readout
`MULTIACCUM`
`BRIGHTOBJ`
	
	(4.5+ NREAD × 0.6) seconds
	4 seconds
	(exptime × 16384 + 10) seconds

Target acquisition (for coronagraphy)	157 seconds + 2 × exptime seconds (includes slew)
Dithering/Chopping of x arcsecs (< 1–2 arcmin)	(x + 10) seconds
Data management (for every 94 read-outs within an orbit)	3 minutes

Table 10.2: Overheads (in seconds) for camera change. These include times for telescope slews and for refocus of the NICMOS Cameras.

Going From:	Going To:				
	Coronagraph	NIC 1	Intermediate	NIC 2	NIC 3
Coronagraph	0	40	80	125	620
NIC 1	55	0	40	85	580
Intermediate	95	40	0	45	540
NIC 2	150	95	55	0	285
NIC 3	645	590	550	285	0

10.3 Orbit Use Determination

The easiest way to learn how to compute total orbit time requests is to work through examples. We provide below two examples. The first example describes a thermal IR observation, with the `TWO-CHOP` pattern. The second example describes a coronagraphic acquisition and subsequent observations.

10.3.1 Observations in the Thermal Regime Using a Chop Pattern and MULTIACCUM

Observations at long wavelengths will be obtained for target A in NICMOS Camera 2 and 3. The `F222M` filter is used in each of the two cameras in turn. The observer requires exposure times of 128 seconds in each exposure, in `MULTIACCUM` mode. A good sequence for the target is considered to be `STEP8` with `NSAMP`=21. The target is extended and the selected chopping throw is one detector width. Note that this changes the time to chop for each camera. The `NIC-TWO-CHOP` pattern is used to obtain background measurements.

The declination of the source is –40 degrees, so the visibility period during one orbit is 57 minutes. The orbit requirement is summarized in Table 10.3.

Table 10.3: Orbit Determination for Observations of Target A.

Action	Time (minutes)	Explanation
	Orbit 1	
Initial Guide Star Acquisition	6	Needed at start of observation of new target 19 seconds setup at beginning of each orbit
Science exposure, NIC2 F222M	2.2	128 seconds exposure time on target 4 seconds for MULTIACCUM overhead
Small Angle Maneuver (chop)	0.9	Move off-target, allow for filter wheel motion
Science exposure, NIC2 F222M	2.2	128 seconds exposure time on background 4 seconds for MULTIACCUM overhead
Small Angle Maneuver (chop)	0.9	Move on-target, allow for filter wheel motion
Science exposure, NIC2 F222M	2.2	128 seconds exposure time on target 4 seconds for MULTIACCUM overhead
Small Angle Maneuver (chop)	0.9	Move off-target, allow for filter wheel motion
Science exposure, NIC2 F222M	2.2	128 seconds exposure time on background 4 seconds for MULTIACCUM overhead
Small Angle Maneuver (from NIC2 to NIC3) + Reconfigure Instrument	6.1	move on-target in NIC3 plus instrument reconfiguration (change focus from NIC2 to NIC3), and filter wheel motion
Science exposure, NIC3 F222M	2.2	128 seconds exposure time on target 4 seconds for MULTIACCUM overhead
Small Angle Maneuver (chop)	1.1	Move off-target, allow for filter wheel motion
Science exposure, NIC3 F222M	2.2	128 seconds exposure time on background 4 seconds for MULTIACCUM overhead
Small Angle Maneuver (chop)	1.1	Move on-target, allow for filter wheel motion
Science exposure, NIC3 F222M	2.2	128 seconds exposure time on target 4 seconds for MULTIACCUM overhead
Small Angle Maneuver (chop)	1.1	Move off-target, allow for filter wheel motion
Science exposure, NIC3 F222M	2.2	128 seconds exposure time on background 4 seconds for MULTIACCUM overhead

The total time spent on the target is 35.7 minutes, with a visibility period of 54 minutes. Note that for multi-filter observations, exposures for all filters can be obtained at each pointing before moving to the subsequent pointing.

If the observation were of a moving target, the slews to the new targets would be taken up in the tracking overhead, and the small angle maneuvers (SAMs) would all take 0.25 minutes, regardless of the camera.

More detailed estimates may also be obtained by building test Phase II proposals and processing them through APT; some observers may wish to

use this approach for estimating time required for the observations. Not shown in the above example is one parallel memory dump.

Coronagraphic Overhead Example

The following table (Table 10.4) shows the overheads for one visit of a coronagraphic observation with two identical visits (acquisitions) in adjacent orbits with a roll of the spacecraft between orbits. The overhead associated with the spacecraft roll is accounted for by the scheduling software; it therefore does not appear in this table.

- Target: HR4796
- Declination: –39 degrees
- Visibility: 57 minutes

Table 10.4: Time Estimator Example for NICMOS Coronagraphy—Visit 01.

Action	Time (minutes)	Explanation
	Orbit 1	
Initial Guide Star Acquisition	6	Needed at start of observation of new target 19 seconds setup at beginning of each orbit
NIC2 target acquisition for coronagraph	2.6	2 × 0.284 s F171M acquisition exposures 157 s overhead including slews
Dark Imaging	0.6	25 × 0.6 s dark exposure to remove persistence
Science exposure, NIC2 F160W	3.5	1 × 191.96 s science exposure 4 s MULTIACCUM overhead 15 s filter change overhead
Repeat 2 × without filter change		

APPENDIX A:

Imaging Reference Material

In this appendix...

This appendix provides basic throughput information and plots for the imaging and polarimetric filters. The corresponding information for the grism elements is provided in Chapter 5. The spectral characteristics of the NICMOS flight filters were measured at cryogenic temperature and normal incidence at Ball Aerospace. All filters had their spectral transmission measured from 0.5 to 2.7 microns with a step of 0.001 microns. For each filter, we provide the following information:

- A plot of the total system throughput, which convolves the filter transmission curve with the OTA, the NICMOS foreoptics and the predicted detector's response under NCS operations.
- A listing of the central, mean, and peak wavelengths, of the wavelength range, filter width, transmission peak, and the fraction of the PSF contained in one pixel (assuming the source is centered on the pixel) is also given.

All throughput curves and band parameters in this section were built with the DQE curve corrected to 77.1 K. The values for most of these parameters come directly from the **synphot** task in **STSDAS**. The graph (grtbl) and component (cmptbl) tables used for these calculations were:

grtbl = "`k511557nm_tmg.fits`"
cmptbl = "`m7t1443mm_tmc.fits`"

The above tables used for these calculations are available from CDBS at STScI.

The filter transmission curves and OTA and NICMOS optics reflectivities are the ones listed in these files. The only change made relative to these tables is that the `nic?_dqe*` table for each camera was modified to reflect changes from the reference temperature of each curve to the nominal NCS operating temperature (77.1 K, at the NDWTMP11 Mounting Cup temperature sensor). Based on the NICMOS standard star photometry, each DQE curve + filter transmission curve is correct for the temperature at which the standard star observations were made (NIC1: 61.3 K, NIC2: 61.3 K, NIC3: 62.0 K).

The correction of the original DQE curves were made based on the ratio of the mean value of lamp-flat images taken at the current operating temperature of 77.1 K to flats taken at the above temperatures. The correction factor as a function of wavelength is then multiplied by the original curve to get the new curve. Note that the DQE can vary by factors of 2–3 across each array.

The band parameters correspond to the output of the **STSDAS** task **bandpar** where:

Central wavelength = PIVWV
Mean wavelength = AVGWV
Peak wavelength = WPEAK
Maximum throughput = TPEAK

The FWHM is defined as the intersection between the transmission curve and the half-maximum-transmission value. Since the transmission curve shape is strongly affected by the DQE (particularly for the broad filters), the measured FWHM will change with temperature. This is NOT the FWHM value returned by the **bandpar** task.

The "Wavelength range" values are just measured by-eye from the throughput curves to serve as a rough estimate.

The "central pixel fraction" is the fraction of the total light from a point source that is contained in the central pixel of the point spread function (PSF). This assumes that the source is centered on a pixel, and that the pixel response function is unity across the pixel. All PSFs were made from **TinyTim** V6.0, using the following parameters, in each of the filters:

- 1.80 mm PAM for NIC1
- 0.20 mm PAM for NIC2
- –9.50 mm PAM for NIC3
- source centered at pixel 128 128 (detector center)
- aberrations for 31/12/1998
- 10.0" diameter, no subsampling, no jitter
- default **TinyTim** V6.0 throughput tables and the G2V source spectrum

Camera 1, Filter F090M

Central wavelength:	0. 90332 μm
Mean wavelength:	0. 90505 μm
Peak wavelength:	0. 91751 μm
Wavelength range:	0.8–1.0 μm
FWHM:	0.1731 μm
Maximum throughput:	8.2466%
Central pixel fraction:	0.123

Figure A.1: F090M Throughput

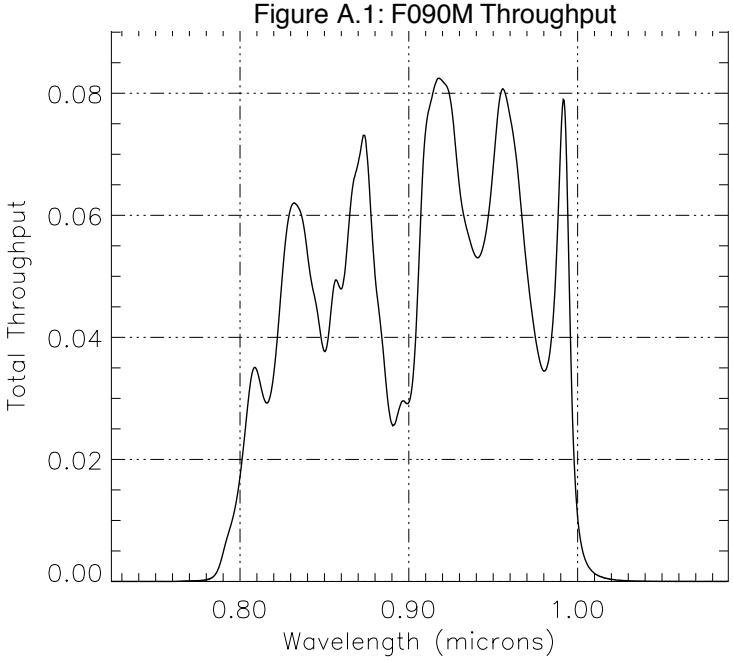

Camera 1, Filter F095N

Notes:
[S III] line.

Central wavelength:	0.9537 μm
Mean wavelength:	0.9537 μm
Peak wavelength:	0.9564 μm
Wavelength range:	0.949–0.958 μm
FWHM:	0.0093 μm
Maximum throughput:	6.7631%
Central pixel fraction:	0.114

Figure A.2: NIC1, F095N Throughput

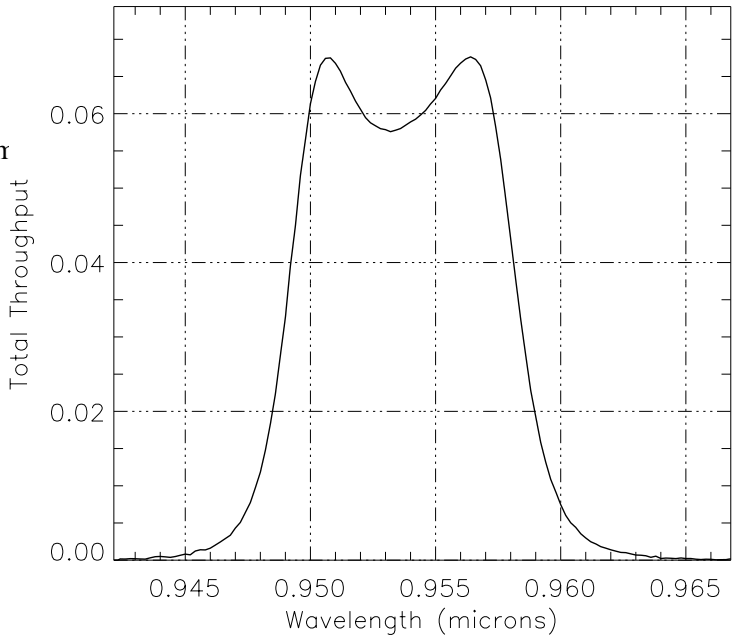

Camera 1, Filter F097N

Notes:
[S III] continuum.

Central wavelength:	0.9716 μm
Mean wavelength:	0.9716 μm
Peak wavelength:	0.9740 μm
Wavelength range:	0.967–0.977 μm
FWHM:	0.0097 μm
Maximum throughput:	8.0253%
Central pixel fraction:	0.111

Figure A.3: F097N Throughput

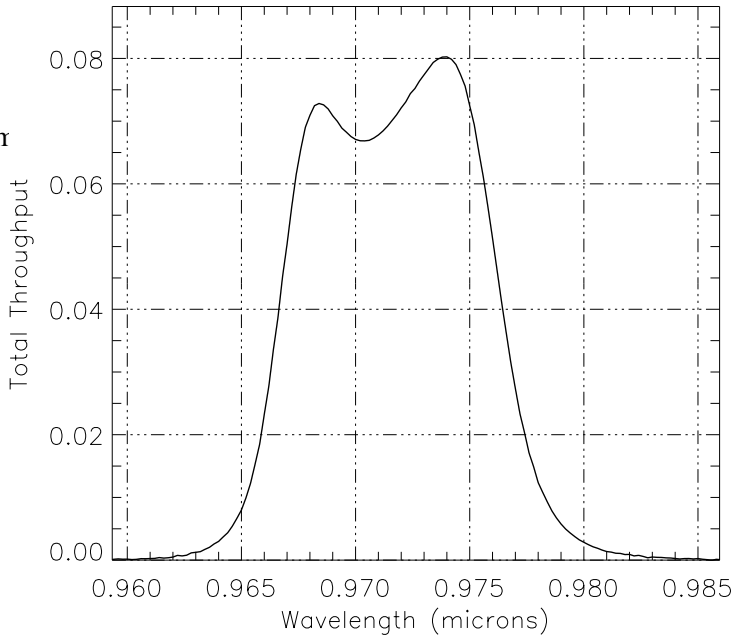

Camera 1, Filter F108N

Notes:
[He I] line.
See also “Camera 3, Filter F108N”

Central wavelength:	1.0816 μm
Mean wavelength:	1.0816 μm
Peak wavelength:	1.0790 μm
Wavelength range:	1.0–1.2 μm
FWHM:	0.0099 μm
Maximum throughput:	9.5904%
Central pixel fraction:	0.094

Figure A.4: NIC1, F108N Throughput

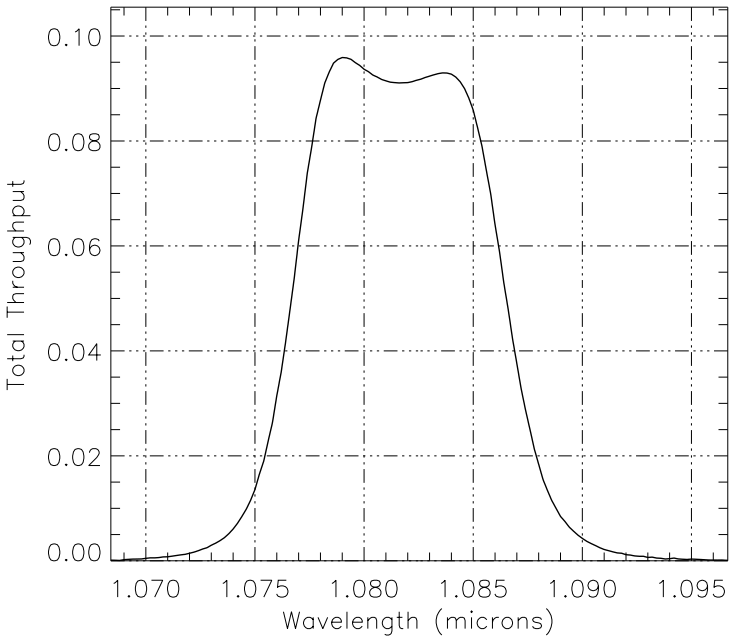

Camera 1, Filter F110M

Notes:
See also “Camera 1, Filter F110W”.

Central wavelength:	1.1016 μm
Mean wavelength:	1.1032 μm
Peak wavelength:	1.1295 μm
Wavelength range:	1.0–1.2 μm
FWHM:	0.1982 μm
Maximum throughput:	12.262%
Central pixel fraction:	0.092

Figure A.5: NIC1, F110M Throughput

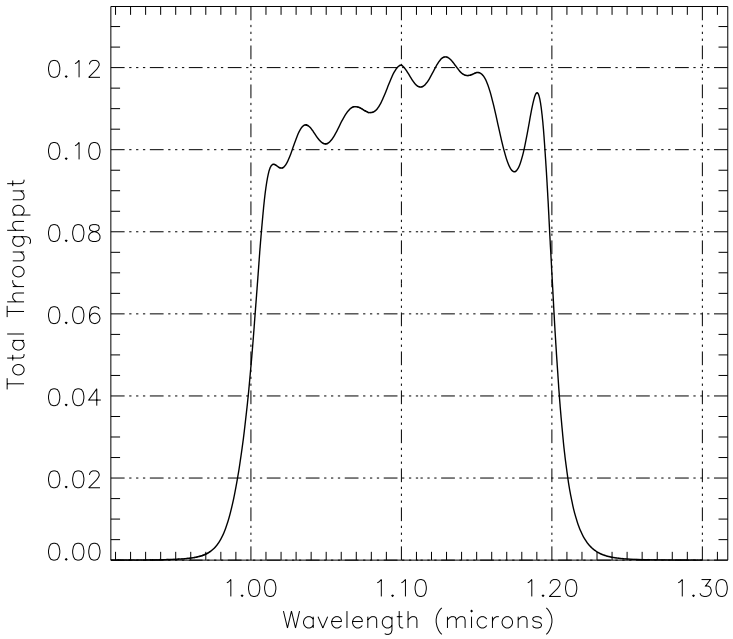

Camera 1, Filter F110W

Notes:
See also “Camera 2, Filter F110W” and “Camera 3, Filter F110W”.

Central wavelength:	1.1220 μm
Mean wavelength:	1.1341 μm
Peak wavelength:	1.3430 μm
Wavelength range:	0.8–1.4 μm
FWHM:	0.5277 μm
Maximum throughput:	15.233%
Central pixel fraction:	0.095

Figure A.6: NIC1, F110W Throughput

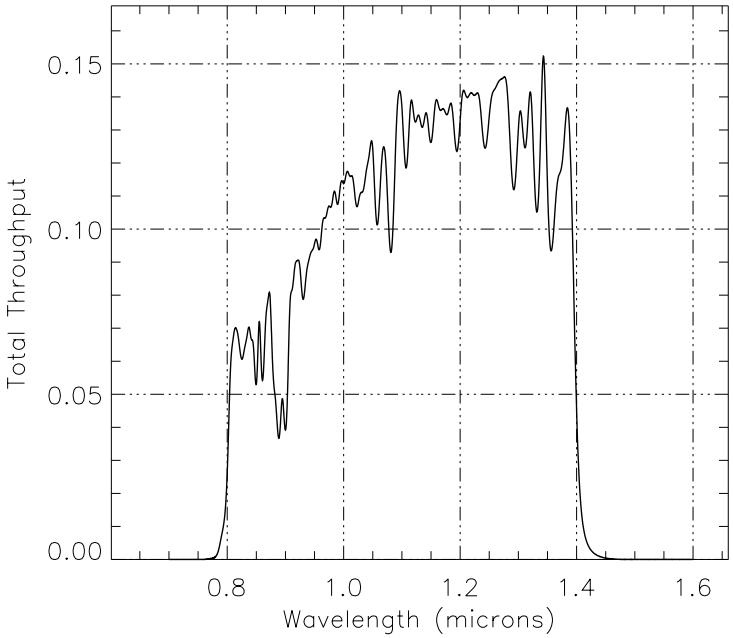

Camera 1, Filter F113N

Notes:
[He I] continuum.
See also “Camera 3, Filter F113N”.

Central wavelength:	1.1298 μm
Mean wavelength:	1.1298 μm
Peak wavelength:	1.1312 μm
Wavelength range:	1.124–1.135 μm
FWHM:	0.0113 μm
Maximum throughput:	11.162%
Central pixel fraction:	0.088

Figure A.7: NIC1, F113N Throughput

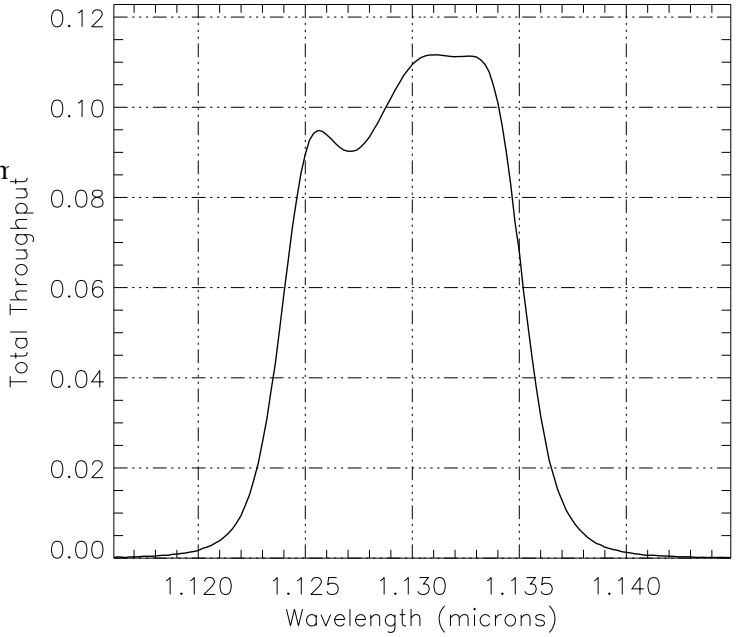

Camera 1, Filter F140W

Central wavelength:	1.4236 μm
Mean wavelength:	1.4433 μm
Peak wavelength:	1.7769 μm
Wavelength range:	1.0–1.8 μm
FWHM:	0.7509 μm
Maximum throughput:	22.215%
Central pixel fraction:	0.066

Figure A.8: NIC1, F140W Throughput

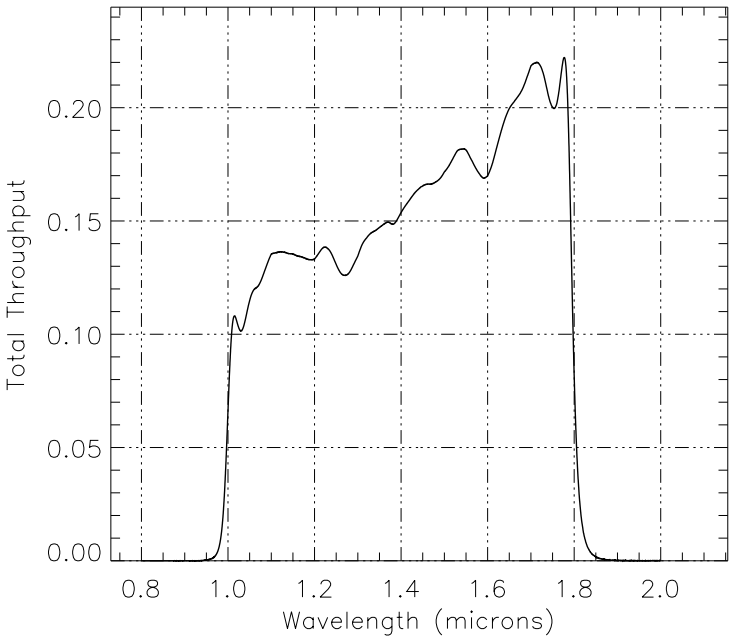

Camera 1, Filter F145M

Notes:
H_2O band.

Central wavelength:	1.4546 μm
Mean wavelength:	1.4558 μm
Peak wavelength:	1.5100 μm
Wavelength range:	1.35–1.55 μm
FWHM:	0.1963 μm
Maximum throughput:	18.233%
Central pixel fraction:	0.057

Figure A.9: NIC1, F145M Throughput

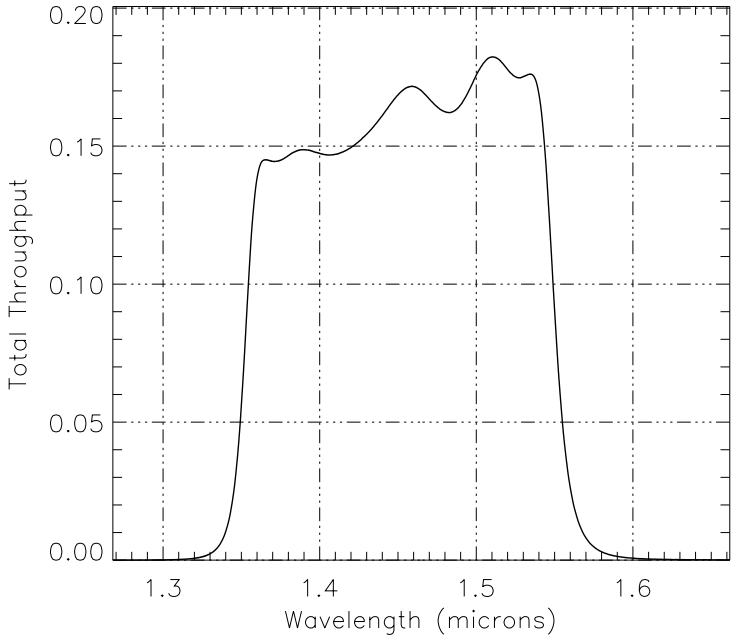

Camera 1, Filter F160W

Notes:
Minimum background.
See also “Camera 2, Filter F160W” and “Camera 3, Filter F160W”.

Central wavelength:	1.6028 μm
Mean wavelength:	1.6071 μm
Peak wavelength:	1.7725 μm
Wavelength range:	1.4–1.8 μm
FWHM:	0.3989 μm
Maximum throughput:	22.395%
Central pixel fraction:	0.049

Figure A.10: NIC1, F160W Throughput

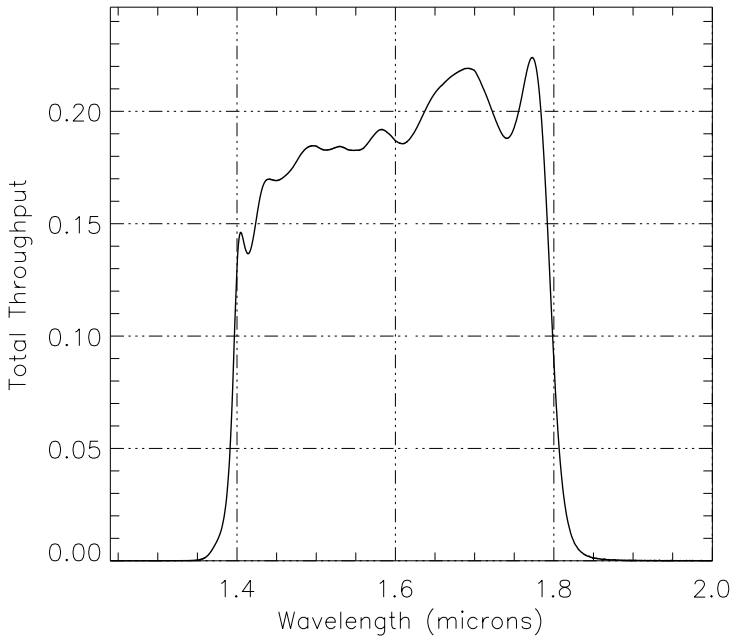

Camera 1, Filter F164N

Notes:
[Fe II] line.
See also “Camera 3, Filter F164N”.

Central wavelength:	1.6460 μm
Mean wavelength:	1.6460 μm
Peak wavelength:	1.6476 μm
Wavelength range:	1.636–1.655 μm
FWHM:	0.0173 μm
Maximum throughput:	0.0173%
Central pixel fraction:	0.046

Figure A.11: NIC1, F164N Throughput

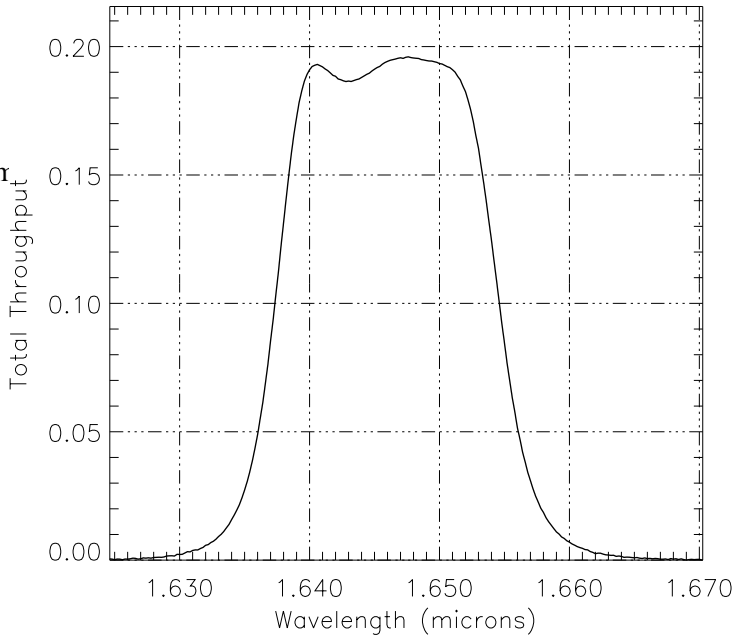

Camera 1, Filter F165M

Notes:
H_2O continuum.
See also “Camera 2, Filter F165M”.

Central wavelength:	1.6478 μm
Mean wavelength:	1.6488 μm
Peak wavelength:	1.7085 μm
Wavelength range:	1.54–1.74 μm
FWHM:	0.1985 μm
Maximum throughput:	22.12%
Central pixel fraction:	0.046

Figure A.12: NIC1, F165M Throughput

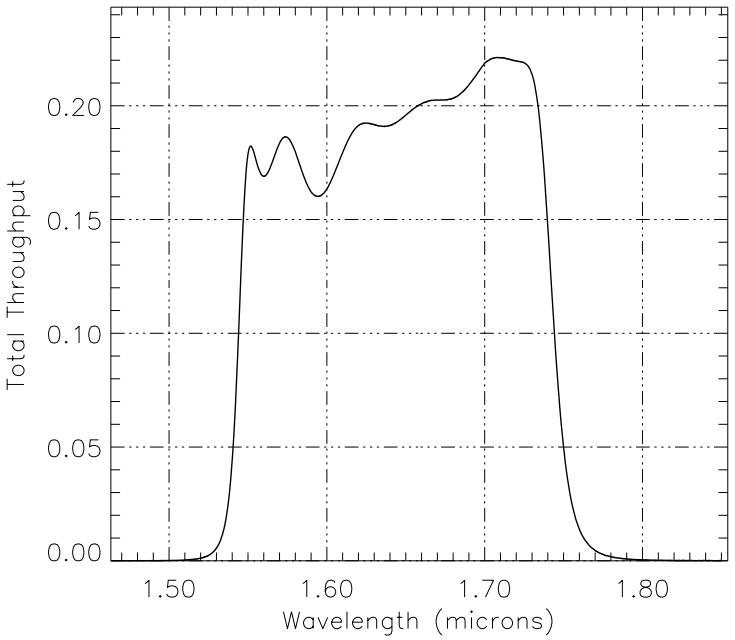

Camera 1, Filter F166N

Notes:
[Fe II] continuum.
See also “Camera 3, Filter F166N”.

Central wavelength:	1.6607 μm
Mean wavelength:	1.6607 μm
Peak wavelength:	1.6624 μm
Wavelength range:	1.652–1.668 μm
FWHM:	0.0170 μm
Maximum throughput:	19.895%
Central pixel fraction:	0.045

Figure A.13: NIC1, F166N Throughput

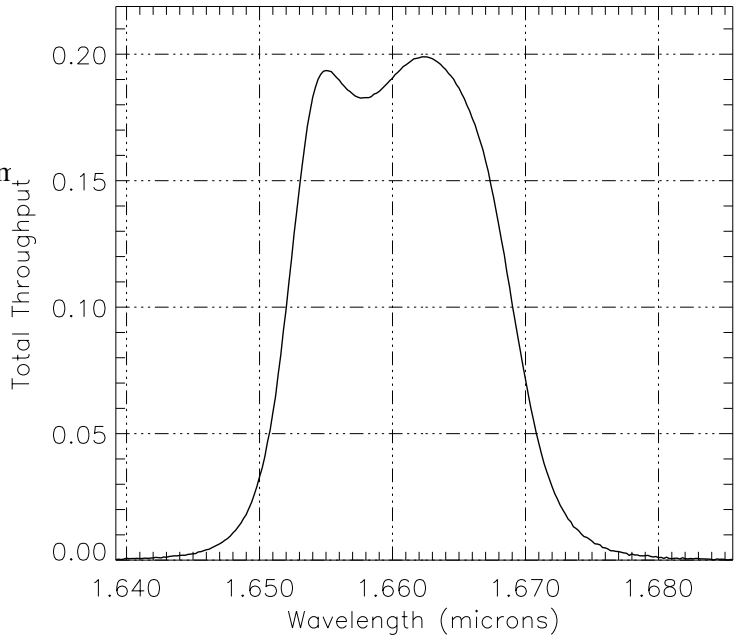

Camera 1, Filter F170M

Notes:
See also “Camera 2, Filter F171M”.

Central wavelength:	1.7055 μm
Mean wavelength:	1.7066 μm
Peak wavelength:	1.7885 μm
Wavelength range:	1.6–1.8 μm
FWHM:	0.2025 μm
Maximum throughput:	22.517%
Central pixel fraction:	0.043

Figure A.14: NIC1, F170M Throughput

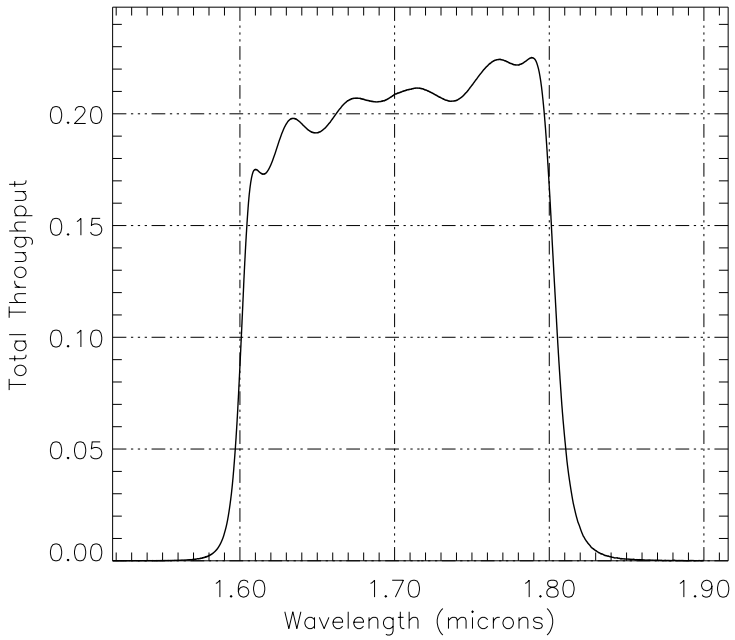

Camera 1, Filter F187N

Notes:
Paschen α.
See also "Camera 2, Filter F187N" and "Camera 3, Filter F187N".

Central wavelength:	1.8748 μm
Mean wavelength:	1.8748 μm
Peak wavelength:	1.8756 μm
Wavelength range:	1.865–1.885 μm
FWHM:	0.0191 μm
Maximum throughput:	21.7%
Central pixel fraction:	0.036

Figure A.15: NIC1, F187N Throughput

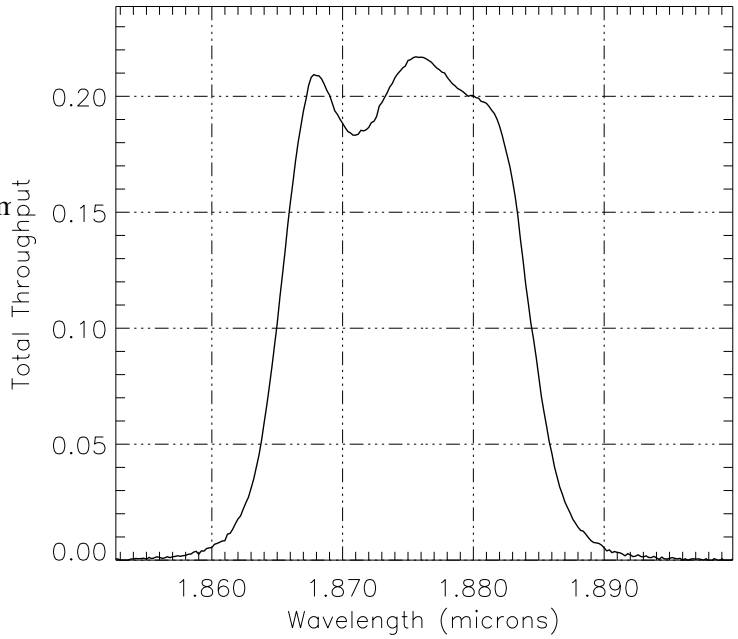

Camera 1, Filter F190N

Notes:
Paschen α continuum.
See also "Camera 2, Filter F190N" and "Camera 3, Filter F190N".

Central wavelength:	1.8986 μm
Mean wavelength:	1.8986 μm
Peak wavelength:	1.8942 μm
Wavelength range:	1.890–1.907 μm
FWHM:	0.0178 μm
Maximum throughput:	22.139%
Central pixel fraction:	0.035

Figure A.16: NIC1, F190N Throughput

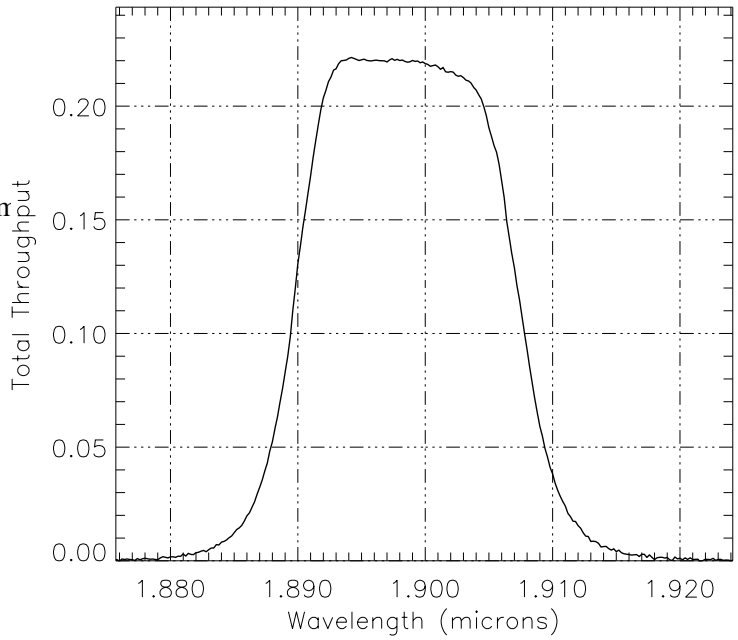

Camera 1, Polarizer POL0S

Notes:
See Table 5.2 for characteristics of polarizers POL120S and POL240S.

Central wavelength:	1. 0557μm
Mean wavelength:	1.0639 μm
Peak wavelength:	1.1435 μm
Wavelength range:	0.8–1.3
FWHM:	0.4473 μm
Maximum throughput:	5.798%
Central pixel fraction:	0.101

Figure A.17: NIC1, Short Polarizer Throughput

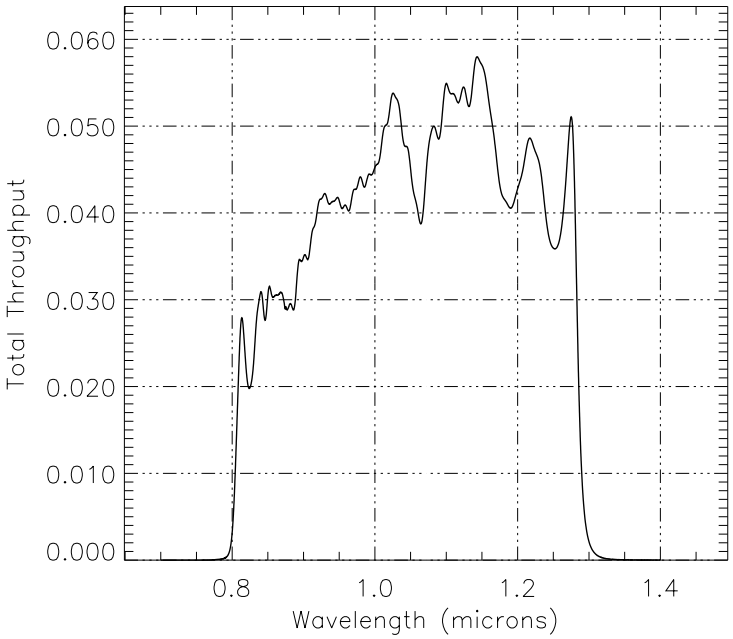

Camera 2, Filter F110W

Notes:
See also “Camera 1, Filter F110W” and “Camera 3, Filter F110W”.

Central wavelength:	1.1246 μm
Mean wavelength:	1.1364 μm
Peak wavelength:	1.3404 μm
Wavelength range:	0.8–1.4 μm
FWHM:	0.5261 μm
Maximum throughput:	17.141%
Central pixel fraction:	0.235

Figure A.18: NIC2, F110W Throughput

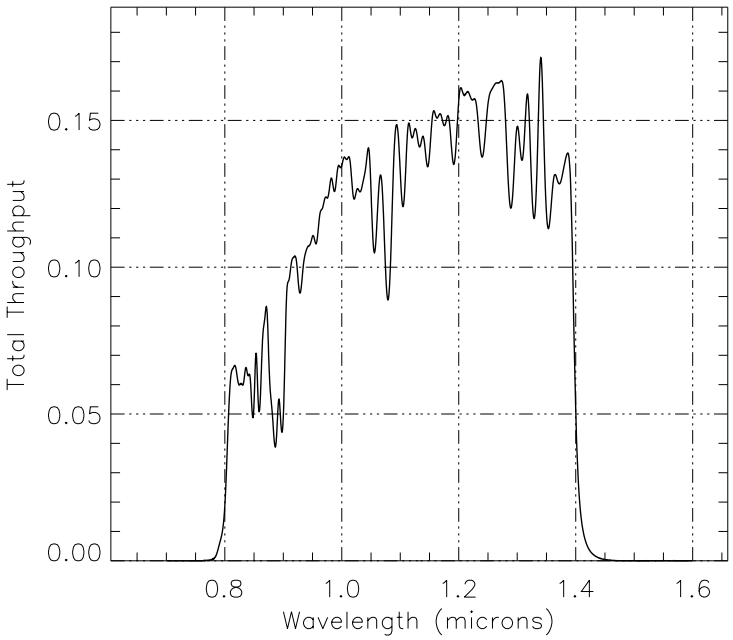

Camera 2, Filter F160W

Notes:
Minimum background.
See also “Camera 1, Filter F160W” and “Camera 3, Filter F160W”.

Central wavelength:	1.6037 μm
Mean wavelength:	1.6080 μm
Peak wavelength:	1.7720 μm
Wavelength range:	1.4–1.8 μm
FWHM:	0.4010 μm
Maximum throughput:	25.236%
Central pixel fraction:	0.136

Figure A.19: NIC2, F160W Throughput

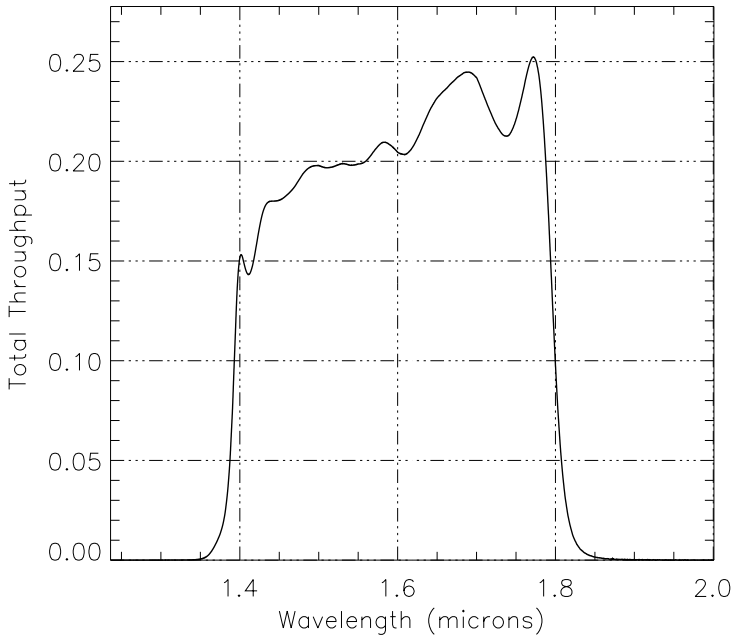

Camera 2, Filter F165M

Notes:
Planetary continuum.
See also “Camera 1, Filter F165M”.

Central wavelength:	1.6511 μm
Mean wavelength:	1.6521 μm
Peak wavelength:	1.7135 μm
Wavelength range:	1.54–1.74 μm
FWHM:	0.1984 μm
Maximum throughput:	25.247%
Central pixel fraction:	0.127

Figure A.20: NIC2, F165M Throughput

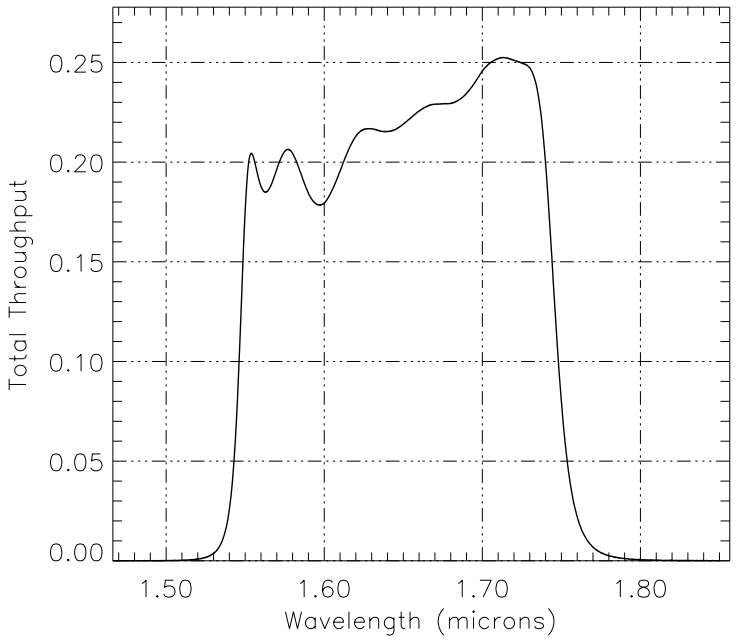

Camera 2, Filter F171M

Notes:
HCO_2 and C_2 continuum.

Central wavelength:	1.7211 μm
Mean wavelength:	1.7213 μm
Peak wavelength:	1.7258 μm
Wavelength range:	1.68–1.76 μm
FWHM:	0.0714 μm
Maximum throughput:	24.333%
Central pixel fraction:	0.119

Figure A.21: NIC2, F171M Throughput

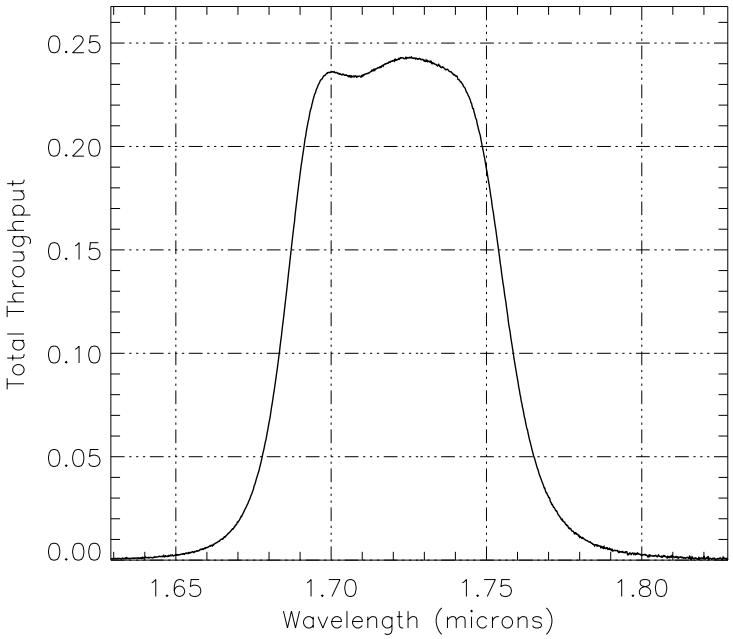

Camera 2, Filter F180M

Notes:
HCO_2 and C_2.
Thermal background important.

Central wavelength:	1.7970 μm
Mean wavelength:	1.7972 μm
Peak wavelength:	1.8132 μm
Wavelength range:	1.76–1.83 μm
FWHM:	0.0686 μm
Maximum throughput:	24.913%
Central pixel fraction:	0.110

Figure A.22: NIC2, F180M Throughput

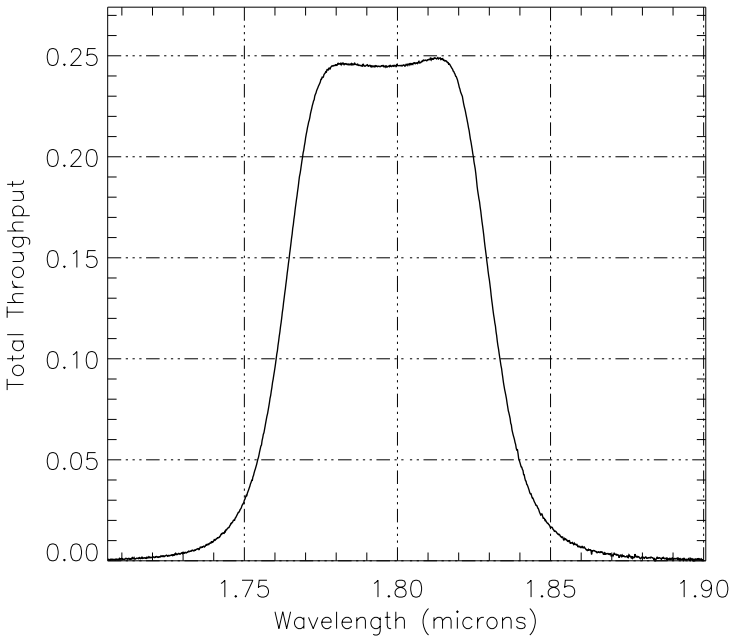

Camera 2, Filter F187N

Notes:
Paschen α.
See also "Camera 1, Filter F187N" and "Camera 3, Filter F187N".

Central wavelength:	1.8740 μm
Mean wavelength:	1.8740 μm
Peak wavelength:	1.8746 μm
Wavelength range:	1.864–1.884 μm
FWHM:	0.0194 μm
Maximum throughput:	24.585%
Central pixel fraction:	0.102

Figure A.23: NIC2 F187N Throughput

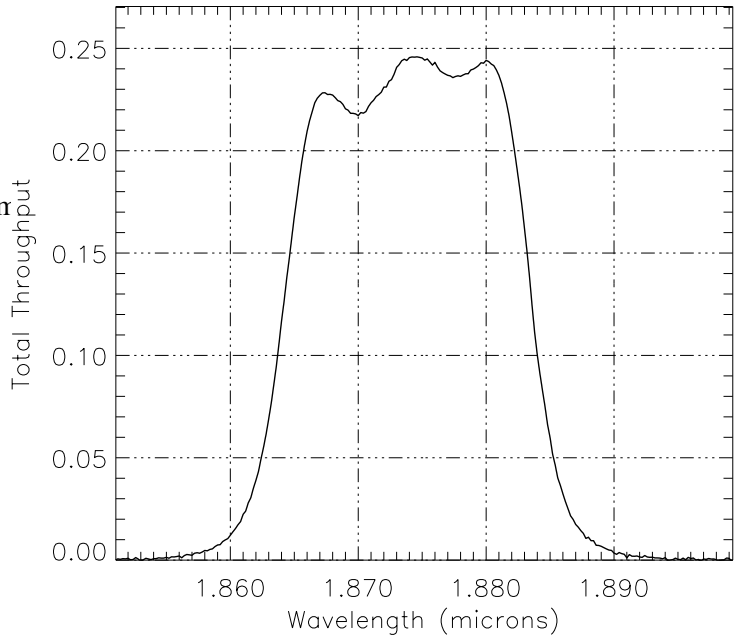

Camera 2, Filter F187W

Notes:
Thermal Background important.

Central wavelength:	1.8708 μm
Mean wavelength:	1.8723 μm
Peak wavelength:	1.8930 μm
Wavelength range:	1.75–2.0 μm
FWHM:	0. 2448 μm
Maximum throughput:	24.079%
Central pixel fraction:	0.103

Figure A.24: NIC2, F187W Throughput

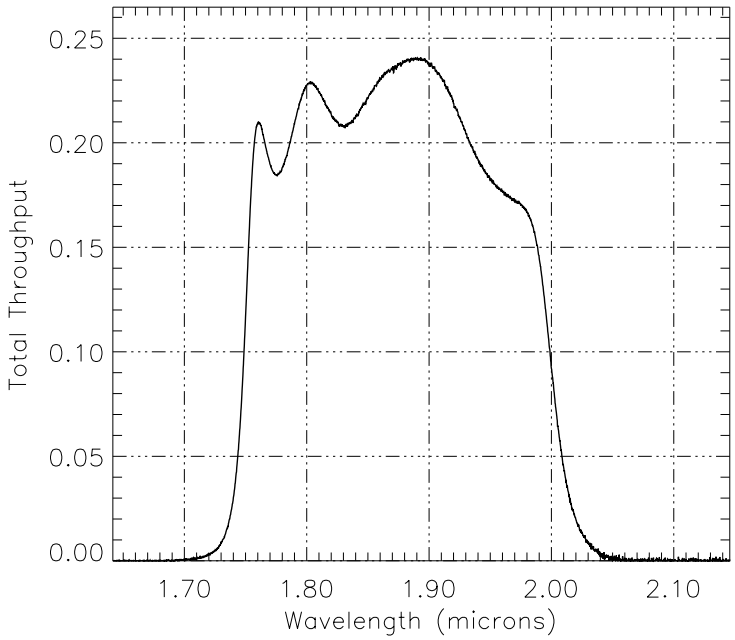

Camera 2, Filter F190N

Notes:
Paschen α continuum.
See also “Camera 1, Filter F190N” and “Camera 3, Filter F190N”,

Central wavelength:	1.9003 μm
Mean wavelength:	1.9003 μm
Peak wavelength:	1.9004 μm
Wavelength range:	1.892–1.908 μm
FWHM:	0. 0177μm
Maximum throughput:	25.697%
Central pixel fraction:	0.100

Figure A.25: NIC2, F190N Throughput

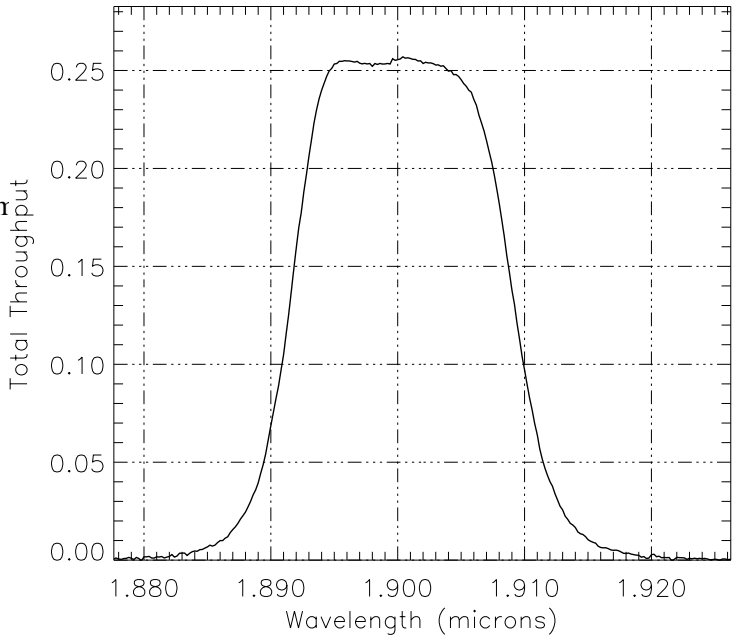

Camera 2, Filter F204M

Notes:
Methane band.
Thermal background important.

Central wavelength:	2.0353 μm
Mean wavelength:	2.0356 μm
Peak wavelength:	2.0634 μm
Wavelength range:	1.98–2.08 μm
FWHM:	0.1043 μm
Maximum throughput:	28.261%
Central pixel fraction:	0.089

Figure A.26: NIC2, F204M Throughput

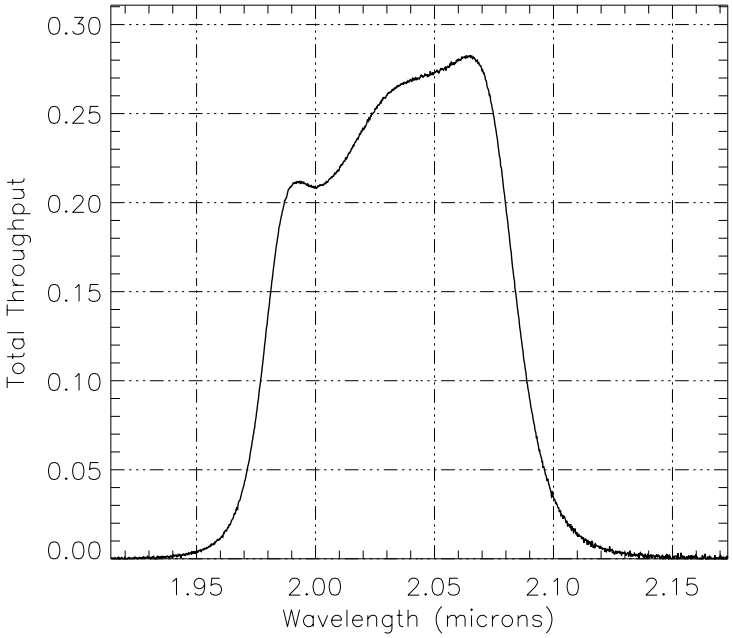

Camera 2, Filter F205W

Notes:
Thermal background important.

Central wavelength:	2.0658 μm
Mean wavelength:	2.0738 μm
Peak wavelength:	2.3150 μm
Wavelength range:	1.75–2.35 μm
FWHM:	0.5983 μm
Maximum throughput:	36.53%
Central pixel fraction:	0.090

Figure A.27: NIC2, F205W Throughput

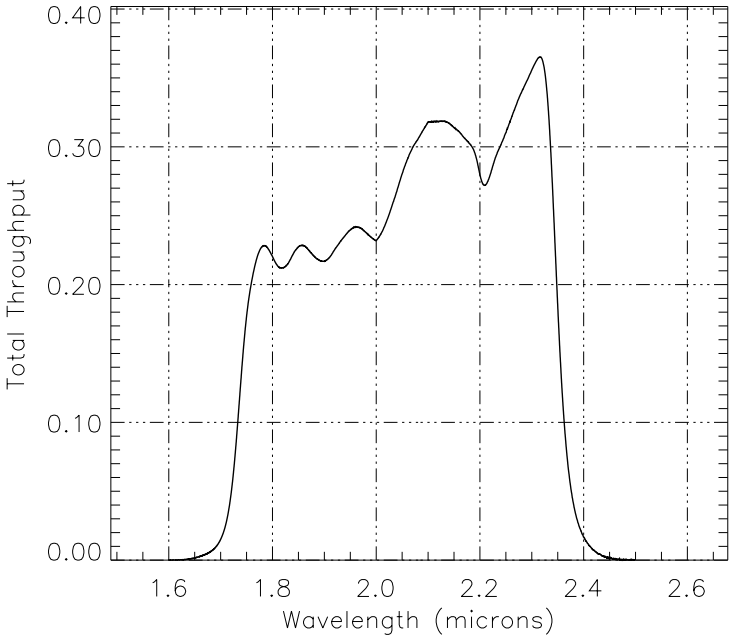

Camera 2, Filter F207M

Notes:
Thermal background important.

Central wavelength:	2.0821 μm
Mean wavelength:	2.0826 μm
Peak wavelength:	2.0672 μm
Wavelength range:	2.01–2.16 μm
FWHM:	0.1524 μm
Maximum throughput:	26.748%
Central pixel fraction:	0.085

Figure A.28: NIC2, F207M Throughput

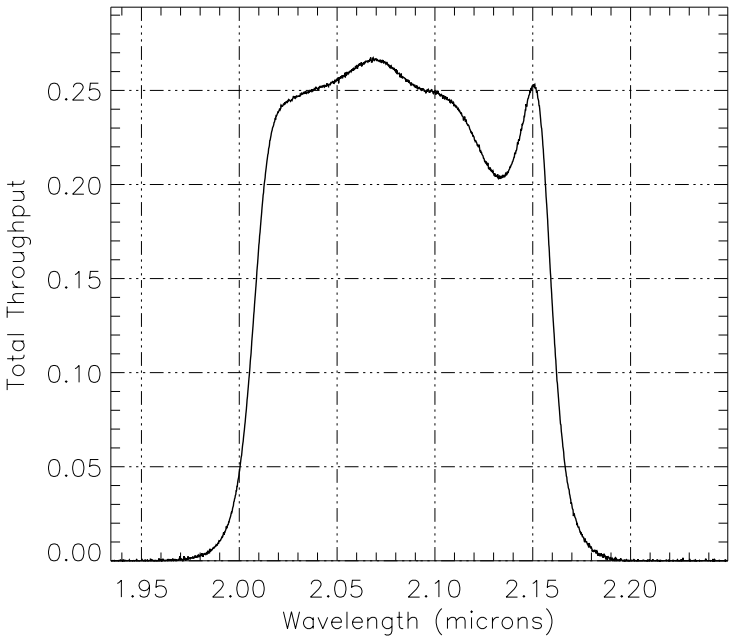

Camera 2, Filter F212N

Notes:
H_2 line.
Thermal background important.
See also “Camera 3, Filter F212N”.

Central wavelength:	2.1213 μm
Mean wavelength:	2.1213 μm
Peak wavelength:	2.1228 μm
Wavelength range:	2.111–2.132 μm
FWHM:	0.0208 μm
Maximum throughput:	27.421%
Central pixel fraction:	0.082

Figure A.29: NIC2, F212N Throughput

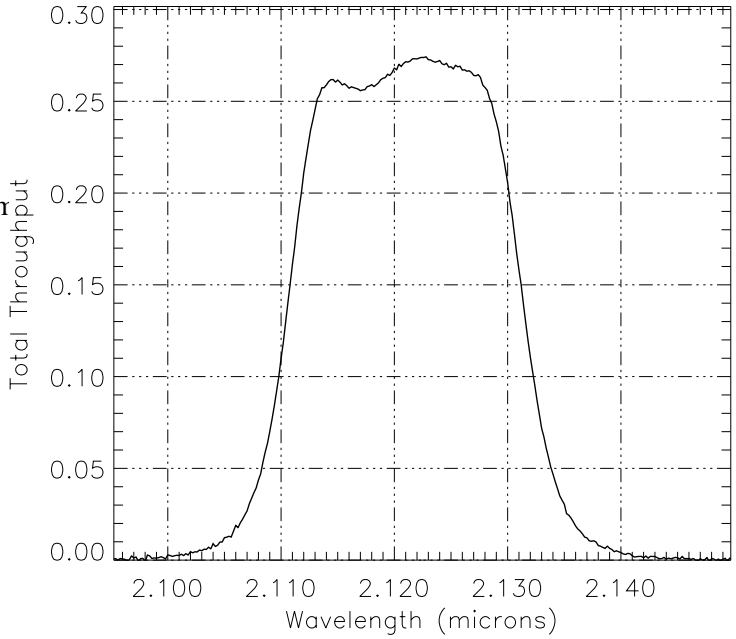

Camera 2, Filter F215N

Notes:
N_2 + Brackett γ continuum.
Thermal background important.

Central wavelength:	2.1487 μm
Mean wavelength:	2.1487 μm
Peak wavelength:	2.1562 μm
Wavelength range:	2.138–2.158 μm
FWHM:	0.0203 μm
Maximum throughput:	26.771%
Central pixel fraction:	0.081

Figure A.30: NIC2, F215N Throughput

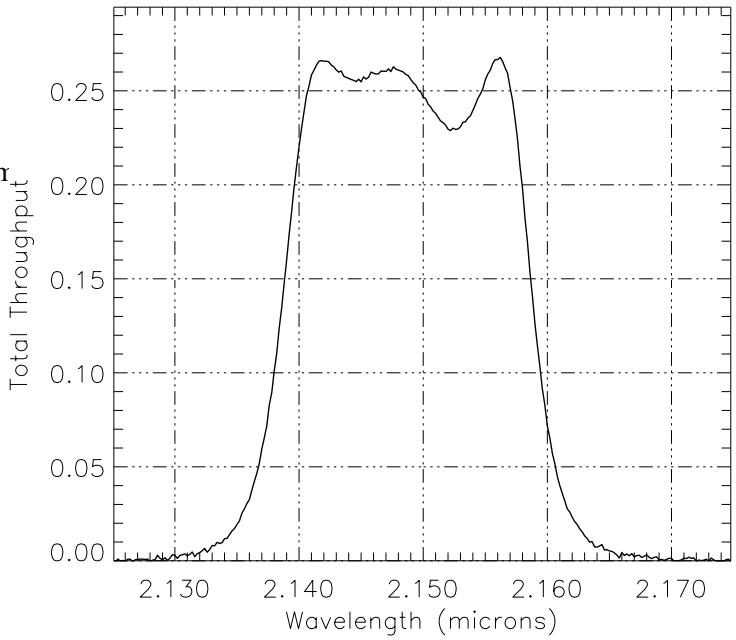

Camera 2, Filter F216N

Notes:
Brackett γ line.
Thermal background important.

Central wavelength:	2.1641 μm
Mean wavelength:	2.1641 μm
Peak wavelength:	2.1668 μm
Wavelength range:	2.154–2.174 μm
FWHM:	0.0212 μm
Maximum throughput:	27.783%
Central pixel fraction:	0.079

Figure A.31: NIC2, F216N Throughput

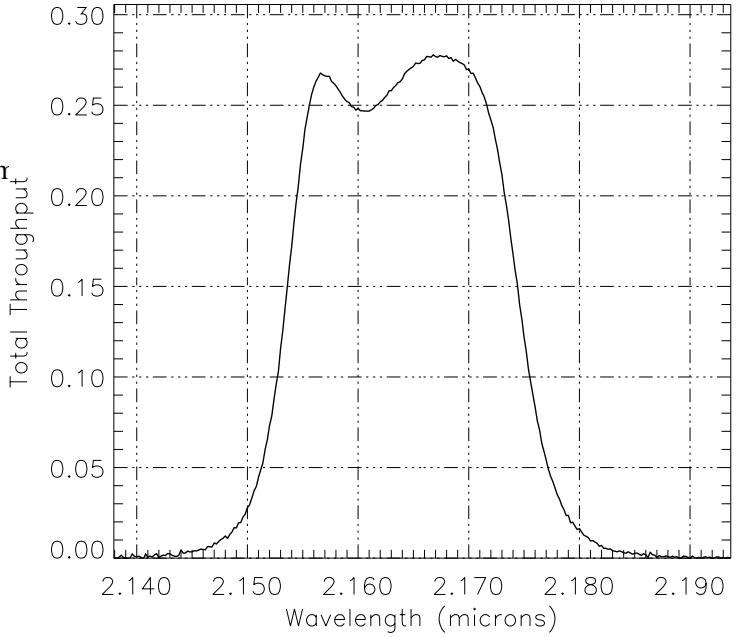

Camera 2, Filter F222M

Notes:
CO continuum.
Thermal background important.
See also “Camera 3, Filter F222M”.

Central wavelength:	2.2177 μm
Mean wavelength:	2.2183 μm
Peak wavelength:	2.1866 μm
Wavelength range:	2.15–2.29 μm
FWHM:	0.1455 μm
Maximum throughput:	28.186%
Central pixel fraction:	0.076

Figure A.32: NIC2, F222M Throughput

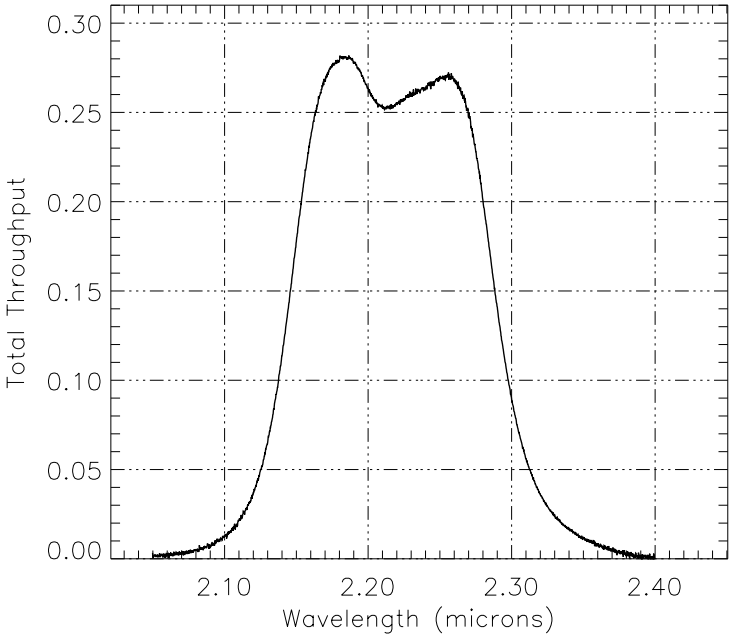

Camera 2, Filter F237M

Notes:
CO.
Thermal background important.
See also “Camera 3, Filter F240M”.

Central wavelength:	2.3692 μm
Mean wavelength:	2.3697 μm
Peak wavelength:	2.4338 μm
Wavelength range:	2.29–2.44 μm
FWHM:	0.1540 μm
Maximum throughput:	34.756%
Central pixel fraction:	0.067

Figure A.33: NIC2, F237M Throughput

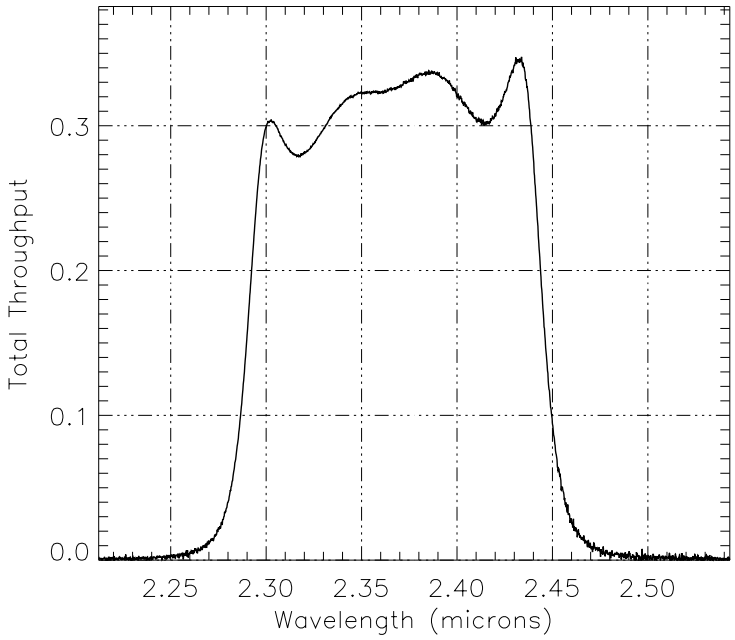

Camera 2, Polarizer POL0L

Notes:
See Table 5.2 for characteristics of POL120L and POL240L.

Central wavelength:	1.9999 μm
Mean wavelength:	2.0009 μm
Peak wavelength:	2.0750 μm
Wavelength range:	1.89–2.1 μm
FWHM:	0.2014 μm
Maximum throughput:	15.546%
Central pixel fraction:	0.092

Figure A.34: NIC2, Long Polarizer Throughput

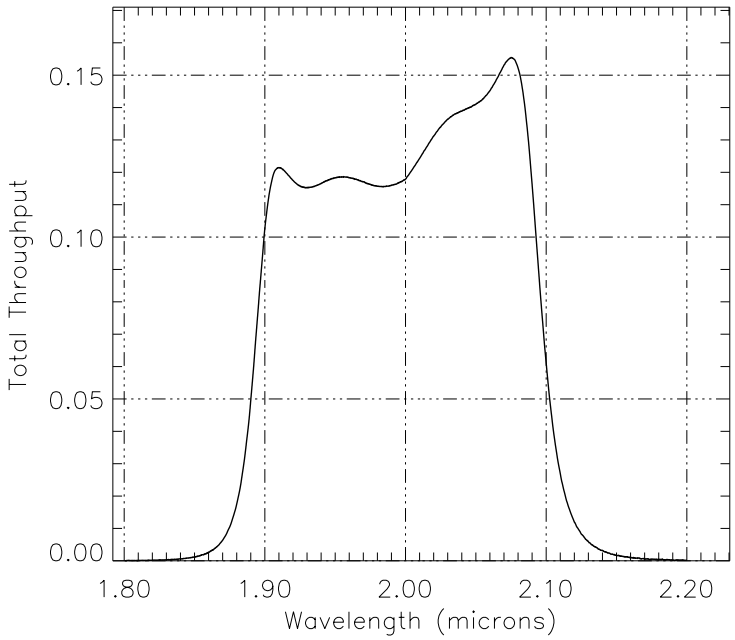

Camera 3, Filter F108N

Notes:
[He I] line.
See also “Camera 1, Filter F108N”.

Central wavelength:	1.0799 μm
Mean wavelength:	1.0800 μm
Peak wavelength:	1.0776 μm
Wavelength range:	1.075–1.085 μm
FWHM:	0.0100 μm
Maximum throughput:	9.7921%
Central pixel fraction:	0.485

Figure A.35: NIC3, F108N Throughput

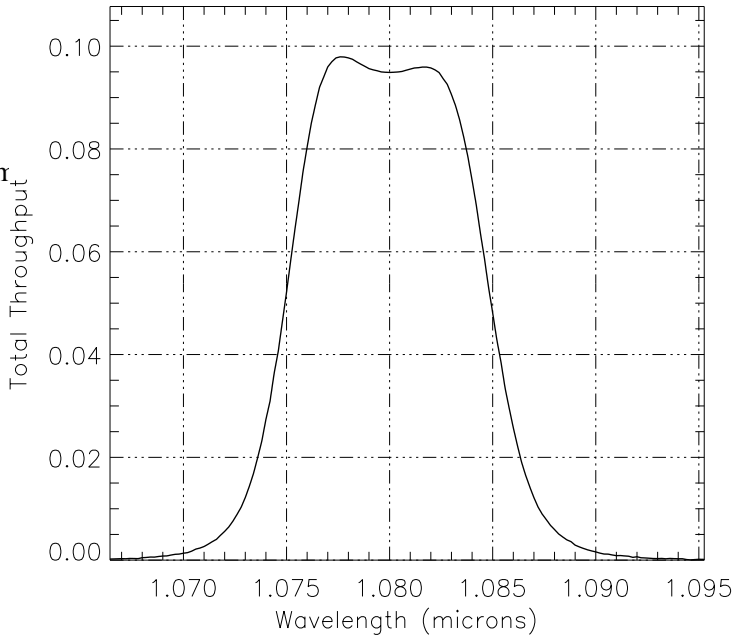

Camera 3, Filter F110W

Notes:
See also “Camera 1, Filter F110W” and “Camera 2, Filter F110W”.

Central wavelength:	1.1191 μm
Mean wavelength:	1.1316 μm
Peak wavelength:	1.3404 μm
Wavelength range:	0.8–1.4 μm
FWHM:	0.5880 μm
Maximum throughput:	15.336%
Central pixel fraction:	0.496

Figure A.36: NIC3, F110W Throughput

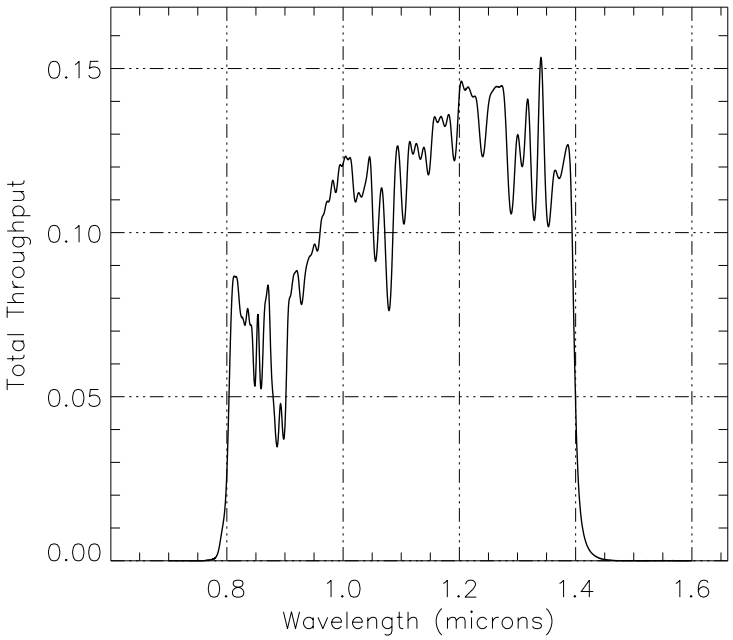

Camera 3, Filter F113N

Notes:
[He I] continuum.
See also “Camera 1, Filter F113N”.

Central wavelength:	1.1284 μm
Mean wavelength:	1.1284 μm
Peak wavelength:	1.1316 μm
Wavelength range:	1.122–1.133 μm
FWHM:	0.0114 μm
Maximum throughput:	11.591%
Central pixel fraction:	0.486

Figure A.37: NIC3, F113N Throughput

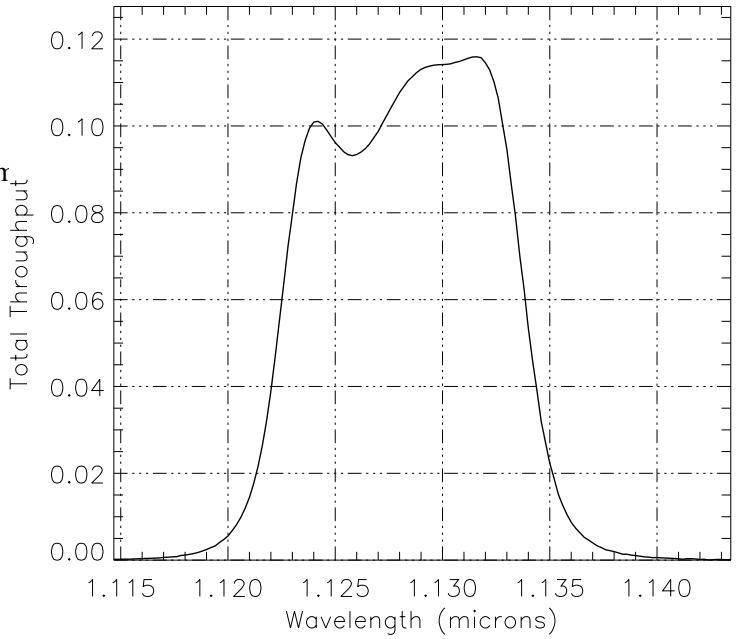

Camera 3, Filter F150W

Notes:
Grism B continuum.
Thermal background important.

Central wavelength:	1.5332 μm
Mean wavelength:	1.5509 μm
Peak wavelength:	1.7675 μm
Wavelength range:	1.1–1.9 μm
FWHM:	0.7738 μm
Maximum throughput:	24.536%
Central pixel fraction:	0.475

Figure A.38: NIC3, F150W Throughput

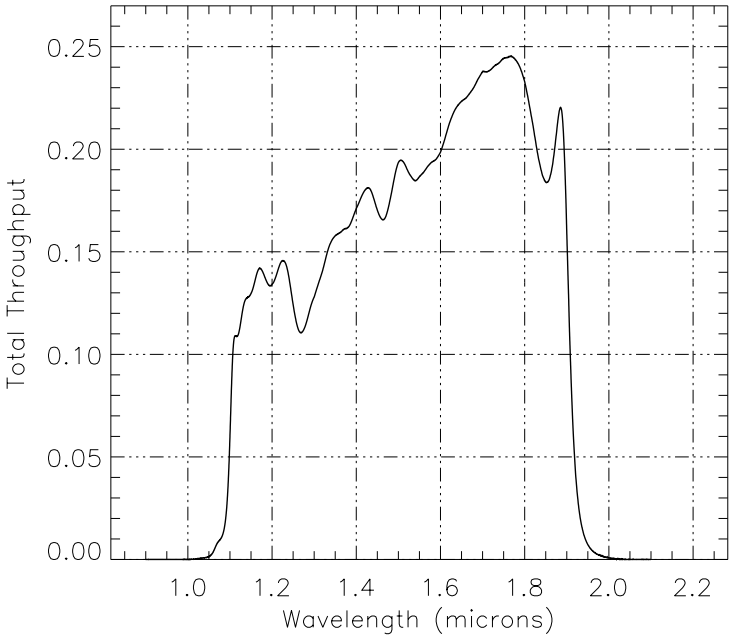

Camera 3, Filter F160W

Notes:
Minimum background.
See also “Camera 1, Filter F160W” and “Camera 2, Filter F160W”.

Central wavelength:	1.6036 μm
Mean wavelength:	1.6079 μm
Peak wavelength:	1.7725 μm
Wavelength range:	1.4–1.8 μm
FWHM:	0.3989 μm
Maximum throughput:	23.465%
Central pixel fraction:	0.474

Figure A.39: NIC3, F160W Throughput

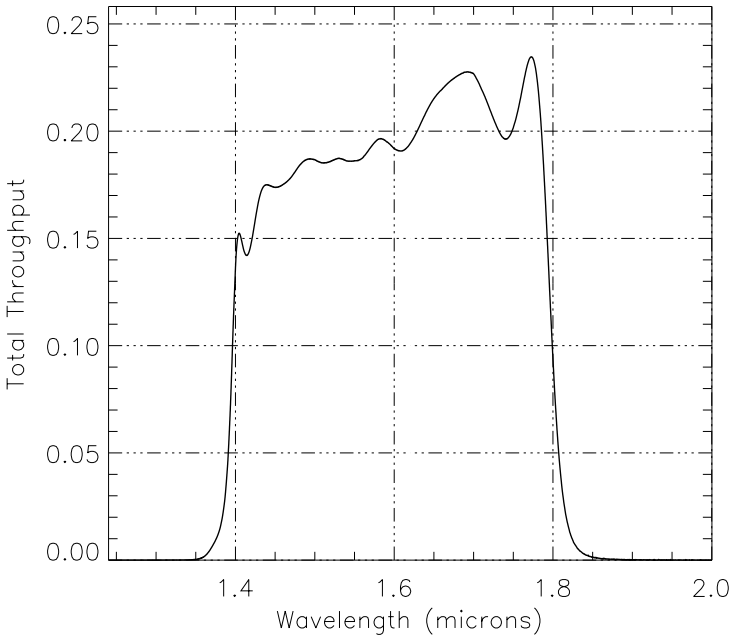

Camera 3, Filter F164N

Notes:
[Fe II] line.
See also “Camera 1, Filter F164N”.

Central wavelength:	1.6460 μm
Mean wavelength:	1.6460 μm
Peak wavelength:	1.6476 μm
Wavelength range:	1.637–1.655 μm
FWHM:	0.0173 μm
Maximum throughput:	20.234%
Central pixel fraction:	0.471

Figure A.40: NIC3, F164N Throughput

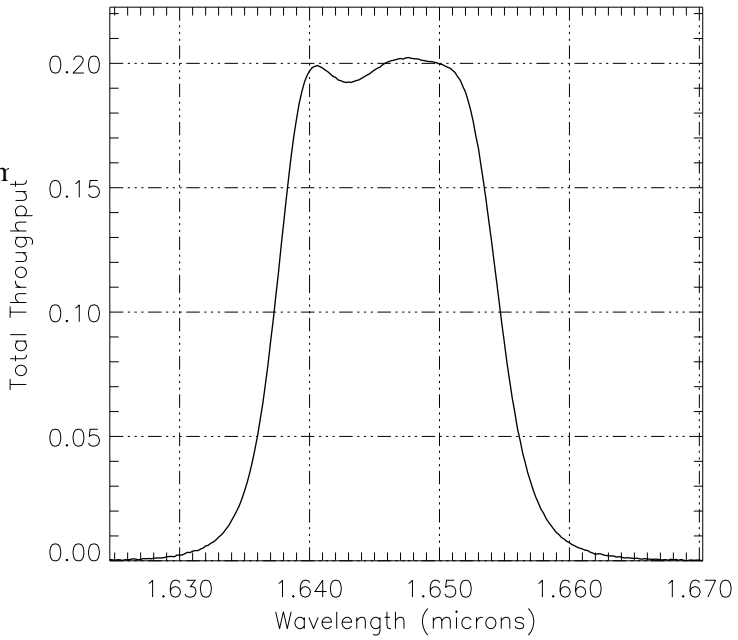

Camera 3, Filter F166N

Notes:
[Fe II] continuum.
See also “Camera 1, Filter F166N”.

Central wavelength:	1.6583 μm
Mean wavelength:	1.6583 μm
Peak wavelength:	1.6602 μm
Wavelength range:	1.649–1.667 μm
FWHM:	0.0169 μm
Maximum throughput:	20.419%
Central pixel fraction:	0.70

Figure A.41: NIC3, F166N Throughput

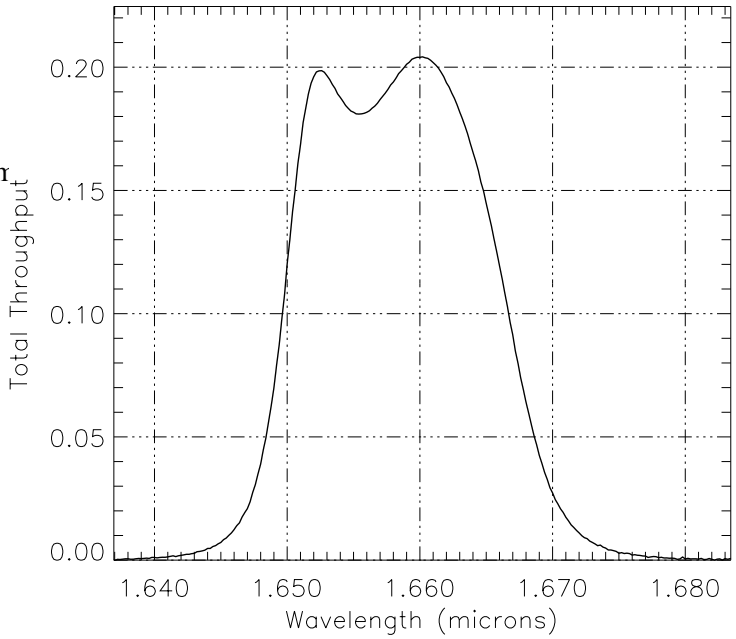

Camera 3, Filter F175W

Notes:
Thermal background important.

Central wavelength:	1.805 μm
Mean wavelength:	1.8333 μm
Peak wavelength:	2.2835 μm
Wavelength range:	1.2–2.3 μm
FWHM:	0.9137 μm
Maximum throughput:	31.531%
Central pixel fraction:	0.448

Figure A.42: NIC3, F175W Throughput

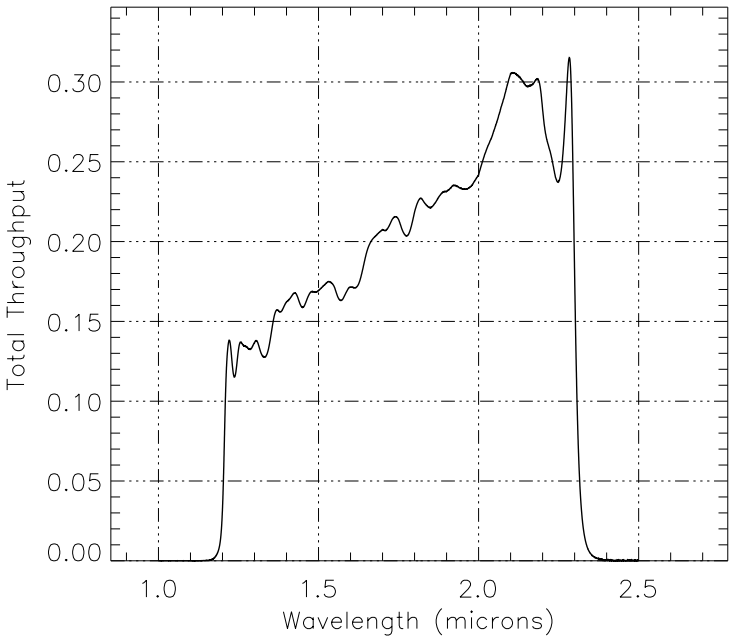

Camera 3, Filter F187N

Notes:
Paschen α line.
See also "Camera 1, Filter F187N" and "Camera 2, Filter F187N".

Central wavelength:	1.8748 μm
Mean wavelength:	1.8748 μm
Peak wavelength:	1.8756 μm
Wavelength range:	1.865–1.884 μm
FWHM:	0.0191 μm
Maximum throughput:	22.56%
Central pixel fraction:	0.439

Figure A.43: NIC3, F187N Throughput

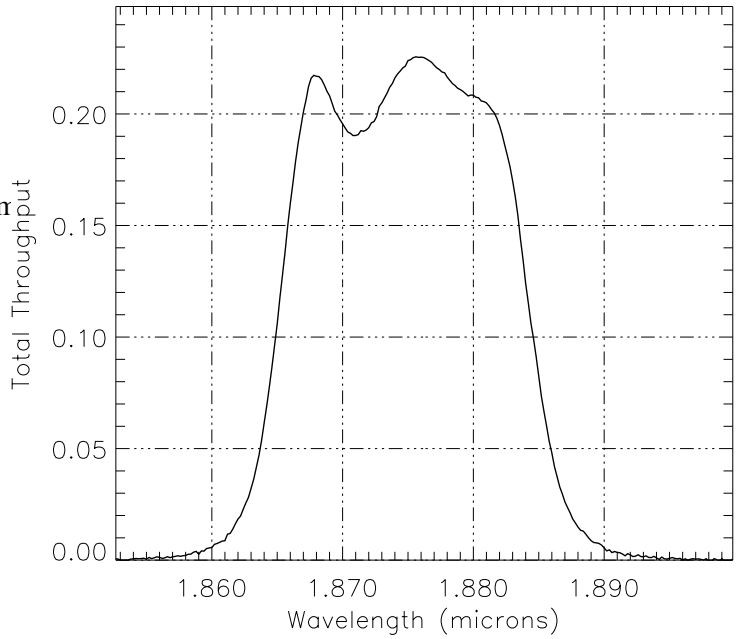

Camera 3, Filter F190N

Notes:
Paschen α continuum.
See also "Camera 1, Filter F190N" and "Camera 2, Filter F190N".

Central wavelength:	1.9003 μm
Mean wavelength:	1.9003 μm
Peak wavelength:	1.9004 μm
Wavelength range:	1.892–1.908 μm
FWHM:	0.0178 μm
Maximum throughput:	24.191%
Central pixel fraction:	0.434

Figure A.44: NIC3, F190N Throughput

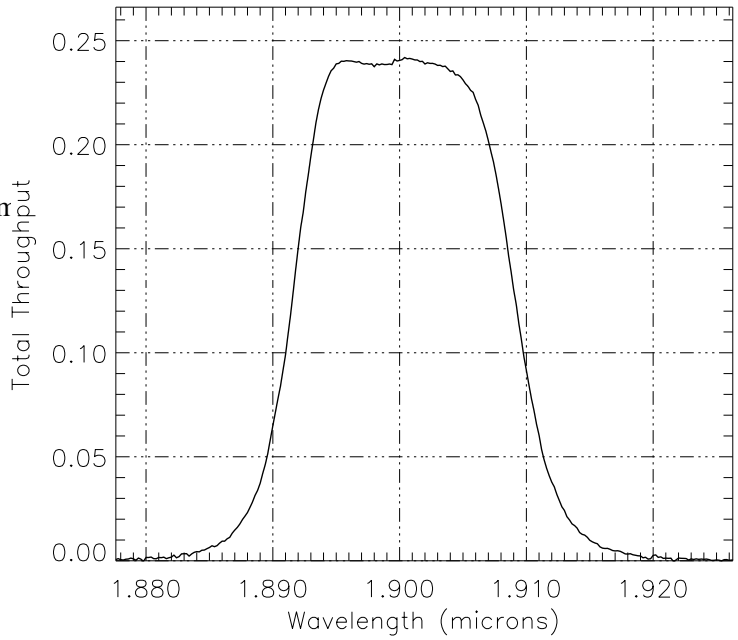

Camera 3, Filter F196N

Notes:
[Si VI].
Thermal background important.

Central wavelength:	1.9639 μm
Mean wavelength:	1.9639 μm
Peak wavelength:	1.9698 μm
Wavelength range:	1.954–1.974 μm
FWHM:	0.0190 μm
Maximum throughput:	24.834%
Central pixel fraction:	0.424

Figure A.45: NIC3, F196N Throughput

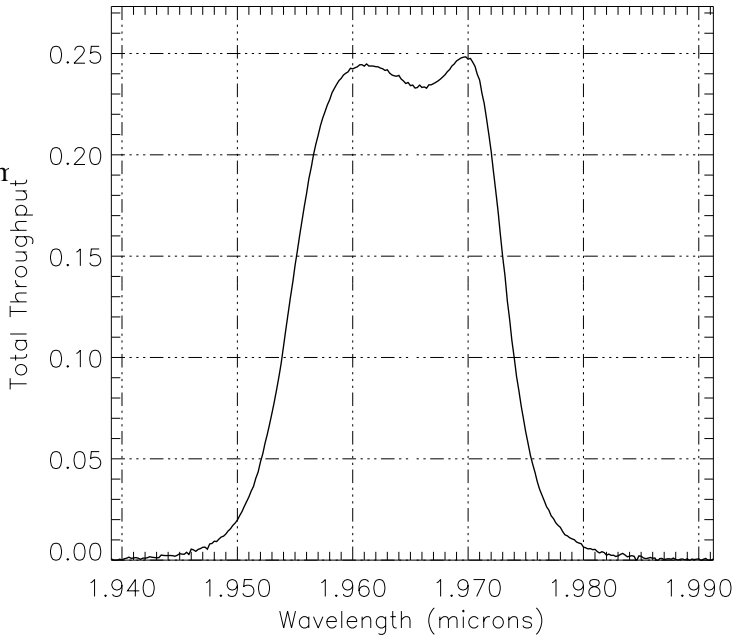

Camera 3, Filter F200N

Notes:
[Si VI] continuum.
Thermal background important.

Central wavelength:	1.9975 μm
Mean wavelength:	1.9975 μm
Peak wavelength:	2.0022 μm
Wavelength range:	1.986–2.007 μm
FWHM:	0.0209 μm
Maximum throughput:	24.012%
Central pixel fraction:	0.418

Figure A.46: NIC3, F200N Throughput

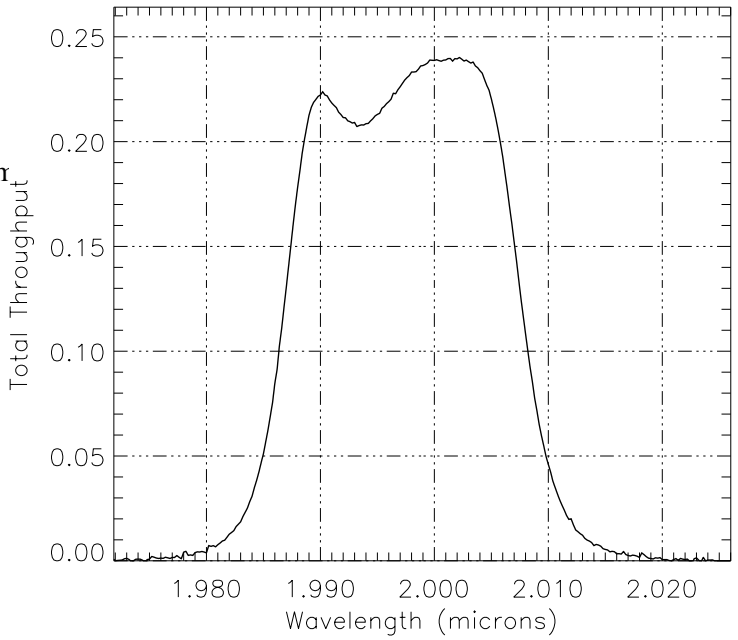

Camera 3, Filter F212N

Notes:
H_2 line.
Thermal background important.
See also “Camera 2, Filter F212N”.

Central wavelength:	2.1213 μm
Mean wavelength:	2.1213 μm
Peak wavelength:	2.1228 μm
Wavelength range:	2.111–2.132 μm
FWHM:	0.0208 μm
Maximum throughput:	24.611%
Central pixel fraction:	0.396

Figure A.47: NIC3, F212N Throughput

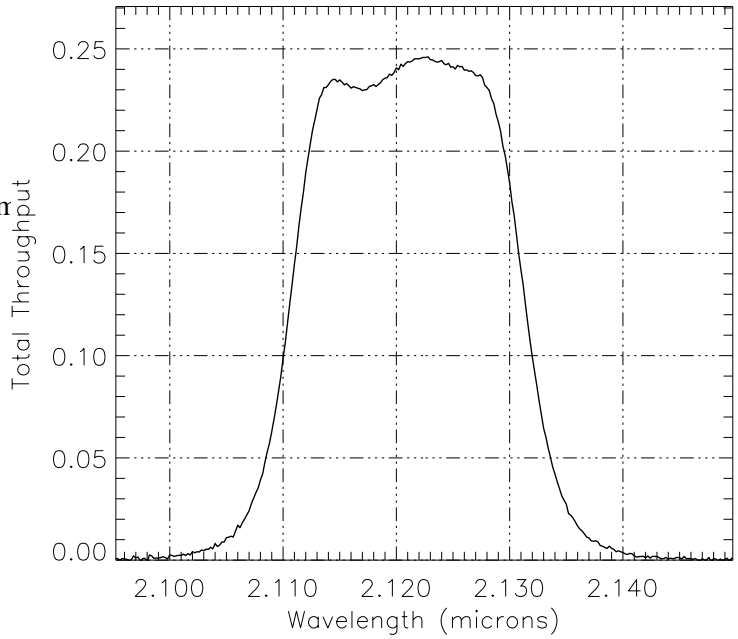

Camera 3, Filter F215N

Notes:
H_2 continuum.
Thermal background important.
See also “Camera 2, Filter F215N”.

Central wavelength:	2.1487 μm
Mean wavelength:	2.1487 μm
Peak wavelength:	2.1562 μm
Wavelength range:	2.138–2.158 μm
FWHM:	0.0202 μm
Maximum throughput:	23.867%
Central pixel fraction:	0.391

Figure A.48: NIC3, F215N Throughput

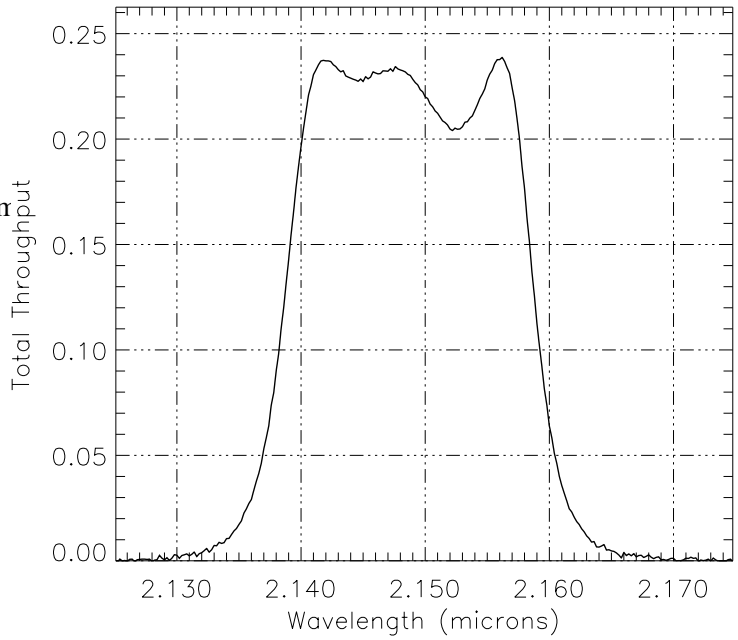

Camera 3, Filter F222M

Notes:
CO continuum.
Thermal background important.
See also “Camera 2, Filter F222M”.

Central wavelength:	2.2174 μm
Mean wavelength:	2.2180 μm
Peak wavelength:	2.1866 μm
Wavelength range:	2.15–2.28 μm
FWHM:	0.1451 μm
Maximum throughput:	25.088%
Central pixel fraction:	0.380

Figure A.49: NIC3, F222M Throughput

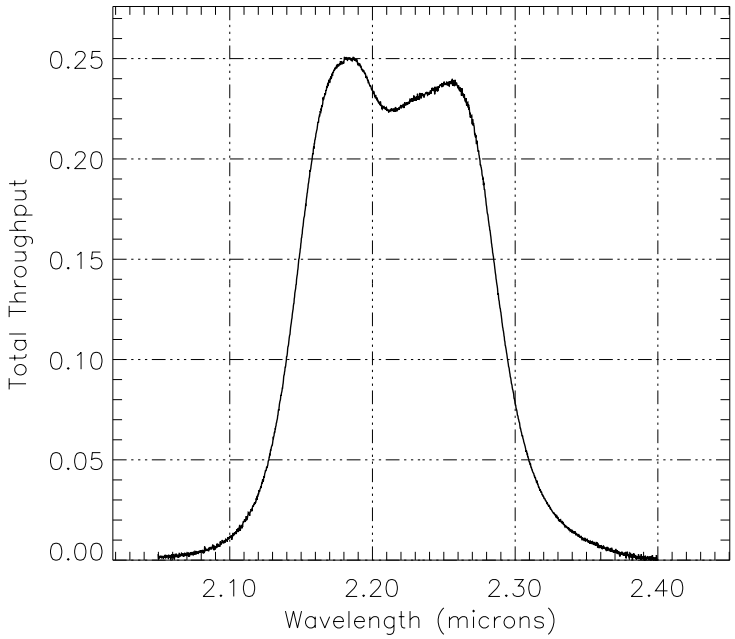

Camera 3, Filter F240M

Notes:
CO band.
Thermal background important.

Central wavelength:	2.3955 μm
Mean wavelength:	2.3963 μm
Peak wavelength:	2.4130 μm
Wavelength range:	2.3–2.5 μm
FWHM:	0.1951 μm
Maximum throughput:	29.697%
Central pixel fraction:	0.349

Figure A.50: NIC3, F240M Throughput

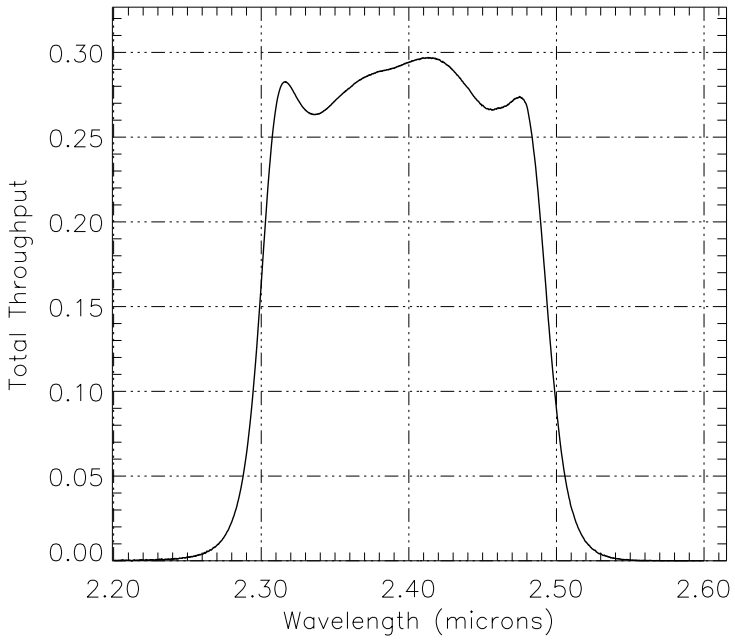

APPENDIX B:

Flux Units and Line Lists

In this appendix . . .

B.1 Infrared Flux Units

In the infrared, as in the optical, the means of reporting source brightnesses and the units employed have varied considerably. In recent years, however, magnitude systems have been used less frequently, and the most popular unit for expressing brightnesses, both for point source fluxes and surface brightnesses, is steadily becoming the Jansky. We have adopted the Jansky as the standard flux unit (and Jansky/arcsec^2 for surface brightness measurements) for NICMOS in our documentation and in observer-oriented software. Here we provide some simple formulae and tables to facilitate the conversion from other units into Jy ($1Jy = 10^{-26} W m^{-2} Hz^{-1}$). A Unit Conversion Tool is also available on the NICMOS WWW site, at the following URL:

http://www.stsci.edu/hst/nicmos/tools/conversion_form.html

B.1.1 Some History

Infrared astronomy really began in the 1960s, when the vast majority of astronomy was still carried out in the visual region. Flux measurements

were routinely reported in the UBV magnitude system, and to attempt to integrate IR astronomy into this system, Johnson (Ap.J., **134**, 69) defined the first IR magnitude system. This involved four new photometric bands, the J, K, L and M bands which were centered on wavelengths of 1.3, 2.2, 3.6 and 5.0 microns. These bands were defined not only by the filter bandpasses, but also by the wavebands of the 'windows' of high transmission through the atmosphere. In this system, all measurements were referred to the Sun, which was assumed to be a G2V star with an effective temperature of 5785K, and was taken to have a V–K color of roughly +2.2. From his own measurements in this system, Johnson determined Vega to have a K magnitude of +0.02 and K–L=+0.04.

Until the early 1980s IR astronomical observations were restricted to spectra or single channel photometry, and most photometry was reported in systems at least loosely based on Johnson's system. These systems added a new band at 1.6 microns known as the H band and two bands were developed in place of the one formerly defined by Johnson as the L band; a new definition of the L band centered on 3.4 microns, and a rather narrower band known as L' centered on 3.74 microns.

As the new science of infrared astronomy rapidly expanded its wavelength coverage, many new photometric bands were adopted, both for ground-based observations and for use by the many balloon- and rocket-borne observations and surveys. The differing constraints presented by these different environments for IR telescopes resulted in systems with disappointingly little commonality or overlap, and today the IR astronomer is left with a plethora of different systems to work with.

The IRAS survey results, which were published in 1986, presented observations made photometrically in four bands in the mid- and far-infrared, and mid-infrared spectra, and all were presented in units of Janskys, rather than defining yet another new magnitude system. Since then, IR data from many sites around the world have been increasingly commonly presented in Janskys (Jy), or in Jy/arcsec^2 in the case of surface brightness data. IRAS maps are often presented in units of MJy/steradian.

Ground-based mid-IR photometry is usually carried out using the N and Q photometric bands, which are themselves defined more by the atmospheric transmission than by any purely scientific regard. *IRAS*, freed of the constraints imposed by the atmosphere, adopted its own 12 micron and 25 micron bands, which were extremely broad and therefore offered high sensitivity. Similarly, NICMOS, being above the atmosphere, is not forced to adopt filter bandpasses (See Chapter 4 and Appendix A) like those used at ground-based observatories, but instead has filters constrained purely by the anticipated scientific demands. Thus in practice NICMOS does not have filters precisely matched to any of the standard ground-based photometric bands. The remaining sections contain simple formulae to convert between systems (magnitudes to Jy, etc.) and look up tables.

B.2 Formulae

B.2.1 Converting Between F_ν and F_λ

One Jansky (Jy) is defined as $10^{-26}\mathrm{Wm}^{-2}\mathrm{Hz}^{-1}$, so it is a unit of measurement of the spectral flux density, F_ν.

For F_ν in Jy, use the following formula:

$$F_\lambda = (\beta F_\nu)/\lambda^2$$

where λ is the wavelength in microns (μm), and β is a constant chosen from Table B.1 and depending on the units of F_λ. (This is simply derived, using the fact that $d\nu/d\lambda = c/\lambda^2$.)

Table B.1:Constants for Converting F_λ and F_ν.

F_λ measured in	β
$\mathrm{Wm}^{-2}\mu\mathrm{m}^{-1}$	3×10^{-12}
$\mathrm{Wcm}^{-2}\mu\mathrm{m}^{-1}$	3×10^{-16}
erg sec^{-1} cm^{-2} $\mu\mathrm{m}^{-1}$	3×10^{-9}
erg sec^{-1} cm^{-2} Å^{-1}	3×10^{-13}

Remember that $1\mathrm{W}=10^7\mathrm{erg\ sec}^{-1}$, and $1\mu\mathrm{m}=10^4\text{Å}$.

B.2.2 Conversion Between Fluxes and Magnitudes

The spectral flux density F_ν can be calculated from its magnitude as

$$F_\nu = 10^{-m/2.5}F_o$$

where m is the magnitude and F_o the zero-point flux for the given photometric band. We list the central wavelengths and zero-point fluxes for the more commonly encountered photometric bands below in Table B.2. The CIT system was originally based on Beckwith *et al.* (1976, Ap.J., **208**, 390); the UKIRT system is in fact based on the original CIT system, but with adjustments made largely owing to different filter bandpasses. It should be noted that for a given photometric band there will be small differences in the effective wavelength and zero-point flux from one

observatory to another, and for astronomical objects with radically different colors, so these figures can only be treated as approximate.

Table B.2:Effective Wavelengths and Zero-points for Photometric Bands.

Band	λ[μm]	F_o[Jy] (CIT)	F_o[Jy] (UKIRT)
V	0.56	3540	3540
R	0.70	2870	—
I	0.90	2250	—
J	1.25	1670	1600
H	1.65	980	1020
K	2.2	620	657
L	3.4	280	290
L'	3.74	—	252
M	4.8	150	163
N	10.1	37	39.8
Q	20.0	10	10.4

B.2.3 Conversion Between Surface Brightness Units

Surface brightnesses are generally measured in Janskys arcsec^{-2}, MJy steradian^{-1} or magnitudes arcsec^{-2}. If you have a surface brightness S_ν in MJy steradian^{-1}, then you can use:

$$S_\nu[\text{Jy arcsec}^{-2}] = S_\nu[\text{MJy ster}^{-1}] \times 2.35 \cdot 10^{-5}.$$

If you have S_ν in magnitudes arcsec^{-2}, you can simply use the formula and zero-points as given in the previous section for point sources.

B.3 Look-up Tables

In this section we provide look-up tables to facilitate rapid, approximate conversion between the different systems mentioned in the preceding section.

For both integrated source fluxes and surface brightnesses, we provide tables of conversions between systems at the wavelengths of the four commonly used photometric bands, which cover the NICMOS operating waveband of 0.8–2.5 microns. We are adopting here the CIT system defined in Table B.2.

Using Table B.3, it is possible to estimate the CIT magnitude corresponding to any flux in Jy by using the property that multiplying or dividing the flux by one hundred adds or subtracts five magnitudes.

Table B.3:F_ν to Magnitude Conversion.

F_ν [Jy]	I	J	H	K
10.0	5.88	5.56	4.98	4.48
8.0	6.12	5.80	5.22	4.72
6.0	6.44	6.11	5.53	5.04
5.0	6.63	6.31	5.73	5.23
4.0	6.88	6.55	5.97	5.48
3.0	7.19	6.86	6.29	5.79
2.5	7.39	7.06	6.48	5.99
2.0	7.63	7.30	6.73	6.23
1.5	7.94	7.62	7.04	6.54
1.25	8.14	7.81	7.24	6.74
1.0	8.38	8.06	7.48	6.98
0.8	8.62	8.30	7.72	7.22
0.6	8.94	8.61	8.03	7.54
0.5	9.13	8.81	8.23	7.73
0.4	9.38	9.05	8.47	7.98
0.3	9.69	9.36	8.79	8.29
0.25	9.89	9.57	8.98	8.49
0.2	10.13	9.8	9.23	8.73
0.15	10.44	10.12	9.54	9.04
0.125	10.64	10.31	9.74	9.24
0.1	10.88	10.56	9.98	9.48

Table B.4:I-Band Flux Conversion.

F_ν [Jy]	I [mag]	F_λ [$Wm^{-2}\mu m^{-1}$]	F_λ [$W\ cm^{-2}\mu m^{-1}$]	F_λ [$erg\ s^{-1}\ cm^{-2}\ Å^{-1}$]
2250	0.0	8.32×10^{-9}	8.32×10^{-13}	8.32×10^{-10}
894	1.0	3.312×10^{-9}	3.312×10^{-13}	3.312×10^{-10}
356	2.0	1.319×10^{-9}	1.319×10^{-13}	1.319×10^{-10}
142	3.0	5.25×10^{-10}	5.25×10^{-14}	5.25×10^{-11}
56.4	4.0	2.09×10^{-10}	2.09×10^{-14}	2.09×10^{-11}
22.5	5.0	8.32×10^{-11}	8.32×10^{-15}	8.32×10^{-12}
8.94	6.0	3.312×10^{-11}	3.312×10^{-15}	3.312×10^{-12}
3.56	7.0	1.319×10^{-11}	1.319×10^{-15}	1.319×10^{-12}
1.42	8.0	5.25×10^{-12}	5.25×10^{-16}	5.25×10^{-13}
0.564	9.0	2.09×10^{-12}	2.09×10^{-16}	2.09×10^{-13}
0.225	10.0	8.32×10^{-13}	8.32×10^{-17}	8.32×10^{-14}
0.0894	11.0	3.312×10^{-13}	3.312×10^{-17}	3.312×10^{-14}
0.0356	12.0	1.319×10^{-13}	1.319×10^{-17}	1.319×10^{-14}
0.0142	13.0	5.25×10^{-14}	5.25×10^{-18}	5.25×10^{-15}
0.00564	14.0	2.09×10^{-14}	2.09×10^{-18}	2.09×10^{-15}
0.00225	15.0	8.32×10^{-15}	8.32×10^{-19}	8.32×10^{-16}
8.94×10^{-4}	16.0	3.312×10^{-15}	3.312×10^{-19}	3.312×10^{-16}
3.56×10^{-4}	17.0	1.319×10^{-15}	1.319×10^{-19}	1.319×10^{-16}
1.42×10^{-4}	18.0	5.25×10^{-16}	5.25×10^{-20}	5.25×10^{-17}
5.64×10^{-5}	19.0	2.09×10^{-16}	2.09×10^{-20}	2.09×10^{-17}
2.25×10^{-5}	20.0	8.32×10^{-17}	8.32×10^{-21}	8.32×10^{-18}
8.94×10^{-6}	21.0	3.312×10^{-17}	3.312×10^{-21}	3.312×10^{-18}
3.56×10^{-6}	22.0	1.319×10^{-17}	1.319×10^{-21}	1.319×10^{-18}
1.42×10^{-6}	23.0	5.25×10^{-18}	5.25×10^{-22}	5.25×10^{-19}
5.64×10^{-7}	24.0	2.09×10^{-18}	2.09×10^{-22}	2.09×10^{-19}
2.25×10^{-7}	25.0	8.32×10^{-19}	8.32×10^{-23}	8.32×10^{-20}
8.94×10^{-8}	26.0	3.312×10^{-19}	3.312×10^{-23}	3.312×10^{-20}

Table B.5:J-band Flux Conversion.

F_ν [Jy]	J [mag]	F_λ [$Wm^{-2}\mu m^{-1}$]	F_λ [$Wcm^{-2}\mu m^{-1}$]	F_λ [erg $cm^{-2}s^{-1}Å^{-1}$]
1670	0.0	3.21×10^{-9}	3.21×10^{-13}	3.21×10^{-10}
665	1.0	1.28×10^{-9}	1.28×10^{-13}	1.28×10^{-10}
265	2.0	5.08×10^{-10}	5.08×10^{-14}	5.08×10^{-11}
106	3.0	2.02×10^{-10}	2.02×10^{-14}	2.02×10^{-11}
42.0	4.0	8.06×10^{-11}	8.06×10^{-15}	8.06×10^{-12}
16.7	5.0	3.21×10^{-11}	3.21×10^{-15}	3.21×10^{-12}
6.65	6.0	1.28×10^{-11}	1.28×10^{-15}	1.28×10^{-12}
2.65	7.0	5.08×10^{-12}	5.08×10^{-16}	5.08×10^{-13}
1.06	8.0	2.02×10^{-12}	2.02×10^{-16}	2.02×10^{-13}
0.420	9.0	8.06×10^{-13}	8.06×10^{-17}	8.06×10^{-14}
0.167	10.0	3.21×10^{-13}	3.21×10^{-17}	3.21×10^{-14}
0.0665	11.0	1.28×10^{-13}	1.28×10^{-17}	1.28×10^{-14}
0.0265	12.0	5.08×10^{-14}	5.08×10^{-18}	5.08×10^{-15}
0.0106	13.0	2.02×10^{-14}	2.02×10^{-18}	2.02×10^{-15}
0.00420	14.0	8.06×10^{-15}	8.06×10^{-19}	8.06×10^{-16}
0.00167	15.0	3.21×10^{-15}	3.21×10^{-19}	3.21×10^{-16}
6.65×10^{-4}	16.0	1.28×10^{-15}	1.28×10^{-19}	1.28×10^{-16}
2.65×10^{-4}	17.0	5.08×10^{-16}	5.08×10^{-20}	5.08×10^{-17}
1.06×10^{-4}	18.0	2.02×10^{-16}	2.02×10^{-20}	2.02×10^{-17}
4.20×10^{-5}	19.0	8.06×10^{-17}	8.06×10^{-21}	8.06×10^{-18}
1.67×10^{-5}	20.0	3.21×10^{-17}	3.21×10^{-21}	3.21×10^{-18}
6.65×10^{-6}	21.0	1.28×10^{-17}	1.28×10^{-21}	1.28×10^{-18}
2.65×10^{-6}	22.0	5.08×10^{-18}	5.08×10^{-22}	5.08×10^{-19}
1.06×10^{-6}	23.0	2.02×10^{-18}	2.02×10^{-22}	2.02×10^{-19}
4.20×10^{-7}	24.0	8.06×10^{-19}	8.06×10^{-23}	8.06×10^{-20}
1.67×10^{-7}	25.0	3.21×10^{-19}	3.21×10^{-23}	3.21×10^{-20}
6.65×10^{-8}	26.0	1.28×10^{-19}	1.28×10^{-23}	1.28×10^{-20}

Table B.6:H-band Flux Conversion.

F_ν [Jy]	H [mag]	F_λ [$Wm^{-2}\mu m^{-1}$]	F_λ [$Wcm^{-2}\mu m^{-1}$]	F_λ [erg $s^{-1}cm^{-2}Å^{-1}$]
980	0.0	1.08×10^{-9}	1.08×10^{-13}	1.08×10^{-10}
390	1.0	4.3×10^{-10}	4.3×10^{-14}	4.3×10^{-11}
155	2.0	1.712×10^{-10}	1.712×10^{-14}	1.712×10^{-11}
61.8	3.0	6.814×10^{-11}	6.814×10^{-15}	6.814×10^{-12}
24.6	4.0	2.713×10^{-11}	2.713×10^{-15}	2.713×10^{-12}
9.8	5.0	1.08×10^{-11}	1.08×10^{-15}	1.08×10^{-12}
3.9	6.0	4.3×10^{-12}	4.3×10^{-16}	4.3×10^{-13}
1.55	7.0	1.712×10^{-12}	1.712×10^{-16}	1.712×10^{-13}
0.618	8.0	6.814×10^{-13}	6.814×10^{-17}	6.814×10^{-14}
0.246	9.0	2.713×10^{-13}	2.713×10^{-17}	2.713×10^{-14}
0.098	10.0	1.08×10^{-13}	1.08×10^{-17}	1.08×10^{-14}
0.039	11.0	4.3×10^{-14}	4.3×10^{-18}	4.3×10^{-15}
0.0155	12.0	1.712×10^{-14}	1.712×10^{-18}	1.712×10^{-15}
0.00618	13.0	6.814×10^{-15}	6.814×10^{-19}	6.814×10^{-16}
0.00246	14.0	2.713×10^{-15}	2.713×10^{-19}	2.713×10^{-16}
9.8×10^{-4}	15.0	1.08×10^{-15}	1.08×10^{-19}	1.08×10^{-16}
3.9×10^{-4}	16.0	4.3×10^{-16}	4.3×10^{-20}	4.3×10^{-17}
1.55×10^{-4}	17.0	1.712×10^{-16}	1.712×10^{-20}	1.712×10^{-17}
6.18×10^{-5}	18.0	6.814×10^{-17}	6.814×10^{-21}	6.814×10^{-18}
2.46×10^{-5}	19.0	2.713×10^{-17}	2.713×10^{-21}	2.713×10^{-18}
9.8×10^{-6}	20.0	1.08×10^{-17}	1.08×10^{-21}	1.08×10^{-18}
3.9×10^{-6}	21.0	4.3×10^{-18}	4.3×10^{-22}	4.3×10^{-19}
1.55×10^{-6}	22.0	1.712×10^{-18}	1.712×10^{-22}	1.712×10^{-19}
6.18×10^{-7}	23.0	6.814×10^{-19}	6.814×10^{-23}	6.814×10^{-20}
2.46×10^{-7}	24.0	2.713×10^{-19}	2.713×10^{-23}	2.713×10^{-20}
9.8×10^{-8}	25.0	1.08×10^{-19}	1.08×10^{-23}	1.08×10^{-20}
3.9×10^{-8}	26.0	4.3×10^{-20}	4.3×10^{-24}	4.3×10^{-21}

Table B.7:K-band Flux Conversion.

F_ν [Jy]	K [mag]	F_λ [$Wm^{-2}\mu m^{-1}$]	F_λ [$Wcm^{-2}\mu m^{-1}$]	F_λ [erg $s^{-1}cm^{-2}Å^{-1}$]
620	0.0	3.84×10^{-10}	3.84×10^{-14}	3.84×10^{-11}
247	1.0	1.53×10^{-10}	1.53×10^{-14}	1.53×10^{-11}
98.3	2.0	6.09×10^{-11}	6.09×10^{-15}	6.09×10^{-12}
39.1	3.0	2.43×10^{-11}	2.43×10^{-15}	2.43×10^{-12}
15.6	4.0	9.66×10^{-12}	9.66×10^{-16}	9.66×10^{-13}
6.20	5.0	3.84×10^{-12}	3.84×10^{-16}	3.84×10^{-13}
2.47	6.0	1.53×10^{-12}	1.53×10^{-16}	1.53×10^{-13}
0.983	7.0	6.09×10^{-13}	6.09×10^{-17}	6.09×10^{-14}
0.391	8.0	2.43×10^{-13}	2.43×10^{-17}	2.43×10^{-14}
0.156	9.0	9.66×10^{-14}	9.66×10^{-18}	9.66×10^{-15}
0.0620	10.0	3.84×10^{-14}	3.84×10^{-18}	3.84×10^{-15}
0.0247	11.0	1.53×10^{-14}	1.53×10^{-18}	1.53×10^{-15}
0.00983	12.0	6.09×10^{-15}	6.09×10^{-19}	6.09×10^{-16}
0.00391	13.0	2.43×10^{-15}	2.43×10^{-19}	2.43×10^{-16}
0.00156	14.0	9.66×10^{-16}	9.66×10^{-20}	9.66×10^{-17}
6.20×10^{-4}	15.0	3.84×10^{-16}	3.84×10^{-20}	3.84×10^{-17}
2.47×10^{-4}	16.0	1.53×10^{-16}	1.53×10^{-20}	1.53×10^{-17}
9.83×10^{-5}	17.0	6.09×10^{-17}	6.09×10^{-21}	6.09×10^{-18}
3.91×10^{-5}	18.0	2.43×10^{-17}	2.43×10^{-21}	2.43×10^{-18}
1.56×10^{-5}	19.0	9.66×10^{-18}	9.66×10^{-22}	9.66×10^{-19}
6.20×10^{-6}	20.0	3.84×10^{-18}	3.84×10^{-22}	3.84×10^{-19}
2.47×10^{-6}	21.0	1.53×10^{-18}	1.53×10^{-22}	1.53×10^{-19}
9.83×10^{-7}	22.0	6.09×10^{-19}	6.09×10^{-23}	6.09×10^{-20}
3.91×10^{-7}	23.0	2.43×10^{-19}	2.43×10^{-23}	2.43×10^{-20}
1.56×10^{-7}	24.0	9.66×10^{-20}	9.66×10^{-24}	9.66×10^{-21}
6.20×10^{-8}	25.0	3.84×10^{-20}	3.84×10^{-24}	3.84×10^{-21}
2.47×10^{-8}	26.0	1.53×10^{-20}	1.53×10^{-24}	1.53×10^{-21}

Table B.8:Surface Brightness Conversion.

mag / arcsec^2	I-Band		J-Band		H-Band		K-Band	
	Jy / arcsec^2	MJy / steradian	Jy / arcsec^2	MJy / steradian	Jy / arcsec^2	MJy / steradian	Jy / arcsec^2	MJy / steradian
0.0	0.6251	2.66×10^{4}	0.4630	1.97×10^{4}	0.2726	1.16×10^{4}	0.1720	7320
1.0	0.2491	1.06×10^{4}	0.1847	7860	0.1083	4610	0.0688	2930
2.0	0.0989	4210	0.0736	3130	0.0430	1830	0.0273	1160
3.0	0.0395	1680	0.0294	1250	0.0172	730	0.0109	462
4.0	0.0157	667	0.0117	496	0.0068	291	0.0043	184
5.0	0.0062	266	0.0046	197	0.0027	116	0.0172	732
6.0	0.0025	106	0.0018	78.6	0.0011	46.1	6.88×10^{-4}	29.3
7.0	9.89×10^{-4}	42.1	7.36×10^{-4}	31.3	4.30×10^{-4}	18.3	2.73×10^{-4}	11.6
8.0	3.95×10^{-4}	16.8	2.94×10^{-4}	12.5	1.72×10^{-4}	7.3	1.09×10^{-4}	4.62
9.0	1.57×10^{-4}	6.67	1.17×10^{-4}	4.96	6.84×10^{-5}	2.91	4.32×10^{-5}	1.84
10.0	6.25×10^{-5}	2.66	4.63×10^{-5}	1.97	2.73×10^{-5}	1.16	1.72×10^{-5}	0.732
11.0	2.49×10^{-5}	1.06	1.85×10^{-5}	0.786	1.08×10^{-5}	0.461	6.88×10^{-6}	0.293
12.0	9.89×10^{-6}	0.421	7.36×10^{-6}	0.313	4.30×10^{-6}	0.183	2.73×10^{-7}	0.116
13.0	3.95×10^{-6}	0.168	2.94×10^{-6}	0.125	1.72×10^{-6}	0.073	1.09×10^{-7}	0.0462
14.0	1.57×10^{-6}	0.0667	1.17×10^{-6}	0.0496	6.84×10^{-7}	0.0291	4.32×10^{-8}	0.0184
15.0	6.25×10^{-7}	0.0266	4.63×10^{-7}	0.0197	2.73×10^{-7}	0.0116	1.72×10^{-8}	0.00732
16.0	2.49×10^{-7}	0.0106	1.85×10^{-7}	0.00786	1.08×10^{-7}	0.00461	6.88×10^{-9}	0.00293
17.0	9.89×10^{-8}	0.00421	7.36×10^{-8}	0.00313	4.30×10^{-8}	0.00183	2.73×10^{-9}	0.00116
18.0	3.95×10^{-8}	0.00168	2.94×10^{-8}	0.00125	1.72×10^{-8}	7.3×10^{-4}	1.09×10^{-9}	4.62×10^{-4}
19.0	1.57×10^{-8}	6.67×10^{-4}	1.17×10^{-8}	4.96×10^{-4}	6.84×10^{-9}	2.91×10^{-4}	4.32×10^{-10}	1.84×10^{-4}
20.0	6.25×10^{-9}	2.66×10^{-4}	4.63×10^{-9}	1.97×10^{-4}	2.73×10^{-9}	1.16×10^{-4}	1.72×10^{-10}	7.32×10^{-5}
21.0	2.49×10^{-9}	1.06×10^{-4}	1.85×10^{-9}	7.86×10^{-5}	1.08×10^{-9}	4.61×10^{-5}	6.88×10^{-11}	2.93×10^{-5}
22.0	9.89×10^{-10}	4.21×10^{-5}	7.36×10^{-10}	3.13×10^{-5}	4.30×10^{-10}	1.83×10^{-5}	2.73×10^{-11}	1.16×10^{-5}
23.0	3.95×10^{-10}	1.68×10^{-5}	2.94×10^{-10}	1.25×10^{-5}	1.72×10^{-10}	7.3×10^{-6}	1.09×10^{-11}	4.62×10^{-6}
24.0	1.57×10^{-10}	6.67×10^{-6}	1.17×10^{-10}	4.96×10^{-6}	6.84×10^{-11}	2.91×10^{-6}	4.32×10^{-12}	1.84×10^{-6}
25.0	6.25×10^{-11}	2.66×10^{-6}	4.63×10^{-11}	1.97×10^{-6}	2.73×10^{-11}	1.16×10^{-6}	1.72×10^{-12}	7.32×10^{-7}
26.0	2.49×10^{-11}	1.06×10^{-6}	1.85×10^{-11}	7.86×10^{-7}	1.08×10^{-11}	4.61×10^{-7}	6.88×10^{-13}	2.93×10^{-7}

B.4 Examples

1. Given a source with a flux of 0.9mJy at 1350Å, convert this flux to erg $s^{-1}cm^{-2}Å^{-1}$. From section 3, Table B.1, we see that the conversion constant β is 3×10^{-13} and the wavelength is 1350Å = 0.135μm. Thus:
$$F_\lambda = (3 \cdot 10^{-13} \times 9 \cdot 10^{-4})/0.135^2 = 1.48 \cdot 10^{-14} \text{erg s}^{-1} \text{ cm}^{-2} Å^{-1}$$

2. Given a V magnitude of 15.6, and knowledge that V–K=2.5 in the UKIRT system, estimate the flux in Jy at K. Since V–K=2.5 we know that K=13.1. From Table B.2, the zero-point flux in the UKIRT system for K is 657Jy. Thus the 2.2μm flux is:
$$F_\nu = 10^{-13.1/2.5} \times 657 = 3.8 \cdot 10^{-3} \text{Jy}$$

3. Given a surface brightness of 21.1 magnitudes arcsec^{-2} at J, convert this into Jy arcsec^{-2}. Taking the zero-point for the J band from Table B.2, we determine that the surface brightness is:
$$10^{-21.1/2.5} \times 1670 = 6.06 \cdot 10^{-6} \text{Jy arcsec}^{-2}$$

4. Given a flux at 0.9μm of 2.3×10^{-7}Jy, estimate the I magnitude. 2.3×10^{-7}Jy is less than 2.3×10^{-1}Jy by three powers of a hundred, or 15 magnitudes. From Table B.3 we see that 0.25Jy is equivalent to an I-band magnitude of 9.89. Thus 2.3×10^{-7} is roughly 15 magnitudes fainter than this, or of order:
$$I = 24.9$$

B.5 Infrared Line Lists

We present here lists of some of the more important atomic and molecular lines in the infrared. It is by no means exhaustive.

Table B.9:Recombination Lines of Atomic Hydrogen: Paschen Series[1].

Transition (N_u - N_l)	Vacuum Wavelength (microns)	Vacuum Frequency (cm^{-1})	I/I(Hβ) $T_e=N_e=10^4$
4-3	1.8756	5531.55	0.332
5-3	1.2822	7799.33	0.162
6-3	1.0941	9139.8	0.0901
7-3	1.0052	9948.1	

1. Intensities from Hummer & Storey, MNRAS 224, 801.

Table B.10: Recombination Lines of Atomic Hydrogen: Brackett Series.

Transition (N_u-N_l)	Vacuum Wavelength (microns)	Frequency (cm^{-1})	I/I(Hβ) $T_e=10^4$
5-4	4.5225	2467.765	0.0777
6-4	2.6259	3808.25	
7-4	2.1661	4616.61	0.0275
8-4	1.9451	5141.14	0.0181
9-4	1.8181	5500.8	0.0126
10-4	1.7367	5758.1	0.00909
11-4	1.6811	5948.45	0.00679
12-4	1.6412	6093.22	0.00521
13-4	1.6114	6205.9	0.00409
14-4	1.5885	6295.3	0.00327
15-4	1.5705	6367.4	0.00266
16-4	1.5561	6426.4	0.00220
17-4	1.5443	6475.3	0.00184
18-4	1.5346	6516.3	0.00156
19-4	1.5265	6551.0	0.00133
20-4	1.5196	6580.7	0.00116
series limit	1.459	6855.	

Table B.11:HeI and HeII Lines.

ID	Transition	λ (μm)
HeI	7F-3D,3Fo-3D	1.0031
HeI	7F-3D,1Fo-1D	1.0034
HeII	14-6	1.0049
HeII	5-4	1.0133
HeI	6D-3P,3dD-3Po	1.0314
HeII	13-6	1.0422
HeI	6S-3P,3S-3Po	1.0668
HeI	2P-2S,3Po-3S,GU=3	1.0832
HeI	2P-2S,3Po-3P,GU=1	1.0832
HeI	2P-2S,3Po-3S,GU=5	1.0833
HeI	2P-2S,3Po-3S,GU=9	1.0833
HeI	6P-3D,1Po-1d	1.0905
HeI	6F-3D,3Fo-3D	1.0916
HeI	6F-3D,1Fo-1D	1.0920
HeII	12-6	1.0938
HeI	6P-3D,3Po-3D	1.0997
HeI	5P-3S,1Po-1S	1.1016
HeI	6D-3P,1D-1Po	1.1048
HeII	7LIMIT	1.1164
HeI	6S-3P,1S-1Po	1.1229
HeII	7-5	1.1628
HeII	11-6	1.1677
HeI	5D-3P,3D-3Po	1.1972
HeII	21-7	1.2256
HeII	22-7	1.2418
HeI	4P-3S,3Po-3S	1.2531
HeII	20-7	1.2719
HeI	5P-3D,1Po-1D	1.2759
HeI	5F-3D,3Fo-3D	1.2789
HeII	10-6	1.2817
HeI	5S-3P,3S-3Po	1.2850

Table B.11:HeI and HeII Lines. (Continued)

ID	Transition	λ (μm)
HeII	19-7	1.2914
HeI	5D-3P,1D-1Po	1.2971
HeI	5F-3D,1Fo-1D	1.2976
HeI	5P-3D,3Po-3D	1.2988
HeII	18-7	1.3150
HeI	5S-3P,1S-1Po	1.3415
HeII	17-7	1.3442
HeII	15-7	1.4273
HeII	8LIMIT	1.4578
HeII	9-6	1.4765
HeII	14-7	1.4882
HeI	4P-3S,1Po-1S	1.5088
HeII	13-7	1.5719
HeII	25-8	1.6241
HeII	24-8	1.6400
HeII	23-8	1.6584
HeII	22-8	1.6799
HeII	12-7	1.6926
HeI	4D-3P,3D-3Po	1.7007
HeII	21-8	1.7053
HeII	20-8	1.7355
HeII	19-8	1.7717
HeII	18-8	1.8167
HeII	9LIMIT	1.8450
HeI	4P-3D,1Po-1D	1.8561
HeII	6-5	1.8639
HeI	4F-3D,3Fo-3D	1.8691
HeI	4F-3D,1Fo-1d	1.8702
HeII	17-8	1.8725
HeII	8-6	1.8753
HeII	11-7	1.8770

Table B.11:HeI and HeII Lines. (Continued)

ID	Transition	λ (μm)
HeI	8S-4P,3S-3Po	1.9068
HeI	4D-3P,1D-1Po	1.9094
HeI	4P-3D,3Po-3D	1.9548
HeII	15-8	2.0379
HeI	6P-4S,3Po-3S	2.0430
HeI	2P-2S,1Po-1S	2.0587
HeI	4S-3P,3S-3Po	2.1126
HeI	3pP-4sS	2.1132
HeI	4S-3P,1S-1Po	2.1138
HeII	25-9	2.1195
HeII	24-9	2.1469
HeI	7S-4P,3S-3Po	2.1500
HeI	7F-4D,3Fo-3D	2.1614
HeI	4dD-7fF	2.1617
HeI	7F-4D,1Fo-1D	2.1623
HeII	14-8	2.1653
HeI	4-7	2.166
HeII	23-9	2.1786
HeI	7D-4P,1D-1Po	2.1847
HeII	10-7	2.1891
HeII	22-9	2.2155
HeI	7S-4P,1S-1Po	2.2290
HeII	21-9	2.2601
HeII	10LIMIT	2.2778
HeI	6P-4S,1Po-1S	2.3069
HeII	20-9	2.314
HeII	13-8	2.348
HeII	19-9	2.3788
HeII	18-9	2.4606
HeI	6D-4P,3D-3Po	2.4734

Table B.12: CO Vibration-rotation Band-heads[1].

Transition (N_u-N_l)	$^{12}C^{16}O$ Vacuum Wavelength (microns)	Frequency (cm^{-1})	$^{13}C^{16}O$ Vacuum Wavelength (microns)	Frequency (cm^{-1})
2-0	2.2935	4360.1	2.3448	4264.7
3-1	2.3227	4305.4	2.3739	4212.4
4-2	2.3535	4250.8	2.4037	4160.3
5-3	2.3829	4196.5	2.4341	4108.3
6-4	2.4142	4142.2	2.4652	4056.4
7-5	2.4461	4088.2	2.4971	4004.7
8-6	2.4787	4034.3		
9-7	2.5122	3980.5		
3-0	1.5582	6417.8		
4-1	1.5780	6337.2		
5-2	1.5982	6257.2		
6-3	1.6187	6177.7		
7-4	1.6397	6098.8		
8-5	1.6610	6020.5		

1. All of the delta v = 2 bandheads occur near J=50.

Table B.13:Important H_2 Lines[1].

Line Name		Wavel (μm)	Freq (cm^{-1})	g(J)	E_{upper} (K)	A ($10e^{-7}s$)	LTE I(line)/I(1-0S(1))			
							1000K	2000K	3000K	4000K
1-0	S(0)	2.2235	4497.41	5	6471	2.53	0.27	0.21	0.19	0.19
1-0	S(1)	2.1218	4712.91	21	6956	3.47	1.00	1.00	1.00	1.00
1-0	S(2)	2.0338	4917.01	9	7584	3.98	0.27	0.37	0.42	0.44
1-0	S(3)	1.9576	5108.40	33	8365	4.21	0.51	1.02	1.29	1.45
1-0	S(4)	1.8920	5282.52	13	9286	4.19	0.082	0.26	0.39	0.47
1-0	S(5)	1.8358	5447.25	45	10341	3.96	0.096	0.52	0.91	1.21
1-0	S(6)	1.7880	5592.9	17	11522	3.54	0.010	0.10	0.21	0.31
1-0	S(7)	1.7480	5720.8	57	12817	2.98	0.008	0.15	0.40	0.65
1-0	S(8)	1.7147	5831.9	21	14221	2.34	0.001	0.022	0.074	0.14
1-0	S(9)	1.6877	5925.1	69	15722	1.68	0.025	0.11	0.22	
1-0	S(10)	1.6665	6000.0	25	17311	1.05	0.003	0.015	0.034	
1-0	S(11)	1.6504	6059.0	81	18979	0.53	0.002	0.014	0.037	
1-0	Q(1)	2.4066	4155.25	9	6149	4.29	1.05	0.70	0.61	0.57
1-0	Q(2)	2.4134	4143.47	5	6471	3.03	0.30	0.23	0.22	0.21
1-0	Q(3)	2.4237	4125.87	21	6956	2.78	0.70	0.70	0.70	0.70
1-0	Q(4)	2.4375	412.57	9	7586	2.65	0.15	0.21	0.23	0.24
1-0	Q(5)	2.4548	4073.72	33	8365	2.55	0.24	0.49	0.62	0.70
1-0	Q(6)	2.4756	4039.5	13	9286	2.45	0.036	0.12	0.17	0.21
1-0	Q(7)	2.5001	3999.9	45	10341	2.34	0.042	0.11	0.40	0.53
3-2	S(0)	2.5014	3997.73	5	17387	3.88	0.001	0.007	0.016	
3-2	S(1)	2.3864	4190.33	21	17818	5.14	0.006	0.035	0.087	
3-2	S(2)	2.2870	4372.49	9	18386	5.63	0.002	0.014	0.037	
3-2	S(3)	2.2014	4542.57	33	19086	5.63	0.006	0.043	0.12	
3-2	S(4)	2.1280	4699.32	13	19912	5.22	0.001	0.012	0.036	
3-2	S(5)	2.0656	4841.3	45	20856	4.50	0.003	0.023	0.088	
3-2	S(6)	2.0130	4967.7	17	21911	3.57	0.006	0.021		
3-2	S(7)	1.9692	5078.1	57	23069	2.54	0.001	0.010	0.038	
4-3	S(3)	2.3446	4265.4	21						
4-3	S(4)	2.2668	4411.5	9						
4-3	S(5)	2.201	4543.5	33						

Table B.13:Important H_2 Lines[1]. (Continued)

Line Name		Wavel (μm)	Freq (cm^{-1})	g(J)	E_{upper} (K)	A ($10e^{-7}s$)	LTE I(line)/I(1-0S(1))			
							1000K	2000K	3000K	4000K
5-4	S(5)	2.3555	4245.4	45						
5-4	S(7)	2.2510	4442.5	57						
2-0	S(0)	1.2383	8075.3	5	12095	1.27	0.001	0.012	0.028	0.043
2-0	S(1)	1.1622	8604.2	21	12550	1.90	0.004	0.061	0.15	0.23
2-0	S(2)	1.1382	8785.5	9	13150	2.38	0.001	0.025	0.070	0.12
2-0	S(3)	1.1175	8948.6	33	13890	2.77	0.002	0.074	0.24	0.43
2-0	S(4)	1.0998	9092.4	13	14764	3.07	0.021	0.078	0.15	
2-0	S(5)	1.0851	9215.5	45	15763	3.28	0.001	0.048	0.21	0.44
2-9	Q(1)	1.2383	8075.3	9	11789	1.94	0.003	0.037	0.082	0.12
2-0	Q(2)	1.2419	8051.9	5	12095	1.38	0.001	0.012	0.029	0.045
2-0	Q(3)	1.2473	8017.2	21	12550	1.29	0.002	0.039	0.098	0.24
2-0	Q(4)	1.2545	7971.1	9	13150	1.27	0.001	0.012	0.033	0.056
2-0	Q(5)	1.2636	7913.3	33	13890	1.23	0.001	0.024	0.093	0.17
2-0	O(2)	1.2932	7732.6	1	11635	3.47	0.001	0.008	0.016	0.024
2-0	O(3)	1.3354	7488.3	9	11789	1.61	0.003	0.028	0.063	0.094
2-0	O(4)	1.3817	7237.5	5	12095	1.03	0.001	0.008	0.020	0.030
2-0	O(5)	1.4322	6982.5	21	12550	0.698	0.001	0.018	0.046	0.074

1. Energy levels calculated using Dabrowski & Herzberg, Can J Phys 62, 1639 (1984). Einstein coefficients from Turner *et al*. ApJ Suppl 35, 281 (1977).

APPENDIX C:

Bright Object Mode

In this appendix . . .

C.1 Bright Object Mode

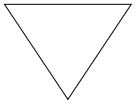

The use of this read-out mode is recommended only for the purpose of determining the centroid of very bright targets which must be acquired under the coronagraphic spot, when any other configuration (e.g., `MULTIACCUM` ***or*** `ACCUM` ***with narrow-band filters) saturates the detector. Any other use is strongly discouraged, because of the strong non-linearity of this mode.***

The time taken to read through a quadrant on the array sets a fundamental limit on the fastest electron collection rate which can be achieved by resetting all the pixels. An inherent consequence of the methods of operating the NICMOS array detectors in the `MULTIACCUM` and `ACCUM` modes is, therefore, that there is a minimum possible exposure time, 0.203 seconds (~ 0.6 seconds for `ACCUM`), set by the time required to read the array. Although the detector arrays are multiplexed by division into four quadrants, each pixel in a 128 × 128 pixel quadrant must be sampled in some order (note that there is no transfer of charge as is done in a CCD). For a very bright object, the time between the reset of a pixel and its final read is sufficiently long that the pixel saturates.

The solution adopted to this problem for NICMOS is the provision of a *bright object mode* which enables targets to be observed which are ~200

times brighter than is possible in the other modes without saturating. In BRIGHTOBJ mode, an ACCUM sequence of operations is performed on *one* pixel in each quadrant at a time. That is, the pixel is reset, read, integrated, and read again with the difference between the final and initial readouts being stored as the measured signal and the interval between the reads being the exposure time. This process is repeated sequentially for all pixels in each quadrant. Users can think of this as integrating on a single pixel at a time. The smallest integration time which can be used is 1.024 milliseconds, the longest 0.261 seconds. Figure C.1 illustrates the operation of bright object mode. Initially, the entire detector is reset. Then the first pixel (solid shading) in each quadrant is read. After the requested integration time, the first pixel in each quadrant is read again. Then the second pixel in each quadrant is reset, then read, integrated, and read again. The process continues until all 16,384 pixels in each quadrant have been read twice, separated by the integration time. The image down linked is made up of the difference between the two reads of each pixel.

The time required to take a BRIGHTOBJ mode exposure can be rather long. Since photons are only collected in one pixel per quadrant at a time, the time associated with obtaining the frame is $10.0 + (EXPTIME \times 16384)$ where *EXPTIME* is the integration time per pixel (i.e. the observation time is approximately $(128^2) \times$ the exposure time). For example, if an integration time of 0.1 seconds is used to observe a bright target then the actual time required to complete the observation would be around 27 minutes! This means that, allowing for acquisition time, only two such exposures can be obtained in a single target visibility period. However, it is not always so serious. In the case of Jupiter, for example, the integration times required per pixel are only of the order of milliseconds and so the total integration time will only be around 20 seconds.

The longest exposure time which is possible in BRIGHTOBJ mode is 0.261 seconds, requiring 4278 seconds in total. Thus it is possible, in the worst case, for a single BRIGHTOBJ mode exposure to use more than an orbit. In general, observers are strongly advised to consider the trade-off between relatively long BRIGHTOBJ mode exposures (which take the longest time) and short MULTIACCUM mode exposures (using a narrow filter).

Figure C.1: Bright Object Mode Operation

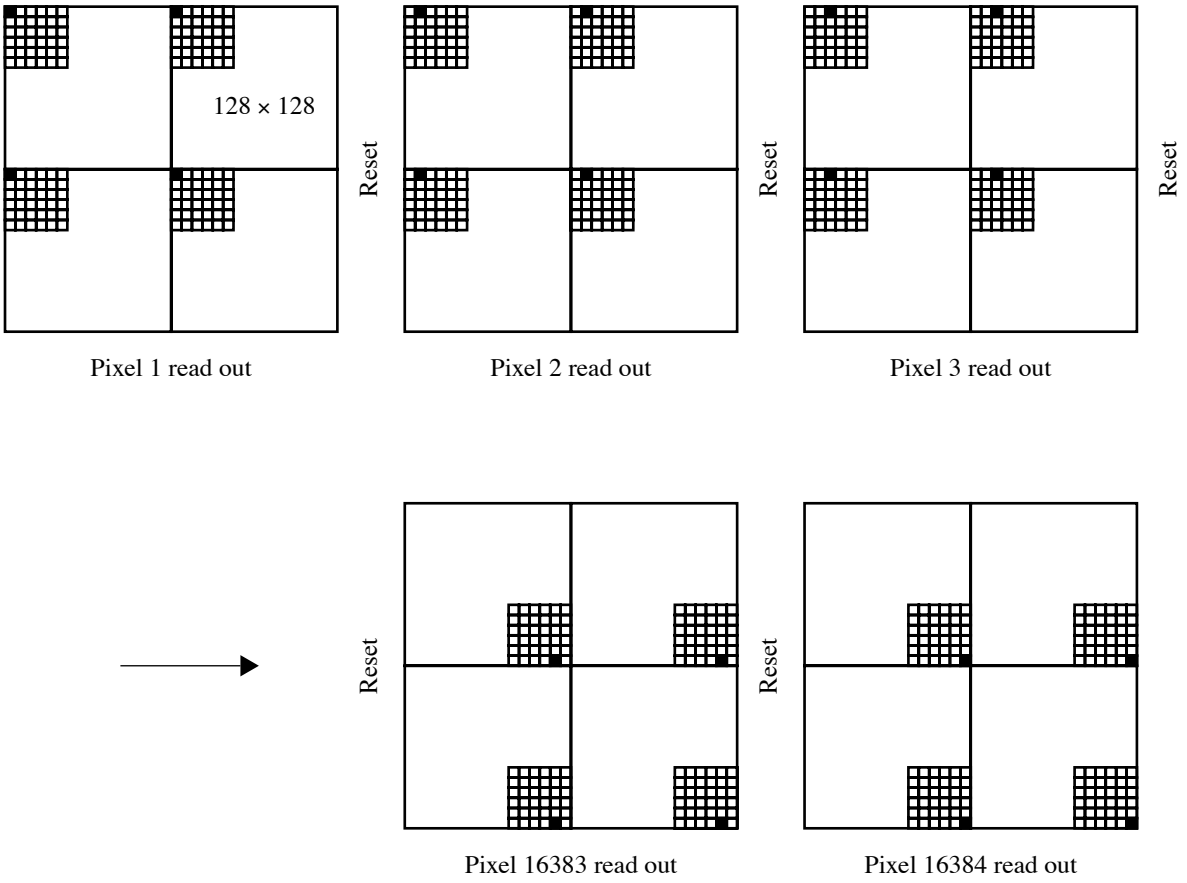

The advantage of this mode of operation is the ability to acquire objects significantly brighter than the normal saturation limit of the detector.

The disadvantages are several:

- The zeropoint in this mode is strongly non-linear, such non-linearity has not been characterized (nor are there plans to do so). Observations obtained with this mode are not calibrated and possibly not easily calibrated.
- Some observations will take a long time. `BRIGHTOBJ` mode exposures are therefore very sensitive to the quality of the pointing of HST. If the object changes (planetary rotation) or if the telescope pointing changes, it will affect different parts of the image differently.
- The D.C. offset of the detector output is not directly removed in this mode of operation. In general, the signal is very high and the offset does not matter. In some cases it will and this can be a detriment to the signal accuracy.
- There is also no cosmic ray correction or saturation detection in this mode of operation. Although they are still susceptible to cosmic rays, events are expected to be very rare as the integration time *per pixel* is very short.

APPENDIX D:

Techniques for Dithering, Background Measurement and Mapping

In this chapter...

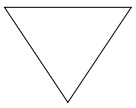

NICMOS patterns have been created to enable observers to perform dithering, chopping, and mapping, and these patterns are significantly different than those described in earlier versions of this handbook.

D.1 Introduction

Multiple exposures with small offsets in the pointing of the telescope between exposures are recommended for NICMOS observations. We distinguish three particular circumstances which may require small offsets:

- **Dithering** to permit the removal of dead or non-calibrated (i.e., non-correctable) pixels on the detectors, and to improve spatial sampling and mitigate the effects of detector's non-uniformities (i.e. sensitivity variations),
- **Chopping** to measure the background associated with an astronomical source, and
- **Mapping** to map a source larger than a single detector field of view.

The techniques described in this appendix may be used to accomplish any one or any combination of these goals.

Experience with NICMOS has shown that the background is spatially uniform (variations no larger than a few percent across the NIC3 field of view) and does not vary much with time (variations of less than 5% on orbit timescales). The description of the thermal background in Chapter 4, Chapter 9 and the Exposure Time Calculator provide a basis for estimating the relative contributions of source and background. It is strongly advised that provision for direct measurement of the background be included in proposals whenever observations at wavelengths greater than 1.7μm are performed. The frequency of such measurements should be about once per orbit, and more frequent measurements should be planned when the background must be measured to high accuracy.

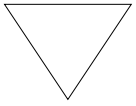

Background measurements are recommended for all observations at wavelengths longward of 1.7 μm.

Background images are obtained by offsetting the telescope from the target to point to an "empty" region of the sky. The ability to routinely offset the telescope pointing is a fundamental operational requirement for NICMOS. Starting in Cycle 9, HST programs use a standard *pattern* syntax, which replaced the old pattern optional parameters, and the even older scan parameters form. The new syntax allows multiple observations (including those with different filters) to be made at each point in the pattern, if desired. Observers should check the "Phase II Proposal Instructions" and APT documentation for instructions on how to set up a pattern, and the "pattern parameter form" that describes the motion. For simplicity, a set of pre-defined observing patterns has been built; the exposures taken under them are combined into one or more *associations*. A *pattern*, then, is a set of images of the same astronomical target obtained at pointings offset from each other, e.g. for the purpose of removing bad or grot-affected pixels from the combined image, for creating background images, or *mapping* an extended target. The *associations* of exposures are created for the purpose of simultaneously processing all the images

(through a given filter) from a single *pattern*. Thus, dithered images can be easily reassembled into a single image with the effects of minimizing bad pixels, or images taken in the long wavelength regime can be corrected for the thermal contribution, or observations of extended targets can be combined into a single large *map*.

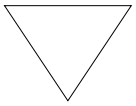

Starting with Cycle 14, previously unassociated NICMOS observations within a visit, using the same detector and filter, will be collected into an association, provided a `POS-TARG` is specified on the exposure line. The assignment of association numbers is determined from the APT Phase II file exposure line specifications for each visit. Currently, the new association assignments are NOT applicable to previously executed observations, nor does it apply to parallel observations.

Three distinct types of pattern motion are defined:

- *Dither*: Individual motions are limited to no more than 40 arcsec. These are intended to be used to perform small dithers, to measure backgrounds for compact sources, and to accomplish sequences of overlapping exposures for the construction of mosaics. Such sequences will be assembled into a single final image by the calibration pipeline.
- *Chop*: Motions up to 1440 arcsec are permitted. These are intended for the measurement of the background at one or more locations significantly removed from the target pointing. Non-contiguous background images and target images will be assembled into their own final image by the calibration pipeline.
- *Mapping*: Large motions the size of the aperture (e.g. 11, 20, or 50 arcsec) are specified. These are intended to cover large regions of the sky in a regular grid pattern.

Telescope motions involve overheads for physically moving the telescope and, if necessary, for re-acquiring the guide stars. Therefore, significant time overheads may be incurred by observations which need background subtraction or propose to map extended regions of the sky. A careful estimate of the overheads associated with a specific observation or set of observations is necessary to evaluate the number of orbits required (see Chapter 10).

D.2 Strategies For Background Subtraction

The most efficient strategy for removing the background from a science exposure strongly depends on the nature of the target and of the science to be accomplished. In general, two types of targets can be defined: compact and extended.

D.2.1 Compact Objects

For compact objects, such as point sources, background subtraction can be achieved by moving the target across the camera field of view (see Figure D.1). A dither pattern, which involves movements of a few arcsec from one exposure to the next, can then be used. This is an efficient way to build background images, since the target is present in each exposure, and a background image can be created from the stacking and filtering of all exposures.

Figure D.1: Dithering.

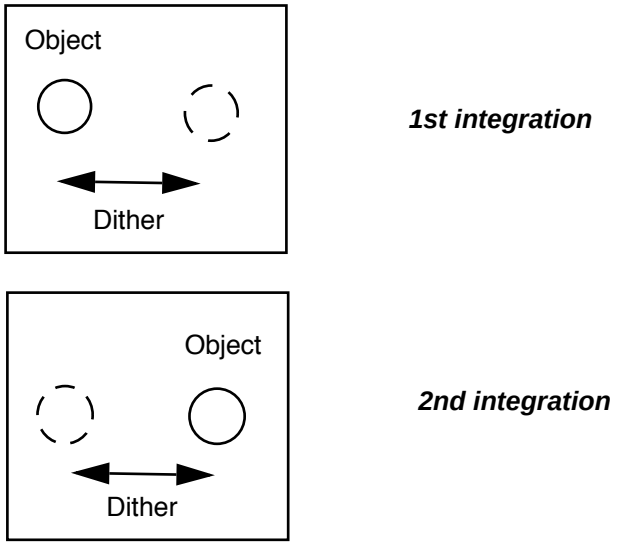

D.2.2 Extended Objects

For an extended object, which occupies a significant portion of the NICMOS field of view (star fields, nebulae, galaxies), the dithering technique cannot be applied to build background images. In this case, offsets to an adjacent field (chopping) chosen to be at least one camera field away in an arbitrary (or user specified) direction, are necessary. By offsetting in different directions, a stacked and filtered sky image can be created which removes the effect of contaminating objects in the offset

fields (see Figure D.2). As in the case of compact objects, these offsets might be quite small, but for large galaxies for example, they may need to be over considerable distances. The user has the ability to specify the offset value, directions, and the number of offsets in the Phase II pattern parameter specification.

Figure D.2: Chopping.

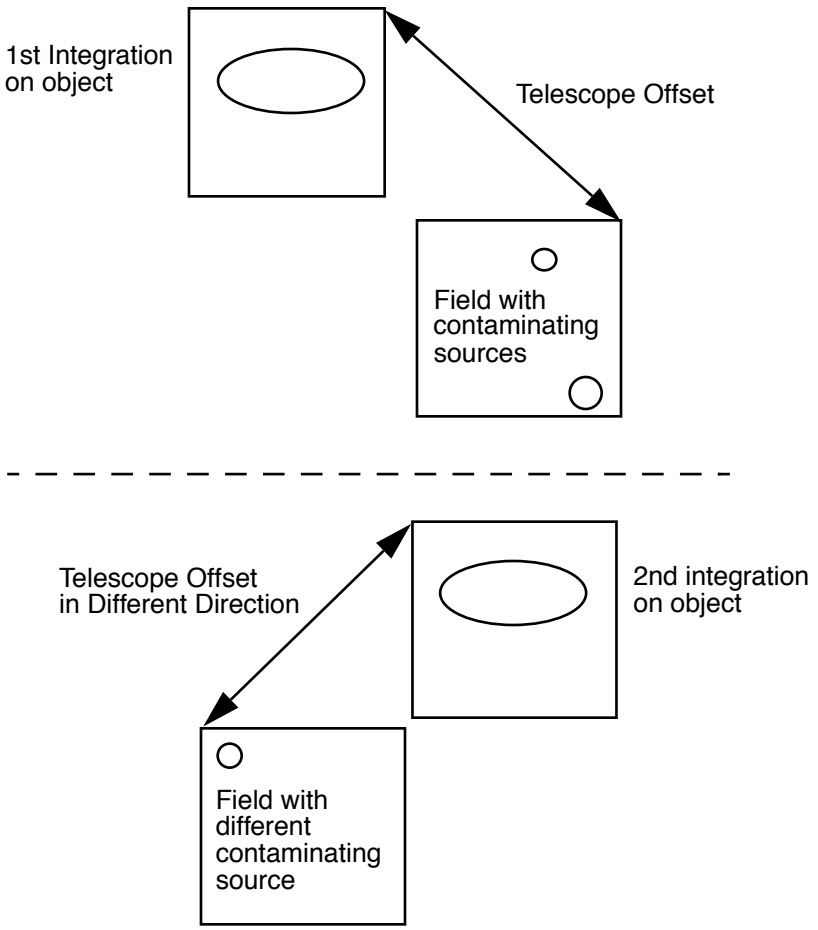

D.3 Chopping and Dithering Patterns

There are a set of fifteen pre-designed patterns available for NICMOS observations. Users may define their own pattern specifications as well in APT, during Phase II development. The pre-defined patterns include four dithering patterns, four chopping patterns, five dither-chop patterns, and two mapping patterns. For each of these, the observer will be able to specify the number of positions desired (1 to 50), the dither size (0 to 40

arcsec), the chop size (0 to 1440 arcsec, also used for mapping), and the orientation of the pattern with respect to either the detector or the sky. The `POS-TARG` special requirement will still be available for offsetting the telescope and creating custom-design patterns as well, but there are a number of advantages to using the pre-designed patterns:

- Patterns simplify the specification of complex observations in the Phase II proposal.
- All the observations pertaining to an exposure specification line in a pattern result in one association and are simultaneously calibrated and combined in the data calibration pipeline, including background calibration, cosmic ray removal, and flat fielding. Observations obtained with `POS-TARG` do not result in associations, and will have to be combined manually by the observer.
- Patterns permit the observation of a region on the sky with a fixed position angle without fixing spacecraft roll, which increases the number of opportunities to schedule the observations.

Multiple exposures may be obtained at each position by the use of the Phase II exposure level parameter for Iterations. This may be useful for cosmic ray removal. In addition, exposures in different filters at each pattern position can be obtained by linking together exposure lines as a pattern group.

The fifteen NICMOS pre-designed patterns are listed in Table D.1, together with applicable parameters, such as the allowed values for the number of steps in the pattern, the dither size, or the chop size. In addition, the figure number where the pattern is graphically shown is given in the last column of Table D.1. Offset sizes and number of steps in a pattern affect the amount of overhead time required to perform an observation (see Chapter 10). The effects of dithering or chopping on an astronomical image are shown in a set of examples in the next section.

Table D.1:NICMOS Pre-designed Observing Patterns and Parameters.

Pattern Name	Num. of Dithers	Num. Chops	Dither Size	Chop Size	Orient frame	See Figure
NIC-SPIRAL-DITH	1–50	NA	0–40	NA	camera	D.3
NIC-SQUARE-WAVE-DITH	1–50	NA	0–40	NA	camera	D.3
NIC-XSTRIP-DITH	1–50	NA	0–40	NA	camera	D.3
NIC-YSTRIP-DITH	1–50	NA	0–40	NA	camera	D.3
NIC-ONE-CHOP	NA	1–50	NA	0–1440	camera	D.4
NIC-TWO-CHOP	NA	1–50	NA	0–1440	camera	D.4
NIC-SPIRAL-DITH-CHOP	1–50	2	0–40	0–1440	camera	D.5
NIC-XSTRIP-DITH-CHOP	1–50	2	0–40	0–1440	camera	D.5
NIC-YSTRIP-DITH-CHOP	1–50	2	0–40	0–1440	camera	D.5
NIC-SKY-ONE-CHOP	NA	1–50	NA	0–1440	sky	D.6
NIC-SKY-TWO-CHOP	NA	1–50	NA	0–1440	sky	D.6
NIC-SKY-XSTRIP-DITH-CHOP	1–50	2	0–40	0–1440	sky	D.6
NIC-SKY-SPIRAL-DITH-CHOP	1–50	2	0–40	0–1440	sky	D.6
NIC-MAP	1–50	1–50	0–1440	0–1440	sky	D.6
NIC-SPIRAL-MAP	1–50	NA	0–40	NA	sky	D.6

Note on Orientation:

The pattern parameter syntax requires additional input on orientation. Specifically, the pattern must be defined in either the POS-TARG (camera) frame or the CELESTIAL (sky) frame. Dithering to remove detector characteristics should always be performed in the POS-TARG frame of reference. A pattern orientation angle may be specified as well. In the POS-TARG frame, this is the angle of the motion of the target from the first point of the pattern to the second, counterclockwise from the x detector axis (the directions are defined in Figure 6.1). In the CELESTIAL frame, the angle is measured from North through East.

Note that some of the pattern names in Table D.1 are doubled except for an additional -SKY-. The chop can be specified either as POS-TARG or CELESTIAL (default—see below for details).

Move the sky or the telescope?

The pattern syntax attempts to resolve the confusing dichotomy in the old pattern implementation, as to whether the pattern moves the telescope

or the target. It does this by providing the two reference frames described above.

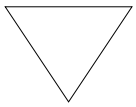

Patterns done in the POS-TARG reference frame will move the target, just as the "POS-TARG" special requirement does.

The telescope is slewed in small angle maneuvers (SAMs) so that the target moves within the detector frame of reference as specified by the pattern. When NICMOS images are displayed with IRAF, the POS-TARG x- and y-axis are as shown in Figure 6.1.

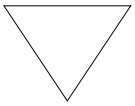

Patterns done in the CELESTIAL frame will move the telescope relative to the sky reference frame.

The target will always move in the opposite direction on the detector to the motion of the telescope.

D.3.1 Dither Patterns

The dither patterns are recommended for measuring the background adjacent to point sources (longward of 1.7 microns), and for the reduction of sensitivity variations and bad pixel effects. The four types of canned dither routines are NIC-XSTRIP-DITH, NIC-YSTRIP-DITH, NIC-SPIRAL-DITH, and NIC-SQUARE-WAVE-DITH. Most of the names are self-explanatory: the NIC-SPIRAL-DITH pattern produces a spiral around the first pointing; the NIC-SQUARE-WAVE-DITH pattern covers extended regions by moving along a square-wave shape; the NIC-XSTRIP-DITH and NIC-YSTRIP-DITH patterns move the target along the x and y directions of the detector, respectively. The difference between the NIC-XSTRIP-DITH and the NIC-YSTRIP-DITH patterns is that the first moves by default along the grism dispersion (orient default = 0˚), while the second moves orthogonal to the grism dispersion axis (orient default = 90˚). These patterns are illustrated in Figure D.3, and the direction of the x- and y-axis are the same as in Figure 6.1.

Note that there is an additional parameter for dithering patterns, to center the pattern on the target. The default is to start the dithering at the target position.

Figure D.3: Dither Patterns. Numbers represent sequence of positions where the target will be on the detector.

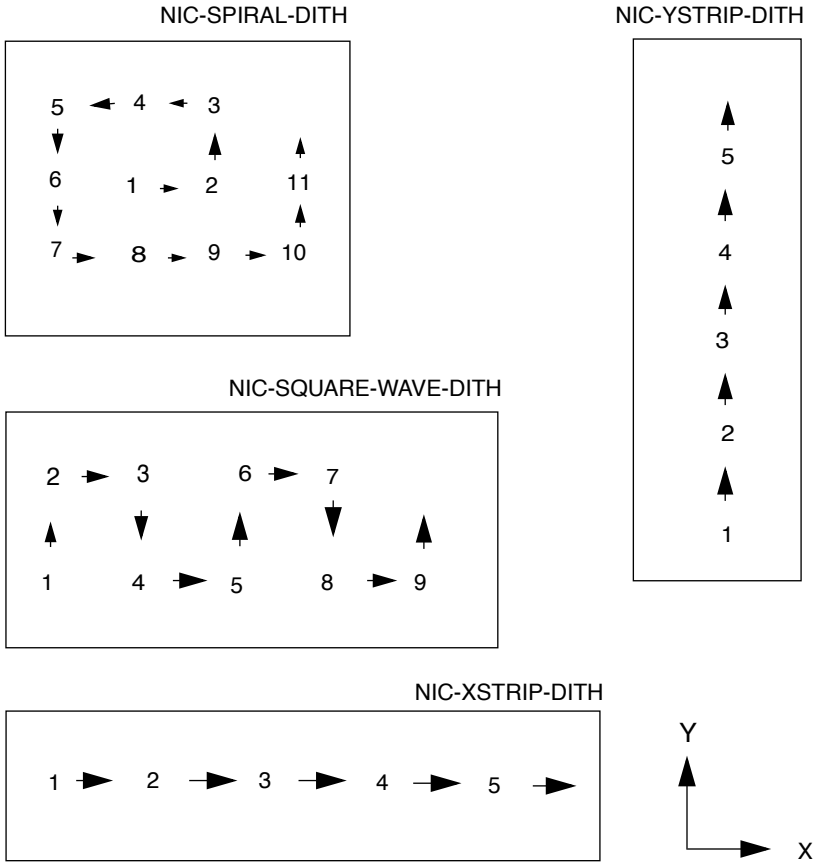

D.3.2 Chop Patterns

The chop patterns are recommended for measuring the background adjacent to extended targets. For each chop pattern, half of the exposures are taken on the target (position 1). There are two basic patterns, `NIC-ONE-CHOP` and `NIC-TWO-CHOP`. The `NIC-ONE-CHOP` pattern produces one image of the target and one image of the background. The `NIC-TWO-CHOP` pattern produces two images of the target and two background images, with the background fields positioned on opposite sides of the target. These patterns may be repeated by specifying the number of points in the primary pattern. For example, calling the `NIC-TWO-CHOP` pattern in an exposure with number of Iterations = 1 will produce four images, one on the target, one off to one side (+x detector direction), one back on the target, and one off to the other side (–x detector direction). If the number of Iterations = 2, the observer gets eight images, two images at each position of the pattern. If the primary pattern has number of Points = 2, the pattern will repeat (1,2,3,4,1,2,3,4), and the

observer will get eight images. Chop patterns are illustrated in Figure D.4, and the direction of the x- and y-axis are the same as in Figure 6.1.

Because chopping is best done to empty regions of the sky, we provide a set of chopping patterns that are in the CELESTIAL coordinate system, as well as the standard set (that are in the POS-TARG frame). These have the word SKY in their name, and must have a pattern orientation angle (degrees E from N for the first motion of the pattern) supplied. These should be used when the region around the target contains some objects that should be avoided when measuring the background. SKY patterns are illustrated in Figure D.6, and the direction of the x- and y-axis are the same as in Figure 6.1.

Figure D.4: Chop Patterns.

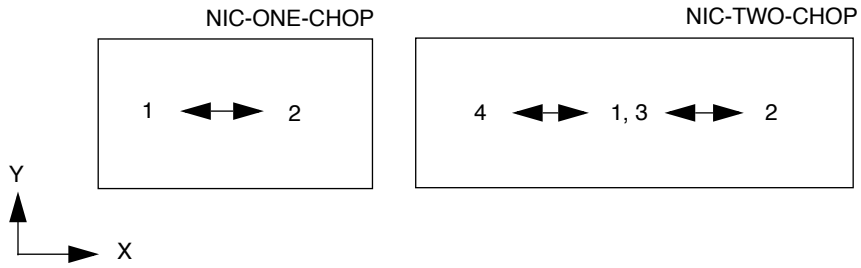

D.3.3 Combined Patterns

The combined patterns permit dithering interleaved with chops to measure the background. They are recommended for simultaneous minimization of detector artifacts and background subtraction, for observations beyond 1.7 microns. Three types of combined patterns are implemented: NIC-SPIRAL-DITH-CHOP, NIC-XSTRIP-DITH-CHOP, and NIC-YSTRIP-DITH-CHOP. Their characteristics are analogous to the dither patterns NIC-SPIRAL-DITH, NIC-XSTRIP-DITH, and NIC-YSTRIP-DITH, respectively, with the addition that each dither step is coupled with a background image obtained by chopping. These combined patterns are shown in Figure D.5, and the direction of the x- and y-axis are the same as in Figure 6.1.

In a manner similar to the regular chopping patterns, the combined patterns have "SKY" versions implemented in the CELESTIAL frame. The chop patterns require an pattern orientation angle which is defaulted to 0.0 (North). The angle is measured from North through East. These are illustrated in Figure D.6.

Figure D.5: Combined Patterns.

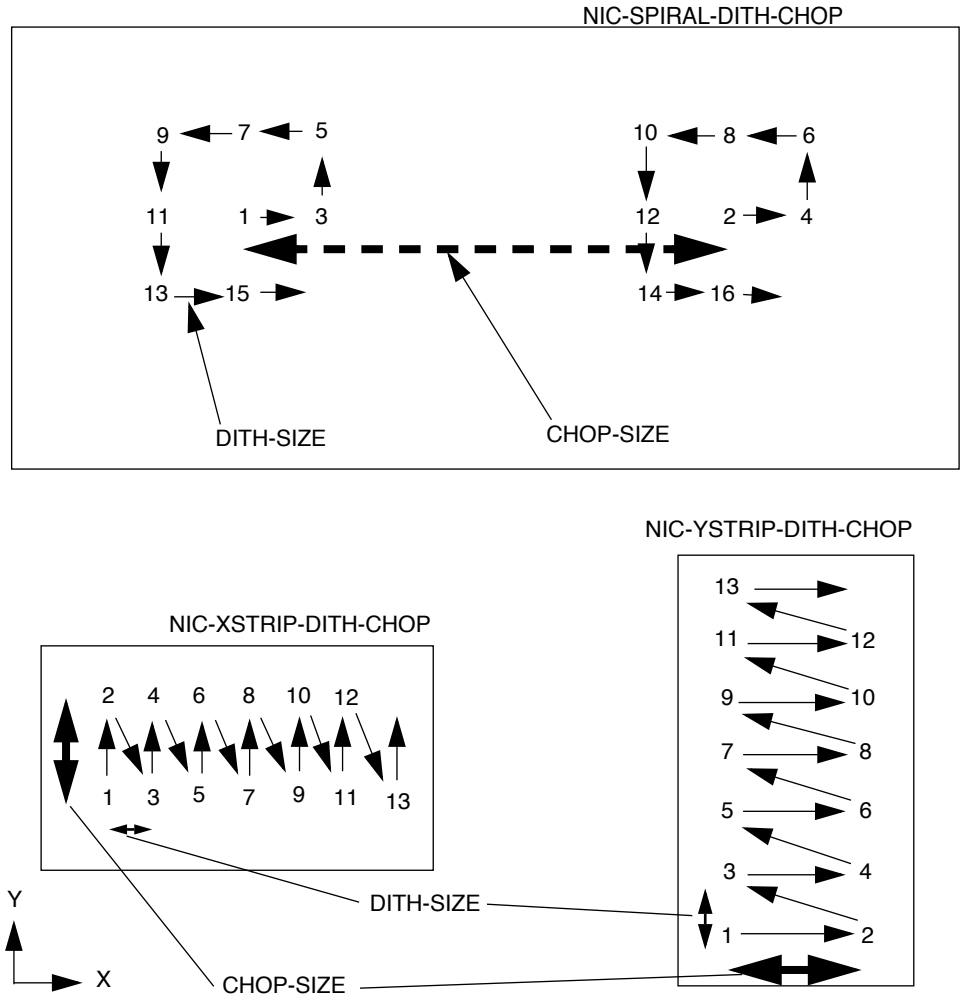

D.3.4 Map Patterns

There are two `MAP` sequences. These allow the telescope to be pointed at a regular grid of points, doing a series of exposures at each point. These are done in the `CELESTIAL` frame, so a pattern orientation angle must be supplied, and the telescope motion on the sky is specified (rather than the target motion relative to the detector, see note above). The `NIC-SPIRAL-MAP` sequence is basically the `NIC-SPIRAL-DITH` sequence in the `CELESTIAL` frame, and automatically maps the (square or rectangular) region around the target. The `NIC-MAP` sequence defines an arbitrary parallelogram on the sky. The observer may specify the number of points in each of two directions, and the position angle (E of N) of each direction.

As with the dithering patterns, the observer has the option of specifying whether the target is centered in the pattern or not. The target will be

centered in the NIC-SPIRAL-MAP pattern if there are 9, 25, 49,... points in the pattern, but will not necessarily be centered otherwise. The observer can specify if the target should be centered along one axis or the other, or both, of the parallelogram defined by the sequence. These are illustrated in Figure D.6.

Figure D.6: Patterns on the sky. Numbers represent sequence of aperture pointings on the sky.

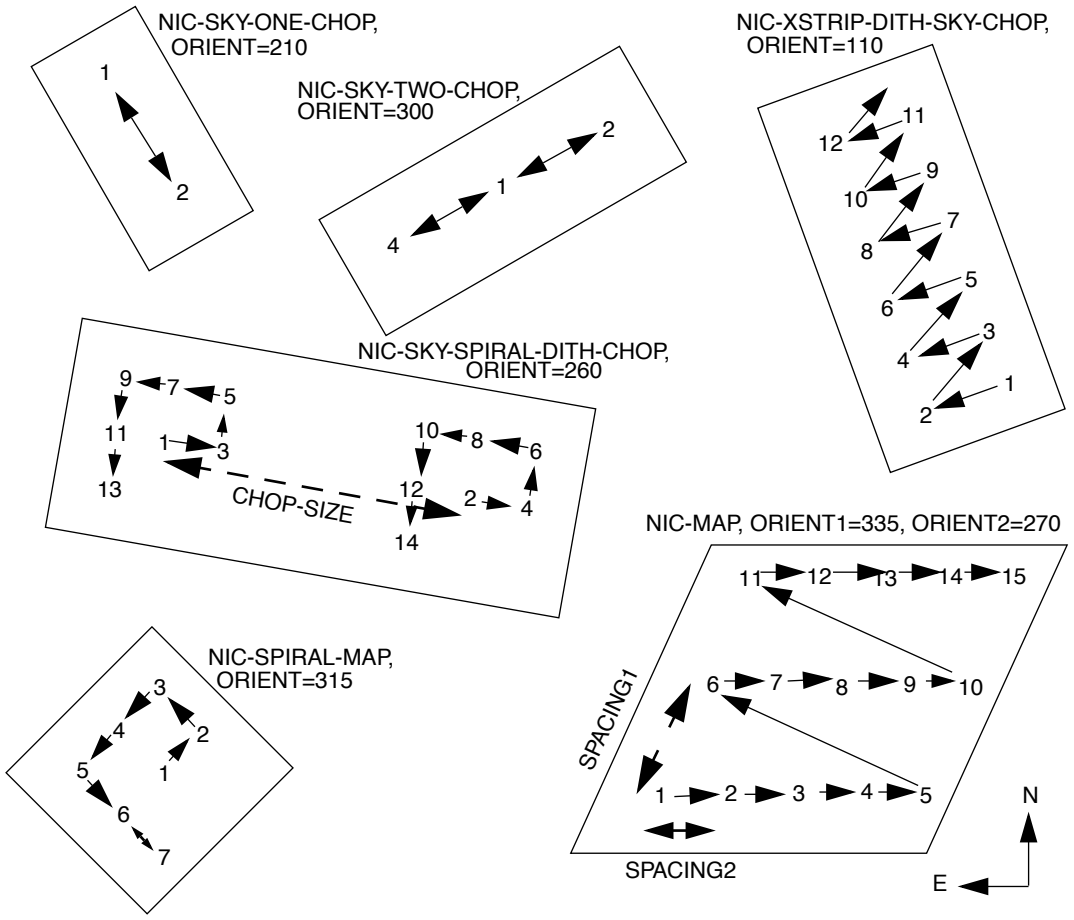

D.3.5 Combining Patterns and POS-TARGs

On occasion, it may be advantageous to specify a POS-TARG on the exposure line to move the target to a different position than the aperture reference point. For this situation, the POS-TARG offset is always performed first to change the telescope pointing. For example, a user wants to position a target in each of the four quadrants in Camera 2. The user specifies the NIC2-FIX aperture for which the aperture reference point is at the center of the array (128×128 pixels) and specifies a POS-TARG –4.8,–4.8. A four point dither pattern using the NIC-SPIRAL-DITH pattern with point spacing = 9.6 arcseconds and pattern orient = 0 would

achieve the desired results. (See the following example.) The target will be in the lower left quadrant of the array for the first position of the pattern, the lower right for the second position, the upper right for the third position, and in the upper left quadrant for the fourth position of the pattern.

D.3.6 Generic Patterns

Predefined convenience patterns are recommended for NICMOS observations. These predefined patterns can be selected using the APT pattern editor. Observers can specify their own pattern by using a generic pattern form. Patterns are not supported by **calnicb** which combines dithered observations into a mosaic. The IRAF/STSDAS task **drizzle** and **MultiDrizzle** (Koekemoer *et al*., 2002 HST Calibration Workshop, p337) can also be used to combine images into a mosaic.

D.4 Examples

The next few pages show some selected examples of how the patterns work on astronomical observations.

Figure D.7: NIC-SKY-TWO-CHOP pattern.

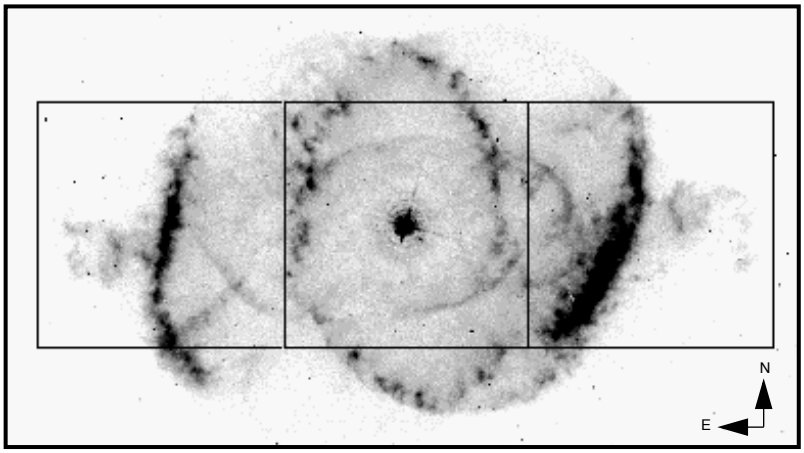

Spacing (chop throw) = 1 detector width,
Pattern Orient = 270°,
Visit Orient = 225°,
(Frame=CELESTIAL)

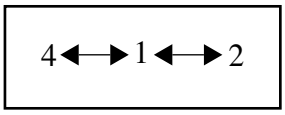

Images Taken:

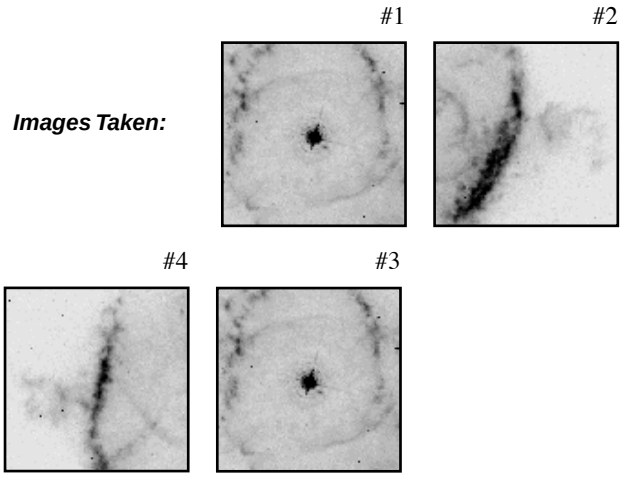

Figure D.8: NIC-MAP Pattern.

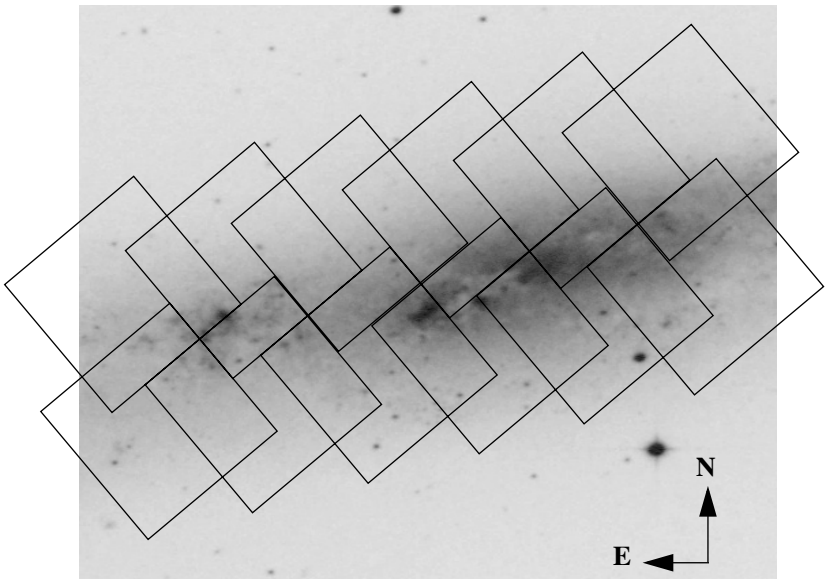

Spacing = detector size/√2
Frame= CELESTIAL
Pattern2 Orient = 284˚
Pattern1 Orient = 14˚

No visit level orient specified: nominal roll (by chance, for this example) puts detector Y at position angle 310˚.

Could cover the area more efficiently with Spacing = 0.866×detector size, and Pattern1 Orient = Pattern2 Orient + 60˚.

In either case, the lack of visit orient specification greatly increases the chance of scheduling the observation.

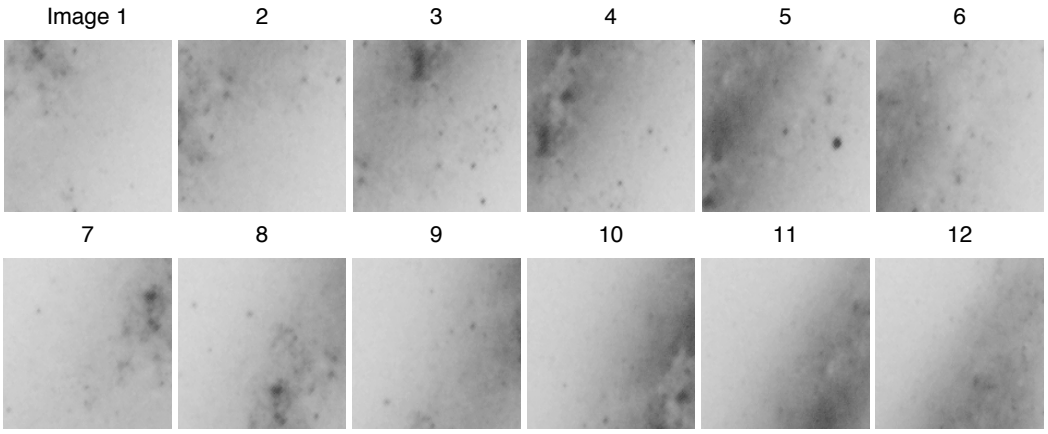

D.5 Types of Motions

The Phase II optional parameter `OFFSET` defines which type of telescope motion will be performed during a pattern. Telescope motions fall into three categories:

- Small angle maneuvers (SAMs) where FGS Fine Lock guiding is maintained. Such SAMs are typically limited to < 2 arcmin from the point of the initial guide star acquisition. This is the practical limit of the radial extent of the pattern. Often it will be smaller due to guide star availability.
- SAMs without FGS guiding (i.e. `GYRO` pointing control). These are necessary for larger motions (> 2 arcmin). The telescope will drift at a rate of 1 to 2 milliarcsec per second of time (elapsed time since dropping to gyro—not exposure time).
- SAMs with `RE-ACQ`uisitions of guide stars at each return to the target position. This can be used to chop between a target and an offset background measurement pointing (which would be observed with `GYRO` pointing control).

The available options for `OFFSET` are:

- `SAM`, the default, will use guide stars whenever possible. If a motion, or the sequence of motions, moves the telescope sufficiently from the original position that guide stars are no longer available, then exposures will be obtained using `GYRO` control. If a subsequent motion returns the telescope to a point where the original guide stars become available then the guide stars will be `RE-ACQ`uired. This incurs an overhead of ~3 minutes for each `RE-ACQ`uisition.

The use of the Field Offset Mirror (FOM) to perform dithering and mapping is an “available” (not “supported”) mode of observation. The FOM is not exactly repeatable, so artifacts on the mirror may appear to move around. Observations requiring small and rapid offsets (or making observations in parallel to another instrument) may benefit from this mode. Note that the astigmatism changes with FOM offsets. Note: flat field calibration reference files are only available for the nominal FOM position.

APPENDIX E:

The NICMOS Cooling System

In this chapter . . .

E.1 The NICMOS Cooling System

The purpose of the NICMOS Cooling System (NCS) is to enable continued operation of NICMOS by cooling the detectors to a scientifically useful temperature. This is achieved by a closed-loop circuit which runs cryogenic gas through a coil inside the NICMOS dewar. The NCS provides excellent temperature control, the detectors are maintained at 77.15±±0.10K. There is margin in the compressor speed to compensate for variations in the parasitic heat load due to orbital and seasonal changes in spacecraft attitude as well as in the operation of the HST science instruments in the aft shroud.

The NCS consists of three major subsystems: 1) a cryocooler which provides the mechanical cooling, 2) a Capillary Pumped Loop (CPL) which transports the heat dissipated by the cryocooler to an external radiator, and 3) a circulator loop which transports heat from the inside of the NICMOS dewar to the cryocooler via a heat exchanger. Additional elements of the NCS are the Power Conversion Electronics (PCE) which provides the up to 400 W of power needed by the cooler, and the Electronic Support Module (ESM) which contains a microprocessor to control the heat flow. Figure E.1 shows a schematic of the system.

Figure E.1: Overview of the NCS.

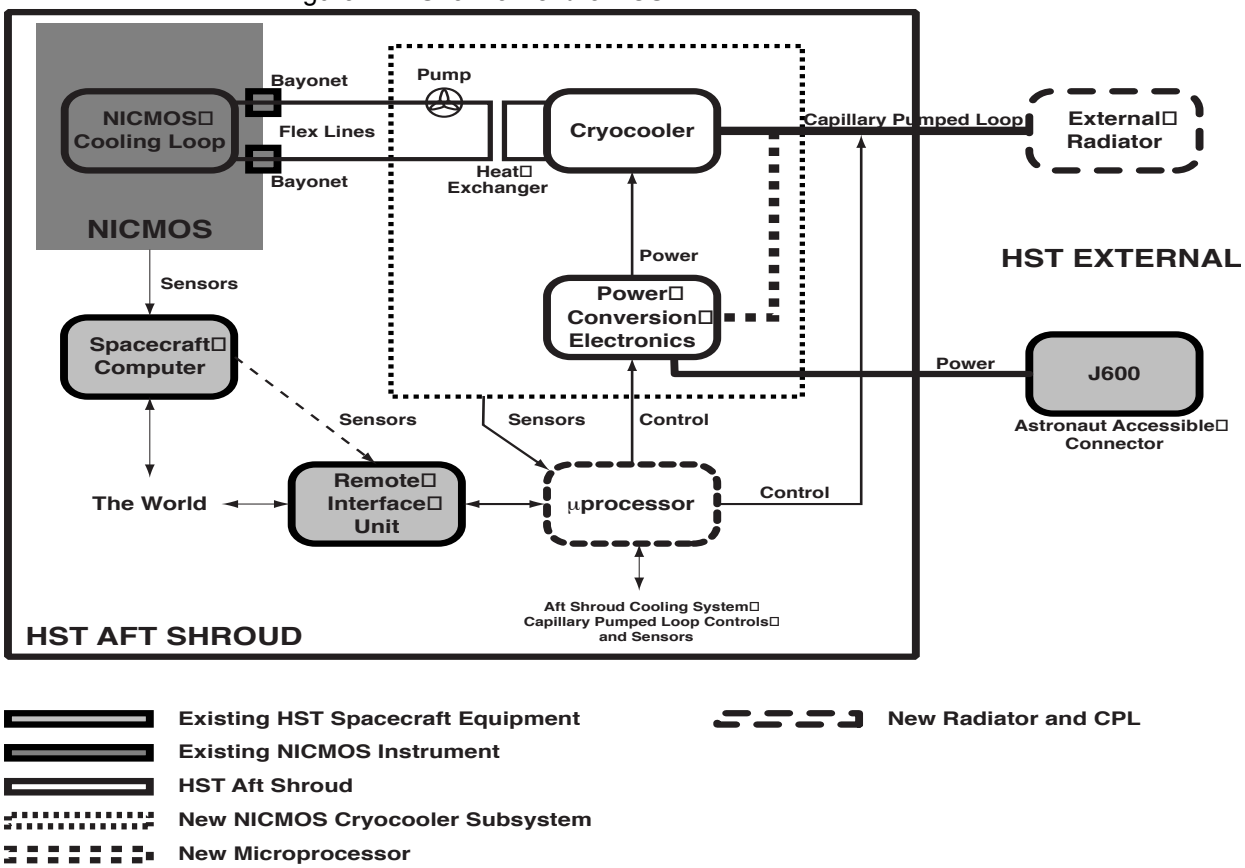

In what follows, we give a more detailed description of the NCS subsystems:

The cryocooler, manufactured by Creare, Inc., is a reverse-Brayton cycle turbine design. The compression and subsequent expansion of the Neon gas results in a net cooling which is used to remove heat from the NICMOS dewar via the heat exchanger to the circulator loop (see Figure E.1). The Creare design has several major advantages for application on HST. First, the closed loop system operates at very high speed—about 7000 revolution per second—which limits the probability of mechanical coupling to the HST structure, thus minimizing the risk of spacecraft jitter. Second, the system is capable of providing large cooling power. Finally, the Creare design is compact enough to fit into the previously unused space between the NICMOS enclosure and the HST aft end bulkhead.

On average, the cryocooler dissipates about 375 W of power which needs to be removed from the aft shroud. This is achieved via a Ammonia-filled Capillary Pumped Loop (CPL) that thermally connects the housing of the compressor pump with an external radiator. The continuous heat flow through the (passive) CPL lines is maintained by a set of heaters that are controlled by the ESM micro controller.

The heat from inside NICMOS is transported to the cryocooler via a set of flex lines. The flex lines connect to the inside of the dewar via bayonet fittings at an interface plate outside of the dewar which was accessible to

the astronauts during SM3B. The circulator loop was then filled with Neon gas from high pressure storage bottles. The bottles provide enough gas to purge, pressurize, and, if necessary, re-pressurize the circulator loop. The Neon gas, driven by a high speed circulator pump and cooled via the heat exchanger to the cryocooler loop, circulates through the cooling coil at the aft end of the NICMOS dewar (see Figure E.2), thus cooling the entire instrument.

The ESM uses the telemetry readings from the inlet and outlet temperature sensors at the NICMOS/NCS interface in an active control law to regulate the cooling power of the NCS, and thus provide stability of the operating temperature of the NICMOS detectors. Because of the sensitive dependence of a number of detector characteristics on temperature (see Chapter 7), the temperature stability is a crucial requirement on NCS performance. To date, the stability has been extremely good with T=77.15 with a variation of ~0.10K

All components of the NCS are combined into a common enclosure, the NICMOS Cryo Cooler (NCC). Figure E.2 shows a line drawing of the NCC, without any Multi-Layer Insulation (MLI). The system was successfully tested in space during the HST Orbital Systems Test (HOST) shuttle mission in fall 1998. Remaining uncertainties about the NCS performance stemmed from the natural lack of tests with the actual NICMOS dewar. This led to a longer than expected cooling time following the NCC installation, but has not affected the temperature stability.

Figure E.2: Line drawing of the NCC structure.

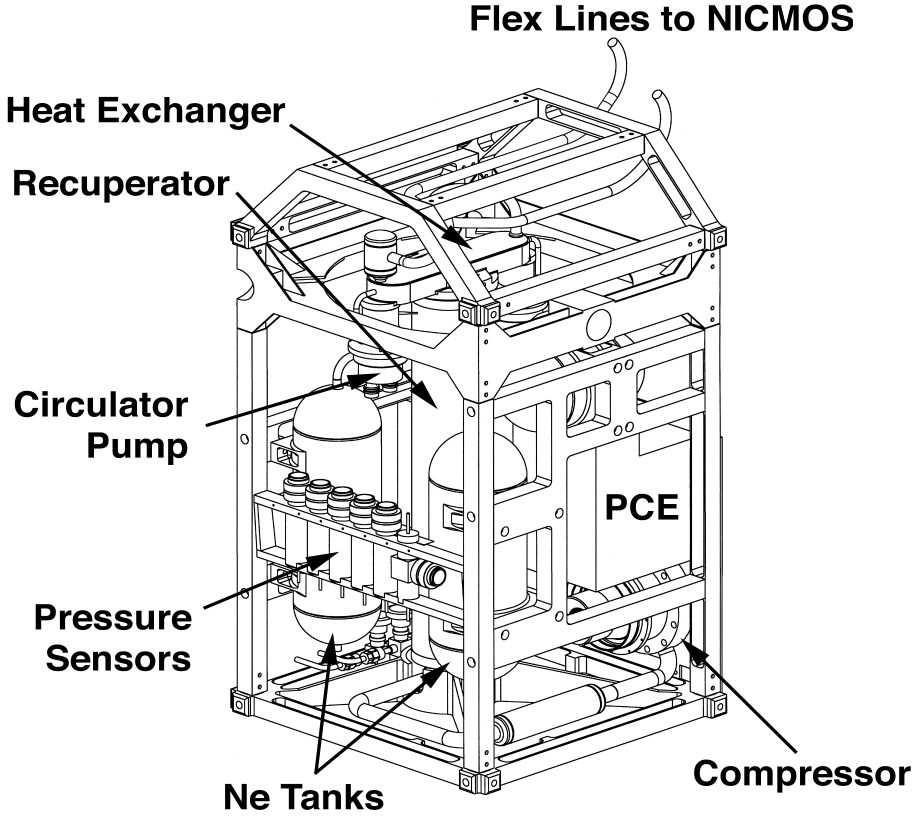

Glossary and Acronym List

The following terms and acronyms are used in this Handbook.

ACCUM: Accumulate readout mode for NICMOS observations.

ACS: Advanced Camera for Surveys.

ACQ: Observing mode in which the brightest source is located in a sub-array and the telescope is repositioned to place the source behind the coronagraphic hole.

A-D: Analog to digital.

ADC: Analog to digital converter.

ADU: Analog digital unit; 1 ADU = 1 DN.

ASCS: Aft Shroud Cooling System.

APT: The Astronomer's Proposal Tool.

Breathing: Short term focus oscillations due to thermal variations on an orbital time scale.

BRIGHTOBJ: Bright object observing mode.

CALNICA: Primary NICMOS calibration task.

CALNICB: Secondary NICMOS calibration task used after CALNICA on those exposures which comprise an association.

CCD: Charge-coupled device. Solid-state, light detecting device.

CDBS: Calibration Data Base System; system for maintaining reference files and tables used to calibrate HST observation datasets.

Chop: A spatial offset of up to 1440 arcsec of the aperture with respect to the target, intended for the measurement of the background at one or more locations significantly removed from the target pointing.

COS: Cosmic Origins Spectrograph.

COSTAR: Corrective Optics Space Telescope Axial Replacement.

CP: Call for Proposals.

CPL: Capillary Pumped Loop.

CR: Cosmic Ray.

CVZ: Continuous Viewing Zone.

CP: Contact Scientist.

Dither: A small spatial offset (no more than 40 arcsec) of the position of the target in the aperture between successive observations.

DN: Data Number.

Drizzle: A technique (and STSDAS task) for the linear image reconstruction of dithered images.

DSS: Digitized Sky Survey.

DQ: Data Quality.

DQE: Detector Quantum Efficiency.

ESM: Electronic Support Module.

ETC: Exposure Time Calculator.

FAQ: Frequently Asked Questions.

FDA: Field Divider Assembly.

FET: Field Effect Transistor.

FGS: Fine Guidance Sensors.

FITS: Flexible Image Transport System. A generic IEEE- and NASA-defined standard used for storing image data.

FOC: Faint Object Camera.

FOM: Field Offset Mirror (or mechanism).

FOS: Faint Object Spectrograph.

FOV: Field Of View.

FPA: Focal Plane Array.

FSW: Flight Software.

FTP: File Transfer Protocol; basic tool used to retrieve files from a remote system.

FWHM: Full Width at Half Maximum.

GHRS: Goddard High Resolution Spectrograph.

GO: General Observer.

GS: Guide Star.

GSC: Guide Star Catalog.

GSFC: Goddard Space Flight Center.

GTO: Guaranteed Time Observer.

HOST: HST Orbital Systems Test.

HSP: High Speed Photometer.

HST: Hubble Space Telescope.

ICD: Interface Control Document; defines data structures used between software or systems to ensure compatibility.

IDT: Instrument Development Team.

IR: Infrared.

IRAF: Image reduction and analysis system. The system on which STSDAS is built.

IRAS: Infrared Astronomical Satellite.

ISR: Instrument Science Report.

Jansky: The standard flux unit for NICMOS documentation and software. 1 Jy = 1.0×10^{-26} W/m^2/Hz = 1.0×10^{-23} erg/s/cm^2/Hz.

Jy: Jansky.

K: Degrees Kelvin.

LSF: Line Spread Function.

MLI: Multi-Layer Insulation.

MOS: Multi-Object Spectroscopy.

Mosaic: A single image produced by combining the multiple images contained in a NICMOS associated data set; this combination is done by the STSDAS task **calnicb**.

MULTIACCUM: Multiple-accumulate readout mode for NICMOS observations.

MultiDrizzle: Automates and simplifies the detection of cosmic rays and the combination of dithered observations using the Python scripting language and PyRAF (Koekemoer *et al*., 2002 HST Calibration Workshop, p337).

NCC: NICMOS CryoCooler.

NCS: Nicmos Cooling System.

NICMOS: Near-Infrared Camera and Multi-Object Spectrometer.

NIR: Near Infrared.

NUV: Near ultraviolet.

OPUS: OSS and PODPS Unified Systems.

OSS: Observation Support System.

OTA: Optical Telescope Assembly.

OTFR: On-The-Fly Reprocessing.

PACOR: Packet process.

POD: Packetized Observation Data.

PAM: Pupil Alignment Mirror (or mechanism).

PC: Program Coordinator.

PCE: Power Conversion Electronics.

PED: Proposal editor.

Phase I: The process of submitting a proposal for HST observations.

Phase II: The process of designing accepted HST observing proposals.

PI: Principal Investigator.

PODPS: Post-Observation Data Processing System.

PSF: Point Spread Function.

QE: Quantum Efficiency.

RA: Right Ascension.

RMS: Root Mean Square.

RTO: Reuse Target Offset.

SAA: South Atlantic Anomaly.

SAM: Small Angle Maneuver.

SAMP-SEQ: Pre-defined sample sequence (readout times) for NICMOS observations.

SLTV: System Level Thermal Vacuum (testing phase).

SM: Servicing mission.

SMOV: Servicing Mission Orbital Verification.

S/N: Signal-to-Noise ratio. Also seen as SNR.

SSR: Solid State Recorder.

STAN: Space Telescope Analysis Newsletter.

StarView: The user interface to the HST data archive.

ST-ECF: Space Telescope European Coordinating Facility.

STIS: Space Telescope Imaging Spectrograph.

STScI: Space Telescope Science Institute.

STSDAS: Space Telescope Science Data Analysis System. The complete suite of data analysis and calibration routines used to process HST data.

TAC: Telescope Allocation Committee.

TEC: Thermal Electrically Cooled shells.

TinyTim: Program which produces simulated HST point spread functions.

URL: Uniform resource locator; address for WWW.

UV: Ultraviolet.

VCS: Vapor Cooled Shield.

WFPC: Wide Field/Planetary Camera.

WFPC2: Wide Field Planetary Camera 2; replacement for WF/PC installed during first servicing mission of December 1993.

WWW: World Wide Web; hypertext-oriented method for finding and retrieving information over the Internet.

YSO: Young Stellar Object.

Index

D

E

F

G

Q

R

S

W

Y

Z